Technische Universität München
Fakultät fur Physik
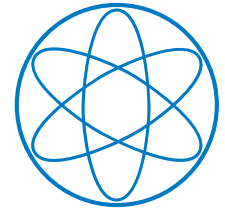
Max-Planck-Institut für Physik
(Werner-Heisenberg-Institut)

In cooperation with CERN
Supported by the Wolfgang Gentner Programme

Doctoral Thesis

Study of the radiation background and of new monitoring tools at the LHC for Run 3 and the HL-LHC

Untersuchung des Strahlungshintergrunds und neuer Überwachungsinstrumente am LHC für Run 3 und HL-LHC

Submitted by:

Daniel Prelipcean

Supervisors:
at CERN: Dr. Giuseppe Lerner
at TUM: apl. Prof. Dr. Hubert Kroha

Technische Universität München
TUM School of Natural Sciences

Study of the radiation background and of new monitoring tools at the LHC for Run 3 and the HL-LHC

Daniel Prelipcean

Vollständiger Abdruck der von der TUM School of Natural Sciences der Technischen Universität München zur Erlangung eines

Doktors der Naturwissenschaften (Dr. rer. nat.)

genehmigten Dissertaion.

Vorsitz: apl. Prof. Dr. Norbert Kaiser

Prüfende der Dissertation:
1. apl. Prof. Dr. Hubert Kroha
2. Prof. Dr. Lothar Oberauer

Die Dissertation wurde am 04.12.2024 bei der Technischen Universität München eingereicht und durch die TUM School of Natural Sciences am 16.01.2025 angenommen.

Abstract

The hostile radiation environment at the Large Hadron Collider (LHC) affects detectors, accelerator beamline elements and electronic devices, requiring the careful characterisation of the radiation levels via both measurements and simulations. This thesis aims to study the mixed radiation field along the LHC tunnel in a previously insufficiently explored area: on one hand, via developing the FLUKA simulation model of the accelerator, benchmarked with measured data, and on the other hand, via assessing the suitability of a Timepix3 detector technology for the new application as a radiation monitor at the LHC and for its upgrade, the High Luminosity LHC (HL-LHC).

The radiation field at LHC is studied based on the role (collimation, collisions, etc.) of each insertion region (IR) (straight region of the accelerator). At insertion region 4 (IR4), responsible for beam acceleration, a plethora of beam instruments are hosted. It is now systematically studied for the first time, focusing on the operation of two beam gas monitors, the Beam Gas Vertex (BGV) and the Beam Gas Curtain (BGC). Demonstrator instruments have been used during Run 2 (3) for the BGV (BGC), allowing to to assess their performance for the radiation measurements at the current LHC accelerator, as well as to predict the radiation levels at the future HL-LHC machine. Neither instrument generates radiation levels that would impede the critical operation of the accelerator, but do exhibit radiation showers that are significantly above background.

Furthermore, a novel radiation monitor based on the Timepix3 detector, a $300 \, \mu$m thick silicon pixel sensor with integrated readout electronics has been characterised in detail. Two test campaigns aimed to perform an energy calibration, i.e. conversion of the measured time over threshold (ToT) signal into deposited energy E_{dep}, carried out using quasi-mono energetic hadron beams from 0.6 to 8.4 MeV. The calibration analysis at the energy deposition cluster level indicates that the detector operates in a linear regime up to a particle energy of 2 MeV with $ToT = E_{dep} \cdot (993 \pm 93)$ [25 ns/MeV] + $N \cdot (23.10 \pm 2.14)$ [25 ns/pixel], with N being the number of pixels in the cluster, while evidence of saturation effects is visible for higher particle energies. Two further test campaigns have been performed using neutron in two different energy regimes: (i) a cold neutron beam (moderated from a nuclear fission reactor) with 6.67 meV peak energy, also using LiF conversion layers, and (ii) neutrons emitted by an americium-beryllium (AmBe) source up to 10 MeV.

The Timepix3 radiation monitor has been deployed in 2023 at LHC IR4 to assess the radiation field during the nominal LHC operation (considered as the background), and compared with the BGC measurements (considered as the signal). The foreseen Timepix3 usages comprise of: (i) complementing the existing standard monitoring of the total ionizing dose and the particle fluence, and (ii) providing new capabilities, such as locating the radiation source and functioning as a linear energy transfer detector. The agreement between the simulated BGC signal and the Timepix3 measurements are slightly undersimulated, but within errorbars.

In addition, the results of a transversal muon flux measurement campaign with the Timepix3 radiation monitor during a luminosity run of the LHCb experiment are presented, yielding a muon rate around 8.6 counts/cm^2/pb^{-1}, matching the normalized FLUKA simulation predictions with a counting rate (CR) ratio $\mathcal{R}_{\mathrm{CR}} = CR_{\mathrm{sim}}/CR_{\mathrm{meas,tpx}} = 1.77 \pm 26\%$.

In all cases, the main advantage of the Timepix3 radiation monitor is twofold: the good timing resolution and the low energy threshold enable the prompt detection of beam losses even in low radiation areas such as the shielded alcoves of the accelerator, where electronics are typically located. It outperforms many conventional detectors by providing more precise measurements, faster real-time data, allowing to eventually classify the incident particles according to their type, incident direction and energy, by measuring the radiation field on a particle by particle basis, which has been demonstrated.

Zusammenfassung

Die hohe Strahlenbelastung im Large Hadron Collider (LHC) beeinflusst die dort platzierten Detektoren, Beschleunigerkomponenten und Elektronik negativ, was eine sorgfältige Charakterisierung der Strahlungsumgebung durch Messungen und Simulationen verlangt. Das Ziel dieser Arbeit ist es, das gemischte Strahlungsfeld in insertion region 4 (IR4), einer bisher unzureichend erforschten Region des LHC, zu untersuchen: einerseits durch die Entwicklung eines FLUKA-Simulationsmodells des Beschleunigers, andererseits durch die Evaluierung der Eignung der bekannten Timepix3-Detektortechnologie für die neue Anwendung als Strahlungsmonitor am LHC und für dessen Erweiterung, den High Luminosity LHC (HL-LHC).

Zum ersten Mal wird die Strahlungsumgebung in IR4 des LHC systematisch untersucht, eine Umgebung reich an Strahlendiagnostikinstrumenten. Ein besonderer Fokus liegt auf der Verwendung von zwei bestimmten Instrumenten, dem Beam Gas Vertex (BGV) und dem Beam Gas Curtain (BGC). Prototypen dieser Intrumente wurden während des Run 2 bzw. Run 3 für den BGV bzw. BGC getestet. Mit diesen Daten können die Auswirkungen auf den derzeitigen LHC Beschleuniger bestimmt werden und Prognosen für die Strahlungsniveaus an der HL-LHC Maschine erstellt werden.

Des Weiteren wird ein neuartiger Strahlungsmonitor, der auf einem Timepix3-Detektor aus Silizium mit einer Dicke von 300 μm basiert, im Detail charakterisiert. Zwei Testkampagnen zielten darauf ab eine Energiekalibrierung, das heißt eine Umwandlung der gemessenen Zeit über dem Schwellenwert, time over threshold (ToT), in deponierte Energie E_{dep}, durchzuführen. Diese beiden Kampagnen verwendeten quasi-monoenergetischen Hadronenstrahlen von 0.6 MeV bis zu 8.4 MeV. Die Analyse der Kalibrierung auf Clusterebene zeigt, dass der Detektor in einem linearen Bereich mit $ToT_{reg} = E_{dep} \cdot (993 \pm 93)$ [25 ns/MeV] $+ N \cdot (23.10 \pm 2.14)$ [25 ns/pixel] operiert, wobei N die Anzahl der Pixel ist. Zwei weitere Testkampagnen wurden mit Neutronenstrahlen in unterschiedlichen Energiebereichen durchgeführt: (i) mit kalten Neutronen mit einer durchschnittlichen Energie von 6.67 meV und LiF Konversionsschichten, und (ii) mit einer americium-beryllium (AmBe)-Quelle, die Neutronen bis zu 10 MeV aussendet.

Mit den Erkenntnissen aus den vorher erwähnten Studien, wurde der Timepix3-Strahlungsmonitor im Jahr 2023 in der IR4 eingesetzt, um das Strahlungsfeld während des nominalen LHC-Betriebs (Hintergrund) und des BGC-Betriebs (Signal) zu bewerten, wodurch die beiden neu entwickelten Instrumente zur Strahlungsüberwachung zusammengeführt werden. Zu den vorgesehenen Anwendungen gehören sowohl (i) die Ergänzung der bestehenden Standardüberwachung von total ionizing dose und der Teilchenfluenz als auch (ii) neue Fähigkeiten, wie die Lokalisierung der Strahlungsquelle und Durchführung einer linear energy transfer Analyse.

Außerdem werden die Studienergebnisse einer eigenständigen erfolgreichen Kampagne zur Messung des transversaler Myonenfluss (8.6 counts/cm^2/pb^{-1}) am LHCb Experiment während der Luminositätsproduktion vorgestellt. Die experimentellen Daten stimmen mit den normierten FLUKA Simulationsvorhersagen mit einem Verhältnis von $\mathcal{R}_{CR} = CR_{sim}/CR_{meas,tpx} = 1.77 \pm 26$ überein.

In allen Fällen ist der Hauptvorteil des Timepix3-Strahlungsmonitors ein doppelter: Die gute zeitliche Auflösung und die niedrige Energieschwelle des Timepix3-Detektors ermöglichen die sofortige Erkennung von Strahlenverlusten auch in Bereichen mit geringerer Strahlung, wie z. B. in den abgeschirmten Nischen des Beschleunigerkomplexes, wo sich normalerweise die Elektronik befindet. Darüber hinaus erlaubt der Timepix3-Strahlungsmonitor, das Strahlungsfeld Teilchen für Teilchen zu messen und die einfallenden Teilchen nach ihrem Einfallswinkel und Energiebereich zu klassifizieren.

Contents

Contents

Prologue

Lasciate ogni speranza, voi ch'entrate.
Dante Alighieri - Divina Comedia

1

Introduction and motivation

1.1 Motivation

The Large Hadron Collider (LHC) [1] is the last chain of the accelerator complex at the European organisation for nuclear research (CERN) and as well the largest synchrotron in the world to date, which will undergo a significant upgrade into its next high luminosity era (HL-LHC) [2, 3]. This project aims to boost the performance of the current LHC machine to increase the potential for discoveries, by raising the total number of collisions in the interaction points by a factor of 10 beyond the LHC's initial design value, thereby providing more data to the experiments, allowing them to observe increasingly rarer processes.

The HL-LHC upgrade is applicable to almost all major LHC experiments, and therefore has a wide physics programme [4, 5], summarized here briefly in five main areas:

1) the study of known mechanisms in greater detail, in particular the Higgs boson [6, 7], probing its connection to the electroweak symmetry breaking.

2) flavor physics of heavy quarks and leptons, as the two general purpose detectors (a toroidal LHC apparatus (ATLAS) [8] and compact muon solenoid (CMS) [9]) will measure the properties of the top quark, the fermion with the largest known mass and largest Yukawa coupling, and together large hadron collider beauty (LHCb) [10], they will test the unitarity of the Cabibbo–Kobayashi–Maskawa matrix.

3) the studies of quantum chromo-dynamics (QCD) matter at high density and temperature, in particular at a large ion collider experiment (ALICE) [11], as jet and photon production in the heavy ion collisions forms the basis of QCD perturbation theory probes.

4) improved standard model (SM) precision measurements, as HL-LHC will advance the knowledge of parton distribution function (PDF) by measuring several SM processes with the jets, top quarks, photons and electroweak gauge bosons in their final state;

5) owing to this high energy, there is also a possibility for HL-LHC to detect beyond the standard model (BSM) phenomena such as baryogenesis, dark matter, answers to the flavour problem, neutrino masses and insights into the strong charge parity (CP) symmetry problem.

The HL-LHC project was announced as the top priority of the European strategy for particle physics in 2013 [12], approved by the CERN council in 2016 [2], and it is planned to become operational from the beginning of 2030 [13, 14]. Its development depends on several new technological innovations, as well as adapting existing strategies and designs to the increase in accelerator performance. This thesis is a prime example of the latter.

During the design phase of an accelerator and its experiments, it is necessary to estimate the harshness of the radiation environment and the associated adverse effects, both on the nominal accelerator operation and on the experiments [15–17]. One one hand, this is of primary importance for the estimation of sensors and electronic components lifetime and failure rates, as well as the power and quench risks on the magnets; on the other hand, the radiation field contributes to the background in physics analysis.

Presently, a consistent knowledge of the radiation

environment can be obtained using standard particle transport codes, and the main tool used in this work is the flukturiende kaskade (FLUKA) [18–20] Monte Carlo code, CERN distributed.

During the accelerator operation, the radiation levels in the entire accelerator complex are meticulously monitored and compared to the simulations for different operational scenarios. Unfortunately, the simulations are affected by various sources of uncertainty and can differ from actually measured radiation levels (e.g. the new accelerators typically operate in new energy regimes that have not been available before, and there are only theoretical predictions on expected values for the interaction cross sections). At the LHC, the highest radiation levels are those in the collimation region, and at the ATLAS and CMS collision points, the two general purpose experiments with the highest number of interactions.

Previously insufficiently explored in a systematic manner, the long straight section responsible for accelerating the beam via the radio frequency (RF) cavities, region called insertion region 4 (IR4), hosts most of the beam diagnostics instruments. The proposed HL-LHC intensity increase leads to the need of a more careful beam monitoring in this region, to avoid unnecessary losses. Since the radiation levels in this area generally scale with the beam intensity, this region comes now under rigorous scrutiny.

An exhaustive overview of the measured radiation levels at an early stage is important to properly anticipate radiation damages to the accelerator, while the comparison of the simulations with measurements allows to adjust and to improve upon the assumptions that have been used into the predictions (e.g. the geometry model). The first measured quantity of interest is the total ionizing dose (TID), for which a beam loss monitor (BLM) system [21] has been implemented. Moreover, there are other detector technologies that can measure particle fluences.

At the same time, new detector technologies have been developed, and a novel Timepix3 radiation monitor [22] is assessed for its suitability as an accelerator beam loss monitor, both in terms of its operational capabilities and limitations, as well as advantages in

the measured data compared to existing monitoring devices. In addition to a dose measurement, by summing the energy deposited in its pixels, it can also be used for charged particle flux measurements. Its excellent time resolution (1.25 ns) and spatial resolution (provided by the pixel array with a pixel pitch of 55 μm) make it an optimal instrument to promptly detect radiation showers caused by localized beam losses and, in some circumstances, to provide information about their origin. The main practical advantage of the Timepix3 detector for this type of study is its ability to measure the radiation field on a particle by particle basis, and then to eventually classify the incident particles according to their incidence and energy range.

1.2 Thesis outline

This section provides an outline of the thesis: an introductory prologue, followed by the main content divided into the three main acts, culminating with the prospects of the work in a coda chapter, and finally concluding with the epilogue. These parts have been written as standalone, i.e. with a brief introduction and summary pages highlighting the impact of this work. The individual chapters within these parts have been written such that each chapter can be read independently, insofar as possible.

The prologue discusses the motivation and why this thesis is valuable and necessary in the accelerator community. Furthermore, the impact of radiation to electronics (R2E) at CERN is summarised, introducing as well the LHC accelerator together with the operational parameters. The last chapter of this part introduces the methods and tools, namely the Monte Carlo simulation tool FLUKA and the available measurements.

The first act focuses on the LHC radiation environment at insertion region 4 (IR4). Its first two chapters are dedicated to introducing the scene, namely the geometry of the accelerator and of the annual measured levels in the past, as well as the source term for the radiation levels that are observed. The next two chapters represent the first results of this thesis,

namely the benchmark on the LHC operation and the predictions for the future HL-LHC operation for the two beam gas instruments that have been studied: the Beam Gas Vertex (BGV) and the Beam Gas Curtain (BGC).

The second act deals with the characterisation of the Timepix3 radiation monitor. Its first chapter introduces the Timepix3 detector technology, the hardware setup of the monitor, as well as the data analysis steps. The second chapter deals with the energy calibration of the detector, for which two test campaigns have been performed. Similarly, the third chapter consists of two test campaigns, this time for neutron detection.

The third act combines and expands on the previous two acts. Having established the key features of the Timepix3 radiation monitor in the second act, the setup has been deployed in 2023 at IR4 in order to assess the radiation field during nominal LHC operation (considered as background), and particularly, by the BGC operation (considered as signal), as described in detail via benchmarked simulations in the first act. These results prove that the Timepix3 radiation monitor is a suitable technology for the monitoring of radiation levels at the CERN accelerator complex, with a wide dynamic range and functionalities.

The coda chapter is meant to highlight the broadness of the applications and usages that the Timepix3 radiation monitor can provide at the CERN accelerator complex. Not just as a beam loss monitor as presented in the third act, but also as a muon flux detector, as it was used to measure signals relevant to the experiments, e.g. at the location of the proposed compact detector for exotics at LHCb (CODEXb) experiment.

Lastly, an epilogue with concluding remarks is given, highlighting how the observed performance of the Timepix3 radiation monitor opens the door for its usage for radiation field measurements at the CERN accelerator complex in a variety of locations and radiation sources. Moreover, it can be used to benchmark simulations of the radiation environment in a different way than traditionally done with other radiation

monitors (such as total ionizing dose or integrated particle fluences), by looking also at directionality or linear energy transfer.

2

Radiation to electronics impact at CERN

High-energy particle accelerators are a prominent source of radiation, to which the various nearby electronics systems, critical to the accelerator operation, are exposed to. Hence, the radiation tolerance of such systems needs to be accounted for during their design phase, and validated experimentally. At CERN, the radiation to electronics (R2E) [16] activity is responsible for providing the necessary support to ensure an adequate performance of its accelerator infrastructure, with regards to radiation exposed electronics. Such support comes mainly in the form of:

1. radiation monitoring and calculation,

2. radiation effects mitigation at circuit and system level,

3. operation of CERN irradiation facilities and,

4. radiation testing of electronic components and systems.

2.1 The CERN accelerator complex

The CERN accelerator complex (shown in fig. 2.1) [23] consists of a succession of experiments and machines with increasing beam energies by a factor of ≈ 30 at each step. To date, it is composed of eight accelerators, two decelerators, the transfer lines which interconnect them and various facilities hosting experiments covering topics within the fields of: (i) particle physics, such as: a toroidal LHC apparatus (ATLAS) [8], compact muon solenoid (CMS) [9], a large ion collider experiment (ALICE) [11] and large hadron collider beauty (LHCb) [10], as well as the recent physics beyond colliders (PBC) initiative [24]),

(ii) nuclear physics, such as isotope mass separator on-line device (ISOLDE) [25] and medical isotopes collected from isolde (MEDICIS) [26], (iii) antimatter, such as antiproton decelarator (AD) [27] and extra low energy antiproton ring (ELENA) [28], and (iv) radiation test facilities, such as CERN high energy accelerator mixed-field (CHARM) [29, 30], CERN linear electron accelerator for research (CLEAR) [31] and neutron time of flight (nToF) [32–34]. Part of them are built on the surface, but the largest ones (from the proton synchrotron (PS) onwards) have been constructed underground. While some of the accelerators only supply particles to the experiments (as is the LHC), others are used also as injectors, accelerating particles for larger accelerators. Mostly, the operation of the CERN accelerator complex uses protons, albeit some runs are also dedicated to ions [35–39] of: lead (Pb), argon (Ar), or xenon (Xe) atoms.

To provide some key operational figures [40], a total approximative number of $13 \cdot 10^{20}$ protons were accelerated in the LHC during Run 2 (2015-2018) and already $40 \cdot 10^{20}$ during Run 3 (2022-to date). However, the LHC represents less than 0.084% of the total number of protons injected in the accelerator complex, as most of these particles are delivered to the ISOLDE (61.45%) and nToF [32] (14.30%) facilities. Approximately 14% of the particles are used for operating tests or are not suitable to be used (triggering beam dumps, losses, etc.) [41, 42].

At such high energies, only the loss of a little fraction of the beam particles could damage the accelerator or the detector equipment. Safe operation of the accelerators requires correct operation of several systems specially designed for machine protection. Some of

them are aimed at monitoring the beam characteristics, such as beam size or beam position.

2.2 The Large Hadron Collider

The largest accelerator in the world, the Large Hadron Collider (LHC) [1] accelerates particles in its two beams circulating in opposite directions and collides them at the four experimental interaction points (IPs). The working principles of an accelerator are extensively covered in literature [43], while here only the concepts of interest for this thesis are summarised. Luminosity and the center of mass energy are the two key figures of merit at a particle collider. Firstly, in order to explore new physics, one attempts to observe rare events (i.e. with small cross sections and branching ratios) involving potentially new heavy particles. Its delivered luminosity (proportional to the number of collisions) recorded more than $\mathcal{L}_{int}$= 270 fb^{-1} since its operation to date (as shown in fig. 2.2 for each year of its operation). Secondly, the higher the center of mass energy $\sqrt{s}$, the more massive the secondary produced particles can be. The LHC has been designed up to an energy of 14 TeV for protons (used at a nominal energy of 13 TeV during Run 2 and 13.6 TeV during Run 3).

The LHC accelerator layout (shown in fig. 2.3) can be divided based on the 8 insertion regions (IR) into octants [1]. An octant starts in the centre of an arc and continues to the centre of the next arc clockwise. Therefore, the IR corresponds to the middle of the octant where it is located. IR1 lies within octant 1, and it corresponds to the interaction point (IP) of the ATLAS experiment. The rest of the IRs and octants are numbered from 1 to 8 following the direction of beam 1 (clockwise).

The octants can be further divided into: (i) the long-straight-sections (LSS), which neighbour the insertion region and is responsible of guiding the beam into collision for the interaction points or to perform momentum cleaning, acceleration or dump; (ii) the dispersion suppressor (DS), that hosts the first curved portion of the accelerator next to the LSS leading into the (iii) ARCs, defined as the part of the ring occupied by 23×2 regular beamline elements called arc half-cells. The LHC arc cell has been designed to optimize the maximum integrated dipole field along the LHC arc using the minimum number of magnet interconnections.

The main functions of the LHC are performed by the following elements:

Injection from the super proton synchrotron (SPS) is performed via two transmission lines.

Acceleration is done in IR4 with the utilisation of radio frequency (RF) cavities that provide longitudinal focusing of the particles in bunches and acceleration.

Colliding is carried out at the centre of four experiments: ATLAS (IP1), ALICE (IP2), CMS (IP5) and LHCb (IP8).

Collimation is performed in both IR3 and IR7. In IR3 the beams are cleaned with respect to too large longitudinal oscillation amplitudes (momentum cleaning), whereas in IR7 with respect to too large transverse oscillation amplitudes (betatron cleaning).

Extraction is realised in IR6. Due to the amount of energy stored in the beams, the LHC needs to have a dedicated beam abort system in order to dispose the beams in a safe manner. Each ring has their own extraction system – fast rising extraction magnets direct the beams into dedicated lines with massive dump blocks at the end where the beams are absorbed.

Bending is achieved by 8.3 T superconducting dipoles in the arcs and, in addition to just curving the beam, it is also necessary to perform **focusing** by quadrupoles, because protons are electrically charged and the particle beam diverges if left on its own. Higher order corrections are taken into account using multipoles.

2.3 Operational cycles of the LHC

In order to accelerate and collide the bunches at such high energies, the beam cycle (also called fill) time of the LHC machine is rather long: the typical operational cycle of the LHC is illustrated in fig. 2.4. As injection and collision energies differ, both accelerator rings need to be filled at first, then the energy is ramped up from the injection energy at 450 GeV to
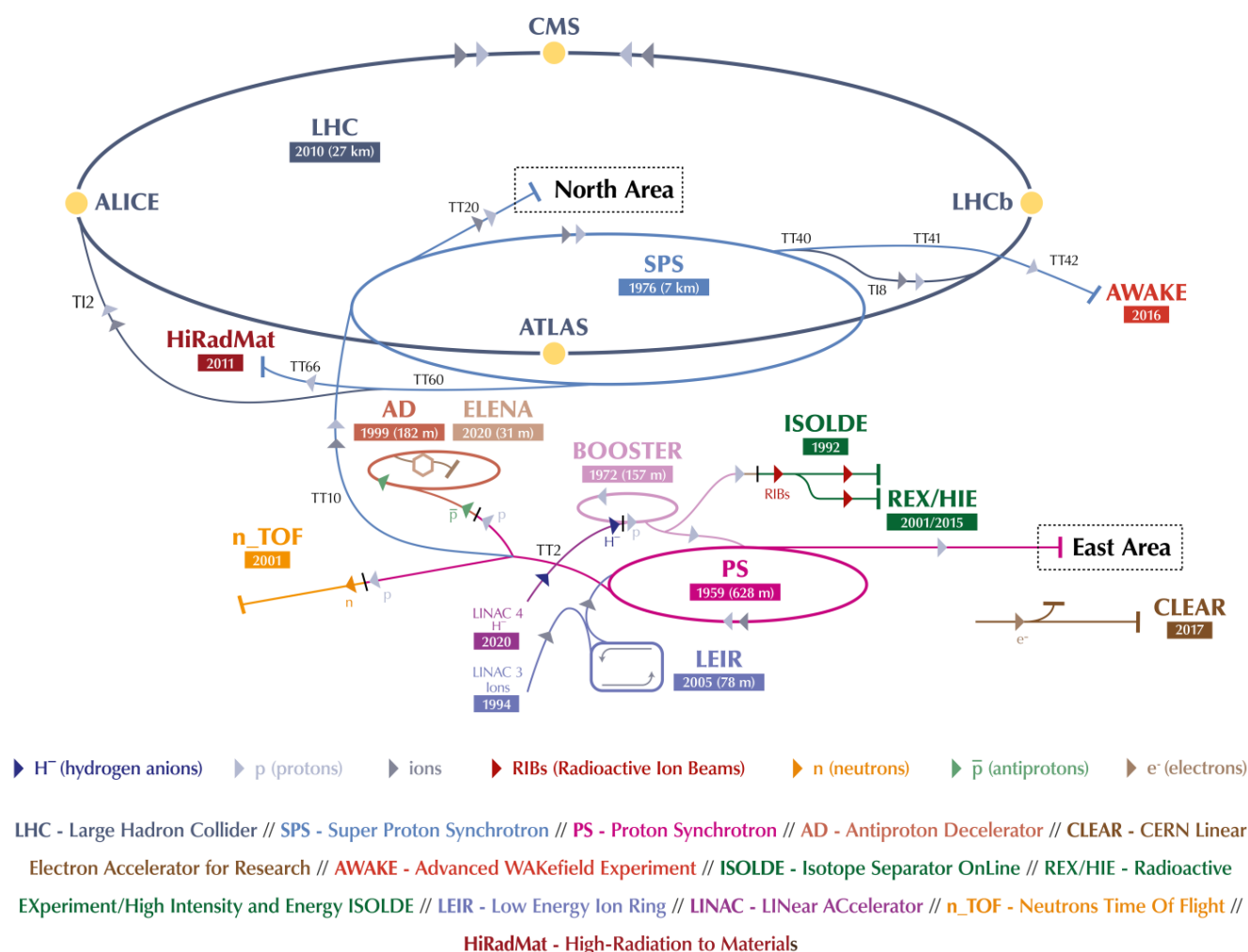
Figure 2.1: CERN accelerator complex (fig. from ref. [23]).

top energy up to 7 TeV, and the beams are brought into collisions at the interaction points. At the end of the fill, they are finally extracted. The different phases of each operational cycle are labelled as beam modes [44]. There are in total 19 classified beam modes, with experimental data taking at the interaction points (IP) signaled by the STABLE BEAMS mode. However, the intensity driven losses such as those in IR4 that are investigated in this thesis oc-cur before declaring STABLE BEAMS, but as soon as there is beam within the accelerator, i.e. starting from the INJECTION beam mode, the losses gradually increase as more particles are injected (and a fraction of them are unavoidably lost). During the energy RAM-PUP, the radiation levels increase more significantly, as the lost particles become more and more capable of powerful radiation showers. At peak energy and intensity, the losses are highest, and then they typ-
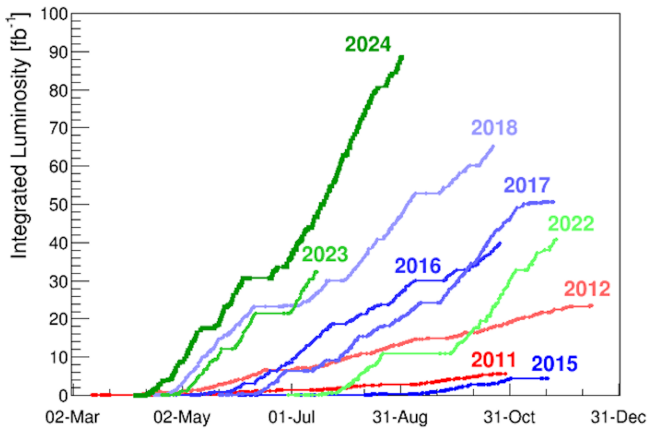
Figure 2.2: Cumulative delivered luminosity $\mathcal{L}_{int}$ to ATLAS during stable beams and for high energy pp collisions versus time since the start of LHC operation in 2011, to date.
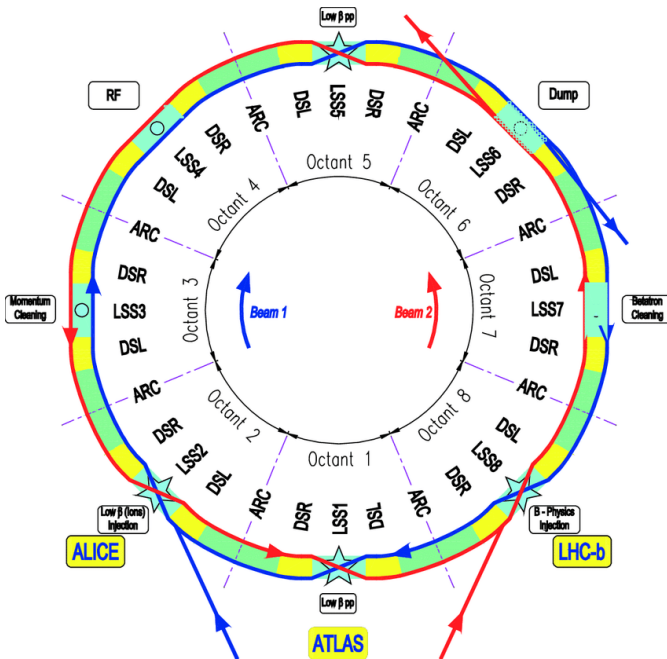
Figure 2.3: The LHC layout: the collision points are indicated with stars, while beam 1 (blue line) is injected upstream of IP2 (TI2) and beam 2 (red line) upstream of IP8 (TI8). [1]

ically decrease following the beam intensity via the mechanisms described later in section 2.6.

Ultimately, a beam dump will either be programmed by the operators at the designated end of a fill (due to beam intensity being to low for efficient luminosity production compared to starting the injection for a new fill with a typical turnover time of 3 h [46]) or be triggered by a machine protection element in case of a technical problem. Once the decision to remove the beam is made, the LHC beam dump system extracts the beam within 3 turns [1].

The beams typically (and ideally) stay in collisions in STABLE BEAMS for about 10 to 20 h, with a record of 34 h [47]. However, unwanted premature dumps may occur, thereby limiting the LHC performance. The motivation for these dumps vary from radiation to electronics (R2E) failures (the context of this work), or to protecting the machine due to unwanted high beam losses, since the immense amount of energy stored in the LHC beams makes them highly destructive [1].

At top beam energy, even the loss of a small fraction of the beam is capable of causing significant energy depositions, large enough to generate a local increase of the temperature. For example, for the Nb_3Sn quadrupoles, a local transient loss of just $4 \cdot 10^7$ protons (compared to the beam of 10^{11} protons) would produce heat depositions on the level of $30\,mW/cm^3$, capable of inducing quenches [2], for which the limits depend on the magnet (for this example, at $40\,mW/cm^3$ [48, 49]). In order to protect the accelerator, the beam dump is then triggered. In the best case scenario, a quench of an LHC magnet would cause a downtime in the order of hours, but in case of damage, the downtime could be in the order of months in order to replace the damaged magnet [50, 51].

---

[1]The total energy in each beam at top energy (6.5 TeV) is approximately 300 MJ, which is approximately as energetic as a 400-ton train, like the German IC, travelling at 140 km/h.

[2]If the temperature increases in a super conducting element beyond the critical temperature, the superconductor transitions to a normal conductor (it quenches), and an ohmic resistance (re)appears.
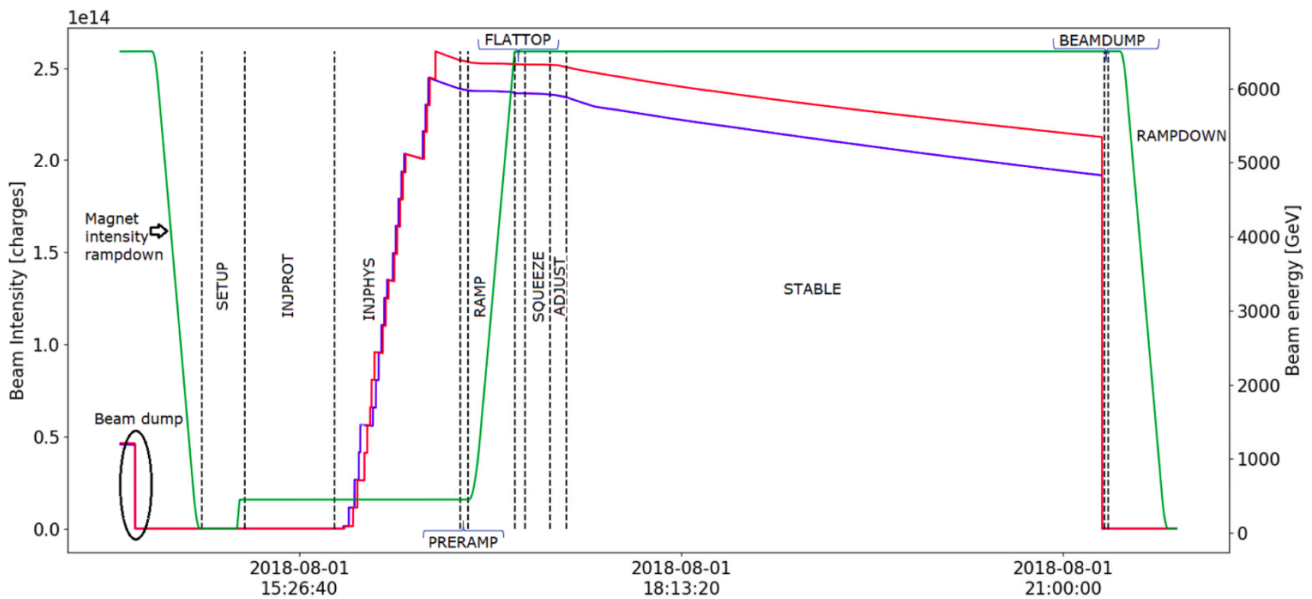
Figure 2.4: The beam cycle of a nominal LHC fill (shown here, fill #7006). The intensity of beam 1 and beam 2 is represented in blue and orange, respectively, while the energy of the beams is represented in green. The dashed black lines represent the moments of time in which the beam mode is changed. The name of each beam mode is placed between two dashed black lines: it represents the period of time in which that beam mode is present (fig. from ref. [45]).

2.4 The radiation to electronics activity

While the physics discoveries require larger integrated luminosities for better statistics and higher center-of-mass energies to probe experimentally unknown territories, the entire LHC machine, in particular its electronics, are taking a toll. During the operation of the accelerator, the beam loss mechanism lead to a prompt radiation field along the LHC, and this mixed radiation field consists of both electromagnetic components and hadrons with wide energy spectra from thermal levels (in particular neutrons) up to hundreds of GeV. The prompt radiation damage is two-fold:

1. accelerated ageing of the exposed elements, which results in a reduced lifetime,

2. single-event effects in the electronics, which might lead to premature beam dumps

The interest for CERN is both to asses the current radiation levels impacting the electronics for the existing machines in the CERN accelerator complex and to estimate the future levels for the upcoming accelerators, e.g. HL-LHC, as well as for feasibility studies for potential new machines, such as the future circular collider (FCC) [52], the muon collider [53] or the compact linear collider (CLIC) [54]. The understanding and modelling of radiation effects in the LHC was originally tested in irradiation facilities, but these do not reproduce entirely the more complex radiation reality of the accelerator environment, and as such there is strong motivation to cross-check and validate. Similarly, the study and design for future machines that push either the energy or the luminosity frontier are limited, either by the collision energies that require extrapolation, or by the higher collision rates, typically leading to harsher radiation environemnts.

The main responsibilities of the radiation to electronics (R2E) activity could be divided into two categories from an operational point of view: (i) to mitigate the issue of premature beam dumps due to electron-

ics failures caused by radiation, and (ii) to mitigate possible lifetime degradation of the beamline components and electronics. The R2E effort assists LHC operations and equipment groups with assessments of radiation-induced failures in electronics of accelerator components (shown in fig. 2.5), in order to minimize all risks of radiation-induced failures at CERN accelerators, starting with the LHC. Mitigation techniques can consist of the (re)placement of shieldings [55] and repositioning of equipment, as well as defining radiation hardness assurance (RHA) procedures [17, 56] for electronics systems.

Modern high-energy hadron accelerators demand a significant number of electronic components being placed close to the beam-line and to the experiments. The LHC requires superconducting technologies (at low temperatures), efficient collimation systems as well as precise and fast monitoring of the operational parameters of the machine. This implies more complex electronics for control, steering and powering, which can contain up to thousands of commercial off-the-shelf (COTS) units, such as power converters (carrying the necessary currents from the external supplies into the magnets), the quench protection system (QPS), protecting the superconducting equipment from incidents (quenches) caused by excessive heat, or the vacuum and beam instrumentation, just to name a few.

The LHC radiation showers that originate from a primary nuclear interaction (e.g. proton on machine element, like the collimators, or alternatively, proton on gas atom) produce cascades of secondary particles, predominantly hadrons (such as protons, neutrons, kaons, pions, etc.). The shower then develops into both: (i) an electromagnetic component (mainly from fast $\pi^0 \to \gamma\gamma$ decay) and (ii) a hadronic component. Decaying charged kaons and pions lead to weaker interacting particles, such as muons and neutrinos. The radiation profile (both in terms of intensity and composition) greatly varies based on several parameters: the energy of the primary interaction, the distance travelled and the amount of shielding material.
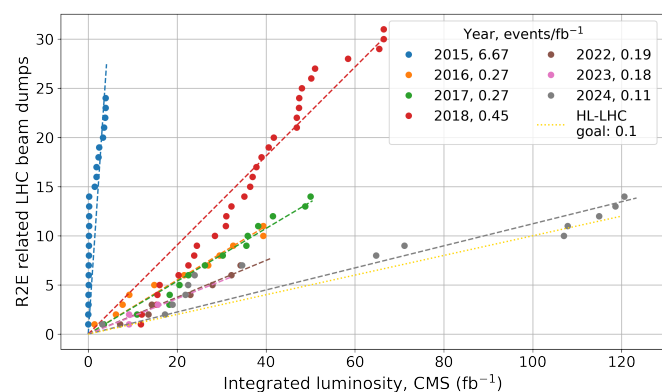
Figure 2.5: Radiation to electronics R2E related (single event effect induced) dumps per fb^{-1} from Run 1 to date, together with the HL-LHC target of 0.1 beam dumps/fb^{-1}.

2.5 LHC availability and radiation to electronics performance

As previously described, a key figure of merit quantifying the performance of the LHC is the integrated luminosity $\mathcal{L}_{int}$ (proportional to the total number of collisions, defined in eqn. 2.1) delivered to its high-luminosity experiments ATLAS and CMS, expressed in inverse femtobarns (fb^{-1}), proportional to the number of collisions in the interaction points (IP). As a consequence, it is useful to measure the R2E performance by counting the number of R2E-induced beam dumps per unit luminosity, where a smaller figure corresponds to a milder impact on the production of LHC collisions. Similarly, the performance targets of the R2E project are defined by performing modelling studies of the LHC availability [57] and deriving the maximum number of R2E-induced beam dumps per unit luminosity (fb^{-1}) that are compatible with keeping the resulting loss of integrated luminosity below a reference threshold (typically 1% of lost luminosity out of the total delivered).

There have been several mitigation measures, implemented during LHC Run 1 (2010-2012) and especially during long shutdown 1 (LS1, 2013-2014). Consequently, radiation effects on electronics causing equipment failures leading to LHC beam dumps and/or machine downtime have been sufficiently

low to yield a minor impact on the accelerator performance. During Run 2 (2015-2018) the R2E related failures per unit luminosity have successfully stayed below the target value of 0.5 events/fb^{-1}, except for the 2015 run dedicated to machine commissioning. However, during 2018, a mild increase in the failure rate has raised the attention of the R2E project. This increase was linked to the increased radiation levels in the dispersion suppressors (DS) of the ATLAS and CMS experimental insertions, affecting the quench protection system (QPS) located underneath the superconducting magnets in the LHC tunnel (from 269 to 340 m) [58].

The number of beam dumps induced by R2E faults is shown in fig. 2.5 as a function of the cumulative integrated luminosity for the LHC in Run 1 (2011-2012), with trend lines from ref. [59]), and in Run 2 (2015-2018), for which the single R2E-induced dumps are shown individually. A similar R2E performance is also targeted for the current LHC Run 3 (2022-to date), during which the performance of the LHC is expected to further improve compared to Run 2, both in terms of beam intensity and annual integrated luminosity. In addition, fig. 2.5 includes the 0.1 dumps/fb^{-1} target for the HL-LHC upgrade, determined by means of machine availability simulations as described above. To be able to meet this ambitious target, the electronic systems are required to follow a dedicated radiation hardness assurance (RHA) procedure [17, 56], where the radiation environment is taken into account already in the early phases of the system development.

2.6 Beam loss mechanisms

Various physical mechanisms can lead to beam losses in particle accelerators [37] due to beam-machine interactions, in addition to the scattering amongst the beam particles or other beam instabilities. Those relevant for this thesis are explained in more detail below:

2.6.1 Luminosity burn-off

As observing more events per time increases the statistical significance of rare events, the integrated luminosity delivered to the experimental interaction points is considered the key figure of merit for the performance of a collider. The luminosity $\mathcal{L}$ is defined as the ratio of the number of detected events N in a certain time t to the interaction cross-section σ:

$$\mathcal{L} = \frac{1}{\sigma}\frac{dN}{dt} = f\frac{I_1 I_2}{4\pi\sigma_x\sigma_y} \tag{2.1}$$

which can of course be translated into the accelerator parameters, assumed here as head-on collisions of two identical Gaussian shaped beams with dimensions in terms of standard deviation σ_x and σ_y, yielding a transverse size of $4\pi\sigma_x\sigma_y$. They circulate in the collider with a revolution frequency f, and I_1 and I_2 are the intensities of two colliding bunches.

Often an integrated luminosity is used, which is an integral of the luminosity with respect to time:

$$\mathcal{L}_{int} = \int \mathcal{L}dt \tag{2.2}$$

Typically, the objective is to maximise integrated luminosity $\mathcal{L}_{int}$ obtained at high energy, but there might be exceptions depending on the physics programme of the accelerator. The luminosity is measured in inverse barns (symbol: b^{-1}). The barn b is a metric unit of area equal to 10^{-28} m^2 (100 fm^2). It is used in all fields of high energy physics to express the cross sections of scaterring processes, and is best understood as a measure of the probability of interaction between particles. A barn b is approximately the cross-sectional area of a uranium nucleus. For the case of LHC, the proton-proton cross section in bunch collisions is estimated to be $\sigma_{pp_{inel}} = 79.3 \pm 0.6$ (exp.) ± 1.3 (lum.) ± 2.5 (extrap.) mb [60]. For practical applications like this thesis, it is approximated to 80 mb.

To further elaborate on the beam size σ_x and σ_y, the beta function β describes optics (i.e. magnet configuration) of an accelerator. The beta function value at

the collision point is denoted as β^*. The beam transverse size σ is connected with the the beta function via the beam emittance ϵ, that describes the spread of particles in position-and-momentum phase space, through the equation (in the simplest case):

$$\sigma_{x,y} = \sqrt{\epsilon_{x,y}\beta_{x,y}} \qquad (2.3)$$

According to this equation, the luminosity can be increased by reducing the cross section of the beam (for example, via decreasing the value of a beta function at the collision point $\beta^*_{x,y}$. Alternatively, it is possible to increase the number of particles in the beam or the revolution frequency. In general, the luminosity of an accelerator gradually increases over time, while accelerator physicists learn how to operate the machine and to squeeze the beam size at the intersection point.

As it can be seen in fig. 2.4, the instantaneous luminosity $\mathcal{L}(t)$ is not constant over time during STABLE BEAMS mode, owing to the collisions that lead to a burn-off loss of particles:

$$k\frac{dN_{1,2}(t)}{dt} = -\sigma_{inel}n_{ip}\mathcal{L}(t) \qquad (2.4)$$

where σ_{inel} is the inelastic cross-section of the colliding particle, k is the number of bunches and n_{ip} is the number of collision points. Assuming momentarily that the burn-off as the only mechanism that affects the initial luminosity $\mathcal{L}_0$ (for an initial bunch intensity N_0), its time behaviour [61] is given by:

$$\mathcal{L}(t) = \frac{\mathcal{L}_0}{\left(1 + t\sigma_{inel}n_{ip}\frac{\mathcal{L}_0}{N_0 k}\right)^2} = \frac{\mathcal{L}_0}{(1 + t/\tau)^2} \qquad (2.5)$$

where in addition τ has been introduced as the beam lifetime. As a numerical example, consider a configuration close to the LHC with proton beams: the total cross-section $\sigma_{burnoff} = \sigma_{inel} =80$ mb (as above), the LHC frequency is $f =11\,245$ Hz, $N_0 = 1.2 \cdot 10^{11}$ protons, n_{ip}=2 equally eager experiments (interaction

points), which doubles the interaction rate, one can obtains $\tau_{burnoff} = 15$ h. This one of the reasons why, as previously mention, the beam is intentionally dumped after about 10 to 20 h.

2.6.2 Beam-residual gas interactions

The luminosity burn-off is not the only source of loss of particles along the accelerator. The vacuum in the LHC is not perfect and some residual gas molecules are present in the beam pipes. Some particles in the beams interact with these molecules, resulting in continuous loss of particles that is roughly constant along the accelerator. It is expected that these losses scale linearly with integrated intensity and residual gas density, leading to lower radiation losses than those from collision debris, and as such, they are most relevant in the arc regions where the contributions from the interaction regions are negligible. The exact point where the IP losses become comparable or negligible wrt. the arc background varies depending on the IP and on the instantaneous luminosity; in ref. [43], some collisions losses can be measurable even in cell 17.

The interaction mechanism and probability is given later in chapter 5, but it follows the same principle as for the luminosity burn-off. For the LHC proton beam configuration, assuming a uniform residual pressure of $p =1 \cdot 10^{-9}$ mbar, composed predominantly of hydrogen (H_2), at $T =5$ K, over the 27 km, one obtains a beam life time due solely to residual gas-beam interactions at $\tau_{residual,gas} =47$ h. Usually, one will design the accelerating machine such that $\tau_{gas,residual}$ is considerably larger than $\tau_{burnoff}$. From the real LHC operation, the beam-gas lifetime is observed to bee much longer than this $\tau_{gas,residual}$.

2.7 Insertion regions: classification based on radiation levels

Collision debris are generated from inelastic collisions at the interaction point (IP): either beam particles that no longer conform with LHC requirements or very forward secondary products. These

debris are lost downstream (up to hundreds of meters away) of the experiments causing locally very high radiation levels. These losses around the IP scale with the total delivered integrated luminosity $\mathcal{L}_{int}$ of the experiment [62] and are considered not to be observed in the arc sections, but only in the long straight section (LSS), from 0 up to 269 m and dispersion supressor (DS) [43], from 269 m to 348 m. As such, one can classify the 8 insertion regions (IR) into two categories based on the dominant source of interaction:

1. At the four experimental interaction points (IP1/2/5/8), the radiation is mainly dominated by the collisions themselves [37, 43, 63].

2. At the other four insertion regions (IR3/4/6/7), the radiation field is dominated by the beam interactions with the machine elements (e.g. collimators) or the residual gas, and the relevant scaling factor is generally taken to be the beam intensity, combined with other parameters specific for each location and intercepting beam element.

In the case of the latter IRs, more complex source terms are present that depend on several operational parameters of the accelerator. The particular scenario of IR4, the host of a plethora of beam instruments, rises several additional challenges, which are explored systematically for the first time in this thesis.

Characterization of the LHC radiation field

The analysis process leading to proposed radiation to electronics (R2E) [16] mitigation techniques includes: (i) calculations based on detailed Monte Carlo simulations, (ii) the monitoring of measured radiation levels (where monitors are available), as well as (iii) comparisons (here, called benchmarks) between the two. Measured data are essential to ensure an accurate description within the computational tools, while the simulations are capable of predicting radiation levels on sensitive equipment or in locations where no measurements are available. For explicit user support, the monitoring and calculation working group (MCWG) [64] within the radiation to electronics (R2E) activity provides to users or equipment owners the radiation levels in their desired locations. To address such requests, the aim is to understand the complexity and heterogeneity of the CERN accelerator complex and its radiation environment, as well as to identify the regions which are most affected by beam losses and should be followed up with the help of radiation monitoring systems. There are several detector technologies currently in operation, described in detail in Appendix 3. In parallel, new or improved technologies are under research and development and tested to asses their suitability for R2E applications at the CERN accelerator complex, such as silicone diodes (monopixel) [65, 66] or the Timepix3 radiation monitor (pixel array) [22] studied in this thesis.

3.1 The simulation approach

In the CERN accelerator complex, highly energetic particles are circulating, which, once lost, lead to a hostile radiation environment that has to be assessed

and well understood for the reliable operation of the accelerators.

Given the complexity and scale of the problem, it must be tackled computationally/numerically, for which well-suited is the Monte Carlo (MC) method, a technique of numerical analysis, based on sequences of random numbers used to obtain sample values for the variables for a given problem. The calculation process used in MC is an artificial construct, usually a computer program that is mathematically equivalent to the problem being analysed [67]. Compared to traditional methods with converging efficiency of $1/\sqrt[d]{N}$, MC converges with $1/\sqrt{N}$, thereby being more efficient when the dimension of the problem is larger than 2. MC is now used routinely in many different fields, from the simulation of complex physical phenomena such as radiation transport in the earth atmosphere to the simulation of the esoteric sub-nuclear processes in high-energy physics experiments. The MC method benefits from the central limit theorem, which states that for a large number of random trials, N, the mean of the Gaussian distribution will move towards the actual expectation value, with the standard variation evaluations decreasing as $\sim 1/\sqrt{N}$.

Particle transport is described analytically by the Boltzmann equation, with a detailed description in the Monte Carlo context given in ref. [68]. It can be seen as a balance equation in phase space: the increment of particle phase-space-density is equal to the sum of all *production terms* (such as particle production, sources, decay and *in-scattering*) minus the sum of all *destruction terms* (such as decay, *out-scattering* and absorption), at any phase-space-point. The MC method solves the radiation transport equation by

numerically calculating the particle tracks and the following energy deposition. As long as the cross sections of the microscopic events are well known and benchmarked, the MC method delivers reliable results for the macroscopic effects.

There are several Monte Carlo codes, of which a selection are geometry and tracking (GEANT4) [69], Monte Carlo n-particle transport (MCNP) [70], multi-dimensional analysis of reactor safety (MARS) [71], particle and heavy ion transport (PHITS) [72], Penelope [73] and flukturiende kaskade (FLUKA) [18–20]. The last one, FLUKA version 4.3.3, CERN distributed, has been used in the scope of this thesis.

These Monte Carlo simulation tools use extended cross section data bases, as well as particle interaction models obtained from both experimental and phenomenological studies. They have been developed through several decades of experience, and are continuously updated in light of recent measurements and/or theoretical advancements. Due to their importance on physics goals and accelerator operation, an extensive effort is usually dedicated to simulations.

As such, Monte-Carlo-based radiation transport simulations are used to quantify the impact of the desired beam-machine interactions, as well as of the undesired beam losses:

(i) The primary question in radiation assessment is the proper identification of the main radiation source, of which several are present in the accelerator operation [37]. Those of relevance for this thesis are those in section 2.6.

(ii) Secondly, the radiation source interacts with matter in the simulation, for which a dedicated geometry modelling collective effort has been carried out within the CERN SY-STI-BMI [1] section covering vast proportions of the CERN accelerator complex. Moreover, magnetic fields can also be present, which heavily influence

the behaviour of charged particles, especially of those who are not nominal beam particles. The interactions between the source particles and matter is done by employing suitable models for the various mechanisms of interaction.

(iii) Thirdly, the main scope of the simulations is to provide an outcome in terms of radiation that can quantified. Experimentally, there are different quantities that can be measured and then compared with the simulations, thereby testing both the theoretical models and the implemented geometry, as well as the assumption on the radiation source. Within the simulation, the equivalent of a measurement is the so-called scoring feature, which, depending on the problem, can take the form of deposited energy, particle spectra, or other quantities related to material damage, biological effects and activation of materials.

3.2 The FLUKA Monte Carlo code

FLUKA [18–20] (FLUktuierende KAskade) is a general multi-purpose particle interaction and transport Monte Carlo code that is capable to handle a wide variety of radiation sources. It can produce and transport neutrons from thermal energies and all other particles from 1 keV upwards to cosmic ray energies. It is applied in different fields, and in the context of this thesis, it is employed to calculate the radiation levels resulting from the proton-nucleus collisions at LHC beam energies. Moreover, simulation method presented in this work is employed in various studies pertaining the present LHC machine [37], but also for the HL-LHC upgrade [74]. Similar simulation methods are also adopted for the design of future machines, for example, within the future circular collider (FCC) study [68] and the Muon Collider collaboration [53, 75–77]. In particular, the FLUKA Monte Carlo code predicts several quantities for which no measurements are available, e.g. the power deposition in the superconducting magnets.

Regarding its physics models, it provides a description of the entire hadronic and electromagnetic

---

[1]Accelerator **SY**stems department, **S**ources **T**arget **I**nteractions group, **B**eam **M**achine **I**nteractions section.
https://sy-dep-sti.web.cern.ch/bmi

particle cascade initiated by secondary particles from TeV scale to thermal energies. The main assumptions of the particle transport MC that allow it to be used in the radiation-matter scenario are:

1. static, isotropic, homogeneous and amorphous media (and geometry).

2. transported particles do not interact with each other, as it is assumed to be negligible.

3. particles do interact with individual molecules/nuclei/atoms.

4. Markovian process: the fate of a particle depends only on its actual properties, not on previous events or histories.

5. material properties are not affected by particle reactions (no change of physical properties).

The accuracy and reliability of a MC code depends on the models or data on which the probability distribution functions are based. Instead, the statistical precision of the results depends on the number of histories and its convergence can be accelerated by *biasing* techniques.

3.3 Scored quantities

The radiation effects on the material are typically differentiated into instantaneous and long-term effects. In general, these effects have a negative impact on the material and should be minimized as much as possible. The machine's beam line elements and electronics exhibit varied responses to the hard radiation field they are exposed to. Elements employing superconducting devices face distinct limitations compared to those operating at room temperature, because of the risk that the instantaneous energy deposition would heat the device and cause the component to lose its superconducting properties (i.e. to quench).

3.3.1 Instantaneous

Not just the life time degradation is impactful to the general feasibility of the components in the acceler-

ator, but also instantaneous effects that can alter their nominal operation.

3.3.1.1 Heat loads

The heat load on the machine components is typically given per beam line element, expressed in units of watts (W). Depending on the beam power, component size and type, and location, the absorbed power can vary from a few mW to several hundred kW. The heat load or absorbed power per component is essential and helpful as the power distribution on the whole setup is assessed. The absorbed power indicates the amount of power directed towards a specific region or component, yet it does not illustrate how the power is distributed.

3.3.1.2 Power density

The power density, in units of W/cm^3, is calculated to understand the head load distribution. If the power density has spikes for even a very short time, this can even lead to component destruction, after which the machine could possibly require a downtime of several months. When the machine functions at low temperatures, in a superconducting state, there's a potential risk of the superconducting magnets experiencing a quench. Consequently, this results in the machine being offline for several hours, requiring the magnets to undergo re-cooling after a quench occurs.

In the LHC accelerator, quenching can be critical, and for low-temperature superconductors that are operated at liquid helium temperature, a quench limit[2] of the order of $10\,mW/cm^3$ applies.

---

[2]This is a conservative lower limit, but it varies depending on the magnet technology and operational conditions. A couple of known limits are:

1. dipoles: $13\,mW/cm^3$ [78].

2. quadrupoles: $40\,mW/cm^3$ [48, 79]

3.3.2 R2E related quantities

3.3.2.1 Cumulative effects - total ionising dose

When charged particles and photons penetrate a medium, they interacts with electrons in the atomic shells, possibly leading to ionisation, which in semiconductors can be considered as electron - hole pairs creation. The total ionizing dose (TID) is a quantity used to describe this cumulative ionisation effect. The main issue with TID is the gradual performance deterioration of the circuits that can potentially lead to system failures. Presented in different units depending on the application, the most common one is the radiation absorbed dose (rad) and the one used in this thesis is the international system unit (ISU), gray (Gy), where $1\,\mathrm{Gy} = 100\,\mathrm{rad} = 1\,\mathrm{J/kg}$.

The TID impacts the conductive properties of the material, such as leakages or threshold voltage shifts. In microelectronics, TID defects imply the accumulation of trapped charges in the field oxides of the circuit. As ionization occurs, electron-hole pairs are formed in the material (e.g. silicon dioxide SiO_2). Not all of the pairs recombine, but some of them move due to the applied electric field. Owing to their much higher mobility, electrons can exit the oxide leading to trapped holes in defect centers in the oxide volume. Furthermore, this process can activate other defects at the oxide interfaces. TID causes device degradation mainly via creation of defects and charge buildup.

Other crucial components within the machine, concerning radiation exposure, involve the electronic parts. In terms of R2E, the TID causes cumulative effects that accumulate over time. These effects mirror, to a considerable extent, the processes observed in organic materials. Generally, oxides tend to accumulate a charge, resulting in threshold shifts and increased leakage currents, ultimately leading to component failure. The acceptable dose thresholds vary depending on the specific machine component under consideration. For superconducting magnets, the typical threshold is assumed to be at 30 MGy [78], after which replacement becomes necessary. Typically, for R2E commercial electronics, the acceptable thresholds remain significantly lower, at a few Gy

or more [80]. The strong recommendation is to qualify the components before operation, to assess this limit.

3.3.2.2 Stochastic - particle fluences causing single event effects in electronics

Not only the beam line elements, but electronics controlling them can suffer from radiation effects. Stochastic events caused by energy deposition by one highly energetic particle in a sensitive volume (e.g. a memory cell) are called single event effects (SEEs) [81]. As one example, in digital devices, information is sent/stored as bits; a type of SEE is the single event upset (SEU), which can flip the bit to its opposite value thereby altering the information.

The SEE can be produced:

- via direct ionization, caused by particles with high linear energy transfer (LET), e.g. heavy ions. The SEE is generated by direct ionisation along the particle path within the device. In this case, the more convenient energy loss metric is not particle energy but the LET, which is the rate of energy loss per unit length on a material. However, this scenario is not relevant for the LHC as only a negligible amount of high-LET ions actually reach electronic equipment.

- via indirect ionization following inelastic hadron collisions, the dominant source of SEEs at the LHC, caused by neutral or low-LET particles, predominantly hadrons.

3.4 Radiation level monitoring

It is of uttermost importance [3] to have measured data in order to benchmark the simulation, and only in doing so one can fully rely on the predictions that

---

[3] *And that shows where Logic gets you, if uncorrected by observation (senses or instruments). If we do not correct our Logic by comparing it with experience, we may go on for centuries elaborating our most ancient errors endlessly* - Robert Anton Wilson, in *Quantum Psychology*

are computationally obtained. The above quantities are typically simulated within dedicated regions, i.e. radiation monitors. If the measured signal is not linear with the deposited energy, then their detector response has to be taken into account differently, typically in a second simulation step. Amongst the available radiation level data, in this thesis only the beam loss monitor (BLM) data has been used. For completion, the other monitors are described in Appendix 3.

3.4.1 Beam loss monitors - dose rates

Machine protection has driven the design and implementation of the beam loss monitor (BLM) system [21, 82], with approximately 4 000 detectors placed along the accelerator. The BLMs are energy deposition detectors, that detect particle showers caused by the beam losses.

BLMs are capable of measuring total ionising dose (TID) rates with a good time resolution, and they are given as 12 different running sum (RS), ranging from 40 μs (one LHC turn is 89 μs) up to approximately 83.8 s. They trigger beam dumps for critical losses using the 80 μs time window to protect the machine equipment against unintended energy deposition, thereby preventing magnet quenches and damage of machine components. In addition to this protective role, the BLM system is exploited (in offline analysis) for measurements and optimization of the accelerator, as they are employed to study the causes of the beam losses, as is the scope of this thesis.

Simulations are performed to analyze the development of the particle showers initiated by lost protons in the most likely loss locations. They allow to determine the most suitable number and positions of the BLM detectors [83]. To summarise, there are BLM detectors placed after each set of collimators, quadrupoles and dipole magnets. Other BLM detectors are located in the injection and dump insertions to monitor losses induced by system failures, or other special cases.

The detectors are placed outside the element they are *protecting*, approximately 1 m downstream of the

most likely loss locations, as it usually corresponds to the location of the particle shower maxima. Therefore, the signal given by the detectors is generated by the energy deposition of the particle showers, which is linear with the primary losses. This detector distribution has proven to be the optimal one to localize the losses as well as to distinguish between the two beams [83].

The main detector type of the LHC BLM system is an ionization chamber (IC), shown in fig. 3.1, of which there are approximately 3 600 monitors. They are made of a stainless steel cylindrical tube, 50 cm long, and with a diameter of 9 cm, leading to an active volume of 1.5 L filled with N_2 at an overpressure of 100 mbar. The chamber contains parallel aluminium electrodes plates with a thickness of 0.5 mm equally spaced by 0.5 cm that are alternatively used as high voltage and signal electrodes. A voltage of 1.5 kV is applied between the electrodes, which generates an electric field of 3 kV/cm inside the chamber.

The ICs convert the particle shower caused by mislead protons into an electric current by the principle of ionization. The charged shower particles ionize the N_2 gas inside the chamber as they traverse it. The high electric field applied between the electrodes causes the resulting electrons and ions to drift to the corresponding electrode. This movement induces a signal current with amplitude proportional to the beam loss rate.

The experimental uncertainties considered in this analysis on the BLM data for the radiation level measurements, namely a 30% systematic error, are derived from a similar benchmark study in the more controlled CHARM facility [30], and also previously reported for the LHC Run 1 (2011-2012) operation [37] for a variety of radiation sources, as well as for the LHC Run 2 (2015-2018) proton-proton pp collision losses around the high luminosity experiments, ATLAS and CMS [43].

3.4.2 Data analysis chain

The LHC status is stored (in real-time, as well as for offline purposes), in the logging database (LDB) [84].

Figure 3.1: Internal part of an ionization chamber (IC) beam loss monitor (BLM) showing the electrodes. The cables to the read-out electronics are located on the right part (fig. from ref. [45]).

Raw meta-data from the LHC detectors (and more in general, for all the experiments) are available via timeseries information mastering: browsing, extraction and rendering (TIMBER) [85] and can be accessed using the CERN accelerators logging service (CALS), and recently with its upgrade, the new CALS (NXCALS) [86]. This meta-data includes valuable quantities such as the delivered luminosity or beam intensity, as well as measurements for the radiation monitors.

For the analysis done within this thesis described, the radiation monitor and beam instrumentation data is retrieved from TIMBER [85] and post-processed (data filtering, curation, etc.) offline, as it is done for example for the BLM dose rates in ref. [43]. To study the instantaneous losses, the BLM running sum 09 (RS09) is used as it corresponds to a time window of 1 s, matching most of the beam instruments acquisition window.

3.4.3 Annual measured levels at IR4

The cumulated radiation levels in insertion region 4 (IR4) are routinely monitored with the standard fleet of monitors (described in appendix 3, consists of beam loss monitors (BLMs), but also radiation monitors (RadMons) and distributed optical fibre system (DOFRS)) and presented as part of the updates on the radiation level measurements in the LHC ring, in the monitoring and calculation working group (MCWG) meetings [87–89], with one example shown in fig. 3.2. The presented levels are those from cell 14 left to cell 14 right (i.e. spanning more than 1.2 km) of the center of the interaction, exhibiting a stable profile in

2023 compared to the year 2022, however with an increase compared to the 2018 operation and assymmetric with more TID measured on the right side of IR4. This is consistent with the expectations from the additional operation of the Beam Gas Curtain (BGC) instrument in IR4, more precisely quantified in the following sections.

Figure 3.2: (**Upper**) Measured annual radiation levels in LSS4 during 2023, indicating the BLMs placed closer to beam 1 (inner, circulating from left to right) or to beam 2 (outer, circulating from right to left) and (**Lower**) their ratios with those measured in 2022 and 2018 (fig. from ref. [87]). The half cell limits are also shown in the midle pannel.

The first act - The radiation environment at LHC IR4

4

Introduction to the LHC IR4

The Large Hadron Collider (LHC) [1] is equipped with a wide range of instrumentation to measure the beam conditions and parameters. Instruments which measure global properties of the beams (e.g. intensity, emittance) are installed in one the 8 long straight sections of the LHC, namely in insertion region 4 (IR4), while other instruments for local measurements (e.g. beam position) and radiation monitors are distributed throughout the accelerator rings. The proposals for devices measuring the beam size and profile[1] for the LHC and the future HL-LHC [2] have been reviewed in 2019 [90]. Among them are the wire scanner (WS) [91], the beam screen radiation telescope (BSRT) [92], the Beam Gas Ionisation (BGI) [93–95], and the devices discussed in this thesis: the Beam Gas Vertex (BGV) [96–98] and the Beam Gas Curtain (BGC) [99–101] monitors. These two devices intentionally inject gas into the beam pipe and measure the interaction of the beam with this gas target, using different methods.

This first act is divided into four chapters. Firstly, the accelerator geometry and layout of IR4 is displayed, as modelled in this work. Secondly, the general theory behind beam gas interactions is described, as well as the beam parameters that impact the generated radiation levels. Then, the first results of this thesis

are shown, as the particular scenarios are explained in detail for the BGV and the BGC in chapters 6 and 7, respectively, with their differences summarized in table 4.1. Demonstrator instruments have been installed during Run 2 (3) for the BGV (BGC).

The beam intensity configurations used for the LHC Run 2 (2015-2018), Run 3 (2022-to date, planned up to 2026) and the best (meaning highest number of charges) for HL-LHC (planned 2030 onwards) are presented in table 4.2. The total number of charges N_t is given by the number of bunches N_b times the number of charges per bunch n_b. In turn, the beam current $I(t)$ (or intensity) is the total number of charges times the revolution frequency f.

4.1 IR4 geometry layout

A systematic study of the radiation levels in the LHC insertion region 4 (IR4) accelerator and adjacent shielded alcoves has not been previously performed. First, a descriptive FLUKA geometry of the beam line consisting of the beam pipe and all the relevant elements (such as magnets, cavities, instruments and shieldings) has to be modelled in the simulation, and a summary of the those used in this work is given in tab. 4.3, mentioning also those implemented as part of this thesis. A short summary of the most relevant (in terms of their impact on the local/global radiation levels) beam line elements is given here. The discussion is separated for the two beam gas instruments:

---

[1]A beam size measurement of the LHC beam is crucial for the determination of the emittance, which in turn is vital for understanding and modelling of the machine, as well as optimising machine parameters to improve machine performance. It is particular challenging in the LHC, due to its high energy and high brightness beams, resulting in small beam sizes. The performance specifications in terms of accuracy for emittance measurements of the LHC cannot be met by any current LHC device. No single device is able to measure throughout the whole cycle. The current LHC beam size measuring devices and their achieved performances during previous runs are summarised in ref. [90]

Table 4.1: Differences between the Beam Gas Vertex (BGV) and the Beam Gas Curtain (BGC) demonstrator instruments.

	BGV	**BGC**
operation	Run 2 (2015-2018)	Run 3 (2022-to date)
gas profile	distributed	curtain + distributed
image	3D vertex reconstruction	2D
distance to IR4 center [m]	-220	-52
beam (shower direction)	2 (towards DS)	1 (towards IR)
measured data analysis	averaged time periods	instantaneous
resolution	1 h	1 min

Table 4.2: Reference values of the operational parameters of the machine and the beam gas monitors, for the past LHC Run 2 and Run 3, and maximum expected for the HL-LHC operation [80].

	LHC Run 2	**LHC Run 3**	**HL-LHC**
number of bunches N_b	2500		2760
protons per bunch [10^{11} charges]	1.2		2.3
total charges N_t [10^{14} charges]	3.00		6.35
intensity $I(t)$ [10^{18} charges/s]	3.37		7.14
energy E [TeV]	6.5	6.8	7.0

Table 4.3: The beamline elements modelled in FLUKA element database (fedb), either already *existing* in the database, *implemented* in this work or *improved* upon. In particular for the vacuumwarm module and valve gates, more types and configurations (lengths, diameters, etc.) have been added.

Beamline element	**Acronym**	**Status in fedb**
beam gas vertex	BGV	implemented
distributor feed box	DFB	improved
lattice dipole magnet	MB	existing
lattice quadrupole magnet	MQ	existing
beam gas curtain	BGC	implemented (partially)
transverse damper	ADT	implemented
accelerating superconding cavities	ACSCA	existing
dipole magnet for beam separation - single aperture	MBRS	existing
dipole magnet for beam separation - twin aperture	MBRB	existing
beam screen radiation telescope	BSRT	implemented
wider vacuum chamber	-	improved
undulator magnet	MU	existing
beam quality Schottky	BQS	implemented
focusing quadrupole	MQY	existing
vacuum warm modules	VMA	added more types
vacuum valve gates	VVGS	added more types
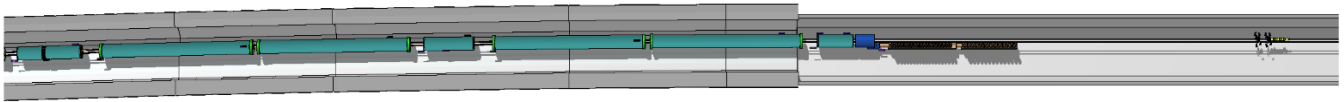
Figure 4.1: FLUKA insertion region 4 (IR4) geometry layout of the accelerator, downstream of the BGV demonstrator, located on the right side, on beam 2.
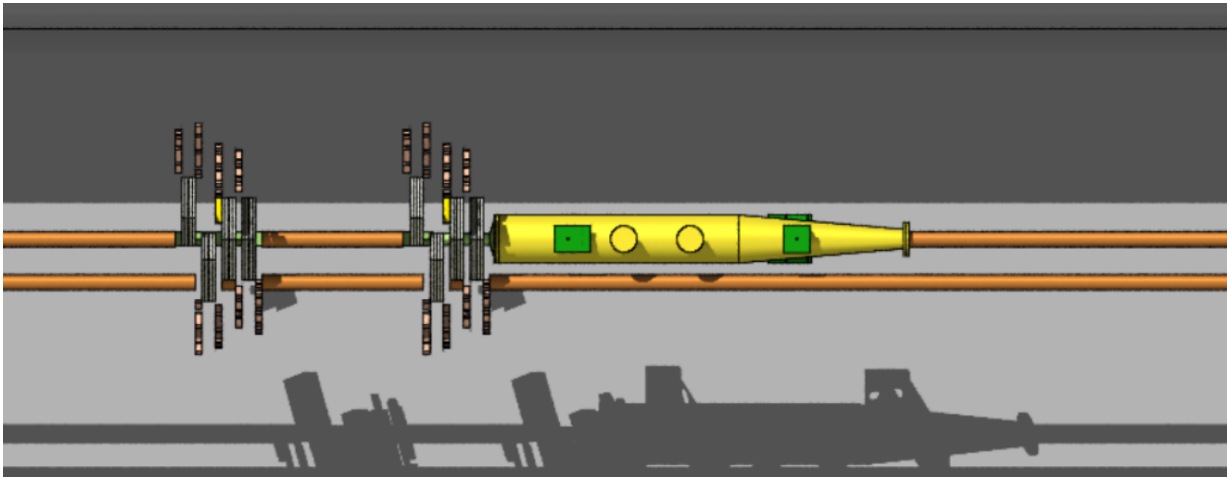
Figure 4.2: FLUKA geometry of the BGV demonstrator, placed on beam 2. The beam is coming from the right side passing through the BGV gas chamber (yellow tank), where it interacts with the injected gas producing secondaries that are measured in the two detector stations downstream.

4.1.1 BGV instrument area

The location of the BGV demonstrator in the accelerator tunnel is at $-220\,\text{m}$ from the centre of IR4, on beam 2 (outer, circulating counter-clockwise), therefore showering towards the exterior of the IR, as shown in the IR4 layout of fig. 4.1. The curved part of the accelerator starts at $\pm269\,\text{m}$, named the dispersion supressor (DS) and followed by the arc sections. This implies that the most impacted beam line elements are the standard superconducting bending dipoles and the quadrupoles, forming the typical FODO lattice of the LHC, with one bending dipole magnet, one **fo**cusing (FO) quadrupole and a second bending dipole magnet and a **defo**cusing (DO) quadrupole. Moreover, the BGV monitor has been implemented in the FLUKA geometry (shown in fig. 4.2), as its material budget downstream could impact the radiation levels. The BGV is primarily based on the

29

use of a gas chamber installed on one of the LHC beam pipes.

4.1.1.1 Distributor feed box (DFB)

Before entering the curved section, one last element exists at about -260 m wrt. the centre of IR4 in the long straight section (LSS) that deals with delivering the cryogenic liquid (He) to the magnets, called the distributor feed box (DFB), illustrated in fig. 4.3. With an impact on the radiation levels, noteworthy components of the DFB are:

1. Next to the beam pipes, there are multiple vertical cylinders, full with the cryogenic liquid, which actually act as a shielding for the tunnel region downstream of them.

2. Towards the end of the module, a beam screen compatible with the dipole exists, which represents an aperture restriction from $R = 3.3$ mm to $R = 2.2$ mm. As such, this will trigger local radiation losses from the beam secondaries that are intercepted.
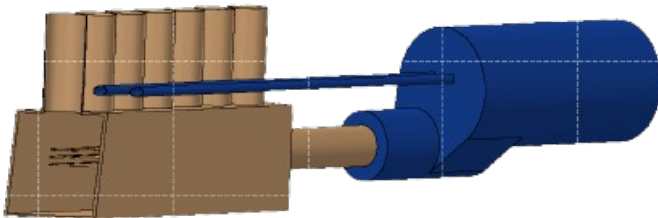
Figure 4.3: FLUKA geometry of the DFB module, showcasing the cylinders containing the cryogenic liquIds (brown) and the beam pipe and the shuffling module (blue).

4.1.1.2 Lattice dipole magnets (MB)

The main budget item and a serious technological challenge are the superconducting (1.9 K) main dipoles (MB) which bend the beams via the Lorentz force around the 27 km circumference of the LHC. For the 7 TeV proton beam, these magnets have to produce a vertical B field of 8.4 T at a current of 11.7 kA. The magnets have two apertures (2-in-1 magnet design), one for each of the counter-rotating beams, as illustrated in fig. 4.4. Each magnet is 14.3 m long and weights around 35 t. A total of 1232 magnets are needed, each costing 0.5 million CHF.

The material budget for the magnets consists, from the exterior to the interior, of:

1. the outer steel cylinder (cryostat) with a thickness of 1.2 cm, and inner radius of $R = 44.5$ cm,

2. the aluminium thermal shield with a thickness of 1 cm, and an inner radius of $R = 38$ cm,

3. the magnet yoke with an outer radius of $R = 28.5$ cm,

4. the two magnet coils, with an inner radius of $R = 2.69$ cm,

5. the beam screen, with an inner radius of $R = 2.325$ cm, and with parallel horizontal planes cutting the circular shape of the beam pipe at $y = \pm 1.845$ cm.

The other magnets typically follow a similar geometry in terms of the beam pipe/screen and outer cryostats, with different implementations for the magnet coils and yokes.

4.1.1.3 Lattice quadrupole magnets (MQ)

In addition to bending the beam, it is also required to focus it, or at least control its divergence. Since the protons are electrically charged, the particle beam diverges on its own, and one needs to focus the beam, such that its width and height are constrained to the vacuum chamber. The focusing is achieved using quadrupole magnets, which act on the charged particle beam similarly as a lens would act on a beam of light. Two quadrupoles are working together to keep the protons tightly bunched: the first quadrupole (QF) takes control of the beam width in the horizontal plane, while the second (QD) one does the same with the beam height in the vertical plane; similarly, the magnetic field of the quadrupoles can be inverted to first defocus and the nfocus. The lattice of the machine consists of alternatively both QF and QD in the arcs, therefore the overall effect is to keep
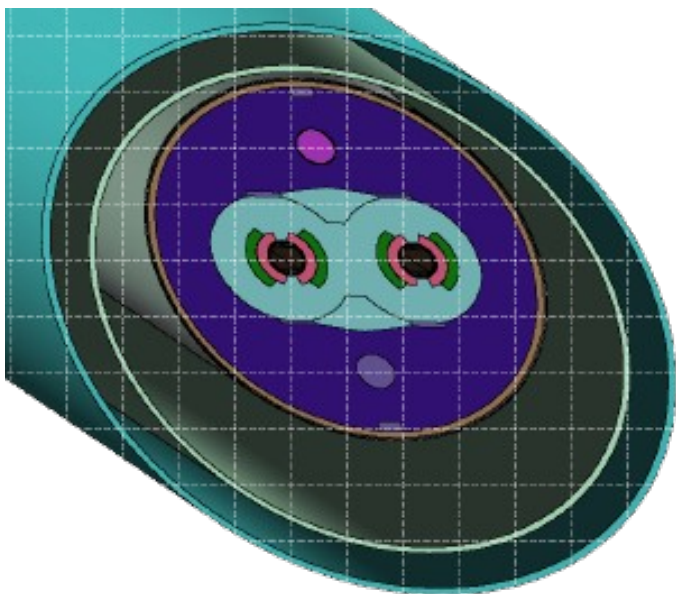
Figure 4.4: FLUKA geometry of the cryogenic bending magnet (MB), showcasing the outer cryostat, and the inner geometry: the magnet yoke (dark purple) and the 2-in-1 magnet technology for the 2 circulating beams.
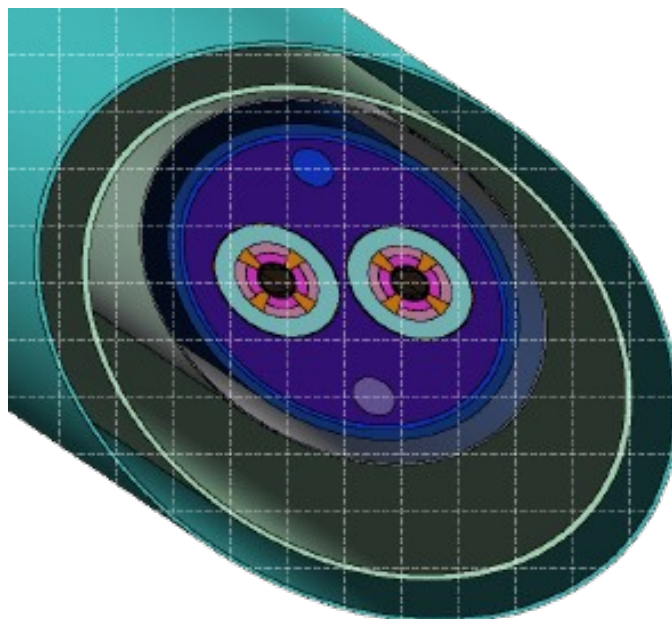
Figure 4.5: FLUKA geometry of the cryogenic quadropole magnet (MQ), showcasing the outer cryostat, and the inner magnet geometry.

the beam focused. There is a total of 858 quadrupole magnets in the LHC.

4.1.2 BGC instrument area

The BGC demonstrator, placed at -42 m from the centre of the IR4 on beam 1 (inner, circulation clockwise), showers towards the centre of IR4, as shown in the IR4 layout of fig. 4.6. There are multiple instruments, some that are essential for the accelerator operation (e.g. the RF accelerating cavities), and other used for beam monitoring or machine development purposes; some of them play a significant role in the local and/or global radiation levels; starting from the BGC and proceeding downstream of it on beam 1, these beam line elements are:

4.1.2.1 Transverse damper (ADT) system

The LHC transverse damper (ADT) system [102] has become indispensable not only for beam stability, but

also as a tool to excite beam oscillations, and to observe instabilities with its turn-by-turn and bunch-by-bunch observation capabilities. The system consists of two kickers (ADTK) and two amplifiers (ADTA), for each beam, and on each side of IR4, in the range ± 24 m to ± 33 m.

Relevant to radiation losses, the implemented FLUKA geometry shown in fig. 4.7 consists of:

1. a wider beam pipe with radius $R = 50$ mm,

2. two quarter of circle elements, on the horizontal plane, with an inner radius of $R = 26$ mm and a thickness of 2 mm,

3. mechanical supports with a radius of $R = 38$ mm and a thickness of 3.6 mm.

4.1.2.2 Accelerating superconducting cavities (ACSCA)

Each radio frequency (RF) system is composed of eight cavities, each delivering up to 2 MV at top energy, equivalent to an accelerating field of 5 MV/m.
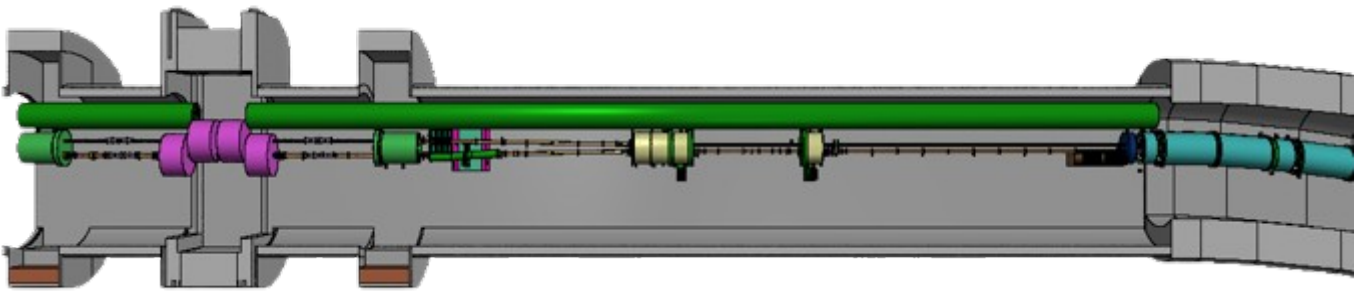
Figure 4.6: FLUKA IR4 geometry layout (not to scale) downstream of the BGC demonstrator in Run 3.
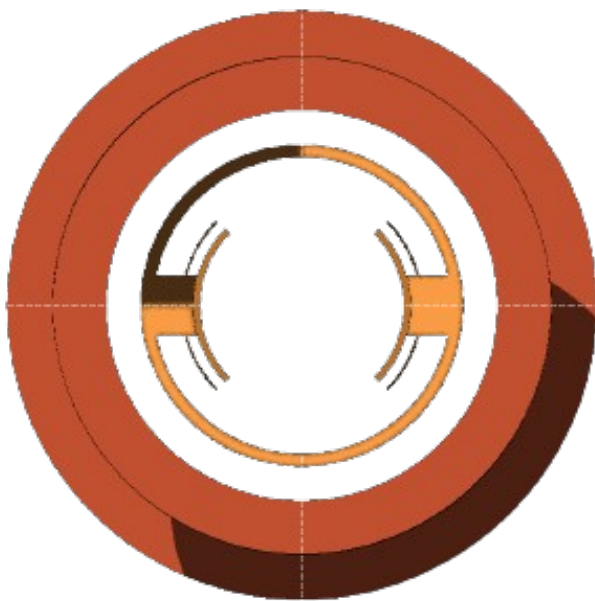
Figure 4.7: FLUKA geometry of the ADT system.

length (about 13 cm at injection and 7.5 cm in collisions).
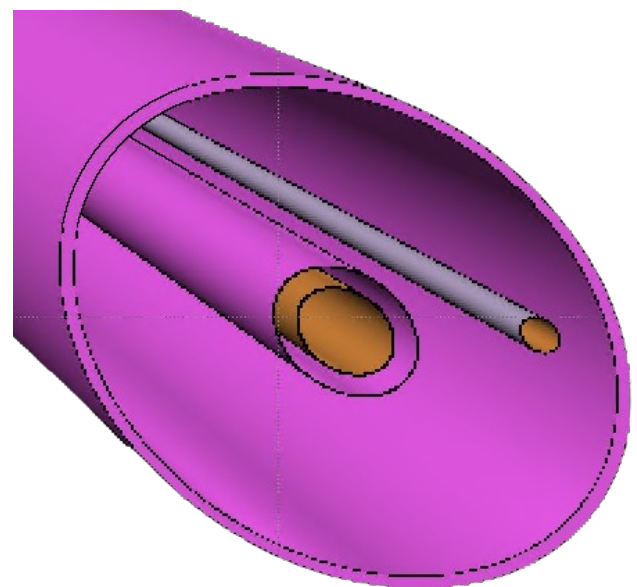
Figure 4.8: FLUKA geometry of one RF cavity, as a 2D section.

With each passage through the RF cavities, each particle gains an energy of 485 keV. The electromagnetic field formed in the cavities in the LHC is tuned to oscillate at 400 MHz. For injection energy each RF system has to provide approximately 8 MV, while at top energy up to 16 MV are required. The 450 GeV injection energy of the particles rises to 6.5 TeV in approximately 20 min, bunches having passed through the RF cavities more than 10 million times. During acceleration to the top energy, the field in the LHC magnets increases as the energy of the particles does. Once the top energy is reached, the main role of the LHC RF cavities is to keep the approximately 2 556 proton bunches tight, controlling the bunch

4.1.2.3 Dipole magnet for beam separation - single aperture (MBRS)

The standard separation between the two circulating beams at the LHC is of 2×9.7 cm, which is preserved in the curved sections of the LHC (the arcs). At the interaction regions, this distance varies depending on the different needs and goals. At the interaction point (IP)s, where the two beams collide, the two beams are actually bent to share a common beam

pipe. At IR4, the two beams are further separated to a distance of 2×21 cm to pass through the radio-frequency cavities, and this is done by the single aperture separation dipole (MBRS), with one magnet on each beam in one cryostat (D3 in IR4), as shown in fig. 4.9. There are total of four magnets, paired in two, symmetrically placed wrt. to the centre of IR4 at ± 50 m.
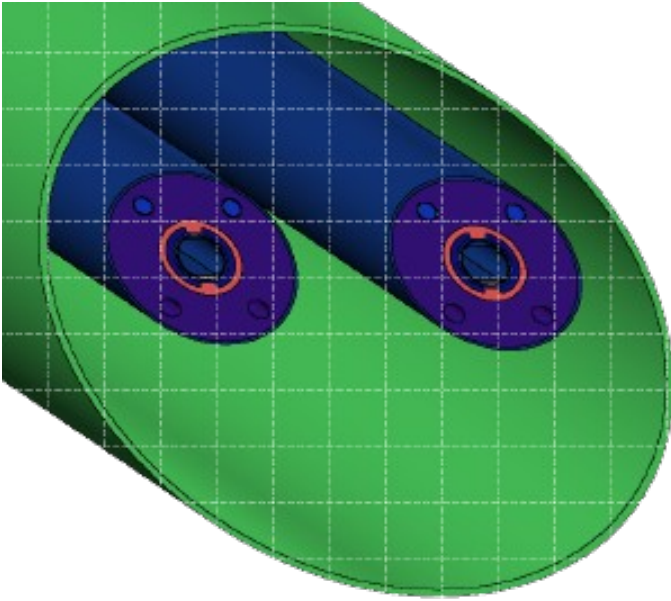
Figure 4.9: FLUKA geometry of the MBRS magnet, showcasing the outer cryostat (green) and the two separated magnet yokes (dark purple).

4.1.2.4 Dipole magnet for beam separation - twin aperture (MBRB)

The MBRS bends the beam and after about 70 m another magnet has to correct this bend to make the two beams parallel again at 9.7 cm to circulate through the arcs of the accelerator. The latter is done by the twin aperture separation dipole (MBRB), out of which there are two symmetrically wrt. the centre of IR4 at 120 m.

4.1.2.5 Beam screen radiation telescope (BSRT)

The beam screen radiation telescope (BSRT) [103, 104] is an instrument that aims to measure the emittance
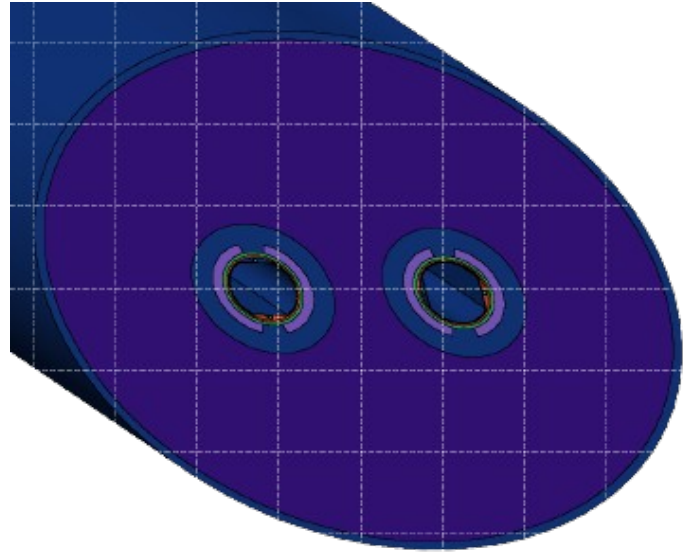
Figure 4.10: FLUKA geometry of the MBRB magnet, showcasing the common yoke (2-in-1 magnet technolgy).

of the beam using synchrotron radiation, emitted by charged particles when their trajectory is deflected, as by the LHC bending magnets, e.g. the MBRS, illustrated in fig. 4.11, and located on both sides of IR4, on the outgoing beam at about 44 m and on the ingoing beam at about 144 m wrt. to the centre of IR4. The BSRT itself does not interact with the beam, but with the secondary synchrotron radiation, as such there are no a priori considerations on their impact on the radiation levels, with the exception of the main modification required for the measurement, namely a wider vacuum chamber.

4.1.2.6 Wider vacuum chamber

The measurement for the BSRT requires a wider beam pipe with an inner radius of $R = 10.635$ cm and a couple of mirrors, placed adjacent to the beam pipe. In fig. 4.12, the BSRT and the shieldings for its electronics, and the wider beam pipe are shown.

4.1.2.7 Undulator magnet (MU)

In the LHC, the radiation from the bending dipole is not sufficient to yield a signal powerful enough
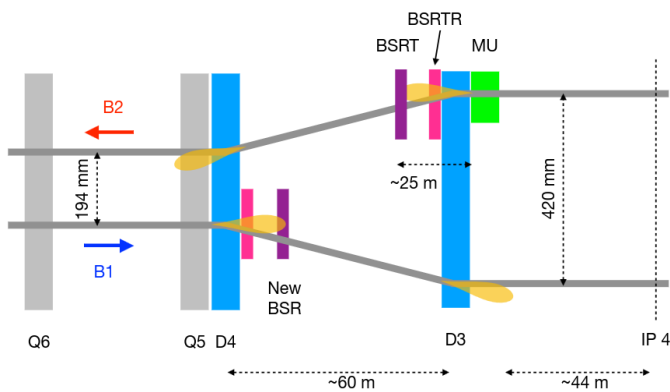
Figure 4.11: BSRT working principle at the LHC (fig. from ref. [103]).
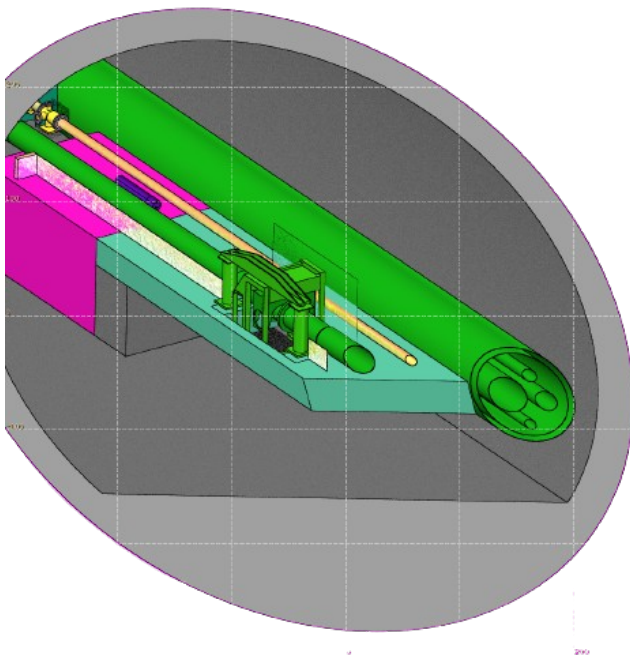
Figure 4.12: FLUKA geometry of the BSRT region. The significantly wider tube to the right is the cryogenic distribution line (QRL), at the same height as the BSRT shieldings, meant to protect electronics placed beneath them. The slightly wider beam pipe to the left is the vacuum chamber of beam 1, while the smaller one in between the wider ones is the vacuum chamber of beam 2.

to be measured by the BSRT. For this reason, a special magnet is used: namely, a short undulator mag-

net (MU) [105] forces an harmonic oscillation of the particles, thereby stimulating the emission of synchrotron radiation. The model of the magnet is shown in fig. 4.13. There are a total of 8 magnets, placed upstream the MBRB and downstream the MBRS, for both beams.
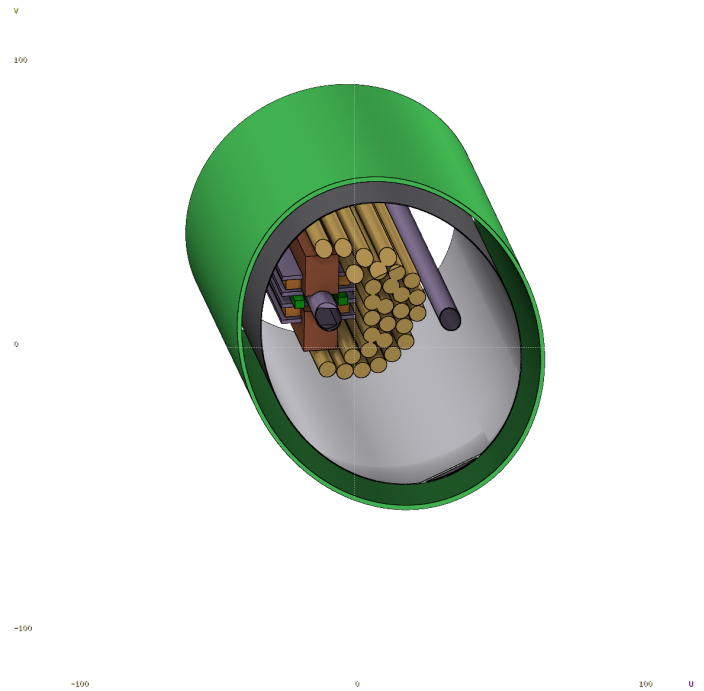
Figure 4.13: FLUKA geometry of the MU magnet.

4.1.2.8 Beam quality Schottky (BQS)

The LHC beam quality Schottky (BQS) [106, 107] beam diagnostics system was designed with the intent of measuring important beam parameters such as tune, chromaticity, synchrotron frequency, momentum spread, etc. Compared to the presently available invasive methods that can cause significant particle losses, the LHC Schottky system is able to measure in a passive way. It does so by detecting internal statistical fluctuations of the beam particles passing through it, as indicated in fig. 4.14. These fluctuations are the so-called Schottky noise, and one extracts the information that is encoded in the frequency spectrum.
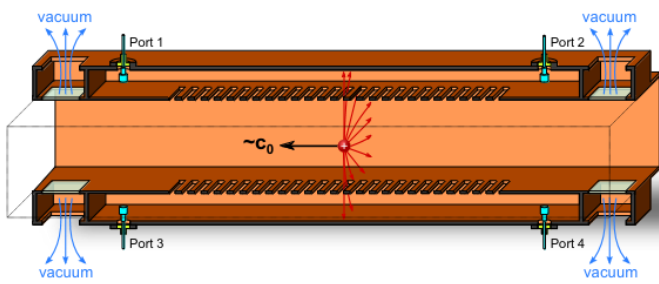
Figure 4.14: BQS working principle at the LHC (fig. from ref. [108]).

4.1.2.9 Focusing quadrupole (MQY)

Before increasing the separation of the beam through the MBRB, there are two focusing quadrupoles (MQY) in cell 5 and 6. These are wide aperture quadrupole in the insertions, with twin aperture, as shown in fig. 4.15.
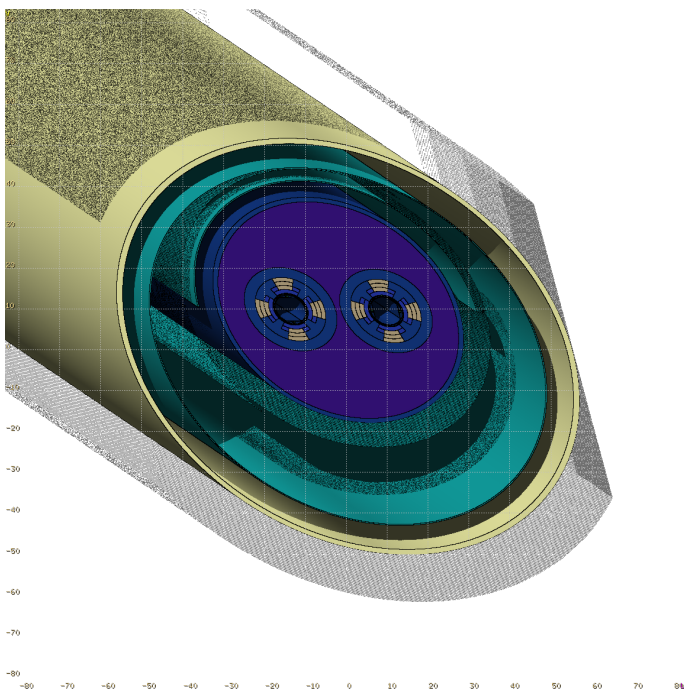
Figure 4.15: FLUKA geometry of the MQY magnet.

4.1.2.10 Vacuum module (VMA) and valve gates (VVGS)

In the arc sections, the beam pipe has a nominal circular shape, with a diameter of 80 mm, but different magnets may have a different (usually reduced) beam screen diameter, with non-circular shapes. Typically, there are special beam pipe transitions for every change of diameters: 66, 68, 80 and 100 mm. Moreover, due to the thermal fluctuations, the vacuum sector requires flexible portions of the beampipe that can stretch/contract depending on the dilatation. For this, Vacuum Modules (VMAs) are used, with a typical geometry shown in fig. 4.16, as well as vacuum valve gates (VVGS).
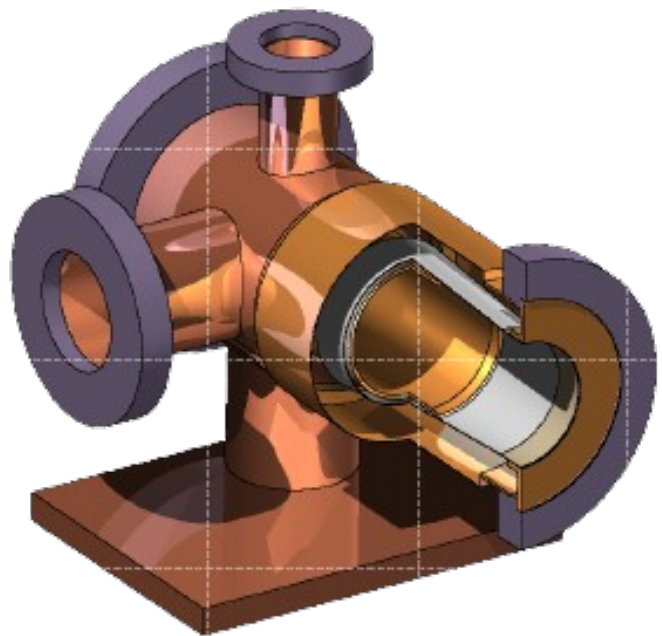
Figure 4.16: FLUKA geometry of the VMA module

Source term: beam gas interactions

The Large Hadron Collider (LHC) [1] radiation field includes different kinds of particles with broad energy spectra, all originating from the interaction of TeV-scale beam particles or secondary collision products, as shown with the FLUKA Monte Carlo code [18, 109]. In the context of this work, the beam-gas collisions are studied. The vacuum of the LHC is not perfect (estimated to be at most 10^{-9} mbar, but with local peaks reaching even 10^{-7} [110, 111]), and thus the particle beam in the accelerator passing through the residual gas will interact with it, either elastically, in which case the beam particles are slightly off trajectory, or inelastically, causing both local radiation showers and perturbing the quality of the beam profile. The latter mechanism is exploited at insertion region 4 (IR4), where there are several beam instruments that intentionally inject gas (e.g. Neon) in the beam pipe to characterise the 2D transverse beam profile, such as the Beam Gas Vertex (BGV) and the Beam Gas Curtain (BGC).

5.1 Mechanism and normalization factors

Since the radiation shower originate from collisions between the beam protons and the gas targets, the instantaneous radiation level rates dR/dt are assumed to be proportional to the interaction rate $I_{collision}$ of inelastic beam-gas collisions, which can then be integrated to cumulative quantities assuming different operational scenarios. The parameters can be divided into two categories, those those that depend on the specific element operation/usage and those that depend on the accelerator operation:

$$\frac{dR}{dt} \propto I_{collision} = \underbrace{\Theta(t;s_a,s_b) \cdot \sigma_j}_{P(element)} \underbrace{(E) \cdot f \cdot N(t)}_{P(machine)} \quad (5.1)$$

with the integrated gas density profile $\Theta(t;s_a,s_b)$ along the s-coordinate in the accelerator region $[s_a,s_b]$ at time t, the (inelastic) cross section for the proton collision on the gas atom, the beam energy E, the LHC revolution frequency $f = 11\,245\,\text{Hz}$ and the number of charges $N(t)$ passing through the gas, Each of these parameters is discussed in the following sections, starting from the last.

5.1.1 Beam intensity

The (HL-)LHC beam is structured time-wise as a bunched beam consisting of (2760) 2500 bunches, with $1.20 \cdot 10^{11}$ ($2.3 \cdot 10^{11}$) protons per bunch on average, and with a constant revolution frequency of $f = 11\,245\,\text{Hz}$.[1] The reference intensity measurement at the LHC is given by the beam current transformer (BCT) instruments [112], providing data with a time resolution of $\Delta t = 1\,\text{s}$. The direct beam current transformer (DBCT) provides a measurement of the total number of charges N_t per beam (summed over all circulating bunches) with an uncertainty of $\Delta N_{rel,DCBCT} = 0.5\%$ for high-intensity beams [113]. The bunch-by-bunch intensity sharing is measured by the fast beam current transformer (FBCT), with

---

[1]At these ultra-relativistic TeV energy scales, increasing the energy even further translates into an increase in mass rather than in the velocity, and thus one can assume that the revolution frequency remains constant over the energy range at the LHC from injection at 450 GeV up to collisions at 7 TeV

the total intensity measured by the FBCT calibrated against the DBCT measurement. Depending on how well the recalibration is done, the error on the intensity is typically $\Delta N_{rel,FBCT}$ =0.5-2%.

When a particle beam (protons or heavy ions in the case of the LHC) is circulating in the accelerator, it continuously interacts via several mechanisms leading to a decrease in the initial beam intensity N_0 (for the LHC, no subsequent injections happen during one fill after ramp up). The time t evolution of the intensity $N(t)$ in a fill then typically follows an exponential behaviour, as:

$$N(t) = N_0 \cdot \exp(-t/\tau) \tag{5.2}$$

where τ would be a fittable parameter for each fill, related to the beam life time described in section 2.6.1, depending on the operational conditions of the LHC. The contributions to the beam intensity reduction comes from the following sources, in order of importance:

1. luminosity burn-off, due to the collisions at the experimental interaction regions, as described upon in section 2.6.1,

2. collimation (betatron losses) in IR7, responsible with cleaning the beam, in particular removing the particles in the tails of its spatial distribution; similarly in IR3, but with significantly lower losses,

3. beam-gas collisions across the entire accelerator, as described in section 2.6.2, but also in the beam gas monitors via their respective injections. This could constrain the beam life time, but for the example of the Beam Gas Vertex (BGV), the probability of interaction corresponds to one interaction (elastic or inelastic) every 11 turns on average, or to a beam life time in the order of 6 years, if considering that all elastic and inelastic interactions lead to a loss of the interacting proton.

Moreover, a secondary effects is that the beam-residual gas collisions leads to an improvement in the vacuum quality, over time. Given the already very good vacuum in the LHC accelerator beam pipe, the inelastic interaction between the beam protons and the rest gas will lead to a slow decrease of the gas density, that can actually be observed over the time-span of one year of operation, if the vacuum is maintained (i.e. no significant faults occurred that required intervention and removing the vacuum).

5.1.2 Interaction cross section at LHC beam energies

The total cross-section of the interactions is comprised of the elastic and inelastic components, which depend heavily on the gas constituent (whether hadronic or leptonic) and the center of mass energy $\sqrt{s}$ as:

$$\sigma_{AB}^{tot}(\sqrt{s}) = \sigma_{AB}^{el}(\sqrt{s}) + \sigma_{AB}^{inel}(\sqrt{s}) \tag{5.3}$$

- Elastic σ_{el}: If the interaction is electromagnetic, the most likely scenario is Coulomb scattering, which changes the trajectory of one or more protons in the bunch causing them to deviated from the ideal trajectory of the accelerator. Thus, their behaviour becomes unpredictable and they are lost somewhere along the path of the accelerator, typically in the collimators of IR7.

- Inelastic σ_{inel}: If the interaction is a due to the strong force, then a shower of secondary particles is generated around the interaction vertex leading to local losses.

For the case of LHC proton-proton collisions, the hadronic pp inelastic cross section has been measured extensively [114], yielding $\sigma_{pp}(\sqrt{s}$=13 TeV)=80 mb.

5.1.2.1 General theory on proton-nucleus interactions

Experimental data points for all energies and gas constituents of interest are not available, but ref. [115,

116] provides a cross section σ_{pA} extrapolation considering a fixed target experiment of proton on proton, and then scaled up to the number of nucleons A of the actual gas target as follows:

$$\sigma_{p+A} \approx \sigma_{p+p} \cdot A^{\alpha} \tag{5.4}$$

with the exponent α close to 2/3 (the surface of the nucleus considered as a sphere, projected on a 2D plane). Measurements at this energy regime of interest for this thesis have been performed before at the HERA [115] experiment, yielding numerical values for α as:

$$\sigma_{pA}^{tot} \approx \sigma_{pp}^{tot} \cdot A^{0.7694 \pm 0.0012} \tag{5.5}$$

$$\sigma_{pA}^{inel} \approx \sigma_{pp}^{inel} \cdot A^{0.7111 \pm 0.0011} \tag{5.6}$$

where A is the mass number of the target (20 for Neon). In case of molecules, the sum of the constituents' atomic numbers of the molecule is considered.

For a collision of a particle with mass m_1 and momentum p_1 with another particle with mass m_2 and momentum p_2, the energy in the laboratory frame is given by:

$$E_L = \sqrt{p_1^2 c^2 + m_1^2 c^4} + \sqrt{p_2^2 c^2 + m_2^2 c^4} \tag{5.7}$$

$$|p_L| = |p_1 + p_2| \tag{5.8}$$

$$\sqrt{s} = E^* = \sqrt{E_L^2 - p_L^2 c^2} \tag{5.9}$$

The high energy protons impacting the gas (assumed at rest, as their thermal energy of 0.025 eV at room temperature is negligible) in the LHC beam pipe or in the instruments' vacuum chambers can be seen as a fixed target experiment. To calculate the center of mass energy, one considers that the impinging proton interacts principally with just a single nucleon inside the nucleus, leading to:

$$\sqrt{s_{NN}} \approx \sqrt{2mc^2 c p_{lab}} \tag{5.10}$$

where m could be either the neutron or the proton mass. At the LHC, for a 6.5 TeV proton, the center of mass energy becomes $\sqrt{s} = 110$ GeV, for which the proton-proton cross section is $\sigma_{p+p,inel} \approx 40$ mb. According to eqn. 5.6, this yields an estimate of $\sigma_{p+Ne,inel} = 320$ mb.

During LHC Run 2, the top energy was 6.5 TeV TeV, but during HL-LHC it will increase to 7 TeV (the beam parameters are summarised in Table 4.2). Moreover, there is interest in using some of the beam instruments during energy ramp from 450 GeV (injection) to top energy, as is the case for both the BGV and the BGC.

Figure 5.1 shows the FLUKA estimates of the cross section in the energy range of interest, showing a slight increase of 8% (0.5%) from 450 GeV (6.5 TeV) to 7 TeV. This leads to an increase in the interaction probability. Additionally, with the higher beam energies, the secondary showers will be larger and more powerful, leading to higher radiation levels.

5.1.2.2 FLUKA implementation

The above section represent the current state of the theory and of the available measured data on the pA interaction cross sections. In order to handle this type of interaction, the FLUKA model was implemented in 1983 [118] with the following parametrization as a function of energy:

$$\sigma_{tot}^{pA}(s) = a + b \cdot \ln^2 \frac{s}{s_0} \tag{5.11}$$

where a and b are fitted parameters on the measured data for various center of mass energies $\sqrt{s}$. Concerning the dependence on the atomic mass A, cross-section tables are constructed for a given set of momenta and materials, given in fig. 5.2 for FLUKA. From these table the actual cross-section for a given material is obtained by interpolating according to eqn. 5.4, as follows for $A_1 < A < A_2$:
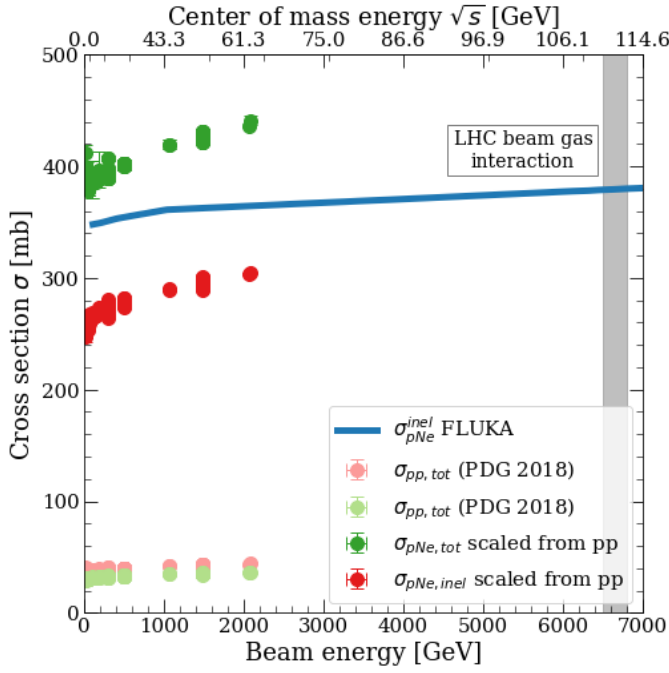
Figure 5.1: Total and inelastic cross section σ_{pNe} of the proton beam hitting the Neon gas target at rest, as function of the beam energy (and center of mass energy computed according to equation 5.10), as scaled via via equation 5.6 on the measured data pp from ref. [117], and the inelastic cross section estimated by FLUKA (blue line). The knee present in the FLUKA estimate at 1 TeV stems from patching different theoretical models. The vertical dashed green line represents the beam-gas collision energy.

the expected accuracy; in the absence of more measured data points). Until future measured data or theoretical models appear that provide a better description of the proton-nucleus interaction at such high energies, there is also no urgent need to update the FLUKA description that models this interaction.
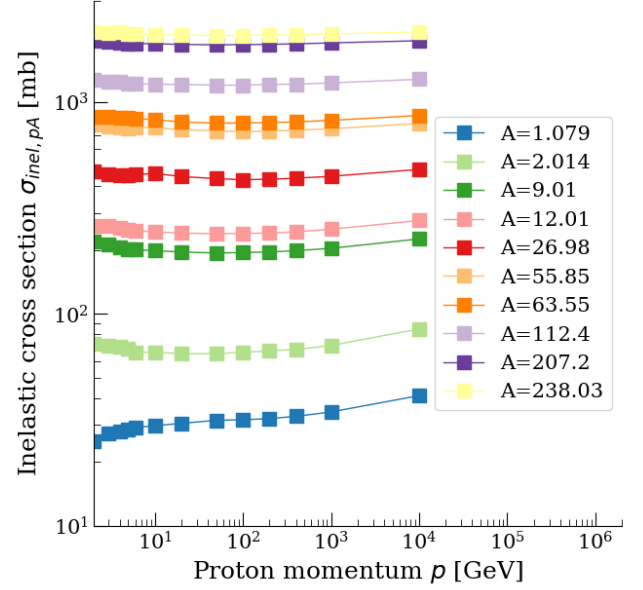
Figure 5.2: FLUKA data for the parametrization of the inelastic pA interactions, valid only above 1 GeV, and for different atomic masses A. Neon has an atomic number of $A = 10$.

$$\alpha = \ln \frac{\sigma_{pA_1}}{\sigma_{pA_2}} / \ln \frac{A_1}{A_2} \qquad (5.12)$$

$$\sigma_0 = (\sigma^{pA}) / A^{\alpha} \qquad (5.13)$$

Numerically, the values mostly used in this work are based on the beam energies during Run 2 (3), for the time period 2015-2018 (2022-to date) for the BGV (BGC) demonstrator, at 6.5 TeV (6.8 TeV), for which the cross section is $\sigma_{pNe,inel} = 381.99$ (383.03) mb. The difference that can be observed in fig. 5.1 between the FLUKA estimated cross section described in this section and the values suggested by the theory of the previous section is considered acceptable (within

5.1.3 Gas density profiles

Each beam gas instrument under study here injects gas inside the beam pipe vacuum to increase the local density of atoms in order to enhance the collision rate. At the LHC, the vacuum system is capable of achieving a very low pressure in the beam pipes, in the order of $p = 1 \cdot 10^{-9}$ Pa (or $1 \cdot 10^{-11}$ mbar), roughly equivalent to the lunar surface atmosphere. This corresponds to a density of $\rho = 10^5$ particles/cm^3, per

the ideal gas law[2], assuming room temperature of $T = 300\,\mathrm{K}$:

$$pV = Nk_BT \rightarrow \rho = \frac{N}{V} = \frac{p}{k_bT} \qquad (5.15)$$

where N is the number of atoms or molecules of the gas, k_b is the Boltzmann constant, and V is the volume of the gas.

Generally, the residual gas in the LHC is a mixture of N different gas constituents, such as H, C, O, and other species. In this case, each constituent will contribute to the total beam-gas interaction according to their density ρ_j (in number of atoms of species j per volume) and interaction cross section σ_j, as:

$$\Theta(s, s_a, s_b) = \int \sum_{j=1}^{N} \sigma_j \rho_j(s)ds \qquad (5.16)$$

In the case of the beam gas instruments, the intentional injections of neon at orders of magnitude above the background pressure simplifies the analysis to just one gas species:

$$P(element) = \Theta_{Ne}(s; s_a, s_b) = \sigma_{Ne} \cdot \int_{s_a}^{s} \rho(s)ds \qquad (5.17)$$

The interaction probability per proton given via eqn. 5.17 in this work yields values of the order of 10^{-10}, meaning that for each 10^{10} protons only one would collide with the gas generating particle showers. To increase computational efficiency for the FLUKA simulations, a method for simulating the beam-gas interactions has been developed based on random sampling of a cumulative distribution

---

[2]One could also consider the Van der Waals equation:

$$(p + \rho^2 a')(\frac{1}{\rho} - b') = k_BT \rightarrow p = \frac{k_bT}{\frac{1}{\rho} - b'} - \rho^2 a' \qquad (5.14)$$

However, for the use case of this work, of Neon with $a = 0.2135\,\mathrm{L}^2/\mathrm{bar}/\mathrm{mol}^2 = 5.89 \cdot 10^{-52}\,\mathrm{m}^6/\mathrm{mbar}$ and $b = 0.01709\,\mathrm{L}/\mathrm{mol} = 4.71 \cdot 10^{-53}\,\mathrm{m}^3$, the difference between eqn. 5.15 and 5.14 is of $3.68 \cdot 10^{-8}$ %.

---

function (CDF), generated from a given gas density profile within the beam pipe. This simulation procedure has been previously used to study the Beam Gas Ionisation (BGI) element [119], and as it is described in further detail in Appendix 3.

From a measurement perspective, one employs pressure gauges from various producers and of several designs, which at CERN are typically calibrated in-house [120], albeit for N_2, but other gas species exhibit different sensitivities [121]. The raw values measured by the pressure gauge have to be scaled up by a factor of 4, to take into account the Ne to N_2 sensitivity. The measurement uncertainty for these pressure measurement devices vary depending on the pressure range (typically, the higher the pressure, the more molecules reach the pressure gauge, thereby increasing the statistics of the measurement process). Moreover, the gauges are calibrated in the lab, but when installed at the LHC, several more effects can occur that perturb the calibration: aging effects due to radiation, temperature dependencies, etc. As a global systematic uncertainty, a value of $\Delta p_{meas} = 30\%$ is considered [122].

5.1.4 Produced secondaries

The inelastic collision between the beam proton and the gas generates secondary products, by definition. Figure 5.3 shows the energy and the angular distributions of the products, averaged per interaction, for four categories of particles. There is a large proportion of forward scattered products, namely protons p and neutrons n, with some of them retaining almost the full beam energy close to 7 TeV. Anti-protons $\bar{p}$ and anti-neutrons $\bar{n}$ are also produced, albeit with smaller energy. Heavier fragments, such as alpha particle α, deuterons d and triton t are produced, with significantly smaller energy and larger scattering angle. However, most of the generated particles are pions ($\pi^\pm, \pi^0$) and a smaller proportion of kaons ($k^\pm$); for this reason the detector modules for the BGV instrument were actually aiming to measure pions. Depending on the decay channel, the inelastic proton-nucleon collision can generate more exotic particle states (Σ, Ξ, Λ), with lower probability. Members
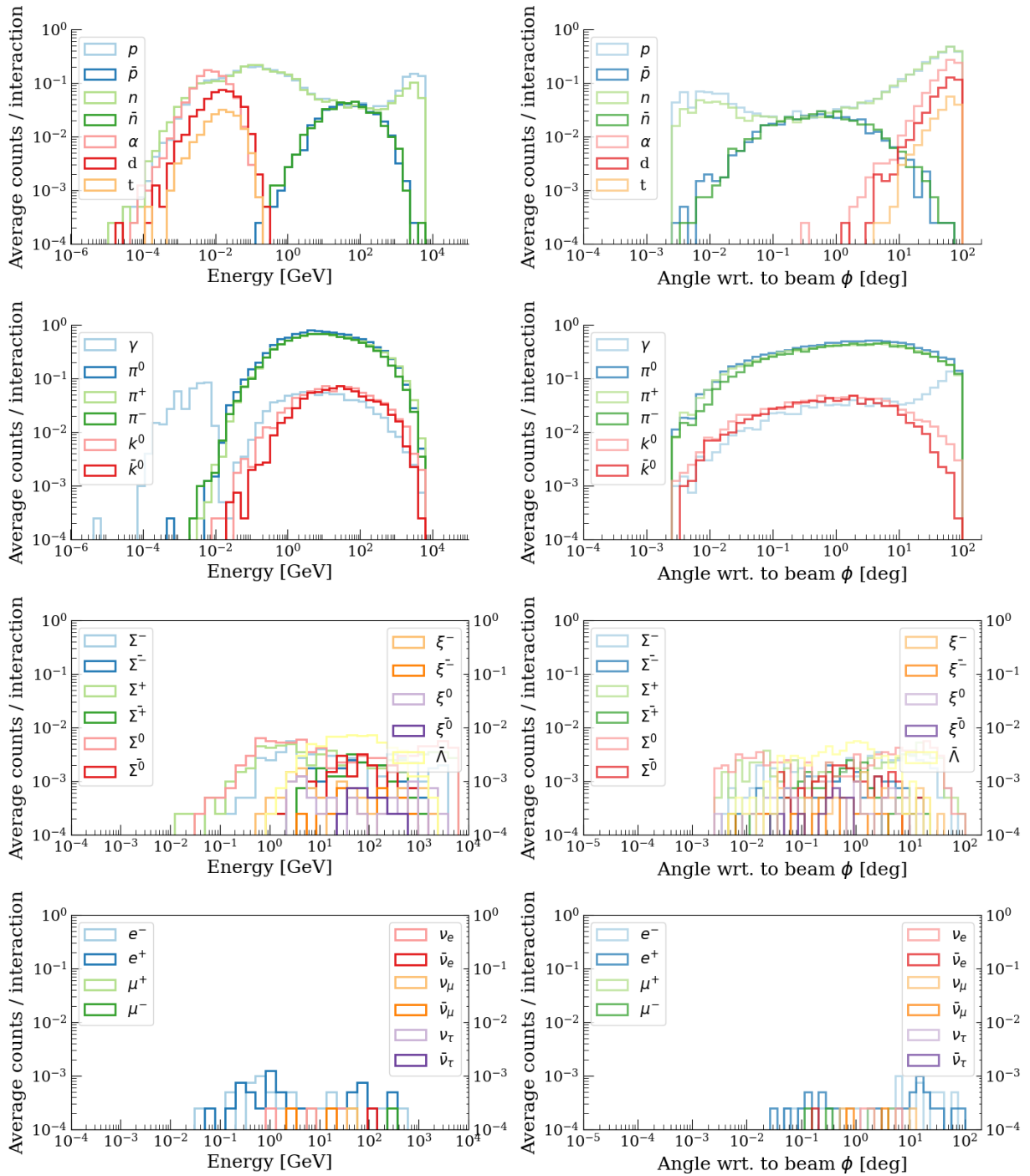
Figure 5.3: Secondary products from the *pNe* collision, with their (**Left**) energy and (**Right**) angular distributions.

of the lepton family (*e*, *μ*, *τ* and their anti-particles, as well as neutrinos) are also generated, however with a very low probability. Figure 5.4 additionally displays the correlation between the energy and the angle of the secondary particles, for the most abundant particle species: protons *p*, neutrons *n*, gammas

γ and neutral pions π^0. It indicates that the very forward peaked particles also retain most the beam energy.

5.1.5 Beam phase space

The beam does not maintain a constant phase space (momentum and position distribution), but it varies along the accelerator depending on the beam optics, with the priority to have the smallest beam sizes at the interaction points to maximise the collision rates. The beam shift, divergence and size are given in fig. 5.5, together with the 2023 BGC measurements on the beam size.

One typically assumes that the gas is uniformly distributed in the transversal plane, implying that the beam size would not play a role in the interaction rate. This is the reason why the gas density profiles take into account just the longitudinal z distribution. However, the Beam Gas Curtain (BGC) gas target (jet) is about 1-2 cm in width, implying that the beam might completely miss the gas target, if not aligned correctly. Not only the beam size, but also the beam divergence could a priori play a role. However, the expected beam divergence shown in fig. 5.5 is at the order at most $6\,\mu\text{rad}$ (or $3 \cdot 10^{-4\circ}$), one order of magnitude lower than the expected minimum angular distribution values from the inelastic proton-nucleus pNe interaction, at a value of $60\,\mu\text{rad}$ (or $3 \cdot 10^{-3\circ}$. Nevertheless, one simulation has also been performed using the twiss beam values for the beam size and divergence, revealing no differences compared to when the beam properties are not taken into consideration.

5.2 Measured data - selected time periods of operation

Amongst the several measurable accelerator parameters that are of relevance when studying intensity driven losses at the LHC, which affect the radiation levels in the subsequent regions of the tunnel at IR4, there are the beam intensities and the measurements from the pressure gauges in the beam pipe. The starting point of the present analysis is to select periods of the LHC operation with stable operational parameters, such that their radiation level data can be compared to a corresponding FLUKA simulation that represents as accurately as possible the LHC configuration under examination. Subsequently, within a single LHC fill, some parameters, such as the gas pressure or the beam intensity, change. When gas is injected in the beam instruments, one typically expects the beam loss monitor (BLM) total ionizing dose (TID) rate signal to be proportional to the product of intensity and pressure, as described in eqn. 5.1.

5.3 Ion operation radiation levels

In terms of cumulated radiation levels, the ion operation is scheduled to run for about a month per year [13], and thus the focus has been on the proton runs which consists of several months. There are several notable changes in terms of radiation levels when using a heavy ion beam. Again, following the parameters from eqn. 5.1, the discussion can be divided into three pillars:

1. The beam intensity in number of charges is approximatively a factor of 4 lower, from a nominal proton intensity of $10 \cdot 10^{13}$ charges down to $1.4 \cdot 10^{13}$ charges.

2. For a value of the beam momentum p_{lab}, the fraction of p_{lab} carried by each nucleon of the heavy ion nucleus A can be approximated to:

$$p \approx \frac{p_{lab}}{A} \qquad (5.18)$$

implying that the energy per nucleon for ion operation is foreseen to reach $p_n = 2.76\,\text{TeV}$, compared to the proton $p_{lab}=7\,\text{TeV}$. This leads to a center of mass energy when the heavy ion $M_A = A \cdot m$ impinges on a rest gas nucleus B as:
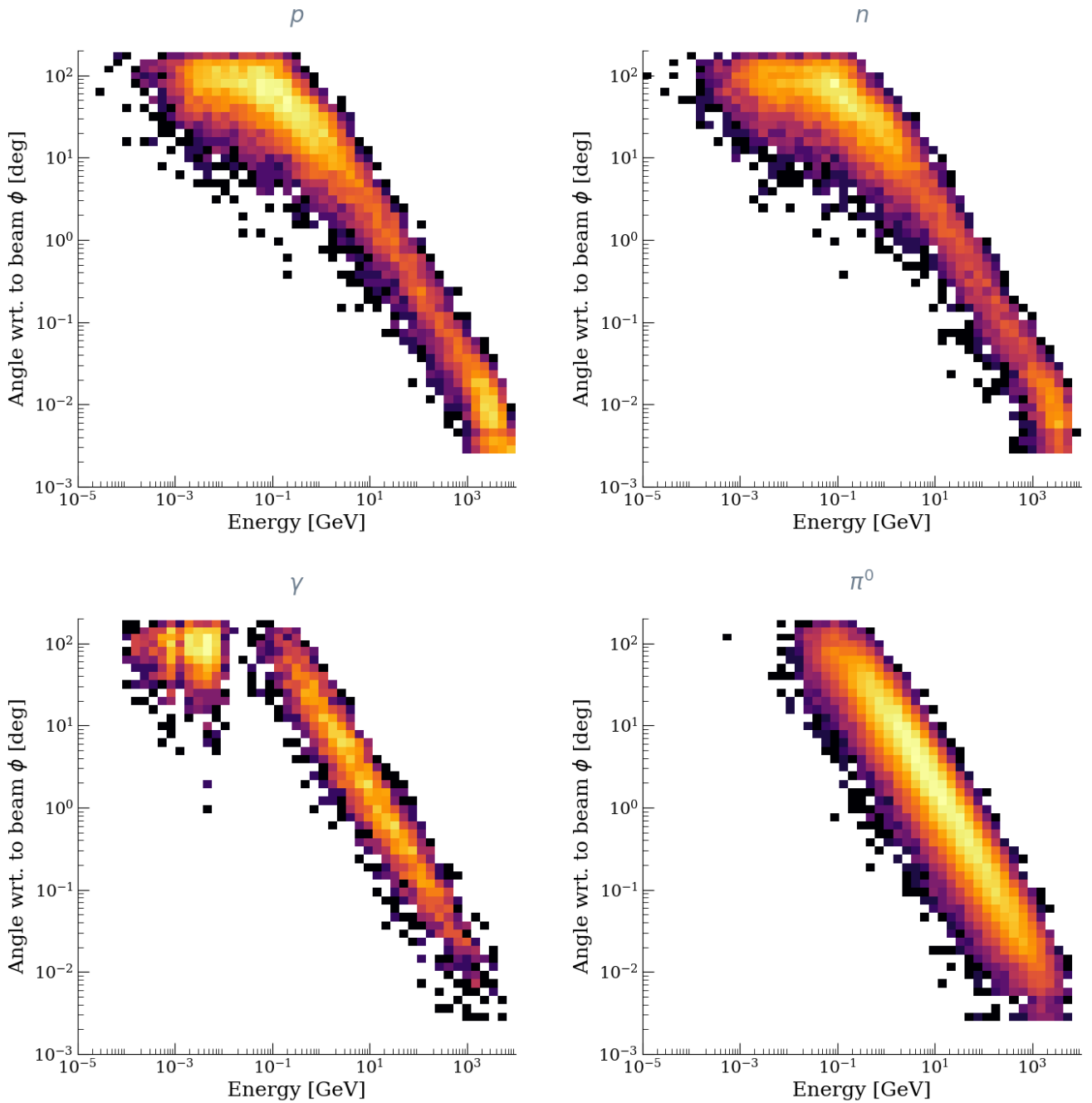
Figure 5.4: Secondary products from the *pNe* collision, shown as 2D distributions, for individual particles species: **(top left)** protons *p*, **(top right)** neutrons *n*, **(bottom left)** gammas *γ* and **(bottom right)** neutral pions π^0.

$$\sqrt{s_{NN}} \approx \sqrt{(2Mc^2cp)} = \sqrt{\left(2Amc^2\frac{cp_{lab}}{A}\right)}$$

$$(5.19)$$

independent of the target type *B*. For the LHC lead beam, this leads to $\sqrt{s_{NN}} \approx 61\,\text{GeV}$, al-
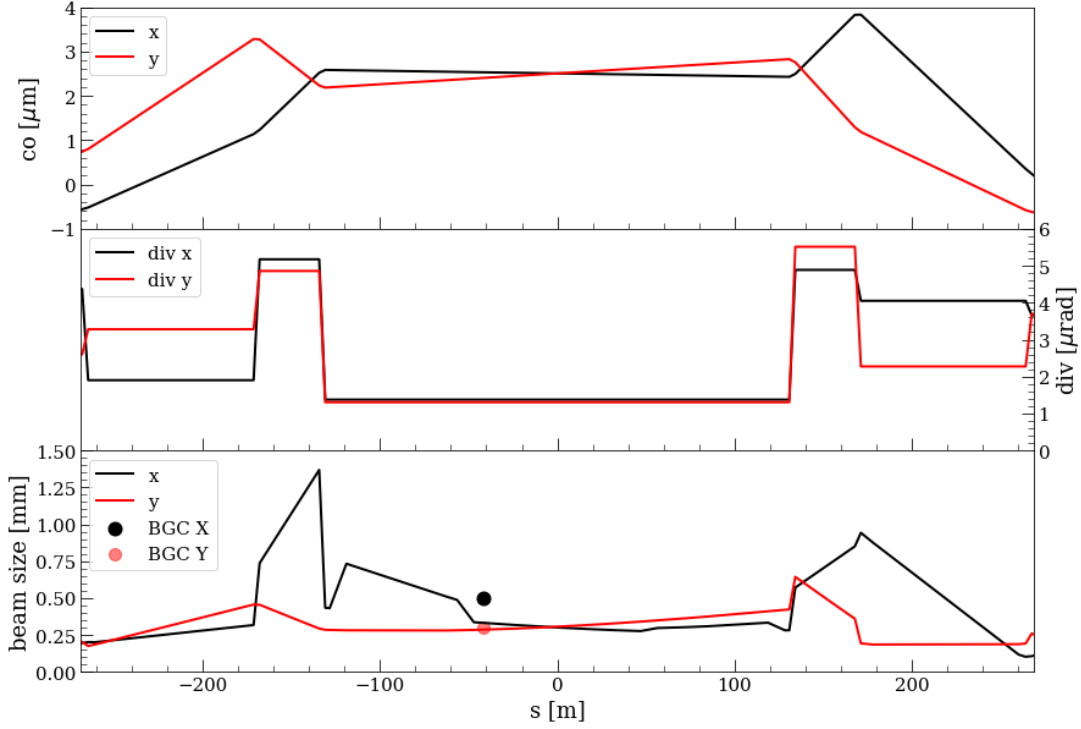
Figure 5.5: insertion region 4 (IR4) beam optics, showing the **(top)** beam coordinate/position within the beam pipe within µm distance, **(centre)** beam angular divergence in the µrad range, and **(bottom)** the beam size as full width at half maximum (FHWM), together with the beam size Beam Gas Curtain (BGC) measurements from 2023 [123].

most a factor of two lower than the proton beam $\sqrt{s} = 110\,\mathrm{GeV}$.

3. The cross-section σ_{pA} for an ion beam A impinging on hydrogen nuclei, i.e., protons p, is easily obtained from the *reversed* case, where the proton beam impinges on the ion at rest. For gases other than hydrogen, a naive formula for an order-of-magnitude estimate of the inelastic cross-section at high energy is [116]:

$$\sigma_{AB} = \sigma_{pp} \cdot \left(A^{1/3} + B^{1/3} \right)^2 \qquad (5.20)$$

where A and B are the atomic masses of the ions. For the LHC $^{208}_{82}Pb$ ion beam hitting the $^{20}_{10}Ne$ gas target, this leads to an estimate on the cross section that is scaled up by ≈ 75 times.

To conclude this section, with a *Pb* ion beam instead

of protons, the inelastic interactions leading to local radiation levels from the operation of beam gas instruments will be almost two order of magnitudes more probable, but at half the center of mass energy and four times lower beam intensity.

5.4 Systematic errors and uncertainties

The considered systematic uncertainties are summarised for the measurements in Table 5.2 and for the theoretical assumptions in Table 5.1. Moreover, there are a number of errors and uncertainties associated with the Monte Carlo method and computational physics. Within the scope of this thesis based on FLUKA calculations, the main contributing factor is the accuracy of the geometry. This is in term of posi-

Table 5.1: Uncertainties stemming from theory

Source	Uncertainty Δ_{rel} [%]	Reference/Description
Cross section estimation	14	section 5.1.2, fig. 5.1
Pressure equation	$\mathcal{O}(10^{-8})$	eqn. 5.14 in Footnote
CDF Taylor approximation	$\mathcal{O}(10^{-8})$	appendix 3

Table 5.2: Uncertainties stemming from measurements

Source	Uncertainty Δ_{rel} [%]	Reference/Description
Pressure measurement	30	section 5.1.3
Dose rate (BLM)	20	ref. [30]
Beam intensity (BCT)	0.5-2	section 5.1.1
Beam energy	0.1	ref. [124]

tion of objects inside the main simulation geometry,
materials and dimensions.

6

The Beam Gas Vertex (BGV) instrument

The radiation levels in the tunnel and on the downstream equipment caused by the secondary products from the beam gas collisions in the Beam Gas Vertex (BGV) [96, 97, 121] on beam 2 are non negligible, as the radiation shower is directed towards cryogenic magnets in the dispersion supressor (DS), ahead of the Large Hadron Collider (LHC) arcs [1]. Based on the BGV demonstrator operation in Run 2 (2015-2018), the radiation levels measured by the beam loss monitor (BLM) system [21] are compared with dedicated FLUKA [18–20] simulations to quantify the the systematic uncertainties on this type of analysis. The discussion is restricted to proton operation. Finally, predictions of the expected radiation showers during the operation of the BGV in the HL-LHC [2] era are discussed.

This chapter summarises the new results done as part of the work for this thesis, presented both internally at CERN, regularly within the BGV collaboration [96] and at the 150th and 193rd technical coordination committee (TCC) of the LHC [125, 126], as well as externally at the 14th international particle accelerator conference (IPAC) [127].

6.1 Instrument description

6.1.1 Introduction

The Beam Gas Vertex (BGV) is a non-invasive transverse beam size and profile monitor designed for the High Luminosity LHC (HL-LHC). It is based on the reconstruction of vertices of inelastic hadronic beam-gas interactions, and aims at providing a continuous emittance and beam profile measurement throughout the LHC accelerator cycle. The principle

of the BGV is illustrated in fig. 6.1: the LHC beam passes a gas target that is installed in its pathway, where a low pressure gas is injected. Some of the beam protons collide inelastically with the injected gas (Neon), leading to secondaries that are detected by the detector modules positioned downstream, outside the vacuum beam pipe. With these detectors, the secondary tracks can then be reconstructed, and subsequent interaction vertices are determined. The beam profile is then inferred from the spatial distribution of the reconstructed vertices. The BGV measures the beam profile in two dimensions, therefore one device per beam would be foreseen for nominal operation. The feasibility of the method was demonstrated during Run 2 (2015-2018) with a BGV demonstrator device [98, 128], and its performance reviewed, among other devices, after Run 2 [90].

6.1.2 Injected gas profile

In addition to the gas target of the BGV meant to produce the secondaries for vertex reconstruction, the residual gas profile and the tails of the gas target contribute as well to the radiation levels downstream of the BGV. The integrated gas density $\Theta(z)$ along z is given as:

$$\Theta(t; s_a, s_b) = \rho_{max} \cdot \int_{s_a}^{s_b} \frac{\rho(s)}{\rho_{max}} \mathrm{d}s \qquad (6.1)$$

where $\rho(s)$ is the number density of gas atoms and ρ_{max} is the peak value of the profile. From a measurement perspective, just one data point is available at the BGV via a pressure gauge located at the as-
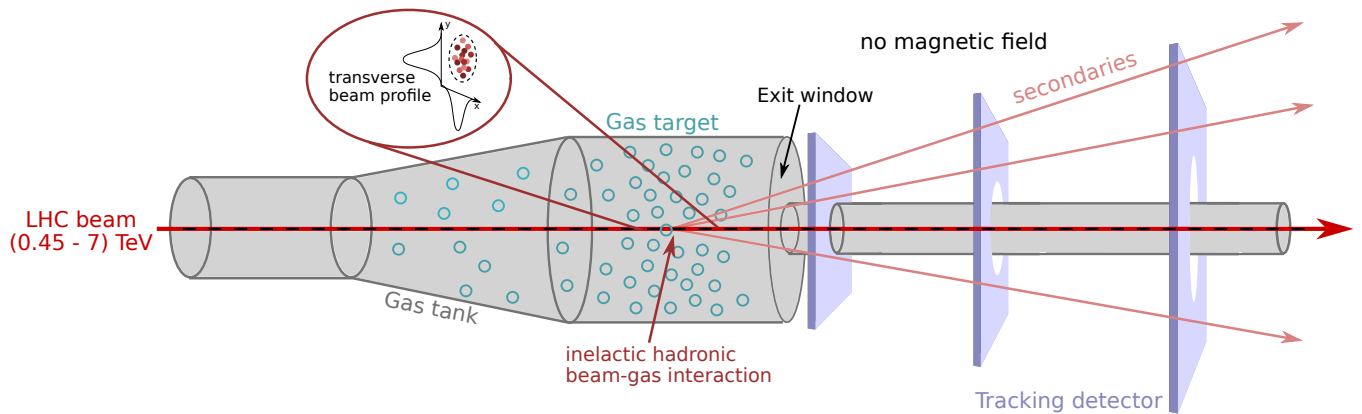
Figure 6.1: Sketch of the BGV instrument and its working principle (fig. from ref. [129]). A gas target is injected in the gas tank, thereby increasing the local gas density and the interaction rate for inelastic hadron beam-gas collisions. The secondary products from the interaction are then detected via three tracking detector planes, whose measurements can be used to reconstruct a 2D transverse beam profile.
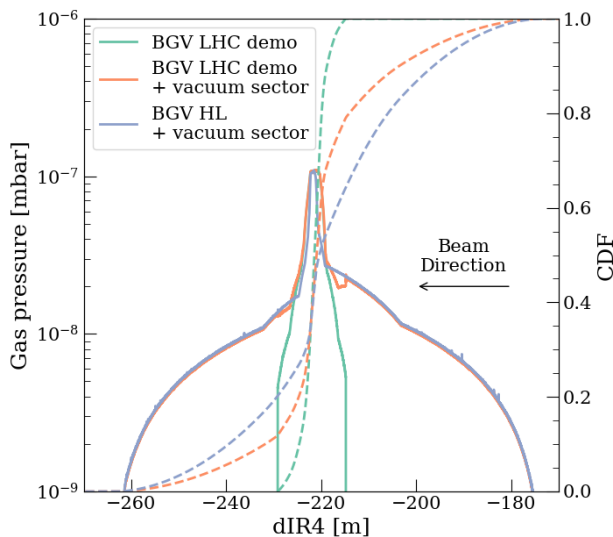
Figure 6.2: MOLFLOW [130] simulated gas profiles used for the FLUKA simulations, and their cumulative distribution function (CDF) for three scenarios: the BGV demonstrator injected gas profile during Run 2, (i) without, and (ii) with the vacuum sector residual gas profile, and (iii) the planned BGV profile for HL-LHC operation.

sumed peak ρ_{max}, but no measured information is available on the distribution width. Nevertheless,

the gas density profile used for the BGV demonstrator in FLUKA (shown in fig. 6.2 and exhaustively described in Ref. [131]) has been simulated using the molecular flow (MOLFLOW)+ simulation package [130]. Moreover, the amount of injected gas is not constant throughout a single fill (as shown later in fig. 6.3), yielding a time dependent gas profile whose shape might not always be the one shown in fig. 6.2.

6.2 Results

6.2.1 Measured radiation Levels

The available radiation level measured data consists of one data set, the total ionizing dose (TID) as measured by beam loss monitor (BLM). Figure 6.3 showcases that when gas is injected in the BGV, the BLM TID rate signal increases proportionally to the product of pressure and intensity. To improve the robustness of the analysis, the fill duration of 10 h was divided into multiple time periods of roughly 1h, such that the gas pressure is rather constant, and within different beam modes (PRERAMP, FLATTOP, STABLEBEAMS). Considering all such time periods, one can quantify the radiation levels in relation to the beam parameters as shown in eqn. 5.1, e.g. by
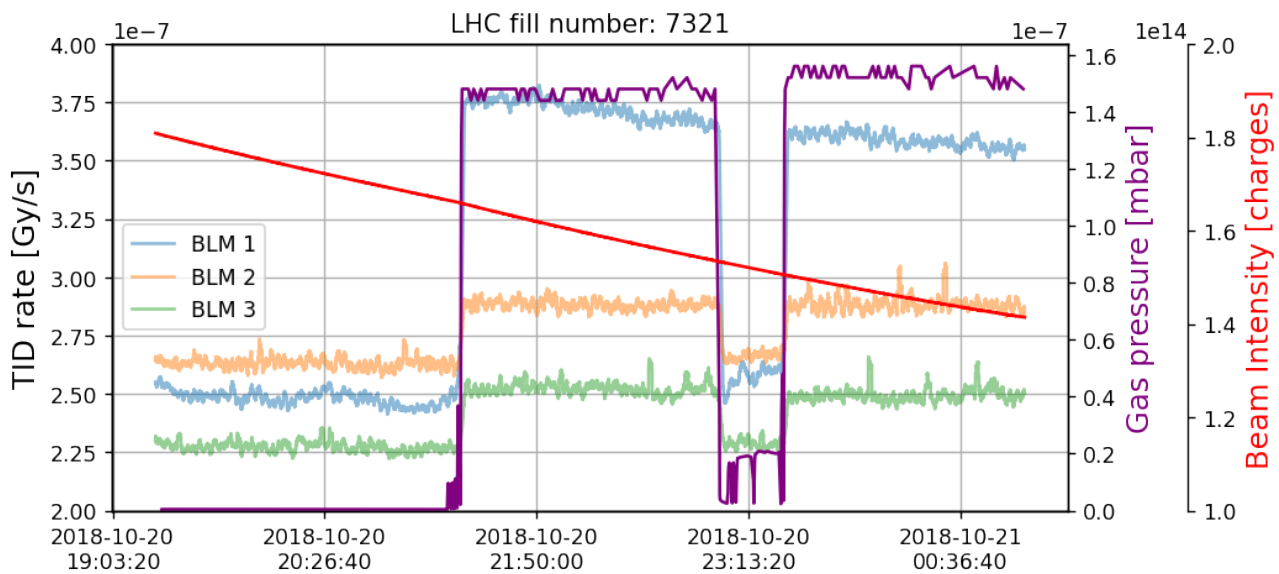
Figure 6.3: The total ionizing dose (TID) rate measured by the first three beam loss monitor (BLM) downstream of the Beam Gas Vertex (BGV) during LHC fill number 7321, together with the beam intensity N_p (red) as measured by the beam current transformer (BCT) instruments for beam 2 and the raw BGV pressure gauge reading p_{BGV} (purple). For the analysis of the BGV radiation levels, the duration of the fill is divided into time periods with roughly constant pressure levels.

plotting the measured TID normalized by the number of passing charges as measured by the beam current transformer (BCT) instruments, to the injected BGV pressure gauge reading p_{BGV}, shown in fig. 6.4. One observes that when there is significant ($p_{BGV} > 2 \cdot 10^{-8}$ mbar) gas injected in the BGV gas chamber, the radiation levels downstream of the instrument correlate very well with the beam intensity and the gas pressure, indicating that the BGV is the main source of prompt radiation where the presented BLMs are located. For each BLM, we hence defined signal time periods as the windows of operation during which the peak BGV pressure was at least $3 \cdot 10^{-8}$ mbar. In total, 169 hours of operation with an average pressure of $p_{BGV,operation} = 7.89 \cdot 10^{-8}$ have been recorded. Similarly, one can identify background time periods with $p_{BGV} < 1 \cdot 10^{-9}$ mbar, where the measured radiation levels can come from the residual gas along the accelerator or other less relevant sources, and this is designated as the background, summing up to 116 hours.

The LHC accelerator tunnel is divided into cells (as

described in ref. [1]), and by examining all BLMs up to cell 13 in the dispersion supressor (DS), visible correlations between the TID per unit intensity and the peak pressure in signal time periods can be observed up to cell 9, indicating that the BGV is a dominant (or, at least, non-negligible) source of radiation in the tunnel for more than four half-cells downstream of it.

6.2.2 FLUKA simulation

The FLUKA Monte Carlo code is capable of simulating the radiation shower caused by the beam-gas interactions. To improve the computational convergence time, the gas density profile is used to compute a cumulative distribution function (CDF) as shown in fig. 6.2 to sample the location and explicitly force the occurrence of the inelastic collision as describen in Appendix 3. The secondaries thus produced are then propagated in the geometry of the BGV encapsulated in the LHC IR4 tunnel, as shown in the advanced
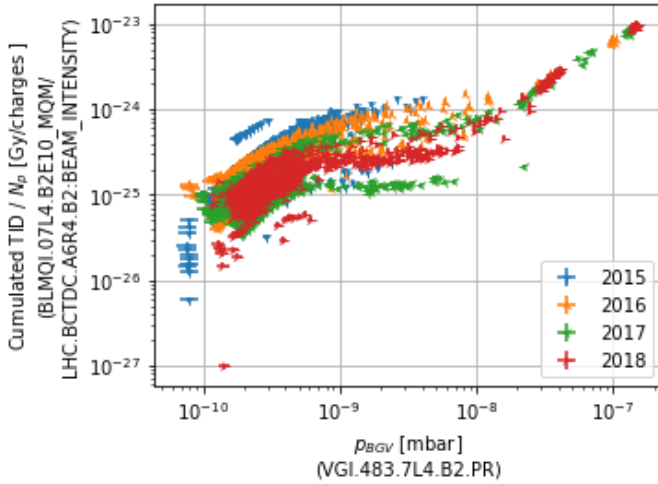
Figure 6.4: Cumulated total ionizing dose (TID) per time period measured by the BLM BLMQI.07L4.B2E10_MQM (first one downstream of the BGV instrument) divided by the beam intensity measured in charges N_p, plotted against the BGV pressure gauge reading p_{BGV} for all the time periods under consideration, for each year of Run 2 operation (2015-2018).

graphical user interface for particle simulation programs (FLAIR) [132, 133] view of fig. 4.2.

Figure 6.5 displays a top (ZX) view of the TID at beam height due to the radiation shower caused by the beam-gas collisions, which extends longitudinally over several tens of meters. In addition to the TID, the FLUKA simulation can be used to compute different radiation level quantities in the tunnel that are relevant for R2E applications and beyond, as well as energy deposition and heat loads in the inner layers of the exposed magnets.

The radiation levels obtained from the FLUKA simulation are given normalized per nuclear inelastic interaction. In order to obtain the same parameters as in eqn. 5.1, one has to multiply by the longitudinal integrated gas density $\Theta_{BGV,LHC,demo} = 3.35 \cdot 10^{-6}$ 1/cm (with the distribution shown in fig. 6.2) and the beam intensity, thereby yielding the radiation levels as a rate per second. These values can now be linearly scaled to the desired time of BGV operation.

6.2.3 LHC BGV demonstrator benchmark in Run 2

The radiation levels as simulated by FLUKA are compared to the radiation monitor measurements taken during the operation of the BGV demonstrator in Run 2, in fig. 6.6, where the shape of the BLM TID profile is well reproduced in the simulation, with just one outlier (the BLM at about -285 m from IR4). The global agreement between the simulated to measured data is given as the average (weighted on the measured data) ratio as:

$$\mathcal{R} = 1.09 \pm 29\% \qquad (6.2)$$
$$\mathcal{R}_w = 0.74 \pm 0.43\% \qquad (6.3)$$

where the error is the standard deviation from the mean. Usually, a few ten percent agreement can be achieved in the complex accelerator scenario [37, 43].

Moreover, the BGV was the main contributor for integrated yearly radiation levels in cell 7 and for selected BLMs in the next two cells downstream. The analysis shown here stops at -360 m from the center of IR4 (or 150 m downstream of the BGV on beam 2), because the measured radiation levels induced so far away by the BGV operation generally fall below other sources of radiation.

A good level of agreement can be observed from the comparison of the measured BLM data and the simulation results for Run 2. This gives confidence in the HL-LHC predictions that are made in the following sections based solely on FLUKA simulations.

6.3 Radiation level specifications for HL-LHC

The annual radiation levels depend additionally on the total operational time, for which it is estimated at a minimum of 200 h per year during HL-LHC operation, compared to approx. 170 h in total during Run 2 (2015-2018) when the gas was injected above
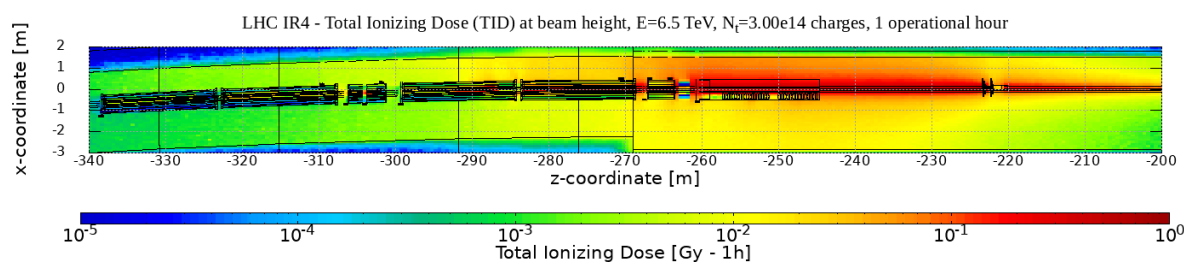
Figure 6.5: FLUKA simulated radiation shower caused by the BGV demonstrator, positioned on beam 2 at -224 m, for LHC operation, as ZX view, displaying how the shower extends over several tens of meters. The TID is provided at beam height, for a beam at $E_p = 6.5\,\text{TeV}$ with an intensity of $N_t = 3 \cdot 10^{14}$ charges, and normalized to 1 operational hour, for a gas pressure profile peak at $0.73 \cdot 10^{-7}$ mbar, corresponding to the averaged measured maxima during Run 2 (2015-2018).

$p_{BGV} > 2 \cdot 10^{-8}$ mbar. Together with the larger beam intensity and energy (shown in Table 4.2), this could result in the radiation levels that could represent a threat to the accelerator operation.

There is also interest in operating the BGV during energy ramp up (i.e. from injection to top energy). Although the increase in the cross section over the investigated energy range is small, with higher beam energies, the secondary showers will be larger, leading to higher radiation levels. In the absence of BGV injections during ramp up, several data points during the energy increase have been simulated. The TID levels thus obtained in the BLM downstream of the BGV are shown in fig. 6.7, indicating a linear increase in the radiation levels with the beam energy at the location of the BLM under exam, with a slope of approx. $10\,\text{mGy}/(\text{h}\,\text{TeV})$. Similar behaviour is expected also for the other BLMs.

From a machine protection point of view, the simulated radiation levels are not an issue for what concerns the heat loads on the magnets, both as maximum power density as shown in fig. 6.8 or as total power dissipated on the entire magnet as summarised in tab. 6.1. For the assumed gas density profile with a peak pressure of $p_{BGV,max} = 10^{-7}$ mbar and the max HL-LHC intensity of $N_{t,max} = 6.35 \cdot 10^{14}$ protons at 7 TeV, there is no risk of quenching in the magnets, if compared to the studied magnet limits [48] that are a factor of 100 higher:

- **Dipoles**: at $0.85\,\text{mW}/\text{cm}^3$, below the $13\,\text{mW}/\text{cm}^3$ quench limit [49].

- **Quadrupoles**: at $0.45\,\text{mW}/\text{cm}^3$, below the $40\,\text{mW}/\text{cm}^3$ quench limit [78].

Similarly, the TID levels shown do not rise any concerns in terms of cumulated damage, as the limit is reported at $25\,\text{MGy}$ [48].

Table 6.1: FLUKA simulated total power deposition in the inner coils of the magnets for the Beam Gas Vertex (BGV) demonstrator, placed on beam 2, for the LHC Run 2 operation, as well as for the foreseen HL-LHC era. The distance from the magnets to the centre of insertion region 4 (IR4) and to the BGV instrument are also provided.

Magnets	d IR4 [m]	d BGV [m]	LHC Total Power [mW]	HL-LHC Total Power [mW]
QM7	−265.27	40.270	110	286
BA8	−276.15	51.15	539	1223
BB8	−291.81	66.81	81	202
QM8	−303.77	78.77	4	15
BA9	−315.21	90.21	6	20
BB9	−330.87	105.87	4	10
QM9	−342.13	117.13	2	2
QMC9	−346.49	121.49	1	1

The radial distribution of the inner coils of the magnets, e.g. the quadrupole in cell 7 (Q7) shown in fig. 6.9 (left) is consistent with expectations. For the
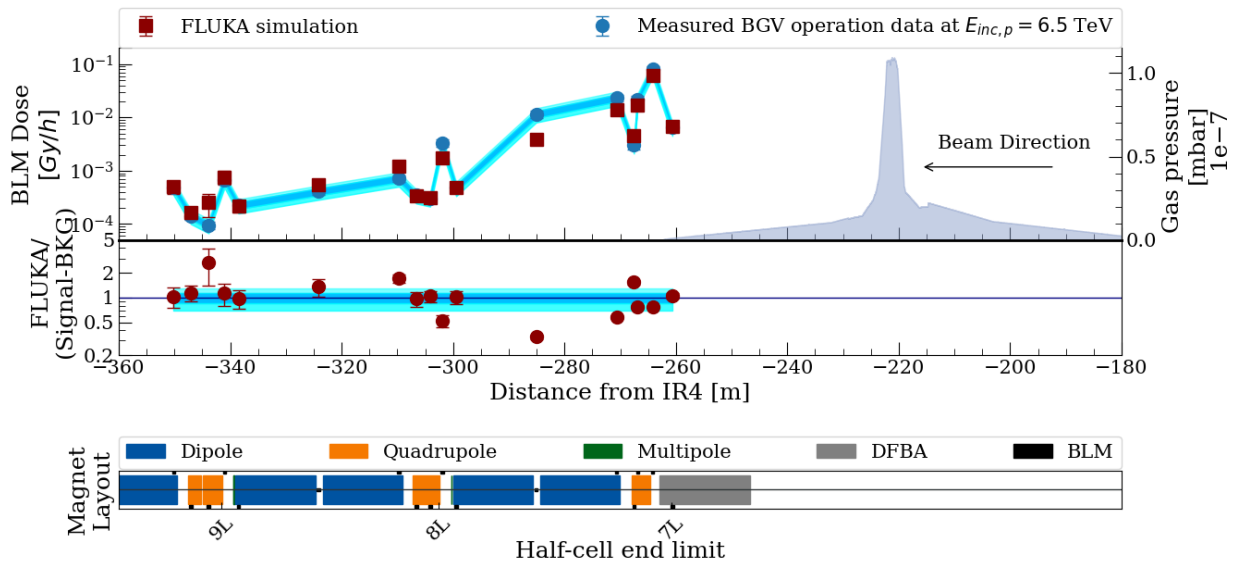
Figure 6.6: Benchmark on the beam loss monitor (BLM) for the Beam Gas Vertex (BGV) demonstrator operation at flattop (6.5 TeV). **Top panel**: BLM pattern downstream the BGV placed on beam 2 as measured over the Run 2 (2015-2018) proton runs (blue points) and as calculated by FLUKA (red points), together with the gas target. **Mid panel**: The cumulative distribution function (CDF) used to sample the interaction point of the beam-gas collision, as well as the ratio between simulation values and measured data. **Bottom panel**: The LHC machine layout and the BLM locations.

beam 2 magnet (where the BGV is placed on), the (de)focusing magnetic fields create four hot spots on the magnet coils. On the other hand, the beam 1 magnet is affected asymmetrically, with more TID deposited on the side closer to the other beam, but nevertheless with a factor of 100 lower than for the beam the BGV is placed on.

The TID distribution in the bending magnets shown in fig. 6.9 (right) display an interesting behaviour, that can be explained longitudinally. At the start of the magnet (side towards the BGV), the magnetic field strongly deflects the collision products that are different than the nominal beam protons, namely the pions, muons and positrons, creating a hot spot on the inner side of the accelerator. At the end of the magnet, a second peak is visible, which corresponds to the impact of the neutrally charged secondary products (neutrons and gammas) which are not deflected by the magnetic field and travel on a straight line, thereby directly hitting the magnet coils.

The complete map of the TID induced by the BGV operation in the tunnel is available, shown here as the 2D projections in fig. 6.5. In order to compare the expected levels solely from the BGV operation, it is visually easier to look at the BLM profile of fig. 6.10, where the annual levels scaled for HL-LHC are shown as well, assuming the same BLM placement. The main conclusion is that even without considering the extra radiation sources, the HL-LHC BGV operation will lead to higher TID levels compared to Run 2 (2015-2018).

Further R2E related concerns arise from the high energy hadron equivalent (HEHeq) fluence that could cause single event effects (SEE) in the electronics, for which the 1D profile at floor level shown reveals a plateau of 10^{10} cm^{-2}/year from the BGV to the second DS dipole. From an R2E perspective,
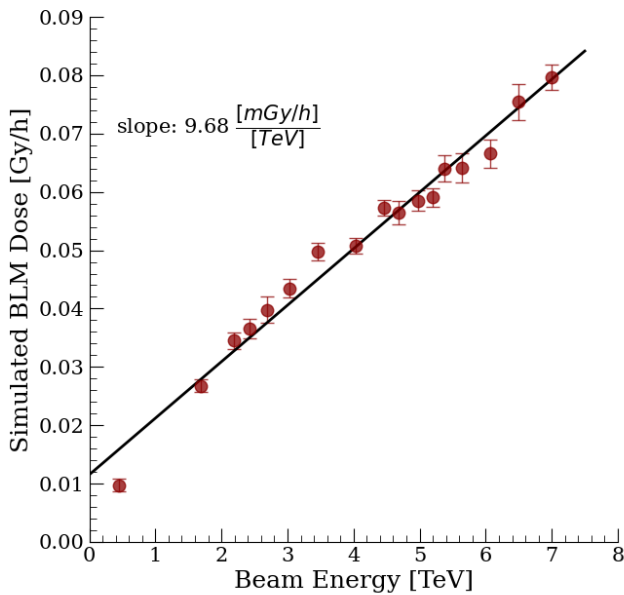
Figure 6.7: Simulated TID deposited in the most irradiated BLM BLMQI.07L4.B2E10_MQM during energy ramp from INJECTION at 450 GeV to FLATTOP at 7 TeV, revealing a linear increase.

Based on the previous work performed during the workshop on non-invasive beam size measurements for high intensity and high energy hadrons in 2013 [137] and the more recent LHC beam size review organised at CERN in 2019 [138], the final recommendations were to study both BGV and BGI. As both budget and resources favour the BGI the recommendation from the review panel is to select the BGI as the baseline instrument for HL-LHC.

levels of 10 Gy/year are a threat in terms of TID lifetime of electronic systems and HEHeq fluences of $3 \cdot 10^{10}$ cm^{-2}/year may lead to stochastic electronic failures. Both are significantly (i.e. orders of magnitude) larger than the arc level "baseline" [134], but lower than the levels near the high luminosity experiments at IP1/5 [43, 135, 136].

6.4 Future BGV operation

Based on the previous work performed during the workshop on non-invasive beam size measurements for high intensity and high energy hadrons in 2013 [137] and the more recent LHC beam size review organised at CERN in 2019 [138], the final recommendations were to study both BGV and BGI. In October 2022, the HL-LHC BGV-BGI review indicated in their final report [129] that:

Figure 6.8: **Top pannel:** FLUKA simulated heat loads in the inner coils downstream of the BGV on beam 2, as max power density. The red curve corresponds to the LHC Run 2 operation at $E_p = 6.5$ TeV and total number of protons at $N_t = 3 \cdot 10^{14}$ charges, while the blue one corresponds to the foreseen HL-LHC operation at $E_p = 7$ TeV and $N_t = 6.35 \cdot 10^{14}$ charges. **Bottom pannel**: The machine, showcasing the standard dipole and quadrupoles, and the DFBA module.
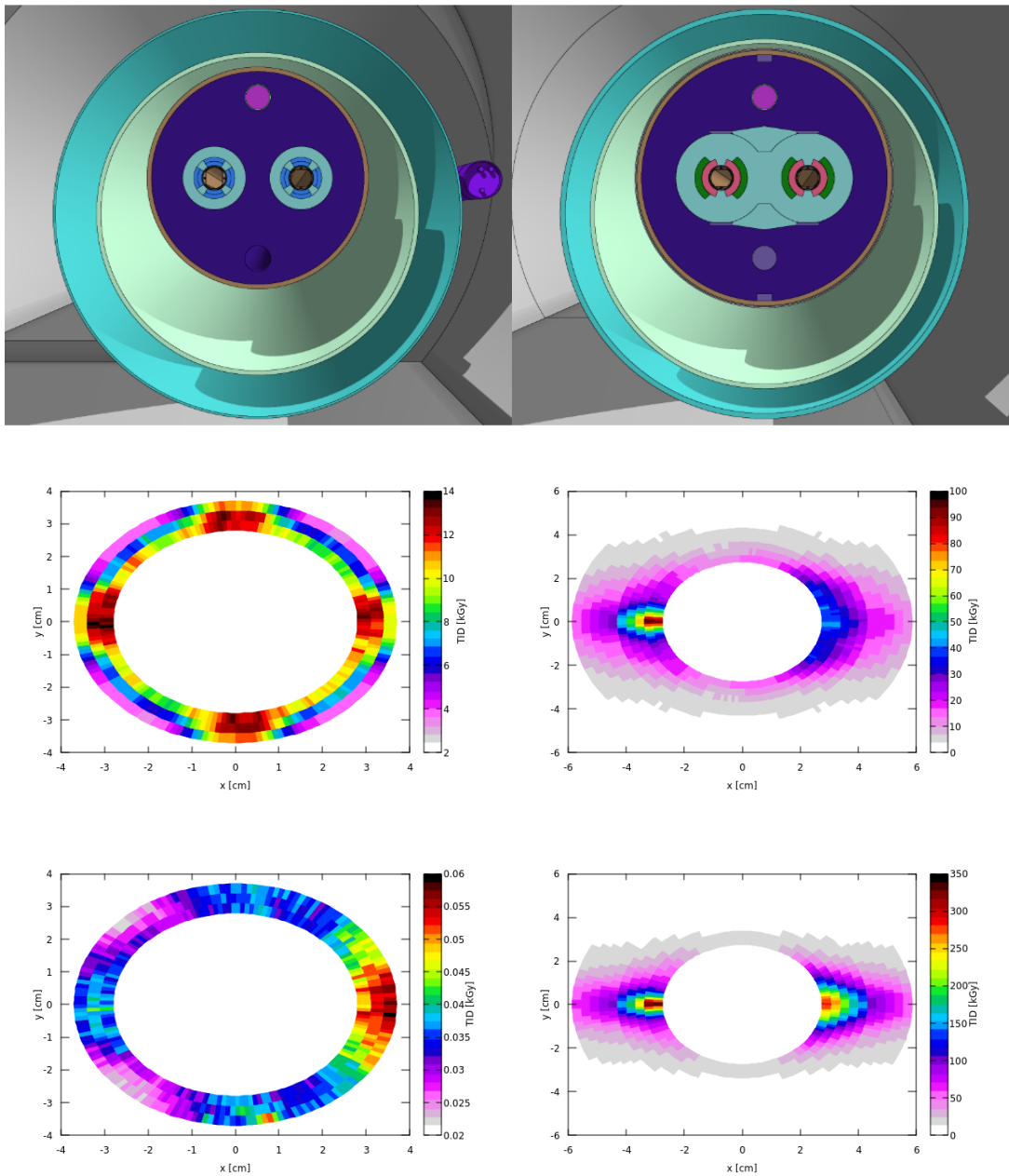
Figure 6.9: The two types of magnets affected by the radiation from the Beam Gas Vertex (BGV) instrument, normalzied to the HL-LHC era operation, taking as example **(left)** the first quadrupole (MQ) downstream of the BGV (in Cell 7) and **(right)** the first bending dipole magnet (MB) downstream of the BGV (in Cell 8). The **top pannels** showcase the implemented FLUKA geometry, while the **lower** ones display the FLUKA simulated TID deposition in the inner coils of the magnets. For the quadrupole, **(center left)** displays the coil on beam 2, indicating that the losses are along the vertical and horizontal directions, as expected from the magnetic fields, while **(bottom left)** displays the coil on beam 1, indicating how the radiation originated from beam 1 (i.e. the right side). For the dipole magnet, **(center right)** displays the coil on beam 2 at the beginning of the magnet, indicating how the radiation comes from secondary products that are over-bent into the magnet, while **(bottom right)** displays the coil on beam 2 at the end of the magnet, indicating a secondary hot stop given by the neutral particles that are not bent on the accelerator trajectory, thereby hitting the magnet directly.
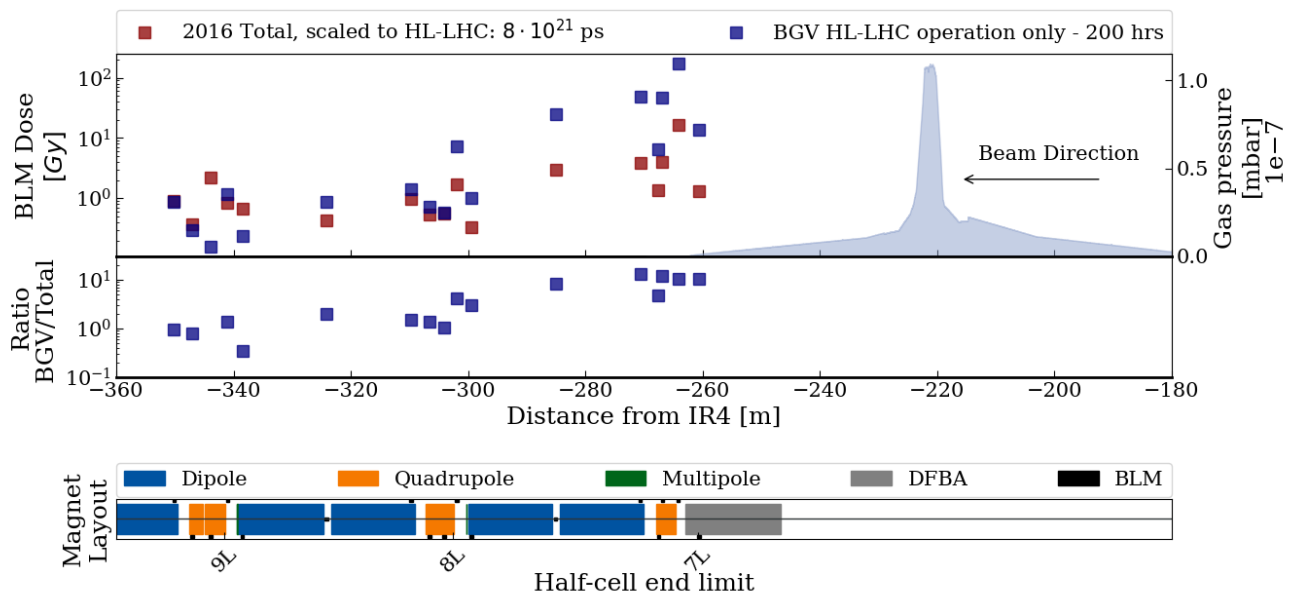
Figure 6.10: **Top panel:** Distribution of TID measured by the BLM system during 2016 proton operation, rescaled to the reference year of HL-LHC operation via integrated beam intensity scaling, together with the BLM pattern downstream the BGV placed on beam 2 as measured over the Run 2 (2015-2018) proton run, scaled to HL-LHC operation via instantaneous beam intensity scaling and BGC operational time. The BGV gas profile is also displayed. **Mid panel:** The ratio between the BGV induced signal and the 2016, both scaled to HL-LHC operation. **Bottom panel:** The machine layout and the BLM locations, assumed the same for the HL-LHC machine as for the LHC.

<div style="text-align: right; font-size: 4em; color: gray;">7</div>

The beam gas curtain (BGC) instrument

Similarly to the Beam Gas Vertex (BGV) [96, 97, 121] instrument described in chapter 6, the radiation levels in the tunnel and on the downstream equipment caused by the secondary products from the beam gas collisions in the Beam Gas Curtain (BGC) [99–101] on beam 1 are non negligible, especially because the shower is directed towards the radio frequency cavities in the center of IR4 and the super conducting bending magnets on the right side. Based on the BGC demonstrator operation in the Large Hadron Collider (LHC) during Run 3 (2022-to date), the radiation levels measured by the beam loss monitor (BLM) system [21] are compared with dedicated FLUKA [18–20] simulations to quantify the systematic uncertainties on this type of analysis. The discussion is restricted to proton operation. Finally, predictions of the expected radiation showers during the operation of the BGC in the HL-LHC [2] era are discussed.

This chapter summarises the new results done as part of the work for this thesis, presented both internally at CERN, regularly within the BGC collaboration, at the 9th [139] and 10th [140] meetings, and at 193rd technical coordination committee (TCC) of the LHC [126], as well as externally at the 15th international particle accelerator conference (IPAC) [141]. Together with the full results of Run 2 (2015-2018) of the Beam Gas Vertex (BGV) and after the completion of Run 3 (2022-scheduled 2026), a benchmark paper of the operation of beam gas demonstrator at the LHC is envisaged.

7.1 Instrument description

7.1.1 Introduction

The High-Luminosity LHC (HL-LHC) upgrade of the LHC is under construction [3] and planned for commissioning from 2026, during long shutdown 3 (LS3). The HL-LHC aims to increase the integrated luminosity of the LHC by a factor of 10, for which an active beam halo control will be required for the upgrade due to the increased beam intensity. Even the small amount expected to appear as a beam halo will contain considerable energy, which must be constantly cleaned to avoid unacceptable losses on the collimation system or elsewhere along the accelerator. The baseline technical proposal used to be[1] a hollow electron lens (HEL) instrument [142–146], which uses a hollow cylindrical electron beam, constrained by a superconducting solenoid which is passed concentrically around the circulating proton beam over about 3 m of beamline, assuming that the proton beam and hollow electron beam can be kept well aligned in such a device.

Monitoring the concentricity of these two beams during operation will require simultaneous, minimally-invasive, transverse profile measurement of both proton and hollow electron beams. In addition, this measurement must be in close proximity to the solenoid field constraining the electron beam. An instrument is being developed to image fluorescence generated by the interaction between these beams and a thin, supersonic, gas curtain [100, 101]. By tilting this Beam Gas Curtain (BGC) with respect to the beam axis, a 2-D image of both beams can be

---

[1]However, descoped after 2022.

obtained in much the same way as for a traditional solid screen beam observation system, as illustrated in fig. 7.1.
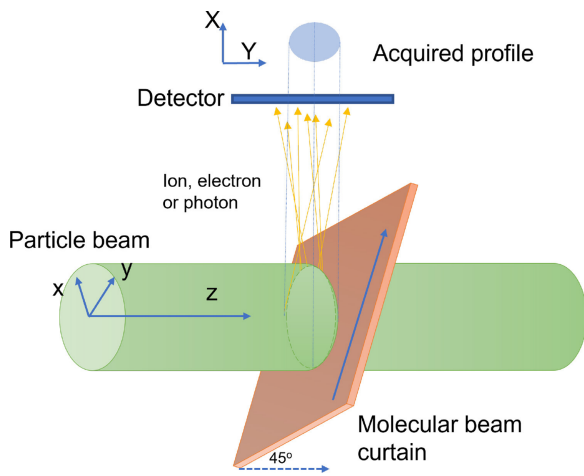
Figure 7.1: Working principle of the Beam Gas Curtain (BGC) instrument (fig. from ref. [100]). The particle beam travels horizontally, and a molecular beam curtain jet is shot at a 45° angle wrt. the beam. The particle beam ionises a fraction of the gas atoms, generation charged ions, electrons or photons that are then detected (e.g. with a camera).

A BGC demonstrator was installed at the LHC at CERN to provide 2D images of the beam during the ongoing Run 3 (2022-to date) and in view of the HL-LHC upgrade. By design, the BGC operation generates collisions between the beam particles and an injected gas target proportionally to the beam intensity and the gas density, possibly causing radiation-induced damage to the downstream LHC equipment.

The BGC monitor consists of a sequence of vacuum chambers of different diameters, with the readout systems adjacent to them. That is to say, that the material budget that would impact the radiation shower downstream consists of just the beam pipe transitions (reductions/enlargements), and only these have been implemented in the FLUKA model.

The location of the BGC demonstrator in the accelerator tunnel is at -42 m from the centre of insertion region 4 (IR4), on beam 1 (inner), therefore showering towards the centre of the IR, as indicated in the layout of fig. 4.6. The most important beam line elements that could be affected by the BGC operation, are thus, in order: (i) the superconducting accelerating radio frequency cavities, (ii) the cryogenic bending dipoles that decrease the beam separation from 21 to 9.7 cm. Furthermore, there are several instruments along the beam line for beam diagnostics whose operation could be impacted as well.
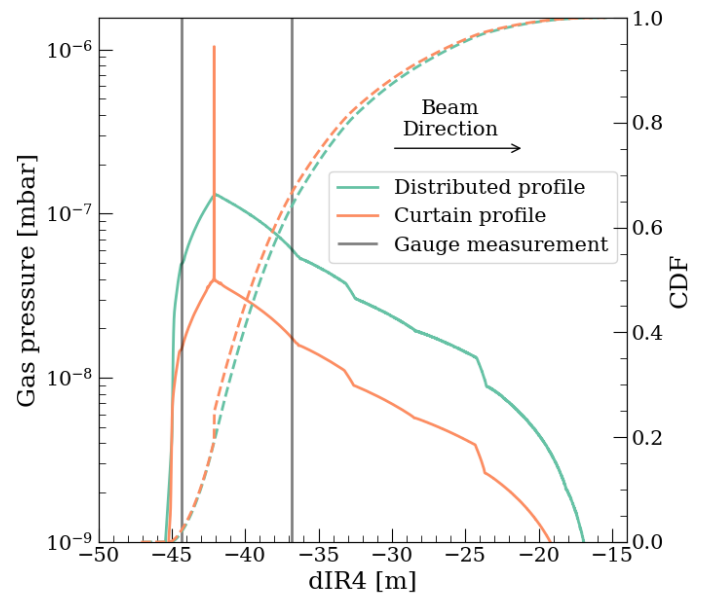
Figure 7.2: MOLFLOW [130] simulated gas profiles used for the FLUKA simulations, and their cumulative distribution function (CDF) for two scenarios of the BGC demonstrator operated in Run 3: (i) distributed gas profile, in 2022, and (ii) gas curtain, in 2023.

7.1.2 Injected gas profile

During the Run 3 operation of the BGC demonstrator, two gas profiles have been used, as shown in the molecular flow (MOLFLOW) [130] simulated gas profiles in fig. 7.2. More description about how these profiles are obtained can be found in ref. [147]. In 2022, a distributed injection, similar to the BGV, has been used, while in 2023, the actual gas curtain has been used. From a measurement point of view, there
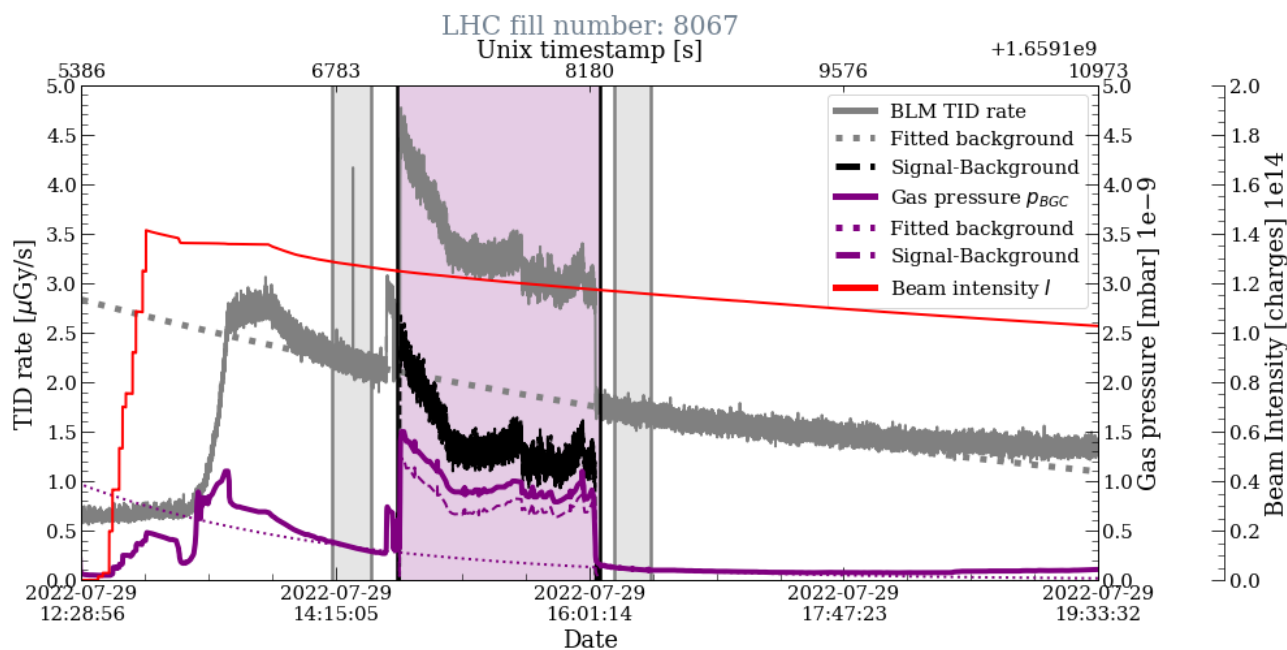
Figure 7.3: The total ionizing dose (TID) rate (gray) downstream of the BGC, measured by the most irradiated beam loss monitor (BLM) BLMEI.05R4.B1I10_BSRTM, plotted with with the beam intensity N_p (red) as measured by the beam current transformer (BCT) instruments for beam 1 and the raw BGC pressure gauge reading p_{BGC} (purple), during LHC fill number #8067, which is divided into one signal time period between the BGC gas injection timestamps (light purple shaded area) and two background time periods (gray shaded areas), before and after the gas injection. In addition to the absolute BLM TID rate and BGC pressure reading, the fitted function on the background time periods data is shown (dotted line), as well as the signal obtained after the subtraction of the fitted background (black line). The background has been fitted with an exponential decaying curve (eqn. 7.1) or a constant value (eqn. 7.2). The shown BLM is located at a distance of 115 m from the BGC, just downstream the beam screen radiation telescope (BSRT) instrument, in LHC cell 5, right of IR4.

are two data points available via two vacuum pressure gauges on the beam pipe (VGPB)[2]:

1. VGPB.443 - located 2.3 m upstream wrt. the BGC,

2. VGPB.368 - located 5.2 m downstream wrt. the BGC.

---

[2]To obtain the timeseries information mastering: browsing, extraction and rendering (TIMBER) variable, one just needs to append .5L4.B.PR to the pressure gauge name, thereby indicating the cell (5), the side (left) with respect to which insertion region (4), for which of the two beams (B), and that it is a pressure reading (PR).

7.2 Results

7.2.1 Measured radiation levels

The available radiation level measured data for benchmarking purposes consists of the total ionizing dose (TID) data set, as measured by BLMs. Exemplarily, the TID rate of the most irradiated (the BLM with the highest increase during BGC operation) BLM downstream of the BGC in a typical fill with gas injection in the BGC is used to showcase the analysis (e.g. fill #8067), shown in fig. 7.3. There are a couple of behaviours to be noted:

• The TID rate increases at the beginning of the
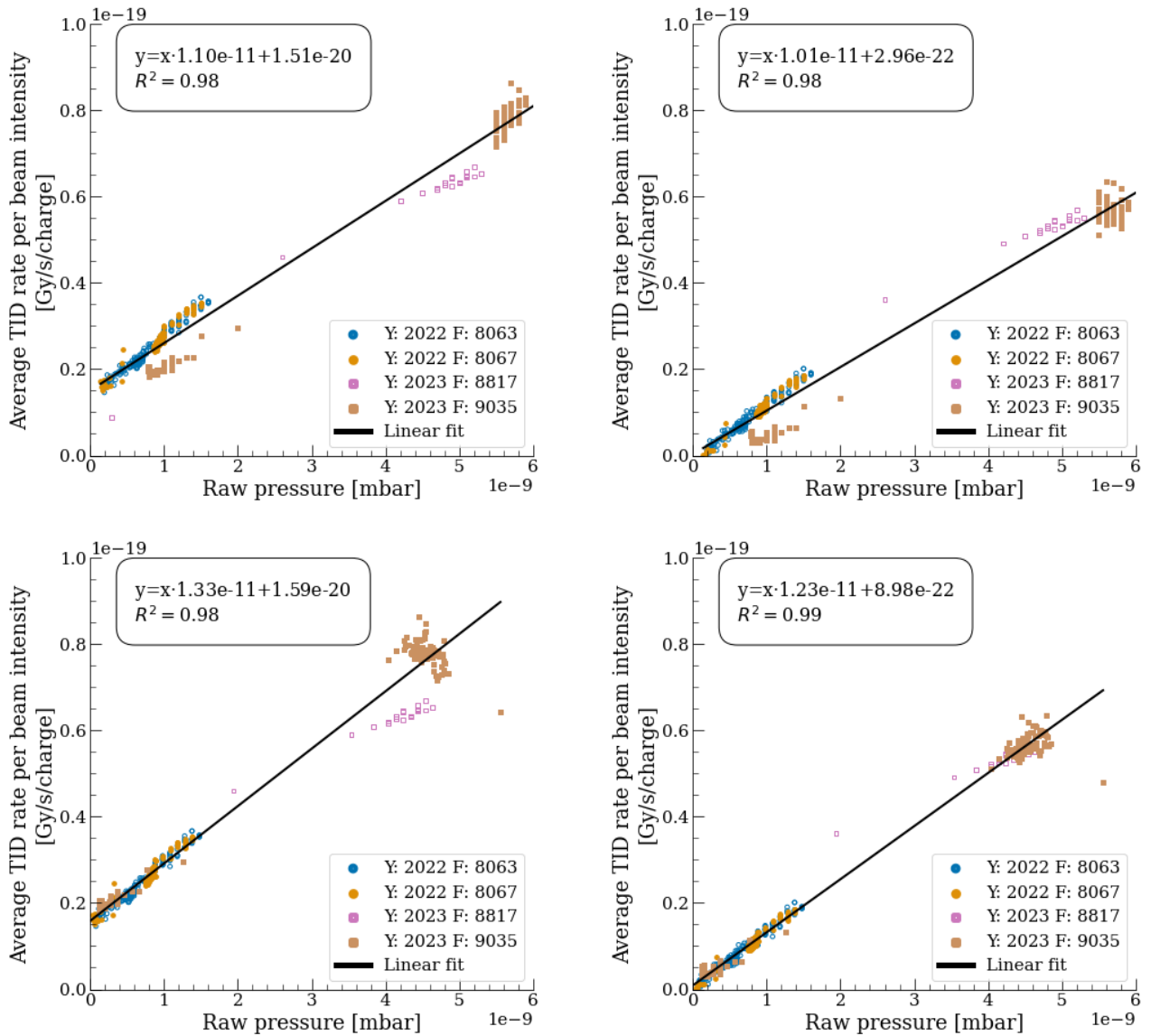
Figure 7.4: The dose rate measured by the the most irradiated beam loss monitor (BLM) BLMEI.05R4.B1I10_BSRTM, divided by the number of charges N_p as measured by the beam current transformer (BCT), plotted against the BGC pressure gauge reading p_{BGC} (for the downstream pressure gauge #368), for all the timestamps and for four selected time periods with gas injection in 2022 and 2023, highlighting the impact of the background subtraction procedures shown in fig. 7.3. Subfigure **(top left)** shows the data without any background subtraction (i.e. using the full curves from fig. 7.3); in subfig. **(top right)**, only the TID background subtraction is applied, using the dashed black curve from fig. 7.3 for the TID rate; in subfig. **(bottom left)**, only the pressure background subtraction is applied, using the dashed purple curve from fig. 7.3 for the pressure reading, and in subfig. **(bottom right)**, both TID and pressure background subtraction area applied.
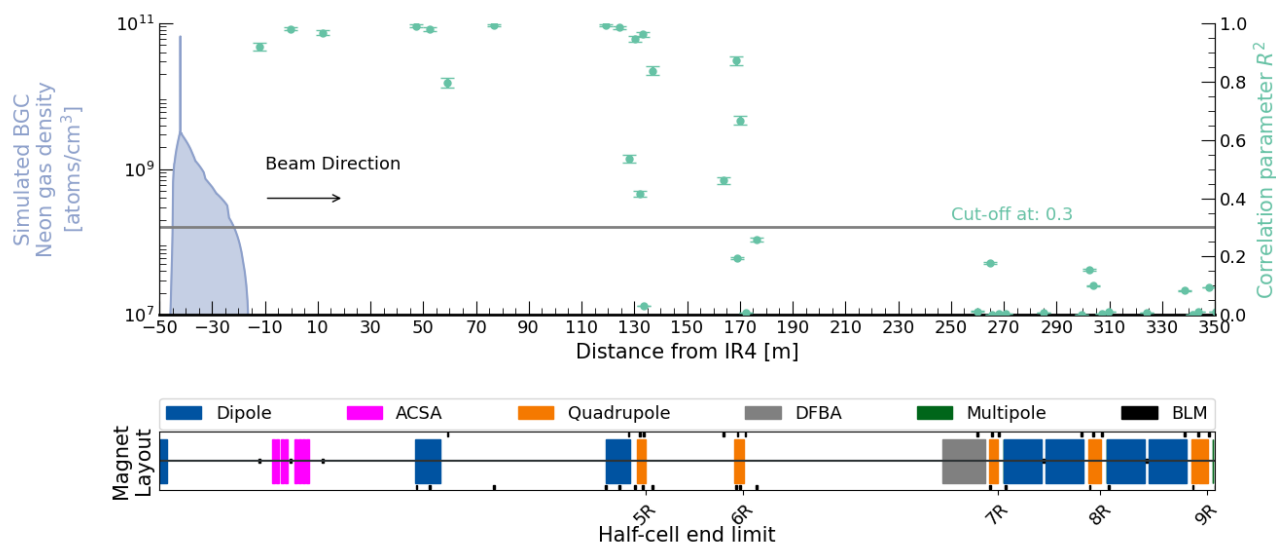
Figure 7.5: **Top pannel**: Correlation parameter R^2 obtained from fitting the TID rate normalized to unit beam intensity, against the measured pressure gauge. A threshold at $R^2 = 0.3$ is used to filter the BLMs used for comparison with the simulated data. Additionally, the simulated BGC Neon gas density and the beam direction are shown. **Bottom pannel**: The LHC machine layout and the BLM locations.

fill, regardless of the BGC operation. This behaviour is deemed to outgasing effects in the beam pipe generating local increases in the residual gas density that will produce radiation showers. As it can be observed, this effect very rapidly decreases after the beginning of the fill leading to a *stable* gas density inside the beam pipe.

- Most importantly for this work, when gas is injected in the BGC, the TID rate signal of the BLMs downstream increases, assumed proportionally to the product of pressure and intensity.

- Not visible in fig. 7.3, which shows just one BLM, but the increase is uneven across the BLMs, and the correlations are quantified for each monitor, both in terms of the correlation parameter R^2 obtained from a linear fit (shown in fig. 7.5), as well as the slope, represeinting the extracted measured signal.

Table 7.1: Operation of the BGC demonstrator instrument in Run 3 (2022 and 2023), with the used profile in each year, and the number of injections (at top energy) and hours for proton and ion beams.

year	profile	No. injections (top energy)	protons (ions) [hours]
2022	distributed	15 (15)	71 (38)
2023	curtain	4 (2)	10 (>70)

Unlike the case of the BGV for which 4 years of operational data with numerous gas injections were available, for the BGC fewer injections were made, as summarised in tab. 7.1: only 15 injections were done in 2022 with a distributed gas profile and 4 (2 at injection, 2 at flattop) in 2023 with a gas curtain profile. The same analysis procedure as for the BGV (described in chapter 6) has been applied on the BGC, leading to poor results. As such, a different analysis procedure was needed to cope with the lower statistics, but also to the lower signal-to-noise ratio (SNR).

7.2.1.1 Background subtraction

As noticeable in fig. 7.3, the BLM TID rates during the nominal operation of the accelerator (i.e. outside BGC gas injections) are in the same order of magnitude as those during gas injection, meaning that the background is not negligible, but has to be quantified. The background radiation levels stem either from unavoidable beam losses, in a more systematic way that are expected to be very similar across the fills, or from fluctuations in the beam size or divergence, leading to stochastic losses that may vary significantly from fill to fill. Therefore, a fill-by-fill background TID rate has to be taken into account and subtracted from the measurement for each BLM.

Similar considerations can be done about the pressure gauge measurements. Typically maintained at a level of about 10^{-11} to $1 \cdot 10^{-9}$ mbar [110, 111], the vacuum of the LHC is not uniform across the entire 27 km long accelerator, nor constant in time throughout the fill. Therefore, a fill-by-fill value for the resid-

ual gas pressure (background) also has to be taken into account and subtracted from the BGC injected gas pressure.

For the above reasons, the fill duration is divided into two:

- Signal time periods: given by the timestamps of the gas injection system. Nevertheless, it can be identified in the measured data with plateaus in the pressure gauge reading at about $1 \cdot 10^{-8}$ mbar.

- Background time periods: outside the gas injection, time periods are manually selected such that they are close enough to injection to be a representative background, but also far enough not to overlap with residual effects (e.g. remnant gas after the injection). Moreover, the highly non-linear TID rates and pressure readings (due to outgassing) at the beginning of the fill are discarded. Ideally, two background time periods, one before and one after the injection, are considered, but this is not always possible as the gas injection could have been done during injection or a beam dump could have been triggered.

A functional model is fitted on the background time periods according to an exponential decay function following the beam intensity as:

$$TID_{bkg,exp}(t) = A_0 \cdot \exp{-t/\tau} \qquad (7.1)$$

where the parameters obtained from the fitting are A_0, the initial amplitude of the dose rate, and τ, the decay rate of the beam intensity, related to the beam life time described in section 5.1.1. When the fitting is not possible (e.g. if the second background time period has a higher amplitude than the first one), a constant function is used as:

$$TID_{bkg,const}(t) = TID_{bkg,const} \qquad (7.2)$$

In the absence of the injected gas profile, it is assumed that the losses scale globally with the beam

intensity, but locally residual gas peaks can introduce additional sources of uncertainty.

7.2.1.2 Analysis results

If for the BGV, the typical fill duration of about 10 h was divided into multiple time periods of roughly 1 h, for the BGC **each** timestamp of the pressure gauge measurement (about 1 per minute) has been considered as a data point. As such, one can plot the measured TID normalized by the number of passing charges as measured by the beam current transformer (BCT) instruments to the injected BGC pressure reading for the two gauges. Again, exemplarily, the most irradiated BLM is shown, where the dose rate values correlate very well with the beam intensity and the gas pressure, indicating that the BGC is the main source of prompt radiation where this BLM is located. The results are presented incrementally to showcase the impact of each background subtraction procedure:

a) The raw results (without any background subtraction procedure) are shown in fig. 7.4 (top left). An artefact from the pressure gauge measurement is present, namely the values above $1 \cdot 10^{-9}$ mbar exhibit an oscillatory behaviour with defined increments of $0.1 \cdot 10^{-9}$ mbar, while the readings below showcase a more continuous behaviour.

b) The (partial) results where one fits the background TID rate (dotted gray curve in fig. 7.3) and subtracts it from the full signal (full gray curve) to obtain just the BGC induced signal (dashed black curve) are shown in fig. 7.4 (top right), practically setting the y-intercept to 0.

c) The (partial) results where one fits the background pressure gauge reading (dotted purple curve in fig. 7.3) to obtain just the BGC injected gas (dashed purple curve) are shown in fig. 7.4 (bottom left), slightly removing the discontinuities from the pressure gauge measurement from fig. 7.4 (top left).

d) The full results, with both backgrounds subtrac-

ted (from the TID and the pressure gauge), are shown in fig. 7.4 (bottom right), showcasing a better linear behaviour. The few outliers could be linked to more subtle instantaneous effects.

Similarly to the BGV, the question that arises is to quantify the measured radiation levels generated by the BGC operation, and to identify the most impacted region(s) of the accelerator. The BGC induces additional radiation levels that can be measured by downstream BLMs, however they become comparable in order of magnitude to other sources of radiation (e.g. outgassing effects at the beginning of the fill), thereby disturbing the linearity shown in fig. 7.4. Moreover, it is possible to compute the correlation parameter R^2 from the fitted line, which is plotted in fig. 7.5 over distance. For the comparison with measured data, only the BLMs that exhibit a correlation stronger than $R^2_{thres} = 0.3$ are used for the benchmark with the measured data.

7.2.2 FLUKA simulation

The FLUKA Monte Carlo code is capable of simulating the radiation shower caused by the beam-gas interactions. To improve the computational convergence time, the gas density profile is used to compute a cumulative distribution function (CDF) as shown in fig. 7.2 to sample the location and explicitly force the occurrence of the inelastic collision. The secondaries thus produced are then propagated in the LHC IR4 tunnel, towards the centre of the interaction region.

Figure 7.6 displays a top (ZX) view of the TID at beam height due to the radiation shower caused by the beam-gas collisions, which extends longitudinally over several tens of meters. In addition to the TID, the FLUKA simulation can be used to compute different radiation level quantities in the tunnel that are relevant for radiation to electronics (R2E) applications and beyond, as well as energy deposition and heat loads in the inner layers of the exposed magnets.

The simulation predictions reveal some interesting features that are pointed out here. The radiation
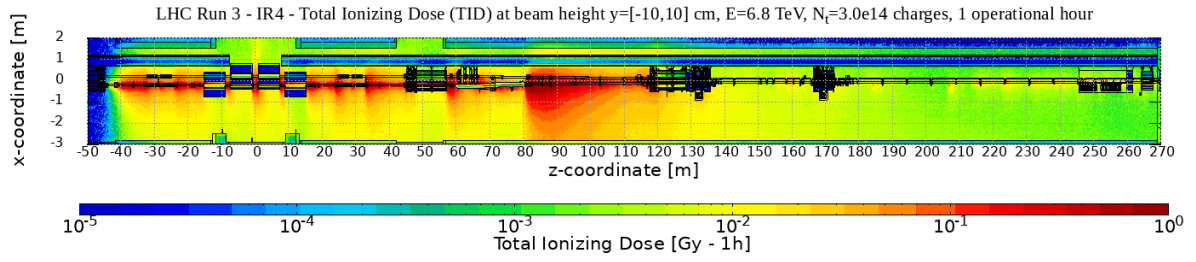
Figure 7.6: FLUKA simulated radiation shower caused by the Beam Gas Curtain (BGC) demonstrator, positioned on beam 1 at $-42\,$m, for LHC operation, as ZX view, displaying how the shower extends over several tens of meters. The TID is provided at beam height, for a beam at $E = 6.8\,$TeV with an intensity of $N_t = 3 \cdot 10^{14}$ charges, and normalized to 1 operational hour.

levels do not spatially originate from the collision point inside the BGC gas chamber, but the secondary collision products propagate downstream of the instrument, through the vacuum of the beam pipe until subsequently interacting with the beam line elements (typically, correlated with beam-pipe aperture restrictions. Thus, one can define several radiation regions/patterns:

- the radio frequency (RF) cavities: in the centre of the IR, are the first beam elements hit by the showers, but do not receive most of the radiation. The radiation levels are similar in the region from -10 to 50 m.

- the first bending dipole magnet (D1), which reduces the beam separation from 21 cm to the nominal 9.7 cm: all secondary products that are not nominal protons in the accelerator will suffer deflections that cause them to hit the beam pipe, thereby causing the highest radiation levels in a region from 50 to 120 m.

- the second bending dipole magnet, which deflects the beams back parallel to each other, and the quadrupole in cell 5 (Q5): similarly, radiation levels are generated peaking between 130 and 170 m.

- the subsequent radiation levels become milder, below other sources of radiation.

The radiation levels obtained from the FLUKA simulation are given normalized per nuclear inelastic interaction. In order to obtain the same parameters as in eqn. 5.1, one has to multiply by the longitudinal integrated gas density $\Theta_{BGC} = 5.27 \cdot 10^{-6}\ 1/\text{cm}^2$ (with the entire profile shown in fig. 7.2) and the beam intensity, thereby yielding the radiation levels as a rate per second. These values can now be linearly scaled to the desired time of BGC operation.

7.2.3 LHC BGC demonstrator benchmark in Run 3

The radiation levels as simulated by FLUKA are compared to the radiation monitor measurements taken during the operation of the BGC demonstrator in Run 3, in fig. 7.7, where the shape of the BLM TID profile is well reproduced in the simulation. The global agreement between the simulated to measured data is given as the average (weighted on the measured data) ratio as:

$$\mathcal{R} = 2.19 \pm 80\% \qquad (7.3)$$
$$\mathcal{R}_w = 2.19 \pm 115\% \qquad (7.4)$$

where the error is the standard deviation from the mean. Usually, a few ten percent agreement can be achieved in the complex accelerator scenario [37, 43].

Moreover, the BGC was the main contributor (compared to background or other identifiable sources of radiation) when gas is injected within the instrument. The analysis shown here stops at 170 m from
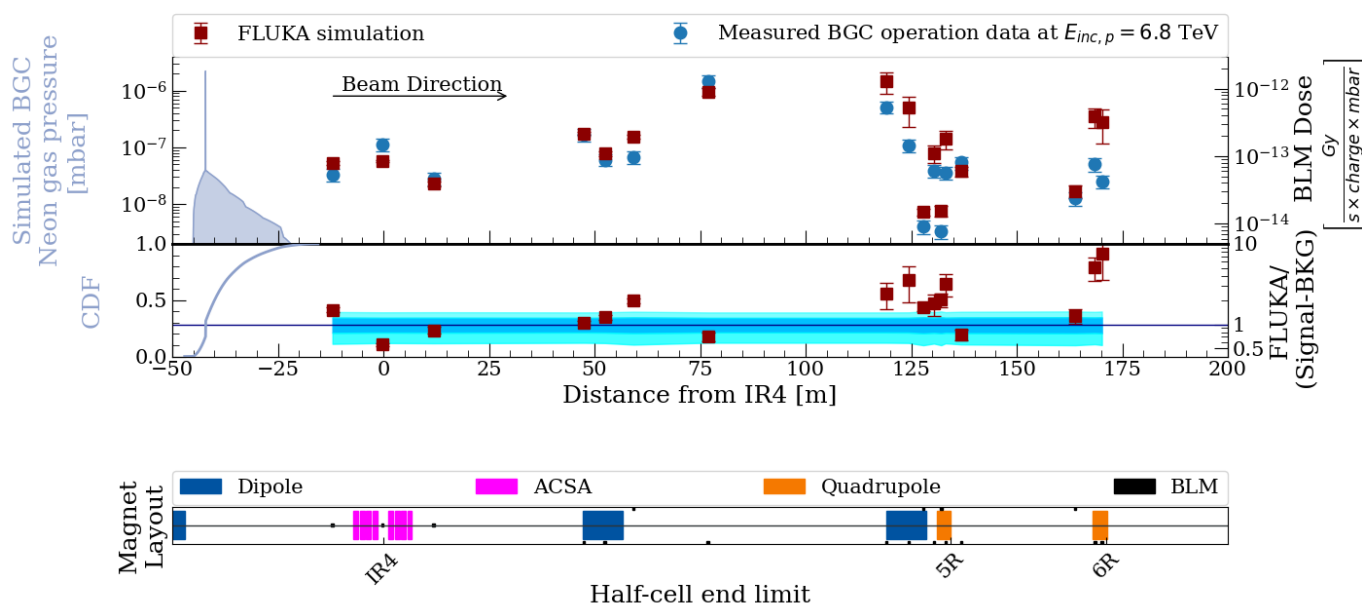
Figure 7.7: BLM benchmark for the BGC demonstrator operation at top beam energy (6.8 TeV). **Top panel**: Gas density of the BGC target, with the BLM pattern downstream the BGC placed on beam 1 as measured over the Run 3 (2022 and 2023) proton runs (blue points) and as estimated by FLUKA (red points). **Mid panel**: The cumulative distribution function (CDF) used to sample the interaction point of the beam-gas collision, as well as the ratio between simulation values and measured data. **Bottom panel**: The LHC machine layout and the BLM locations.

the center of IR4 (or 220 m downstream of the BGC on beam 1), because the measured radiation levels induced so far away by the BGC operation generally fall below other sources of radiation. Moreover, the further away from the radiation source, the more the geometric modelling uncertainties stack up, leading to worse agreements, as is this case as well: at 170 m right of IR4, there is visible simulated overestimation of the dose rate. Nevertheless, the good level of agreement gives confidence in the HL-LHC predictions that are made in the following sections based solely on FLUKA simulations.

7.3 Radiation levels specifications for HL-LHC

The HL-LHC radiation level specifications are typically given per annum, as outlined in ref. [80]. As already mentioned in section 2.7, the radiation levels in IR4 are assumed to scale with integrated beam intensity, for which the past (foreseen) values for LHC (HL-LHC) are given in tab. 7.2.

7.3.1 Accelerator tunnel

To put the BGC impact into perspective, the total integrated TID per year in the tunnel is plotted in fig. 7.8, divided in 2 components. The background level is given for 2016, as a baseline year (and as done in the HL-LHC radiation levels specifications document [80]) without any BGC operation, whose

Table 7.2: Annual integrated beam intensity for proton operation for the sum of the two beams in Run 2 [87], the on-going Run 3 [40] and planned for HL-LHC [80].

year	Integrated beam intensity (beam 1 + beam 2) [10^{21} p s/year]
2015	0.71
2016	2.6
2017	2.5
2018	3.1
2022	1.87
2023	1.21
2024	3.25
HL-LHC	8.0

measured radiation levels are scaled up via integrated beam intensity to HL-LHC parameters. The BGC induced only signal, as measured during Run 3 operation (2022 and 2023) for the BLMs downstream of the BGC, and scaled up via instantaneous beam intensity scaling (from $3.0 \cdot 10^{14}$ charges for LHC to $6.35 \cdot 10^{14}$ charges for HL-LHC) and a BGC operational time of 200 h per year.

From an instantaneous radiation effects perspective, it is instructive to look at the ratio of the BGC induced TID rate over the interpolated background TID rate without the BGC gas injection, for each BLM, and for each fill, shown in fig. 7.9. Although the instantaneous TID rate can be as much as 3.5 times larger than the background (for the closest BLMs downstream of the BGC), these BLMs around the radio frequency (RF) cavities also correspond to the the lowest cumulated yearly TID levels in IR4.

From a machine protection point of view, the simulated radiation levels are not an issue for what concerns the heat loads on the magnets, both as maximum power density as shown in fig. 7.10 or as total power dissipated on the entire magnet as summarised in tab. 7.3. For the assumed gas density profile with a distributed peak pressure of $p_{BGC,distributed} = 10^{-9}$ mbar and a 1-2 cm long gas curtain peaked at $p_{BGC,curtain} = 10^{-5}$ mbar, as well as the max HL-LHC

intensity of $N_{t,max} = 6.35 \cdot 10^{14}$ protons at 7 TeV, there is no risk of quenching in the magnets, if compared to the studied magnet limits [48] that are a factor of 100 higher:

- **Dipoles**: at $0.10\,\mathrm{mW/cm^3}$, below the $13\,\mathrm{mW/cm^3}$ quench limit [49].

- **Quadrupoles**: at $0.03\,\mathrm{mW/cm^3}$, below the $40\,\mathrm{mW/cm^3}$ quench limit [78].

Similarly, the TID levels shown do not rise any concerns in terms of cumulated damage, as the limit is reported at 25 MGy [48].

Table 7.3: FLUKA simulated total power deposition in the inner coils of the magnets for the BGC demonstrator, placed on beam 1, for the LHC Run 3 operations, as well as for the foreseen HL-LHC era. The distance from the magnets to the centre of IR4 and to the BGC instrument are also provided.

Magnets	d IR4 [m]	d BGC [m]	LHC Total Power [mW]	HL-LHC Total Power [mW]
MBRS5L	-56.7	-14.2	0	0
ACSCA2L	-15.4	27.1	27.5	60.2
ACSCA1L	-7.6	34.9	56.6	121.9
ACSCA1R	0.7	43.2	60.9	133.1
ACSCA2R	8.7	51.2	30.6	68.4
MBRS5R	56.7	99.2	248.4	542.8
MBRB5R	118.8	161.3	172.8	336.1
QY5	130.8	173.3	4.4	15.4
QY6	167.8	210.3	15.8	16.1
QM7	264.6	307.1	24.7	69.2
MBA8	270.4	312.9	11.8	32.3

7.3.2 UX45 Shielded alcove

Not only in the accelerator tunnel, the radiation levels in the adjacent alcoves and galleries are of particular importance for the impact on electronics and their operation. Annual HL-LHC specifications were previously defined for the UX45 alcove, based on both RadMon measurements in 2016 from ref. [148] scaled with integrated beam intensity, as described in tab. 7.2. Since the radiation levels are relatively low in
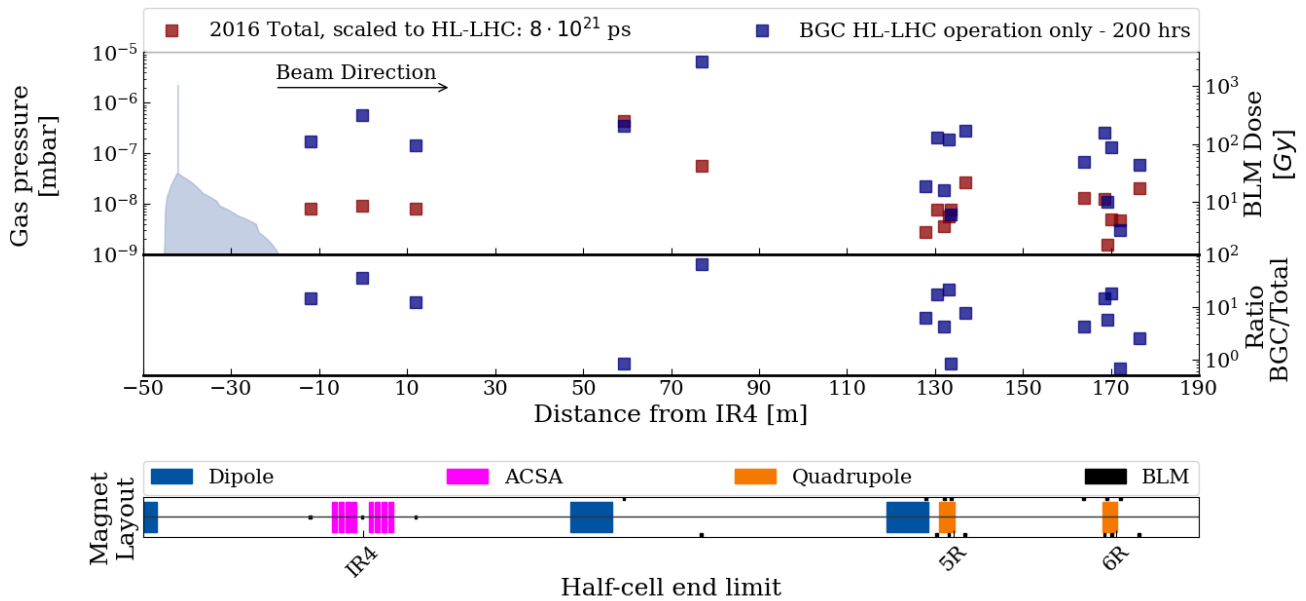
Figure 7.8: **Top panel:** Distribution of TID measured by the BLM system during 2016 proton operation, rescaled to the reference year of HL-LHC operation via integrated beam intensity scaling, together with the BLM pattern downstream the BGC placed on beam 1 as measured over the Run 3 (2022 and 2023) proton run, scaled to HL-LHC operation via instantaneous beam intensity scaling and BGC operational time. The gas densitz profile fo the BGC target is shown as well. **Mid panel:** The ratio between the BGC induced signal and the 2016, both scaled to HL-LHC operation. **Bottom panel:** The machine layout and the BLM locations, assumed the same for the HL-LHC machine as for the LHC.

this area, one employs a conservative approach and selects the RadMon that measured the highest levels in 2016 as representative of the whole alcove. These background values from the nominal LHC operation are scaled up to the HL-LHC beam intensity and compared to the BGC only values, resulting in tab. 7.4. Moreover, the radiation level specifications typically include four quantities: TID, 1-MeV neutron equivalent fluence and thermal neutron fluence, obtained from the HEH fluence specifications by applying the same standard conversion coefficients used for the definitions of radiation level categories in the DS as: $1\,\mathrm{Gy} \sim 1{\cdot}10^9\,\mathrm{HEH/cm^2} \sim 1{\cdot}10^{10}\,\mathrm{1MeVn\text{-}eq/cm^2} \sim 1\cdot10^{10}\,\mathrm{THN/cm^2}$. The BGC values are obtained irectly from the simulation, and all these values are summarised in tab. 7.5.

7.4 Future BGC operation

The new monitor will be important to give a precise measurement of the detailed beam properties, to be used either as a standalone even during injection and rampup, or together with another proposed instrument, the hollow electron lens (HEL). This will help ensure safe operation of the accelerator, further improving our understanding of the beam dynamics, and ultimately allows to optimize the physics output. Moreover, there is current interest in installing one BGC instrument on beam 2 for the the HL-LHC operation, for which several locations are under investigation and a similar study for its impact is also planned. The instrument was designed as part of a collaboration between CERN's beam instrumentation (BI) group, Liverpool university, the Cockcroft
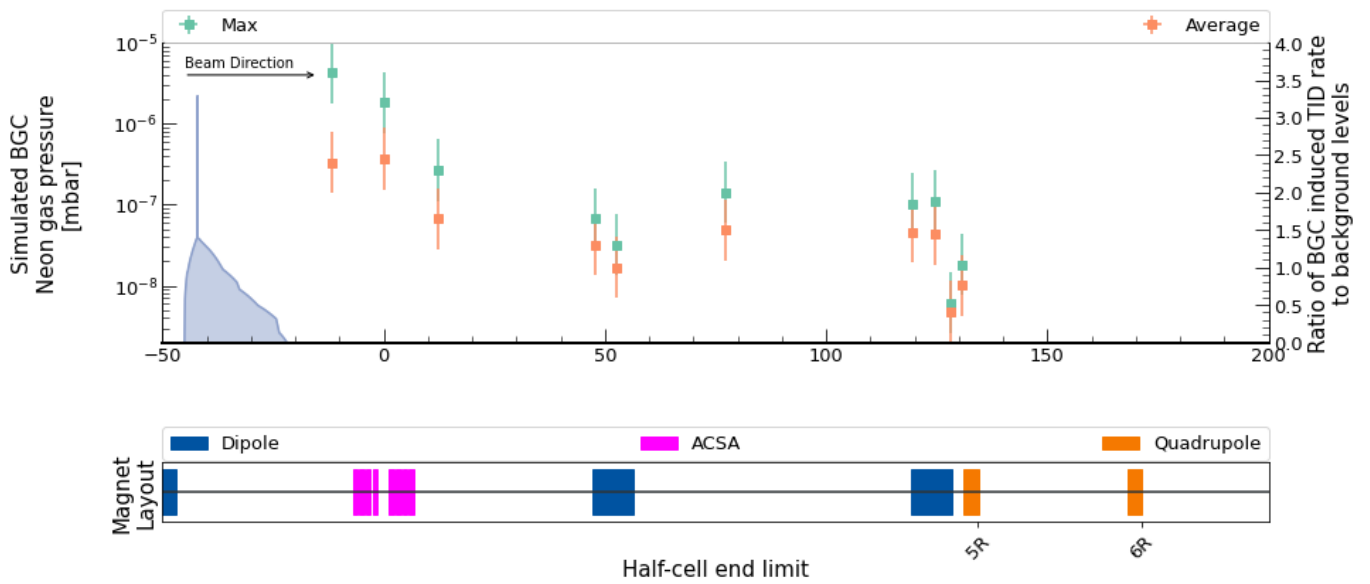
Figure 7.9: **Top panel:** The ratio of the BGC induced TID rate, as extracted for each fill, to the fitted background TID rate stemming from the nominal LHC operation. The average value for all the fills is shown, as well as the maximum amongst the fills. The simulated BGC Neon gas pressure is also shown on the left side. **Bottom panel:** The machine layout, showcasing the superconducting cavities (ACSCA), as well as the cryogenic dipoles and quadrupoles.

Table 7.4: HL-LHC radiation level specifications of HEH fluence in the UX45 shielded area in IR4, obtained from 2016 radiation monitor (RadMon) measurements scaled with the integrated beam intensities in tables 7.2, as well as the BGC induced FLUKA simulated fluence. The highest RadMon measurement is used as reference for the entire alcove.

	RadMon	2016 measured HEH [cm^{-2}]	HL-LHC scaled HEH [cm^{-2}]	BGC induced FLUKA simulated HEH [cm^{-2}]
UX45	SIMA.UX45.4RM01S	$3 \cdot 10^7$	$8.0 \cdot 10^7$	$2.5 \cdot 10^8$

institute and Gesellschaft für Schwerionenforschung (GSI).
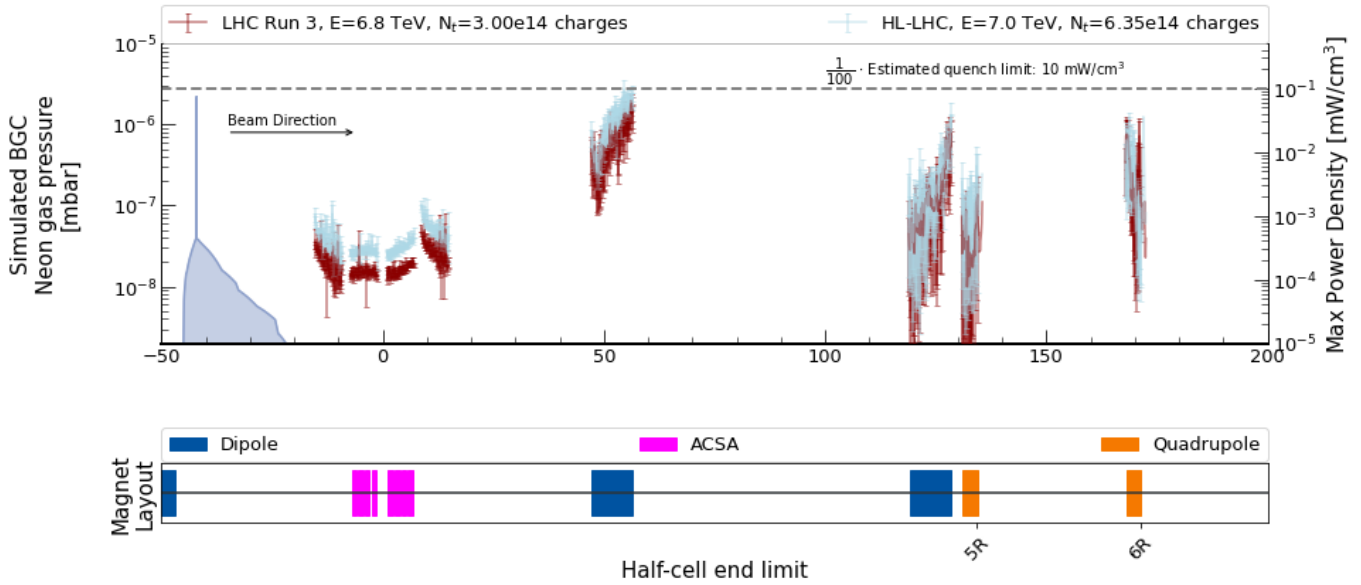
Figure 7.10: **Top panel:** FLUKA simulated heat loads in the inner coils downstream of the Beam Gas Curtain (BGC) on beam 1, as max power density. The red curve corresponds to the LHC Run 3 operation at beam energy $E_p =6.8$ TeV and total number of charges of $N_t = 3 \cdot 10^{14}$ charges, while the blue one corresponds to the foreseen HL-LHC operation at $E_p = 7$ TeVand $N_t = 6.35 \cdot 10^{14}$ charges. The horizontal dashed line corresponds to 1/100 of the estimated quench limit of $10\,\mathrm{mW/cm^3}$. The simulated BGC Neon gas pressure is also shown on the left side. **Bottom panel:** The machine layout, showcasing the superconducting cavities (ACSCA), as well as the cryogenic dipoles and quadrupoles.

Table 7.5: Annual HL-LHC radiation level specifications of TID, HEHeq fluence, 1-MeV neutron equivalent fluence and thermal neutron fluence in the UX45 shielded area in IR4. The HEHeq fluence specification is obtained from rescaled RadMon measurement, while the others are derived by applying the same standard conversion coefficients used for the definitions of radiation level categories in the categories in the DS (1 Gy $\sim 1{\cdot}10^9$ HEHeq/cm$^2 \sim 1{\cdot}10^{10}$ 1MeVn-eq/cm$^2 \sim 1 \cdot 10^{10}$ THNeq/cm^2, with an extra safety margin of a factor 2 and with result rounded by excess). The BGC induced levels are obtained from FLUKA simulations, scaled to HL-LHC operation. The FLUKA simulated values have an associated statistical error of $\Delta_{sim,stat} = 5\%$, and a systematic error estimated at $\Delta_{sim,syst} = 14\%$ (described in tab. 5.1).

RadMon	HEHeq [10^7 cm^{-2}]	TID [mGy]	1MeVn-eq [10^8 cm^{-2}]	THNeq [10^8 cm^{-2}]
HL-LHC background (scaled measurements)	8.0	200	20	20
BGC induced (FLUKA simulated)	3.1	3.49	2	0.8

The first act - summary

The main result of these studies on the radiation levels generated by the Beam Gas Vertex (BGV) and the Beam Gas Curtain (BGC) instruments is the observed proportionality between the total ionizing dose (TID) rate measured by the beam loss monitor (BLM)s, normalized to the beam intensity as measured by the beam current transformer (BCT)s, and the pressure gauge values measuring the injected gas profiles. This proportionality confirms the good understanding of the source of radiation and its scaling factors. The instruments lead to losses that are quantifiable even hundreds of meter downstream of their location, indicating that they are indeed a measurable and locally the dominant source of radiation.

The BGV demonstrator, operated in Run 2 (2015-2018) and placed at $-220\,\text{m}$ on beam 2, showered towards the dispersion supressor (DS) part of the accelerator, where the main beamline elements that could be impacted consists of the LHC arc FODO lattice, namely the standard 8.3 T dipoles and the **fo**cusing/**d**efo**c**using quadrupoles. The BGC demonstrator, operated in Run 3 (2022-to date) and placed at $-42\,\text{m}$ on beam 1, showers towards the center of the insertion region (IR), where a more variety of critical beam line elements are located, amongst which the accelerating superconducting radio frequency (RF) cavities, as well as the beam separation/recombination cryogenic dipoles. Both beam-gas instruments were planned with an estimated total operational time of 200 h per annum during the HL-LHC era.

The comparison between the Run 2 (3) measurements for the BGV (BGC) and the FLUKA simulation reveals a good agreement, typically within a factor of 2, which is a further confirmation that the origin of the radiation levels is well understood, thereby serving as a reliable basis for predicting the radiation levels for the HL-LHC era.

The instantaneous power deposition on the magnets are estimated to be more than two orders of magnitude below the quench levels, and the cumulated dose lifetime degradation does not pose any critical issues regarding the nominal operation of the accelerator. Nevertheless, the levels are above the typical arc level "baseline" for the LHC, hence the high energy hadron (HEH) could pose single event effects (SEE) related availability issues; however, in this case, it would only affect a small portion of the machine, and hence limited number of units. Similarly, the TID levels of about 10 Gy per year are not radiation to electronics (R2E) safe for commercial off-the-shelf (COTS) electronics.

The second act - The Timepix3 radiation monitor and its characterisation

8

The Timepix3 radiation monitor

The characterization of the radiation field generated by the accelerators at the European organisation for nuclear research (CERN) is an essential task to ensure their smooth and reliable operation, preventing radiation-induced failures of critical equipment and electronics. For this purpose, the radiation to electronics (R2E) [16, 17] effort at CERN employs different types of radiation monitors distributed throughout the accelerator complex, including the beam loss monitor (BLM) system [149], the radiation monitor (RadMon) system [150, 151] and its battery-powered version (BatMon) [152], the distributed optical fibre system (DOFRS) [153], and passive HLD [154], all capable of measuring the total ionizing dose (TID) via different technical solutions. Additionally, the RadMon system can also measure single event effects (SEE) and silicon 1-MeV neutron equivalent fluence. A detailed description of these detectors is given in apendix 3.

In addition to the above detectors, this work presents a recently developed Timepix3 radiation monitor setup, of which the suitability to be used in the scope of R2E radiation level monitoring activities at CERN is being assessed. Timepix detectors have been successfully applied for a wide range of activities: medical radiotherapy [155], high-resolution photon counting [156], radiation monitoring on the international space station (ISS) [157], 3D color X-ray [158], radiation imaging [159], luminosity measurements and radiation field characterization in the a toroidal LHC apparatus (ATLAS) detector [160].

This second act is divided into three chapters. Firstly, a description of the Timepix3 radiation monitor takes the reader through the entire analysis chain: from explaining the charge deposition in the sensor and its conversion into the digital signal based on literature

review about the Timepix3 technology, to the data post-processing using a clustering framework and cluster classification algorithm developed within the scope of this thesis. Secondly, two energy calibration campaigns have been performed with charged particles, which allow to retrieve not only the ToT to energy conversion parameters, but also include saturation effects that could be mitigated. The calibration efforts lead to the publication of ref. [22]. Thirdly, two neutron irradiation campaigns at meV and up to MeV energies have been carried out, thereby testing the radiation hardness of the setup, but also techniques to increase the detection efficiency of neutrons. These results are soon to be submitted to the radiation effects on components and systems (RADECS) conference.

8.1 The Timepix3 detector

The Timepix3 detector [161] is part of the Timepix detector family [162], designed by the Medipix collaboration [163]. The Timepix is a hybrid semiconductor pixel detector consisting of a sensor chip with a matrix of 256×256 pixels, $55 \times 55\,\mu m^2$ each, which is bump-bonded to the Timepix3 readout application specific integrated circuit (ASIC) chip. A full description of the Timepix3 [161, 162], and more general of semiconductor devices and detectors [164], can be found in literature, and the focus here shall only be on the features of relevance (as in tab. 8.1) for physics analysis within radiation to electronics (R2E).

The detection layer for the Medipix detector family can be made of different semiconducting or semi-insulating materials (such as Si, GaAs, CdTe, CZT, etc.), in combination with the same application spe-

Table 8.1: Summary of Timepix3 detector features.

Feature	Value
Total Area [cm^2]	2.12
Number of pixels	256 x 256
Pixel pitch [μm]	55
Thickness [μm]	300
Type	p-in-n
Frequency (Timing resolution)	40 MHz (25 ns) for ToT and general ToA
	640 MHz (1.5625 ns) for fToA
Dead time per pixel [ns]	ToT Pulse time + 475
Readout Type	Data-driven or frame-based

cific integrated circuit (ASIC) chip owing to its hybrid structure. The monolithic sensing layer can have various thicknesses, ranging from 100 to 2000 μm. The Timepix3 radiation monitor has a 300 μm-thick silicon layer (typically the minimum thickness required to obtain PID capabilities), with metalization and dead layers both on the top and on the bottom due to the manufacturing process.

The Timepix3 nominal clock time (frequency) is of 25 ns (40 MHz), matching the LHC bunch spacing, which could allow a bunch-by-bunch characterization of the radiation environment. This good timing resolution allows the detector to separate individual particle hits with moderately high flux rate, in this work, up to approximately 10^8 particles/(cm^2·s).

The Timepix3 radiation monitor uses a p-doped silicon sensor, and as such the charge carriers are holes. Moreover, the module is operated with a partial bias voltage of V_{bias}=50 V, leading to a partially depleted sensor thickness of approximately 250 μm, computed with the method described in ref. [95]. Both these choices lead to a relatively long signal collection time, because holes have relatively lower mobility compared to electrons, and the partial bias voltage leads to a lower electric field in the depleted region. Quantitatively, while the charge collection time can typically be around $\mathcal{O}(10\,\text{ns})$, for the Timepix3 radiation monitor it is expected to rise to $\mathcal{O}(100\,\text{ns})$. In operation, The Timepix3 radiation monitor reads all the 65 536 pixels independently of each other. For the
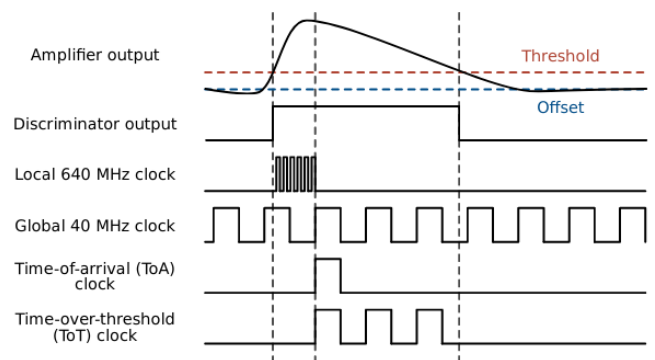
Figure 8.1: Timing diagram for the Timepix3 pixel cell in data driven mode, showing the amplifier output signal, the threshold, and the combined work of the 40 MHz and 640 MHz clocks measuring the time over threshold (ToT) and the time of arrival (ToA) of the hit.

applications described in this paper, it is operated in data-driven readout mode, acquiring both the ToT and the ToA for all hits, i.e., each time the pixel output signals exceed the threshold.

8.1.1 Operational principle: signal formation

When traversed by ionising particles, the silicon sensor of the Timepix3 radiation monitor generates output current pulses by collecting the free charge carriers (electrons and holes) released in each pixel, according to the Shockley-Ramo theorem [165–167]. In particular, the charge carriers collected by the pixel electrodes are those released in the active portion of

the detector, defined as the region where an electric field is maintained via the application of the bias voltage.

The operational principle of the Timepix3 is shown schematically in fig. 8.1, along with its timing structure. The energy deposited in the pixel is proportional to the number of charge carriers collected by the electrodes and moreover amplified. The charges that arrive at the electrode is are then discharged via a constant current I_{krum} (Krumenacher current) [168]. It is a discharge current in the preamplifier feedback loop, which drives the speed of the preamplifier signal return to the baseline, and it can also be considered as the fall time of the signal. Therefore, it directly sets the ToT for a given amount of charge, as shown in fig. 8.2.
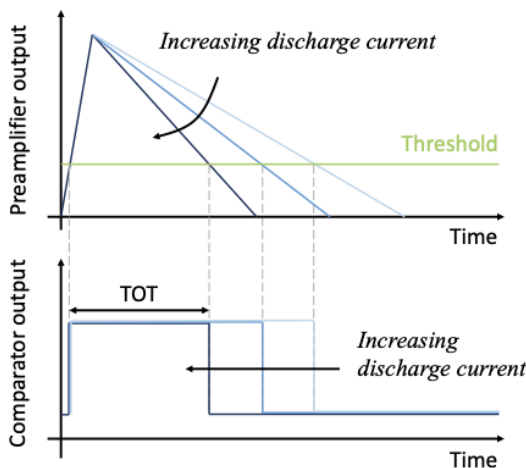
Figure 8.2: Illustration of the influence of the discharge current I_{krum} on the signal shape at the output of the preamplifier and on the corresponding ToT (fig. from ref. [169]).

When the output signal exceeds a pre-set threshold, a global 40 MHz clock measures the time that it takes for the signal to return below it, i.e. the time over threshold (ToT), expressed in clock units (where one time unit corresponds to 25 ns, as determined by the clock frequency). Asynchronously, a local 640 MHz clock starts when the signal exceeds the threshold, thereby defining the fast time of arrival (fToA). The

clock is stopped by the rising edge of the 40 MHz MHz clock, at which moment the time of arrival (ToA) is registered.

In hybrid pixel detectors, only the segmented electrode is connected to the readout electronics, therefore only one type of carrier is collected. For the p-doped Timepix3 radiation monitor, holes are collected and the resulting signal is a positive pulse. Since the mobility of electrons is three times higher than the mobility of holes, this implies a slower collection of the signal (or, as described later, of the cluster time evolution) that could allow more discrimination power between the incident particles.

In the data-driven mode, after a hit is processed by the pixel, a data packet containing the TOT and the TOA information is immediately sent off the chip. This reduces significantly the dead time of the pixels hit while the other pixels stay active and allows to reach very high readout rates of up to 40 Mhits/(s cm^2). The different settings of the chip are controlled using programmable digital to analogue converter (DAC)s, such as the Krumenacher current I_{krum} [168], threshold level V_{thl}, sensor polarity, clock speed, etc.

8.1.2 Clustering and charge difussion

The interaction of a single particle with the Timepix3 radiation monitor typically results in a multi-pixel experimental signature, i.e., in more than just one pixel measuring a non-zero ToT. This can be due to (i) particles arriving with a diagonal trajectory with respect to the module, hence crossing more than just one pixel, or (ii) charge carriers released by the incident particle drifting to nearby pixels before being collected by the electrodes [170–172]. In both cases, the clusters of pixels from the particle hit must be reconstructed by combining time and space information via dedicated clustering algorithms [173–175]. For the analysis presented in this thesis, several clustering algorithms have been used:

1. the data processing engine (DPE) algorithm [175] developed by Advacam [176] within an European space agency (ESA) project

has been used, owing to its computational efficiency for the large data sets collected (millions of particles per configuration).

2. in-house R2E, which exploits the field programmable gate array (FPGA) timestamps as screenshots of chip, and then performs a density-based spatial clustering of applications with noise (DBSCAN) procedure [177] on the pixel array to identify the clusters.

Figure 8.3 illustrates the time evolution of two clusters, formed by the orthogonal hit of an 5.6 and 8.4 MeV alpha particle, respectively, on the Timepix3 sensor. At first (i.e., ToA = 0 ns), the charge is released exclusively in the pixel hit by the particle (unless the hit occurs at pixel boundaries, in which case it can be distributed among a maximum of four). Subsequently, due to the charge diffusion process, the nearby pixels begin to collect a portion of the released charge, expanding the dimension of the cluster until the full size is reached (with the external pixel having a ToA that exceeds 100 ns in the case shown). The extent of this effect is determined by the charge collection time, which in turn is determined by the applied sensor bias and by the depth of the energy deposition [178, 179].

Moreover, if the sensor is partially depleted (as is the case for the Timepix3 radiation monitor presented in this work), then the charge collection process is slow and the diffusion effects are enhanced, leading to clusters with more pixels. This feature is exploited in this work to reduce the collected energy per pixel in order to operate in the linear regime of the sensor for the large majority of incoming particles.

When tilted at an angle, the particle tracks inside the detector cross over several pixels. In such cases, the combined effect of the diagonal trajectory of the particle and the charge diffusion process lead to the formation of elongated clusters, that can be exploited to extract information about the direction of the hit.

8.1.3 Energy calibration principles

In order to retrieve an energy value, a calibration procedure of the Timepix3 radiation monitor must be performed, deriving the relation between the measured output ToT value in each pixel and the corresponding deposited energy E_{dep}[1] [170, 180]. Therefore, the aim of the calibration is to compare the measurements done by the readout chip with the known values of the deposited energy from the beam particles.

In the absence of test beams, the threshold DAC and ToT calibration can be achieved using two methods. The first one consists of the use of photons with a well-defined energy. These photons can either come from radioactive sources with a characteristic decay energy or from X-ray fluorescence (XRF) with a characteristic emission energy [181]. The photon being stopped in the sensor, it deposits its full energy. Since the energy of the photon is known, its relation to the threshold DAC or ToT can be characterised.

The second method consists of the use of an internal analogue test pulse generator. The Timepix3 readout ASICs provide an internal test pulse generator which can be used for calibration. In each pixel, a capacitor allows for injecting a charge by applying a voltage step over it. The injected charge is given by:

$$Q = C \cdot \Delta V \tag{8.1}$$

where Q is the injected charge, C the injection capacitance and ΔV the voltage difference applied.

The injection capacitance can vary from pixel to pixel and also from chip to chip. From chip design simulations, the metal-to-metal capacitance (assuming the parallel plate capacitor model) can be extracted.

---

[1]The energy deposited in the sensor can be expressed directly in keV or in the number of electron-hole pairs produced knowing that the average energy required to produce an electron-hole pair in silicon is ∼3.6 eV. In Silicon, the bandgap energy E_g is 1.12 eV and the ionisation energy (or the average energy deposition required to produce an electron-hole pair) is about 3.6 eV. The ionisation energy is higher than the bandgap. Only a fraction of the absorbed energy creates the signal charge and the rest goes into phonon excitation which will be dissipated as thermal energy.

(a) *t*=3.125 ns (b) *t*=25.000 ns (c) *t*=53.125 ns (d) *t*=96.875 ns

(e) *t* = 0.00 ns (f) *t* = 17.1875 ns (g) *t* = 40.625 ns (h) *t* = 112.5 ns
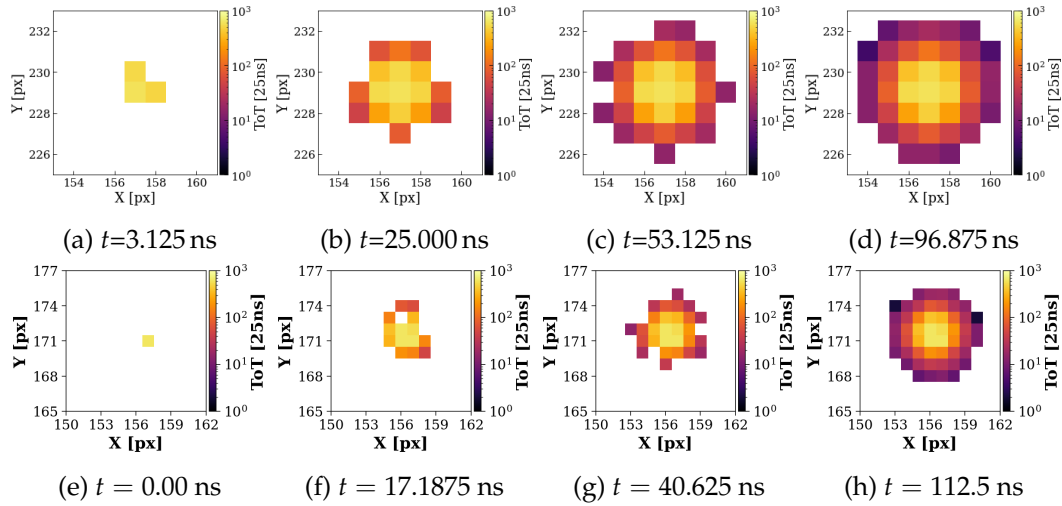
Figure 8.3: Example of two full **(top row)** 5.6 MeV and **(top row)** 8.4 MeV alpha clusters evolution. The particle hits just one pixel at perpendicular incidence in pixel (x, y)=(157,229) and (157, 181) for the 5.6 MeV and 8.4 MeV alpha particle, respectively. The charges diffuse to adjacent pixels over time leading to clusters with more pixels. The timing information refers to the combined ToA (40 MHz, or 25 ns) and fToA (640 MHz, or 1.5625 ns) counters, when the charge first exceeds the threshold (as shown in fig. 8.1), and it is uncorrelated with the ToT that is read at the end, when the signal falls below the threshold.

For the Timepix3 readout chip a capacitance of 20.2 e^-/mV (or about 3.2 fF) is expected. This value has also been cross-checked with X-ray sources and the expected value has been validated [162]. For calibration with the chip bump-bonded to a sensor, the sensor has to be biased to full depletion to reduce the capacitive noise. However, the Timepix3 radiation monitor was used with a partial bias to increase charge diffusion and reduce the known saturation effects (explained later in section 8.1.4).

Moreover, the test pulse procedure has to be validated against test beams, and for the Timepix3 radiation monitor, the setup calibration has been performed with a variety of test beams and radiation sources (isotopes), to study the ToT response of detector, which were later correlated with the energy deposition results obtained with simulations in fluk-turiende kaskade (FLUKA) [18–20] and geometry and tracking (GEANT)4 [182–184].

8.1.4 Pixel level energy calibration principles

The general features of the pixel-level ToT vs energy calibration have been identified in the literature [170], as illustrated qualitatively in fig. 8.4, where different regions with distinct features can be isolated.

8.1.4.1 Normal regular regime - regions A and B

The range for the ToT and the boundary between low energy response and the normal regular region (A and B, for $E < E_{sat}$) can be modelled using a surrogate function [185] for $t = E_{thres} < E_{dep} < E_{sat}$ as:

$$f(E_{dep}) = ToT(E_{dep}) = a \cdot E_{dep} + b - \frac{c}{E_{dep} - t} \tag{8.2}$$

where this nonlinear region is parametrized by c_{ToT}, which defines the curvature, and $E_{thres} = t$ is the threshold parameter that defines the lower limit of
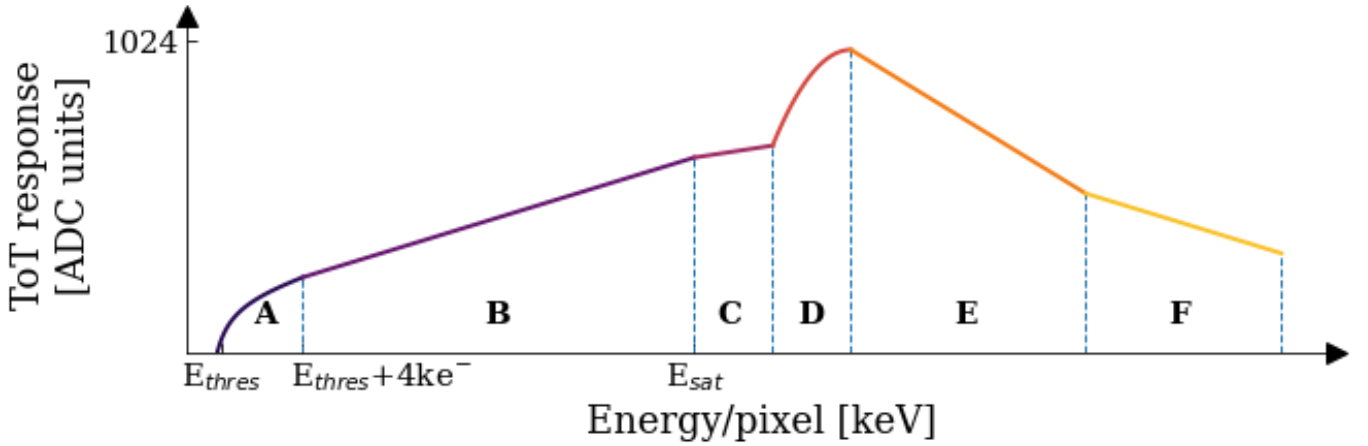
Figure 8.4: Illustration of the pixel-level spectral response of the Timepix, with regions of distinct dependency [170]. The maximum ToT response is limited by the 10 bit registry at 1024 ADC units (here, at 25 ns), while the lower detection limit is operationally set (here, at $E_{thres} = 5.3$ keV).

detection (below the threshold no charge can be detected). It is given by the operational voltage of the detector threshold, set here at 0.57 mV (corresponding to a 5.3 keV energy deposition). The measured response is linear if the input charge is 3-4 ke$^-$ above this threshold (corresponding to about a 2.2 keV energy deposition) [162]. Moreover, the relative energy resolution increases with larger ToT. For these reasons and for the high energy calibration scope of this work, the low energy regime is neglected by filtering out the clusters with pixels measuring less than 8 keV, and as such only the linear parametrization is kept.

The range for the ToT and the boundary between low energy (non-linear response) and intermediate energy (linear response) depend on the clock frequency, the applied threshold and the I_{krum} value. An asymptote occurs at $E = t = E_{thres}$. The point at which the fit crosses the x-axis ($ToT = 0$) corresponds to the threshold: below the threshold no charge can be detected.

The energy calibration is slightly different for each pixel. After performing the pixel equalisation procedure (described in section 8.2.3), one assumes that the energy calibration is practically identical for each pixel, and thus valid for the entire Timepix3 detector.

Conversely, one is interested to convert from ToT to energy. The inverse function of Eqn.8.2 in a more intuitive format is:

$$E(ToT) = ToT^{-1}(E) = \frac{1}{2a} ToT \cdot [1+ \tag{8.3}$$

$$\sqrt{1 - 2\frac{at+b}{ToT} + \left(\frac{at+b}{ToT}\right)^2 \left[1 + \frac{4ac}{(at+b)^2}\right]}$$

$$+ \frac{at-b}{2a} \tag{8.4}$$

where for large ToT values, the square root can be expanded using its Taylor series. Neglecting the second order term for large ToT values, and using $\sqrt{1-x} \approx 1 - x/2$, one retrieves the linear relationship:

$$E(ToT) = \frac{ToT}{a} - \frac{b}{a} \tag{8.5}$$

8.1.4.2 High energy regime: saturation effect - regions C and D

Considering the TeV scale of the accelerator beams at the LHC, the radiation showers of interest for the

Timepix3 radiation monitor are highly energetic, possibly containing particles with high linear energy transfer (LET), and the high energy calibration is also of interest. Above a certain number of charges collected per pixel, the pixel-level spectral response of the Timepix3 gets distorted [170, 180, 186–191], initially as a saturation effect at high energies leading to lower ToT measurements at very high energies (region C), followed by non-linear effects. For example, previous measurements [180, 188] indicate that above $\mathcal{O}(800\,\mathrm{keV})$ the Timepix3 preamplifier exhibits an unexpected saturation effect, whereby the triangular pulse is shortly followed by a second pulse. The additional second pulse is associated with a slow exponentially shaped decay of the preamplifier signal, which can cause extra counts leading to overshooting (erroneously high energy) measurements (region D).

8.1.4.3 Very high energy regime: the volcano effect - regions E and F

The *volcano effect* named after its visible manifestation is a saturation-like effect that causes substantially lowered measurement of ToT in pixels above a certain energy deposition. It is a caldera like hollowing out of the measured energy deposition in the center of a cluster and a net loss of total measured energy deposition with respect to what would be theoretically expected.

It has been observed only in silicon Timepix3 hybrid pixel detectors operating in hole collection mode, while Timepix3 detectors collecting electrons seeming to instead exhibit clusters with a 'flat top' [192]. The manifestation of "volcano effect" is compatible with the fact that the Timepix3 readout chip is equipped with an internal protection circuit for very high input charges that is active only for hole collection mode (for electron collection mode internal protection circuit is not provided). As such, very high energy deposits leading to a large number of generated carriers trigger the chip overload protection system to limit the portion of the signal that exceeds the predetermined threshold (especially in the center of cluster).

Owing to its linearity, region B represents an ideal range of operation for the Timepix3 radiation monitor, whereas all regions below or above it are introducing non-linear or multiple-valued effects, particularly when going beyond region D. In fact, an essential question to be answered by this work is whether the mixed radiation field of CERN accelerators, for which the detector is envisaged, yields energy depositions per pixel that fall (at least for the overwhelming part of the radiation field composition) within the boundaries of region B. For now, it is anticipated that this is mostly the case, therefore the calibration campaign presented in this paper was specifically targeted at the linear region B and at possibly at the first saturation effects (region C), neglecting the higher-energy regions as well as the low-energy one (region A).

8.1.5 Cluster-level calibration

Ideally, the calibration curve of the Timepix3 chip would be obtained by depositing a known amount of energy in a single pixel, and measuring the corresponding ToT response. However, as illustrated in fig. 8.3 for the case of alphas, single particle hits on the sensor lead to the formation of multi-pixel clusters, spreading the deposited energy over several adjacent pixels. This is particularly relevant when the deposited energy is of the order of hundreds of keV or more (i.e., when performing the calibration for relatively high energies), as the number of pixels per clusters increases with the deposited energy.

In the present paper, the calibration of the Timepix3 radiation monitor is performed using clusters formed by protons and alphas with known energy that are stopping within the sensors, thereby depositing all their energy in the depleted region, with a fraction lost in the passive layers in front. To perform the pixel-level calibration from multi-pixel clusters, one has to work under the assumption that all pixels are operating within the same linear response (i.e. region B), by summing the ToTs for all the N pixels:

81

$$ToT_{cl} = \sum_i^N ToT_i = \sum_i^N f(E_i) = \sum_i^N (a \cdot E_{dep,i} + b)$$

$$= a \cdot \sum_i^N E_{dep,i} + \sum_i^N b = a \cdot E_{dep} + N \cdot b \quad (8.6)$$

where ToT_i (E_i) is the per pixel ToT (energy) value, a and b are the linear coefficients parametrising the ToT vs energy curve in region B, E_{dep} is the total energy deposited (the known beam energy minus the energy lost in the top layers), and N is the total number of pixels per cluster (which increases with E_{dep}). The assumption of having the same linear response for all pixels is tested in section 9.2.4.3, especially for high-energy hits, for which saturation effects can occur. In fact, the choice of operating the Timepix3 radiation monitor with partial bias is intended to prevent the deposition of too much energy in the center of the clusters by enhancing the charge sharing, thus ensuring that the conditions of region B can be met in most (if not all) pixels in the cluster. If these conditions are not met, deviations of the measured calibration curve from ref. 8.6 can be expected, especially for high E_{dep} per pixel.

Finally, once the calibration curve parameters are established, the Timepix3 radiation monitor can be used to obtain energy deposition measurements simply by inverting the expression in 8.6.

8.1.6 Time measurement

The signal rise time is independent of the signal height [193]. Therefore, a signal with a larger amplitude crosses the constant threshold value earlier than a signal with a smaller amplitude (as depicted in fig. 8.5a). This phenomenon is commonly called timewalk, and leads to a time shift in the ToA and to non-linearity at signal values close to the pre-defined threshold.

The shift in time with amplitude x can be modelled with a surrogate function, motivated by geometric considerations [193]:

$$f_{ToA}(x) = \frac{c_{ToA}}{x - t_{ToA}} + d_{ToA} \quad (8.7)$$

The three free parameters c_{ToA}, t_{ToA} and d_{ToA} correspond to the curvature, the asymptote and the offset of the response function. It is possible to perform a time calibration [193] in two steps by a combination of test pulses for the non-linear timewalk and beam data to calibrate the delay.

8.2 The Timepix3 radiation monitor setup

While the previous chapter focused on the detection principles of the pixel silicon detector, in particular of the Timepix3 technology, this chapter describes the technical implementation of the chip within a detection setup capable of deployment across the CERN accelerator complex, henceforth called the Timepix3 radiation monitor.

8.2.1 Setup description

The Timepix3 radiation monitor setup has been conceptually designed in three parts:

1. the detector module hosting the Timepix3 chip and sensor, operating in the radiation field to be measured

2. the front-end crate, designed as radiation tolerant in order to operate in the proximity (about 5 m away) of the detector module

3. back-end crate, the data acquisition computer and the power supplies, to be placed far enough from the measurement area to be considered safe for electronics and/or human operation

The full block diagram of the setup is presented in fig. 8.6. The Timepix3 detector module hosts the Timepix3 hybrid pixel detector mounted on a dedicated board and the power regulators for its operation (2 x FEASTMP 1.5 V). The board can be powered
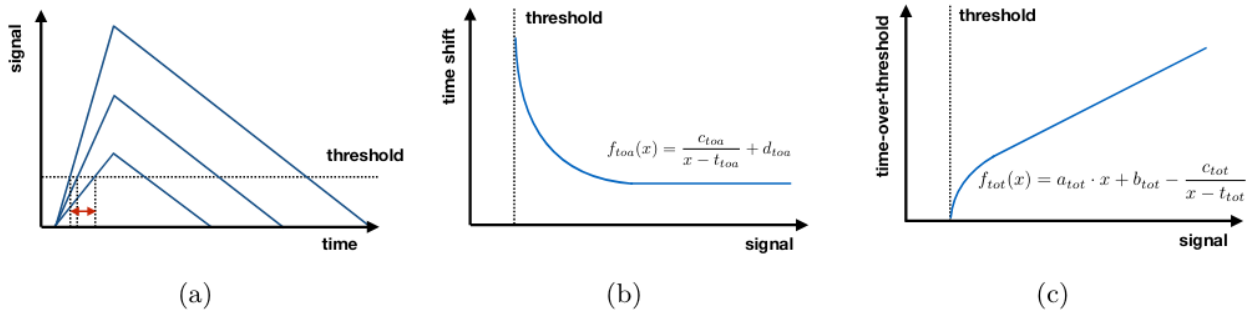
Figure 8.5: The timewalk effect: (a) - amplitude-dependant time of threshold crossing; (b) - the dependency of ToA shift on the pulse amplitude; (c) - the dependency of ToT on the pulse amplitude.

by a single 8 V (5-12 V) power supply, and the expected current consumption at this voltage is about 190 mA. For the data and control signal transmission, the Timepix3 chip uses x and y low-voltage differential signaling (LVDS) lines respectively, that are routed directly on the Timepix3 carrier board to six RJ-45 connectors at the front panel of the detector module. To ensure the proper signal quality, category 6a Ethernet cables (double-shielded) are then used for the connections between the detector module and the front-end crate. The module has a dedicated detector power supply input, which is a LEMO 00 type connector and is located at the front panel. The required power supply depends on the detector type, and for the 300 μm p-in-n type detector a 50 V supply is used, leading to a partial depletion of the silicon sensor. The expected current consumption is dependent on the detector illumination, but it should not exceed several mA at 50 V (with the detector covered, it oscillates around 0.1 μA).

The front-end system consists of a single metal crate, responsible for interfacing with the Timepix3 detector module and for the data transmission to the back-end system through optical fibers. Both front-end and back-end use LC type SFP transceivers. Single-mode optical fibers are used. The system uses FEASTMP power regulators with the allowable input voltage range between 5 V and 12 V. An 8 V power supply with at least 30 W of output power is used, as the expected current consumption at this voltage is roughly
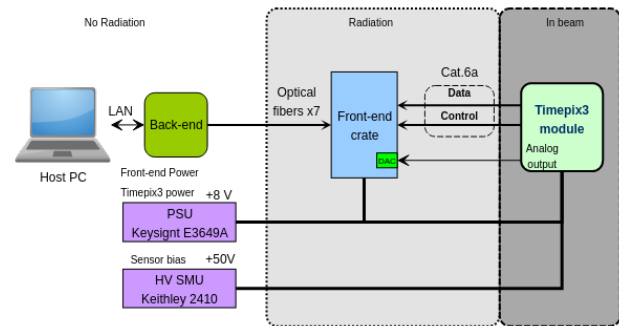
Figure 8.6: Timepix3 setup layout diagram, showcasing the intended operation with the the laptop, backend and power supplies in a no radiation area, the front-end crate that should be radiation tolerant, and the in-beam detector module.

2 A, but can slightly increase for prolonged usage. The same connector with an identical pinout as in the case of the detector module is used (male DB-9). Neither the front-end system nor the detector module have reverse voltage or overvoltage protection.

The main element of the back-end system is the VC707 development board from Xilinx, hosting the Virtex-7 FPGA. An FPGA mezzanine card (FMC) with ten optical fiber transceivers (SFP) is attached to the board and is used for communication with the front-end system. The transceivers' output power is sufficient to operate at distances up to 10 km, but
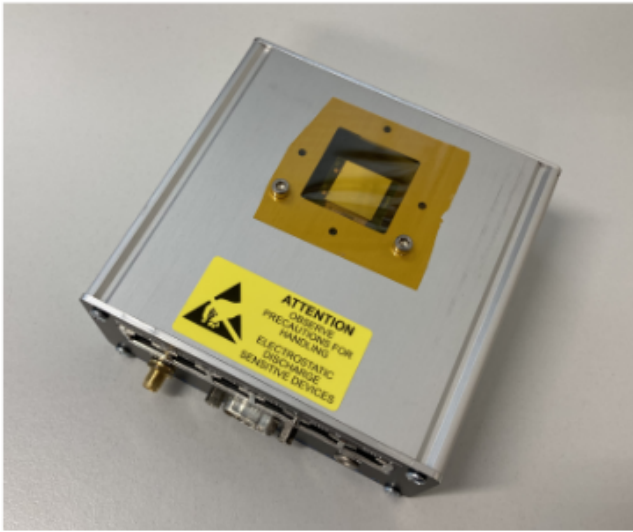
Figure 8.7: Timepix3 detector module, hosting the chip and its DAQ.

Figure 8.8: Timepix3 chip (fig. from ref. [162]).

when (as in most cases) the distance is substantially lower, the receivers at the front-end side are saturated since the signal from the front-end does not face enough attenuation. For this reason, attenuators in the range of 3-5 dB are attached to two of the transceivers, where the signal is transmitted in the direction of the front-end crate. The back-end crate has a dedicated firmware. The power delivery to the system is realized via a dedicated 12 V AC/DC

power converter. The Ethernet interface is used for device communication with the host PC. The readout and processing software on the host PC are based on the PANDA graphical user interface (GUI), allowing the setting of the operational parameters as well as data acquisition.

8.2.2 Operating threshold

The electronic noise (parametrized by its σ_{RMS}) and the threshold dispersion amongst pixels are important parameters to determine the operating threshold of the readout application specific integrated circuit (ASIC). For the Timepix3 chip, the suggested operating threshold should be set to 6 times the σ_{RMS} added in quadrature to the threshold dispersion. This threshold level assures the significant reduction of the probability of pixel triggering by the voltage noise. The very low noise of the Timepix3 chip allows for operating the chip at a low threshold of approximately 500 electrons (charge carriers) and thereby the detection of small signals.

One one hand, at such a low threshold a few pixels might show a high rate of hits in absence of incident radiation due to the excessive output noise. Such pixels are manually masked to be able to operate the chip at the lowest possible threshold. On the other hand, some pixels never fire, and these are called dead pixels. The pixels are usually masked either after the equalisation due to their compromised threshold setting which was significantly different from other pixels or manually since they were deemed to be non-functional (overly noisy, unresponsive or stuck at certain value) at the nominal operating threshold. In total, the number of unusable pixels for the Timepix3 radiation monitor has been less than 0.1% of the matrix.

The operating threshold affects significantly the spatial resolution of the device. Usually, the incident particle triggers multiple pixels on its trajectory, hence for its reconstruction and precise deposited energy calculation it is necessary to capture all such pixels. A lower threshold therefore allows for detecting more events associated with a single particle

hit. For this reason, it is important to minimise the electronic noise and the threshold dispersion.

8.2.3 Threshold dispersion and pixel equalisation

In semiconductor electronics, manufacturing imperfections cause variations in the performance of the devices within the same chip. In this regard, the programmable global threshold of the chip is one of the most affected parameters. A global threshold voltage generated by a programmable digital to analogue converter (DAC) in the periphery of the chip is applied to the discriminators of each of the pixels. However, the effective threshold of each discriminator varies from one pixel to another due to the discrepancy of reference voltage value introduced during the chip manufacturing process. To overcome this dispersion, a 4-bit local threshold adjustment is applied to each pixel in order to achieve a uniform global threshold. The equalisation consists of adjusting this local threshold using an additional trimmer DAC, present in each one of the pixels. Figure 8.9 shows the spread of the threshold before and after equalisation of the R2E Timepix detector.

The chip is operated in a photon counting mode in the procedure. First, the local threshold adjustment (trimmer DAC) is set to its minimum value (mask 0000). For each pixel, the global threshold DAC (THL) is scanned from a level of no counts (threshold above the noise of the pixel front-end circuits) to a level where all the pixels start to be triggered (threshold close to the noise level). As the result of this procedure, the dependency of occupancy (the percentage of time when pixel is triggered) on the global threshold setting is achieved for each one of the pixels. Due to their shape, these dependencies are called S-curves. The middle of this curve, where the occupancy value is equal to 50%, corresponds to the mean value of the noise. The same measurement is then repeated by setting the threshold adjustments to their maximum values (mask 1111) and THL is scanned again.

For each pixel, the operation range is thus known. As-
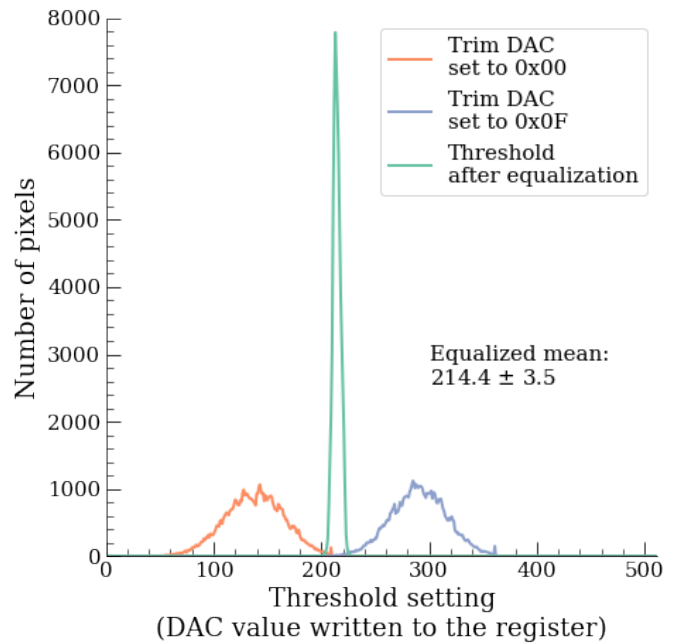
Figure 8.9: Spread of pixel responses for the R2E Timepix3 radiation monitor during equalisation for the local threshold set at its minimum value, to its maximum value and after equalisation.

suming a linear relationship between the two points, the adjustment threshold is set in such a way that the global threshold will remain uniform across the matrix. After equalisation, the ToT response of the chip becomes more uniform even though some dispersion remains ($\sim$ 40 electrons).

8.2.4 Bias voltage and depletion layer

By applying an external voltage across the p-in-n junction we can create an electric field in the same direction as the intrinsic field created by the junction space charge, which will further extend the depletion region. A positive voltage applied to the cathode side relative to the anode side will create this condition and is called reverse biasing of the p-in-n junction. In the high-purity silicon, the width of the depletion region can be increased until it covers the whole volume of the semiconductor, which is also known as the full depletion operation. The voltage could be further brought up to a point of the junction ava-

lanche breakdown, which is not considered in this project as the used detector bias voltages are much lower. The depletion region width can be approximated (according to ref. [95] eqn. 2.27) as:

$$W \approx \sqrt{\frac{2\epsilon_0\epsilon_{Si}}{eN_D}V_{bias}} \approx 253.42 \, \mu m \text{ at } V_{bias} = 50 \, V$$

(8.8)

where $\epsilon_0 = 8.8 \cdot 10^{-12} \, C/(V\,m)$ is the permittivity of free space, $\epsilon_{Si} = 11.68$ is the relative permittivity of silicon, $e = 1.6 \cdot 10^{-19} \, C$ is the elementary charge, $N_D = 1 \times 10^{18} \, 1/cm^3$ is the assumed concentration of donor atoms in the silicon chip and V_{bias} is the externally applied voltage across the junction (bias).

8.2.5 Pile-up limit

Data are shifted from a selected pixel and written into a buffer for readout. This buffer has storage capacity for two events of data to reduce the dead time of the digital pixel front-end, allowing for continuous acquisition and readout with a relatively small dead time of 475 ns per pixel for the Timepix3 chip (compared to 300 μs in the Timepix chip). This dead time increases however when the chip is operating very close to its maximum hit rate, at larger ToT values, or when the data rate exceeds the available bandwidth.

Each Timepix3 pixel provides information about the energy deposition and time of arrival with a time binning of ΔToA=1.5625 ns, yielding a frequency of $f_{ToA} = 640$ MHz/pixel for distinguishing events in different pixels. However, two additional contributions have be considered as well: i) the per pixel dead-time quantified at $\Delta T_{dead} = 475$ ns, and ii) the ToT signal itself since it is a time measurement. From the experimental data in this report, one can have ToT values per pixel as high as $(800 \cdot 25)$ ns, limiting the maximum rate per pixel to $f_{max,ToT} = 50$ kHz.

8.3 Data analysis

As a novel radiation monitor, one unique capability and long term goal for the Timepix3 detector is to be able to differentiate amongst several particles species in a mixed radiation-field, for which several classifications algorithms already exist that rely on the energy deposition patterns and the geometry of the clusters [170, 174, 194]. Typically, particle identification (PID) procedures cannot distinguish between charged particles in the absence of magnetic fields that would help retrieve information about the mass and/or charge of the particles. The advantage of having the pixel matrix is that the different particle interaction mechanisms leave a different track inside the detector. Moreover, the Timepix3 detector contains precise (1.5625 ns) information about arrival time of the charge at the pixels within clusters, that could potentially be used to enhance its PID capabilities.

The first step of the analysis of data from the Timepix3 Radiation Monitor irradiations is the pixel clustering procedure described in Section 8.1.2, aimed at identifying the results of single-particle hits. secondly, several parameters are computed for each cluster, in particular, the cluster ToT volume, given by the sum of the individual pixel ToT values, used for calibration purposes and as a dose rate monitor. Moreover, the cluster shapes are analyzed to define morphological parameters that could allow to distinguish the signal from the background.

8.3.1 Cluster parameters

At this stage, it is beneficial to define the cluster parameters used in this study, and their values for different types of clusters, as shown exemplary for three artificial cluster in fig. 8.10. The cluster parameters are loosely based on the definitions from ref. [194]:

- Cluster size/area A: The number of pixels within the cluster.

- Cluster volume V: The sum of the pixel's ToT,

as:

$$V = \sum_i^A ToT_i \qquad (8.9)$$

- Cluster centre of geometry $C_{geo} = (c_x, c_y)$: The centre of the cluster, computed as the average point amongst the rows and columns, divided by the cluster area.

- Cluster centre of gravity $C_{grav} = (c_x, c_y)$: Similarly to the centre of geometry, but each pixel is weighted by its ToT.

- Cluster radius R: The maximum distance between each pixel p_i and the cluster centre of geometry.

$$R = max(d(p_i, (c_x, c_y))) + 0.25 \qquad (8.10)$$

The extra 0.25 takes ensures that the density is constrained to at most a value of 1.

- Cluster density ρ: Defined as the cluster area divided by the area of a circle:

$$\rho = A/\pi R^2 \qquad (8.11)$$

Therefore, circular clusters will have a density close to unity.

- Cluster extension along rows CE_r (columns CE_c): Defined as the difference between the maximum pixel row (column) index and the minimum:

$$CE_r = Y_{max} - Y_{min} \qquad (8.12)$$
$$CE_c = X_{max} - X_{min} \qquad (8.13)$$

- Cluster linearity $\mathcal{L}$: Computed by fitting a line to the cluster pixels (optionally, weighted on the ToT). Then, calculate the distance of each point in the cluster to the fitted line and compute the least squares parameter R^2, as:

$$R^2 = 1 - \frac{RSS}{TSS} \qquad (8.14)$$

where RSS is the sum of squares of residuals and TSS is the total sum of squares. In order to have this parameter close to 1 for lines/tracks, the cluster linearity is then computed as:

$$\mathcal{L} = 1 - R^2 \qquad (8.15)$$

- Cluster width W (different compared to the cluster extensions): Computed based on the fitted line mentioned above. First, one computes the maximum distance between the line and the left- ($d_{W,L}$) and right-most ($d_{W,R}$) points, then the width is simply:

$$W = 1 + d_{L,L} + d_{L,R} \qquad (8.16)$$

- Cluster length L: Similarly to the width W, based on the perpendicular line to the fitted one for the cluster linearity. Then, one computes the maximum distance between the line and the left- (d_L) and right-most (d_R) points, then the width is simply:

$$L = 1 + d_L + d_R \qquad (8.17)$$

This would be a 2D length on the pixel matrix. Additionally, one could compute the cluster length in 3D by considering also the sensor thickness. By definition, the length should always be larger than the width $L \geq W$.

- Cluster azimuth angle Φ: Computed from the slope of the fitted line, within a $(-\pi/2, \pi/2]$ range.

- Cluster aspect ratio $\mathcal{A}$: Simply the ratio of the width over the length:

$$\mathcal{A} = W/L \qquad (8.18)$$

- ToA orientation: Assuming a more linear cluster, one can try to infer the direction the particle came from by computing the entry and exit points of the particle. In more general

terms, this can be called a Time of Arrival orientation (e.g. either from left or right). It is computed by fitting the ToA values with a line as $mx + n$, and then following variables are considered:

$$ToA_{orientation} = sgn(m) \qquad (8.19)$$

Based on this, the cluster azimuth angle Φ can be extended to cover the $[-\pi, \pi]$ range.

- Cluster polar angle Θ: Based on the cluster length, one can compute the incidence angle geometrically, spanning the range $[0, \pi/2]$.

- Cluster linear energy transfer (LET): Compute as the ratio between the total cluster ToT volume and the cluster length:

$$LET = V/L \qquad (8.20)$$

their sensor material (Si, CdTe, etc.) and operational parameters (threshold level, discharge current, etc.). Moreover, machine learning methods [175, 198] are also investigated for the decision tree into several cluster categories.

Further criteria are as follows, if the cluster:

a) has hollow center

b) has hollow center, with a tail

c) does not fit any of the above

8.3.2 Cluster types

The data analysis for pixel detectors requires a good knowledge of the particle interactions with matter, in particular semiconductor materials [195]. In addition, by taking advantage of the information about the experimental test setup (e.g., perpendicular irradiation for calibration purposes), as well as the beam particles species (hadrons, leaving round blobs inside the detector, as compared to wiggly lines in the case of electrons), one can obtain a set of known tracks and their origin that can be used later on in an unknown radiation environment. For this, the cluster morphology can often be characteristic of the radiation field, and the assignment of particles into broad morphological categories can provide a way to discriminate between particle types. The clusters are sorted into different morphological categories following the selection criteria summarised in tab. 8.2, and a few artificial (custom made) clusters are shown in fig. 8.10. Similar approaches can be found in the literature [160, 196, 197], each slightly customized for their own application and taking into account

Figure 8.10: Artificial clusters used to test the algorithm that computes the cluster parameters, for (**Left**) a straight line, oblique, (**Centre**) a square, and (**Right**) a star. The cluster length and width are plotted with lines, and the other parameters are explicitly given.

Table 8.2: Different types, subtypes and families of clusters, as well as the decision tree/selection criteria to obtain them.

Type	SubType	Family	Cluster Area A	Inner pixels	Aspect Ratio $\mathcal{A}$	Density ρ	Cluster Linearity $\mathcal{L}$	Cluster Length	Cluster Width	Further criteria
Blob	small	monopixel	1							
		twopixels	2							
		L-shaped	3							
		square	4							
		star	5							
		star-broken	5							
	light			1	< 1.25	>0.5				
	medium			1<, ≤ 4	< 1.25	>0.5				
	heavy			>4	< 1.25	>0.5				
		doughnut			< 1.25					a
Track	heavy			>4	> 1.25	>0.25				
		tennis-racket			> 1.25					b
	medium			1<, ≤ 4			>0.7			
	light			0			>0.7		>3	
		short		0				≤5		
	straight			0			>0.7		≤3	
		L-shaped	4							
		3-pixels	3							
	curly					≤0.35	<0.7			
Other	unclassified									c

Test campaigns: energy calibration

Introduction

The Timepix3 calibration procedure, which is used to convert the measured time over threshold (ToT) per pixel into deposited energy, and its key principles have been summarised in section 8.1.3. Experimentally, several calibration techniques have been investigated in the literature, either using internal test pulses [189, 190] or, alternatively, using test beams: protons at 8 [180] or 5 [188] MeV, alpha sources below 2 MeV [170, 191, 199], low energy gamma ray sources [200], pions at 120 GeV [164], etc.

The non-trivial relation between the ToT and the deposited energy per pixel exhibits different dependencies at several energy ranges, which involves threshold effects at low energy, a linear regime at intermediate energies, and complex high-energy effects widely discussed in the literature, e.g., in [170, 180, 188]. Importantly, it is known that the high energy effects can be mitigated by operating the Timepix with a bias voltage that leads to a partially depleted p-in-n sensor [180], reducing the amount of collected charge in the core pixel thanks to the enhanced charge diffusion to the adjacent ones [201, 202]. For this reason, the Timepix3 radiation monitor is operated at a partial bias of V_{bias}=50 V, leading to a depletion layer of around 250 μm instead of the full 300 μm thickness of the silicon sensor.

Two test campaigns using charged particles have been performed to obtain the ToT-energy calibration for the Timepix3 radiation monitor, as sumarised in tab. 9.1.

9.1 CALLAB sources: ^{241}Am and ^{60}Co

9.1.1 Introduction

As the first test campaign with the Timepix3 radiation monitor setup, the scope of these measurements were both to gain in-house expertise about the detector setup (i.e. understanding its technical implementation and limitations), as well as to acquire data points for energy calibration with the available sources.

9.1.2 Facility description

The radiation protection (RP) calibration laboratory (CALLAB) [203] at the Prevessin site of CERN is a state-of-the-art calibration facility designed according to the requirements of ISO 17025 standard [204]. The experiment has been performed employing two radioactive sources:

1. ^{241}Am - 40 kBq (source no. 4276RP) [199, 205], shown in fig. 9.1): thanks to the short range of the alpha particles and because the experiment was performed in air, by varying the distance between the source and the detector one has access to different energy depositions inside the detector (as indicated in fig. 9.2).

2. ^{60}Co - 3.9 kBq (source no. 3982RP). The ^{60}Co is a synthetic (artificially produced in nuclear reactors) radioactive isotope with a half-life of $\tau = 5$ years. It undergoes beta decay to the stable isotope ^{60}Ni, thereby emitting two gamma lines at 1.17 and 1.33 MeV, as indicated in fig. 9.3, via the decay scheme:

Table 9.1: Main features and limitations for the two test campaigns performed with the Timepix3 radiation monitor with the aim of energy calibration.

Laboratory	Features	Limitations
radiation protection (RP) calibration laboratory (CALLAB)	Mainly using an ^{241}Am source emitting alpha particles peaked at 4.8 MeV 1. conveniently located and easily accessible at the CERN Prevessin site. 2. operation in air, allowing to obtain different calibration points by varying the distance.	1. rather large measurement uncertainty of the distance between source and detector (and thus, of the beam energy at detector surface). 2. angular isotropic source, leading to larger energy distribution widths with larger distances. 3. lowest reliable energy peak at 1.4 MeV deposited energy inside the detector, possibly within the saturation regime already.
centro nacional de acceleradores (CNA)	Using monochromatic protons and alphas from 0.6 MeV to 8.4 MeV 1. operating with a TANDEM accelerating the beam particles with an adjustable voltage, giving a maximum of 5% uncertainty on the beam energy. 2. operating in vacuum, reducing the energy and angular scattering of beam particles. 3. lowest available beam energy at 600 keV, possibly within the linear calibration regime.	1. the 600 keV beam energy, if deposited in only one pixels, is at the literature threshold for saturation effects; however, charge sharing compensates and the charge is divided amongst several pixels. 2. the minimum beam flux at about 10^4 particles/(cm^2 s); for calibration purposes, lower fluxes are better suited.

$$\,^{59}_{27}Co + n \rightarrow \,^{60}_{27}Co \rightarrow \,^{60}_{28}Ni + e^- + \bar{\nu}_e + \gamma \quad (9.1)$$
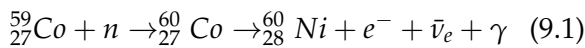
Moreover, the full measured gamma ray γ spectrum for the ^{60}Co source is given in fig. 9.4, where minor background radiation at lower energies can also be observed. Nevertheless, at the MeV level of energies, the gammas will mostly undergo Compton scattering processes, as depicted in fig. 9.5.

9.1.3 Installation

The experiment was set up as shown in fig. 9.6, with the main Timepix3 operational parameters summarised in tab. 9.2. The two radioactive sources were installed on a support at detector height and the distance was adjusted manually, with a precision within a couple of mm.

Table 9.2: Timepix3 radiation monitor operational parameters at the CALLAB test campaign.

Parameter	value
Bias voltage [V]	50
Panda GUI firmware version	2.4.0

9.1.4 Data analysis

The measured data for both sources has been clustered using the data processing engine (DPE) clustering algorithm described in section 8.1.2.
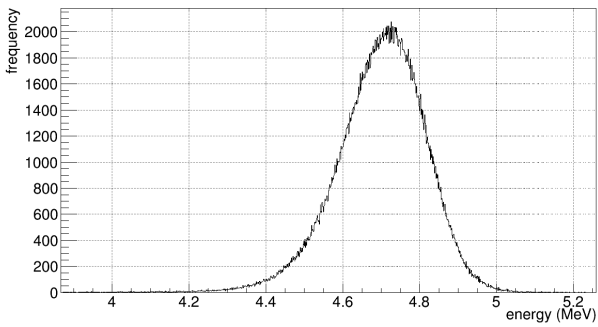
Figure 9.1: The weak ^{241}Am alpha source at CERN, as measured with an alpha spectrometer in vacuum. There is a shift of the spectrum from its nominally emitted 5.486 MeV peak due to the encapsulation of the source. The source was used in air for the test campaign, leading to a further reduction in the energy: 1 mm of air can change the peak position by more than 0.1 MeV.

Figure 9.3: The decay scheme of ^{60}Co and ^{60m}Co (fig. from ref. [207]).
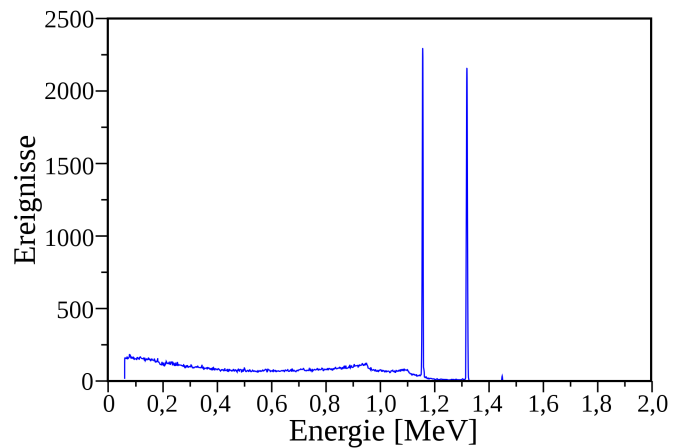
Figure 9.4: The γ ray spectrum of ^{60}Co and ^{60m}Co (fig. from ref. [207]).

Figure 9.2: Alpha particle range and stopping power in silicon (data taken from ref. [206]). The points correspond to the expected energy of the alpha particles after they have traversed the distance from the source to the detector in air, thereby losing a significant part of its energy.

9.1.4.1 ^{241}Am - α particles

The distributions of the total measured ToT per cluster and the cluster size for each distance between the source and the detector are shown in fig. 9.7. The peaks of the deposited energy shift to lower values with increasing distances, as expected from the attenuation of α particles in air and also confirmed by

the FLUKA simulation results, also shown in fig. 9.7 (right). The source of particles was modelled with a Gaussian energy distribution, peaked at 4.677 MeV with a standard deviation (FHWM) of 124.95 keV (294.021 keV). The angular distribution of the source was considered to be uniform isotropic. Similarly to the measured data, the FLUKA simulated results indicate that there are no alpha particles arriving at the detector at $d = 40$ mm; moreover, at $d = 30$ mm the peak is cut from the left, particularly visible in the simulated results. The cluster sizes follow the same pattern as for the energy distributions, decreasing in number of pixels with larger distance.

Nevertheless, the other data points can be fitted well with Gaussian functions, with numerical values for the mean x_0 and the deviation σ presented in
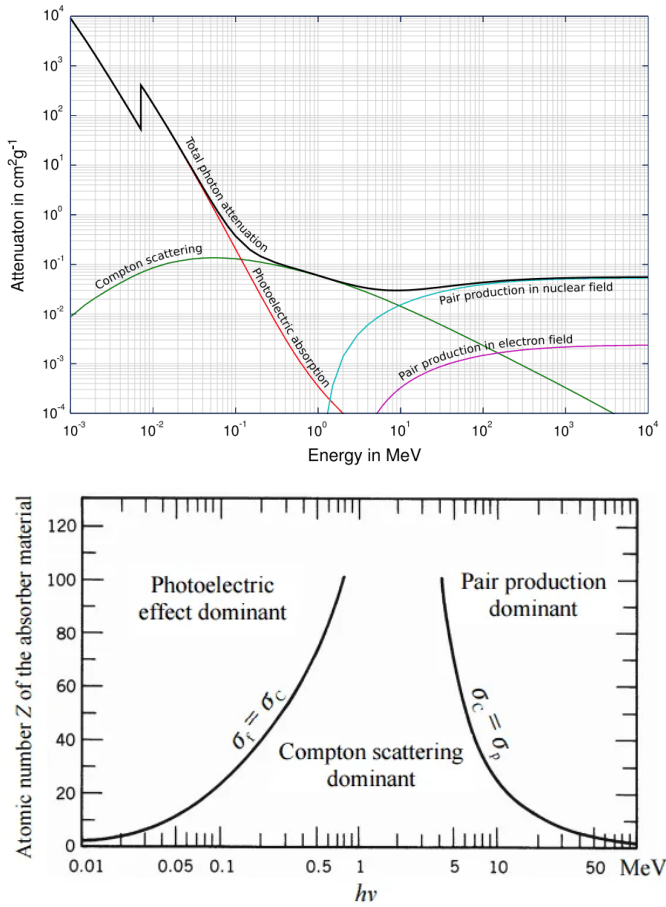
Figure 9.5: The photon interaction mechanisms, as (**top**) the total photon cross sections, as well as (**bottom**) the relative importance, for the three processes (phtotoelectric effect, Compton scattering and pair production). The ^{60}Co source yields two gamma lines at 1.17 and 1.33 MeV, implying that the main interaction mechanism is Compton scattering (fig. from ref. [208]).

Figure 9.6: Timepix3 radiation monitor, as (**top**) installed in the CALLAB hall, with (**centre**) the ^{241}Am source at 12 mm, and the (**bottom**) ^{60}Co source.

Table 9.3. These data points are then plotted in fig. 9.8 to obtain, with several caveats, the first calibration curve for the Timepix3 radiation monitor:

$$ToT_{sat} =$$
$$E_{dep} \cdot \left[306 \pm 45(\sigma_{ToT}) \pm 34(\sigma_{fit}) \pm 30(\sigma_E)\right] \left[\frac{25\,\text{ns}}{\text{MeV}}\right]$$
$$+N \cdot \left[89 \pm 14(\sigma_{ToT}) \pm 10(\sigma_{fit}) \pm 9(\sigma_E)\right] \left[\frac{25\,\text{ns}}{\text{pixel}}\right] \tag{9.2}$$

where N is the cluster size (number of pixels). The uncertainties are as follows: σ_{ToT} is the averaged $1 - \sigma$ of the measured ToT values per cluster for all the

beam energies, σ_E is the beam energy uncertainty, evaluated at an average of 3% over all beam energies as communicated by the facility, and σ_{fit} is the error on the least squares fit of the calibration curve.

Although the interpolated data points based on Eqn. 9.2 matches well the measured data, the caveats previously mentioned pertain to the energy regime the Timepix3 detector is measuring in (described in detail in section 8.1.4). In particular, at these high energy depositions, the detector can already suffer saturation effects with no data point lying in the nominal (regular) regime, which based on literature is at about 600 keV per pixel [22]. To be noted is that not all the pixels in the cluster would be saturated, but just those in the centre of the cluster. Moreover, this hypothesis was also supported by the large value for the threshold, namely 88 keV, as it is known that the Timepix3 detector can detect deposited energies down to about 10 keV. For these considerations, another test campaign that could potentially solve all these issues was planned and executed, described later on in section 9.2.

Table 9.3: Calibration table for the ^{241}Am source with α particles, containing both the measured (ToT and N) and the FLUKA simulated data (E_{dep}).

d	ToT	N	E_{dep}
[mm]	[25 ns]	[pixels]	[MeV]
12	3013 ± 339	23.0 ± 4.2	3.195 ± 0.069
16	2786 ± 318	21.9 ± 3.1	2.679 ± 0.072
20	2310 ± 359	19.0 ± 2.6	2.093 ± 0.077
22	2089 ± 316	4.1 ± 2.3	1.761 ± 0.082

9.1.4.2 ^{60}Co - γ lines

On the lower part of the energy deposition spectrum, the ^{60}Co γ-source leads to smaller ToT compared to the ^{241}Am α-source. From fig. 9.5, one can see that the total photon cross section increases with decreasing energy below the gamma lines of the ^{60}Co source at 1.1732 and 1.3325 MeV. Although the Landau distribution (described in appendix 3) is meant to describe the ionizing energy loss for the charged particles, the energy distribution for photons also exhibit a similar

behaviour pattern. Similarly, a FLUKA simulation was setup using as the particle source an ^{60}Co isotope, with an isotropic angular distribution.

The gamma attenuation in air is almost negligible over lengths of several centimeters, as for this test. Placing the source at the three different distances of 11, 20 and 30 mm reveals a minuscule shift in the fitted energy peaks for both the measured and FLUKA simulated data, shown in fig. 9.9, revealing a minor increase in the deposited energy with increasing distance, opposite to the case of the α particles, but as expected from the total interaction cross section in fig. 9.5. However, the relative standard deviations for the deposited energy distributions are significantly larger. Due to these considerations, even though the energy deposits would be within the normal (regular) regime of the Timepix3 detector, the proximity of the 3 points to each other render their usefulness for calibration purposes as insignificant, as shown in fig. 9.10.

Table 9.4: Calibration table for the ^{60}Co source with γ particles, containing both the measured (ToT and N) and the FLUKA simulated data (E_{dep}).

d	ToT	N	E_{dep}
[mm]	[25 ns]	[pixels]	[MeV]
11	90 ± 105	3.99 ± 0.87	63.3 ± 39
20	103 ± 102	3.98 ± 0.84	68.3 ± 40
30	114 ± 104	4.06 ± 0.87	70.1 ± 41

9.1.4.3 Pile-up

The collected data servers multiple purposes, not just for calibration, but also to better understand the behaviour of the Timepix3 radiation monitor. In situations with a high count rate, the question of pile-up could arise, for which plotting 2D histogram with the deposited energy in units of ToT [25 ns] and the cluster size in pixels as is shown in fig. 9.11 is useful to discriminate between different types of pile-up. The first dominant peak corresponds to the fitted peak in the data analysis section above, while the second scattered peak are the double pile-up clusters. It is interesting to note that they consist of double the
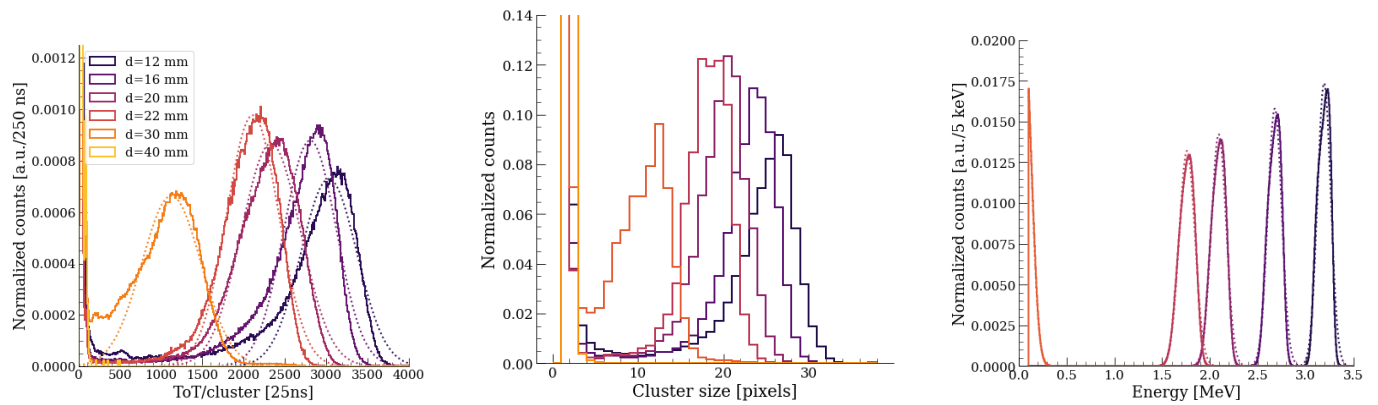
Figure 9.7: Measured data for the ^{241}Am source at various distances from the detector, and fitted using Gaussian functions, showing the (**left**) time over threshold (ToT) and (**centre**) cluster sizes distribution, and (**right**) simulated data using FLUKA.
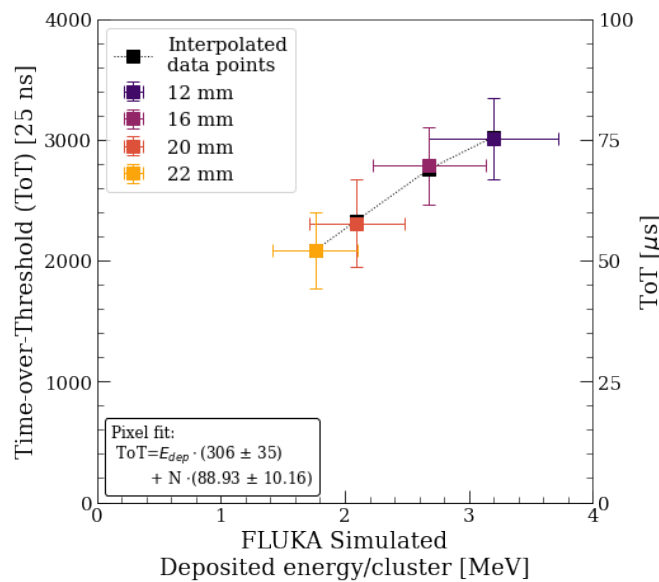
Figure 9.8: Energy calibration of the Timepix3 radiation monitor for the ^{241}Am source at CALLAB with α particles up to 3.2 MeV.

amount of pixels and peak around at double the expected deposited energy, implying that the pile-up is due to an artefact of the clustering algorithm, and not a physical pile-up in the Timepix3 detector, which would correspond to N times the peak energy, but with the same number of pixels in the cluster.

9.1.5 Test campaign summary

The test campaign is considered to have been a good first experience with the Timepix3 radiation monitor setup, in the CERN RP in-house calibration laboratory (CALLAB) facility. The operational settings of the setup have been tested and familiarity with the setup was achieved. Several data points for energy calibration have been collected using the detector, however they could already be part of the saturation regime, and not in the regular (normal) operation for the detector, since their energy deposition is in the MeV regime. In the absence of a cleaner signal in the keV regime, one cannot fully rely on this calibration alone. Moreover, more questions regarding the characterisation of the setup arose during the data analysis, not just pertaining to the calibration, but also to the more general detector manufacturing and response. In particular, a known manufacturing defect is the dead layer on top of the detector, which could potentially impact the calibration efforts for particles with high linear energy transfer (LET), typically at low energies. In order to fully address these concerns, another test campaign with more suitable beam energies and conditions has been executed.
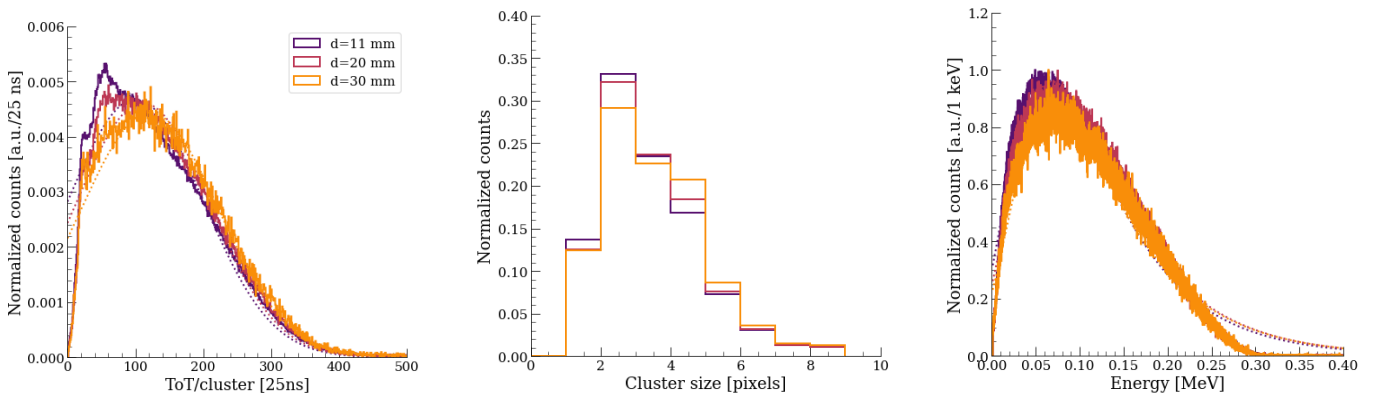
Figure 9.9: Same as fig. 9.7, but for the ^{60}Co source.
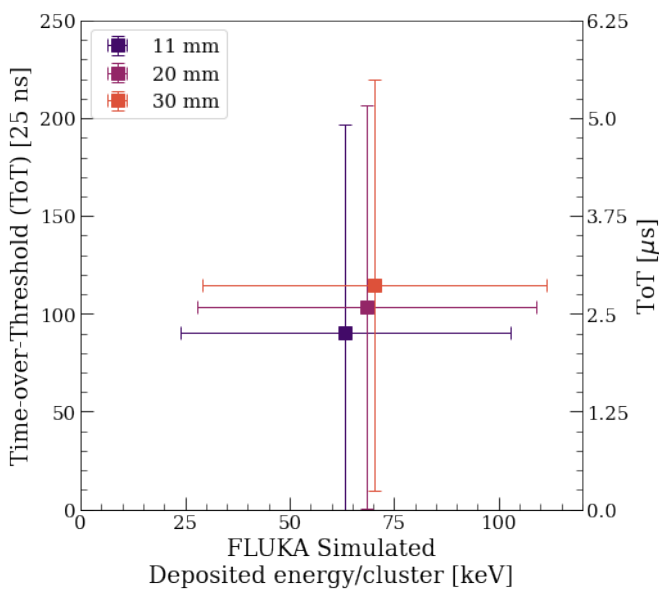
Figure 9.10: Energy calibration of the Timepix3 radiation monitor for the ^{60}Co source with γ particles.

9.2 CNA: protons and alphas from 0.6 to 8.4 MeV

9.2.1 Introduction

An experimental campaign dedicated to the calibration of the CERN Timepix3 radiation monitor was carried out using monoenergetic proton (alpha) beams ranging from 0.6 (1) to 5 (8.4) MeV at the centro nacional de aceleradores (CNA) particle accelerator
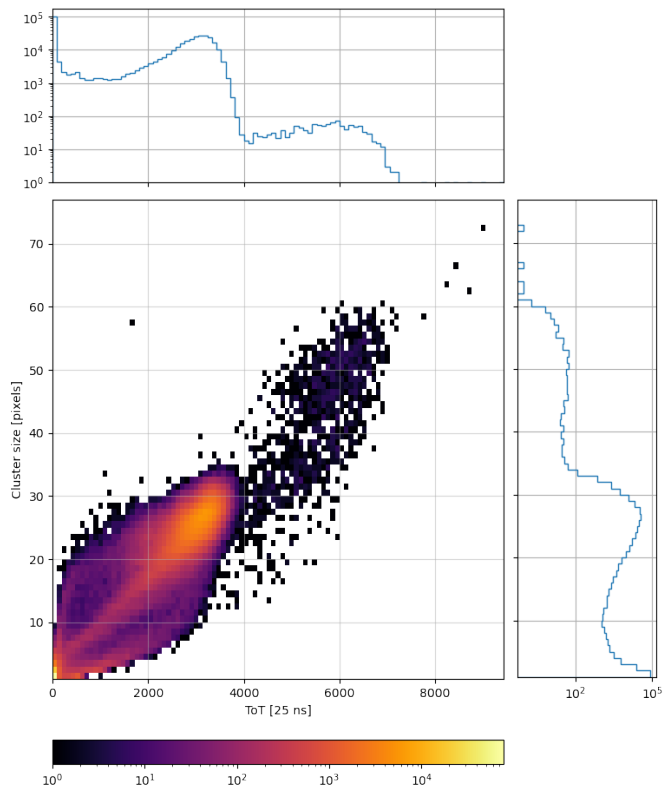
Figure 9.11: 2D histogram with the deposited energy in units of ToT [25 ns] and the cluster size in pixels for the ^{241}Am, at a distance of $d = 12$ mm.

facility [209, 210]. The measurements included the estimation of the thickness of the dead layer in front of the Timepix module, obtained by performing an irradiation scan of the setup with 0.6 MeV protons at

an angle ranging from 0° up to 45°. The results of the test campaign are described, starting with the morphological filters applied on the raw data to clean the signal from any significant background, particularly relevant for the high energy alphas. The selection relies on shape-based cluster parameters, such as cluster radius and density. Subsequently, the cluster-level calibration is presented, as well as the distributions of ToT and cluster size for both proton and alpha beams at different energies. The results of the angular scan for the dead layer estimation are also discussed, along with an investigation of possible pile-up events and a preliminary analysis of the differences between clusters induced by protons and alpha particles.

The goal of the work presented in this section was to characterize the Timepix3 radiation monitor, obtaining a pixel-level calibration curve from ToT to deposited energy using high energy hadron beams, as well as gaining in-house expertise in the operation of the setup to understand its capabilities and limitations. The calibration campaign was carried out by irradiating the detector with quasi-mono energetic ion beams at the centro nacional de aceleradores (CNA) [211, 212]. The campaign was performed using 0.6–5 MeV protons and 1–5.6 MeV alphas, a subset of the energy range at this facility. At these energies, all particles stop within the depleted layer of the 300 μm Timepix3 silicon sensor. For the calibration, the effective deposited energy in the active layer of the sensor was derived as the difference between the beam energy and the energy lost in the following two thin layers in front of it: an aluminium metalisation layer of known thickness, and a dead layer of unknown thickness. In addition, to measure the thickness of the front dead layer, an angular scan was performed using 597 keV protons, studying the variation in the effective energy deposited in the sensor. The experimental setup and the calibration procedure, including the dead layer estimation method, are the subject of the next paragraphs.

9.2.2 Facility description

The test campaign was performed at the Van der Graaf 3 megavolts (MV) Tandem accelerator at CNA, providing quasi-mono energetic protons (alphas) at various energies from 0.6 (1) to 5 (8.4) MeV with an energy spread $\Delta E_{beam} < 3\%$. The full detector module was placed on the specific sample holder into the irradiation vacuum chamber (at a pressure of the order of 10^{-6} mbar). The Timepix3 radiation monitor was masked when the spot beam was focused to set each experimental configuration (i.e., beam energy and flux).

At the present time, the CNA 3 MV tandem facility has six available beam lines to characterize and to modify materials, as well as for nuclear physics research. The test campaign was performed on the +15° beam line: irradiation chamber. This home-made scattering chamber has been designed to allow the irradiation of large areas by raster scanning of the beam through magnetic deflection [213]. On this beamline, on the first portable support, a cubic assembly and the beam scanning system are placed. The cube accommodates two main elements: (i) a 45° pentaprism, which allows to better check the device under test (DUT) position, and (ii) a variable graphite slit which defines the beam size (usually they are selected to obtain a 1 cm^2 beam spot size). For large areas, the special shape of this piece avoids the undesirable production of radiation coming from the collision of the beam with the pipe walls. For the purpose of sweeping uniformly the beam over the sample surface, a magnetic beam scanning system is in place, which consists of two magnets for horizontal and vertical scanning.

A scintillator is used for live flux monitoring in the irradiation chamber. It is based on a sample holder assembly biased at 200-300 V, with an aluminum variable slit in front, and it is electrically insulated from the rest of the line. This assembly collects the secondary electrons and is connected to a current integrator with the purpose of monitoring the flux in a Faraday Cup configuration. The lower limit of this instrument for a reliable current measurement is roughly 50 pA, translating to a minimum flux of

10^6 particles/(cm^2·s). Nevertheless, the facility can provide lower fluxes, but without the live monitoring of the delivered flux. These lower fluxes were previously measured and calibrated with a different instrument [214], not used in this test campaign.

In addition, the raster scanning system was used to spread the beam over larger areas, thereby reducing the local flux. Although this is limited by the sample holder dimensions (16×20 cm^2), depending on the beam features the full range can be further increased. The raster scan is selected as a uniform diamond, shape defined by the type of installed slits, with a 1 cm side, chosen as the optimum parameter for the scan system. When the intensity decreases below the scintillator threshold, one loses the instantaneous information about the raster scan, but the total field of 1 cm × 1 cm is maintained, as is confirmed by the raw detector results in fig. 9.12.

For the Timepix3 campaign, it was requested to use a particle flux below the lower limit of the scintillator, to avoid pile-up events in the physical detector and in the clustering algorithm. During the campaign, a local flux density of around 10^4 particles/(cm^2·s) was typically used, but it was also decreased for some runs down to 10^2 particles/(cm^2·s). In these conditions, no live flux monitoring is provided by the facility. When the entire beam is aimed at the detector, the measured (cluster reconstructed) particle count rate in fig. 9.13 (left) reveals plateaus at 10^4 particles/(s cm^2), as requested. Moreover, one can observe valleys in the measured count rate, corresponding to the raster scan: the frequency of the magnets can be adjusted, so that the beam can be tuned to cover the same route every 20 seconds, guaranteeing the homogeneity of the raster scan.

Table 9.5: Timepix3 radiation monitor operational parameters at the CNA test campaign.

Parameter	value
Bias voltage [V]	50
Panda GUI firmware version	3.18.0

The main Timepix3 operational parameters summarised in tab. 9.5, while the geometry of the Timepix3

radiation monitor detector is shown in fig. 9.14, along with a sketch of the experimental signature of an incoming charged particle at an angle θ releasing charge carriers before stopping. The module presents a first aluminium metalisation layer on top, with a known thickness of $T_{Al} = 500$ nm, followed by a silicon dead layer of an unknown thickness T_{DL}. Beyond this, due to the partial depletion of the sensor, the active region does not consist of the entire $D = 300$ μm sensor thickness, but only a partial thickness $W = 250$ μm. While the thickness W depends on the bias voltage and can be calculated, as is performed for the detector under exam, the dead layer is usually unknown due to intellectual property rights of the manufacturing process. A measurement of the dead layer was obtained by performing an angular scan of the deposited energy with a 597 keV proton beam, as further described in the next paragraphs.

Figure 9.15 presents the data of proton and alpha range and stopping power in silicon, as extracted from the national institute of standards and technology (NIST) database [206]. Notably, the range of alphas is shorter than the one of protons for the same kinetic energy due to the higher mass. All alpha beams used during the test campaign are hence expected to fully stop within the active layer of the sensor. For protons, assuming an orthogonal incidence on the pixel ($\theta = 0°$), the beam range approaches the thickness W of the active layer when the beam energy is around 5 MeV; beyond this, protons are expected to deposit a significant portion of energy in a non-depleted layer of silicon, or even to pass through the entire pixel thickness without stopping.

9.2.3 Energy calibration and dead layer estimation strategy

As already discussed, the main scope of the test campaign is to obtain the cluster-level curve of ToT as a function of the deposited energy in the Timepix3 module by performing irradiations with quasi-monoenergetic beams directed orthogonally on the sensor (i.e., as shown in fig. 9.14, with $\theta = 0°$) and stopping within its active layer. For both protons and alphas and for each beam energy, the energy de-
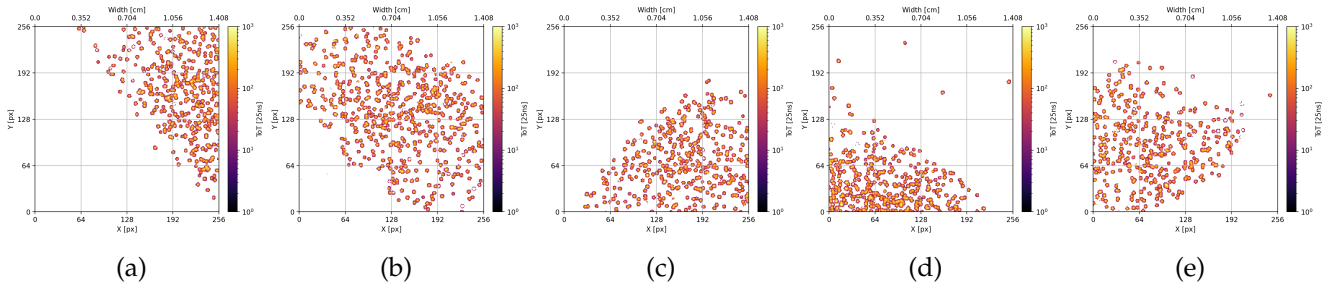
Figure 9.12: Raw particle hits on the Timepix3 radiation monitor, confirming the raster scan procedure inside the irradiation chamber.
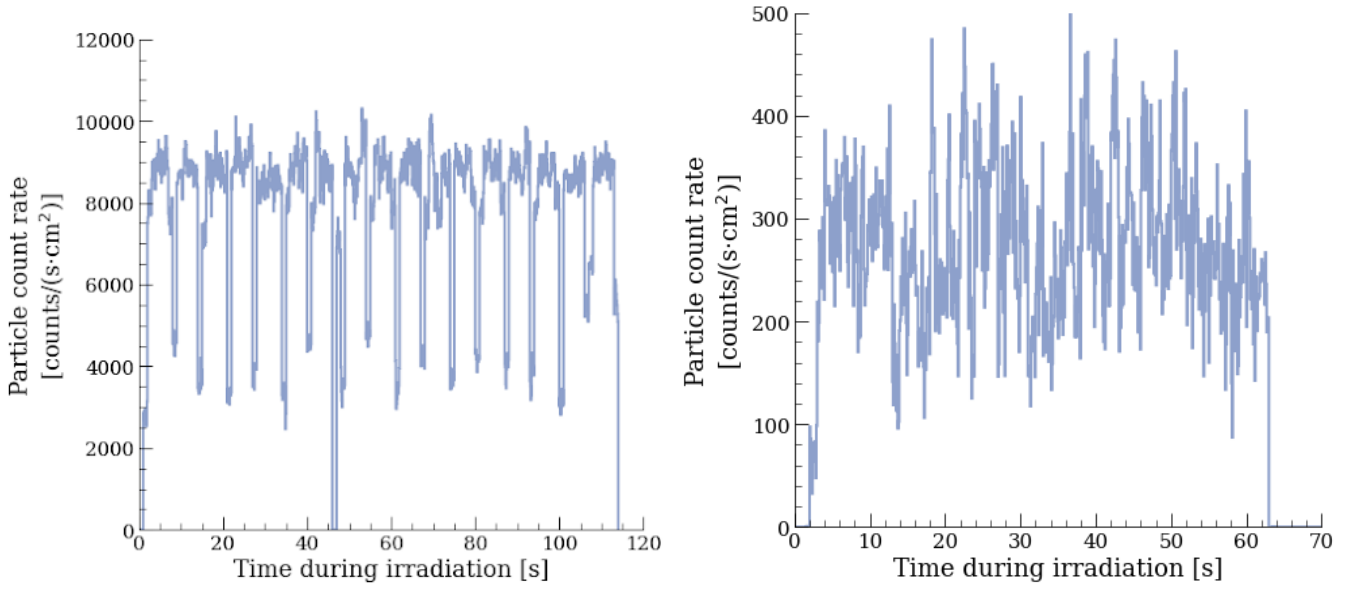
Figure 9.13: Timepix3 radiation monitor measured particle count rate, **(left)** confirming the requested beam intensity of 10^4 particles/(s cm^2) for alpha particles at 1 MeV, and **(right)** the lowest requested flux for protons at 3 MeV.

posited in the active layer of the sensor is effectively given by the difference between the incoming beam energy E_0 and the energy lost in the front layers as follows:

$$
\begin{aligned}
E_{dep,eff}(E_0) = &E_0 \\
&-E_{dep,Al}(E_0, T_{Al}) \\
&-E_{dep,DL}(E_0 - E_{dep,Al}, T_{DL})
\end{aligned} \quad (9.3)
$$

Both front layers are thin, with $T_{Al} = 500$ nm and T_{DL} (to be evaluated as part of the test campaign)

expected to be at a similar scale, but the fraction of energy that they absorb can be significant, especially for particles with very short penetration depth like alphas (e.g., at 1 MeV, their penetration depth is just 4 μm). The irradiation is performed under vacuum, and thus it is assumed that the beam particle reaches the detector front at its nominal energy $E_0 = E_{beam}$.

The energy deposited in each layer is calculated via Monte Carlo simulations performed with FLUKA, and presented numerically in the results section. The source was considered to be a planar wave with
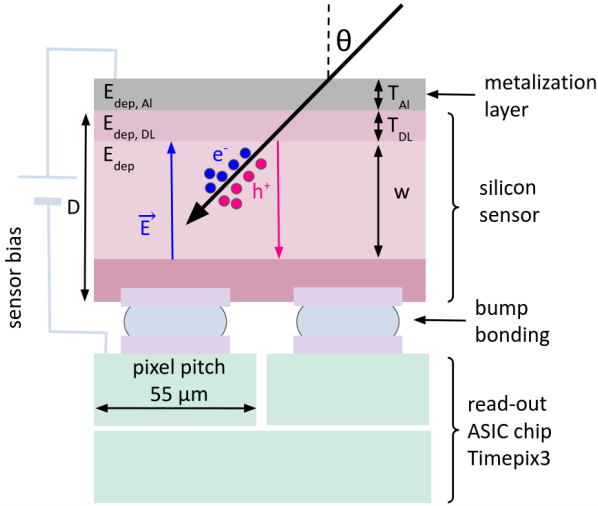
Figure 9.14: Timepix3 detector geometry (not to scale), with a known 500 nm aluminum metalization layer and an unknown dead layer on top, as well as the depletion layer $W = 250\,\mu m$ smaller than the detector thickness $D = 300\,\mu m$.
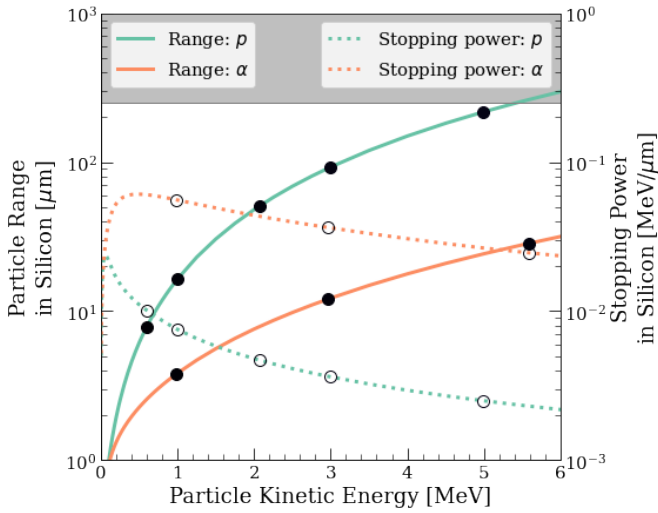
Figure 9.15: Proton and alpha particles range and stopping power in silicon in the energy range of the 3 MV Tandem accelerator at CNA. Data taken from ref. [206]. The horizontal gray area starts at 250 μm, indicating the depletion region thickness.

an energy distribution full width at half maximum (FHWM) of at most 3% (as communicated by the facility), leading to almost delta-peak energy distributions since the particles for all the beam energies

stop within the detector. Given the energy scale of the campaign, the lowest energy thresholds are used (PRECISIOn FLUKA default). It is characterized by particles transport thresholds at 100 keV for hadrons (except for neutrons at 10^{-5} eV), and lowered threshold for the electromagnetic components as follows: electron/positrons at 1 keV and gammas at 100 eV. Moreover, given the small Timepix3 detector geometry, in particular the non-sensitive layers at the sub-micron level, the typical condensed history/multiple Coulomb scattering approach (used in Monte Carlo codes for computational efficiency) has been disabled, thereby allowing the (more computationally expensive) single Coulomb scattering (via the use of the MULSOPT card).

The measurement of the thickness of the silicon dead layer T_{DL} represents a crucial part of the calibration campaign, and it is obtained by irradiating the sensor with a fixed beam type and energy (597 keV protons) at different angles of incidence (from $\theta = 0°$ to $\theta = 45°$). Under the well-justified assumption that the average energy deposited by the through-going particles in the front layers $E_{dep,front}(E_0, d)$ depends only on the particle energy E_0 and on the path length d, from simple geometrical considerations the energy lost in the front layers at different angles can be expressed as $E_{dep,front}(E_0, T/\cos\theta)$, where T is the thickness of the layer under exam. Since the particle stops in the depleted layer, one can express the effective energy deposited $E_{dep,eff}(E_0, \theta)$ by adapting eqn. 9.3 for an angular irradiation as:

$$
\begin{aligned}
E_{dep,eff}(E_0, \theta) = E_0 \\
- E_{dep,Al}(E_0, T_{Al}/\cos\theta) \\
- E_{dep,DL}(E_0 - E_{dep,Al}, T_{DL}/\cos\theta) \quad (9.4)
\end{aligned}
$$

where the dependency of $E_{dep,eff}$ from θ is solely due to the different fraction of beam energy lost in the front layers, as the particles are then stopping within the active sensor layer regardless of the incident angle. By assuming a constant stopping power dE/dx both in the aluminium metalisation and the silicon dead layer (i.e., for a small stopping power gradi-

ent in these thin layers at these energies)[1], eqn. (9.4) becomes the following:

$$E_{dep,eff}(\theta, T_{DL}) = E_0 - \underbrace{\left(\left.\frac{dE}{dx}\right|_{Al} (E_0) \cdot T_{Al} + \left.\frac{dE}{dx}\right|_{Si} (E') \cdot T_{DL} \right)}_{\text{slope } m} \cdot \frac{1}{\cos\theta} \quad (9.5)$$

where $E' = E_0 - E_{dep,Al}$. Finally, by irradiating the detector at several angles and plotting the deposited energy $E_{dep,eff}$ vs. $1/cos\theta$, one can extract the slope m, from which the dead later thickness can be obtained as follows:

$$T_{DL} = \frac{m - E_{dep,Al}(\theta = 0^\circ)}{dE/dx|_{Si}(E')} \quad (9.6)$$

It is clear that the procedure to compute the dead layer thickness T_{DL} via eqn. (9.6) requires a valid calibration of the Timepix3 radiation monitor. In turn, the final calibration can only be obtained by a proper evaluation of the energy lost in the dead layer, requiring the value of T_{DL} as an input. The solution to this puzzle is to set up an iterative process, where a first preliminary calibration of the sensor is derived by assuming $T_{DL} = 0\,\mu m$, and is used to obtain an estimate of T_{DL}. The latter value is then used to update the sensor calibration, iterating the process until both quantities converge to a stable result.

9.2.4 Data analysis

The calibration of the Timepix3 radiation monitor is obtained by irradiating the sensor with mono-energetic protons from 0.6 MeV to 5 MeV and alphas

---

[1]The numerical values and the related level of approximation are presented as follows: the proton stopping power at $E_0 = 0.6\,\text{MeV}$ is $dE/dx|_{Al} = 48\,\text{keV}/\mu m$ in aluminium [206], leading to an energy deposition in the $T_{Al} = 0.5\,\mu m$ thick aluminium layer varying from $E_{dep,Al}(\theta = 0^\circ) = 31\,\text{keV}$ to $E_{dep,Al}(\theta = 45^\circ) = E_{dep,Al}(\theta = 0^\circ)/\cos 45^\circ = 44\,\text{keV}$. At this lowered energy of $E' = E_0 - E_{dep,Al}(\theta) = 565\,\text{keV}$, the stopping power at the end of the aluminium layer increases by 4.8%. Similar values are obtained for silicon

from 1 MeV to 5.6 MeV. For the beam energies explored in this work, both protons and alphas are expected to stop within the active portion of the sensor, and thereby deposit all their kinetic energy into the depletion region (estimated at $W = 250\,\mu m$, for a bias voltage of $V_{bias} = 50\,\text{V}$), with the exception of the fraction lost in the front layers. Numerically, the penetration depth of all these beams in silicon varies from 8 μm to 200 μm, while alpha particles have a shorter range (typically one order of magnitude lower compared to protons at the same energy).

The next paragraphs present the full results of the experimental campaign, starting from the event selection and cluster reconstruction (section 9.2.4.1), and continuing with the key quantities measured during the irradiations at different energies (section 9.2.4.2). The calibration of the Timepix3 radiation monitor is then iteratively derived in section 9.2.4.3, taking into account the front dead layer, which is also experimentally determined by irradiations at an angle with 597 keV protons. Finally, the observed difference in the saturation levels between protons and alphas is explained.

9.2.4.1 Event selection and cluster parameters

The first step of the analysis of data from the Timepix3 radiation monitor irradiations is the pixel clustering procedure described in section 8.1.2, aimed at identifying the results of single-particle hits. Secondly, several parameters are computed for each cluster, in particular, the cluster ToT volume, given by the sum of the individual pixel ToT values, used for calibration purposes. The cluster shapes are analyzed to define morphological parameters that could allow to distinguish the signal from the background, taking advantage of the information about the experimental test setup (namely, perpendicular irradiation for calibration purposes), as well as the beam particles species (hadrons, leaving round blobs inside the detector, as compared to wiggly lines in the case of electrons).

Before the calibration can be carried out, it is beneficial to define a cluster filtering method to ensure

that the clusters from single-particle hits are fully reconstructed and isolated protons, hence removing partially reconstructed clusters and/or pileup events from the analysis. The filtering approach used in this paper is based on the definition of geometric cluster properties [194] described in section 8.3.1.

Figure 9.16 shows the distributions of cluster size, radius, and density parameters, as obtained from the clustered data of 3 MeV protons at CNA. From these quantities, one can define appropriate selections to identify just the nominal clusters, i.e., those corresponding to fully reconstructed single beam particle hits. For instance, by applying a selection on the cluster density (set to $\rho > 0.6$ for all beam energies), one can filter out partially reconstructed clusters or non-hadronic particle species (background), as well as occasional pileup events leading to partially or fully overlapping clusters. By applying an additional cut on the cluster radius (for 3 MeV protons, $3 < R < 4$), one can further remove the lower energy fragments from the clustering.

To assess the performance of the clustering algorithm and the subsequent data filtering procedure, it is helpful to analyse the 2D graphs of the clusters' total ToT volume against the number of pixels (cluster area) before and after the filtering, as shown in fig. 9.17 for 3 MeV protons. For all beam energies, already before the filtering, a central peak is clearly visible, which can be attributed to clusters from single particle hits. Nevertheless, additional clusters are reconstructed, either with a lower cluster size and ToT volume or with higher values of both quantities. Those clusters with a lower size and/or ToT with respect to the main peak are generally the result of partially reconstructed hits in the clustering algorithm or (less likely) interactions of secondary particles. While the fraction of mis-reconstructed clusters tends to increase for higher beam energies, the filtering procedure has proved to be very efficient in removing them, hence providing a clean data set of well-reconstructed clusters for the calibration analysis. On the other end, dedicated analysis on the clusters with higher ToT volume and size than the main peak has shown that they originate from two (or more) closeby particle hits, resulting in two touching clusters that are reconstructed as a single one by the algorithm, denoted here as clustering pile-up. A physical pile-up in the detector, on the other hand (i.e., a second particle hitting the same pixel before reading the signal of the primary particle), would correspond in such a display to a region of twice the ToT with roughly the same number of pixels per cluster. As evident from fig. 9.17, there are no such events for the measured flux rates.

9.2.4.2 Proton and alpha cluster measurements

Following the cluster reconstruction and selection process described in the previous section, it is important to examine the key properties of the clusters measured by the Timepix3 radiation monitor during the CNA campaign, for all particle types and beam energies with which it was irradiated.

As a first step, fig. 9.18 illustrates the average shape and the 2D ToT profile of clusters originating from protons and alphas with different energies directed orthogonally on the sensor (i.e., beams for which the angle θ in fig. 9.14 is 0°). The clusters have been aligned according to their reconstructed centre of gravity, and the value of the ToT in each pixel represents the average over millions of individual clusters, excluding all pixels with an averaged ToT value below 1 DAC unit (25 ns), such that spurious reconstructed clusters are not unnecessarily emphasized. All clusters are consistently showing larger sizes at higher beam energies, as expected, and the cluster height (i.e., the largest pixel ToT of the cluster) is found in their centre for both protons and alphas at all energies. The latter observation is particularly relevant, because it means that the sensor is not exhibiting the known volcano effect described in the literature for very high energy depositions in Timepix3 detectors [180], where the pixels in the core of the clusters measure a lower ToT as a result of them falling in Regions E and F of the pixel-level calibration curve (as shown in fig. 8.4). Hence, while at this stage the analysis is only qualitative, the cluster shapes in fig. 9.18 are already indicating that any saturation effects occurring in the central pixels must not be
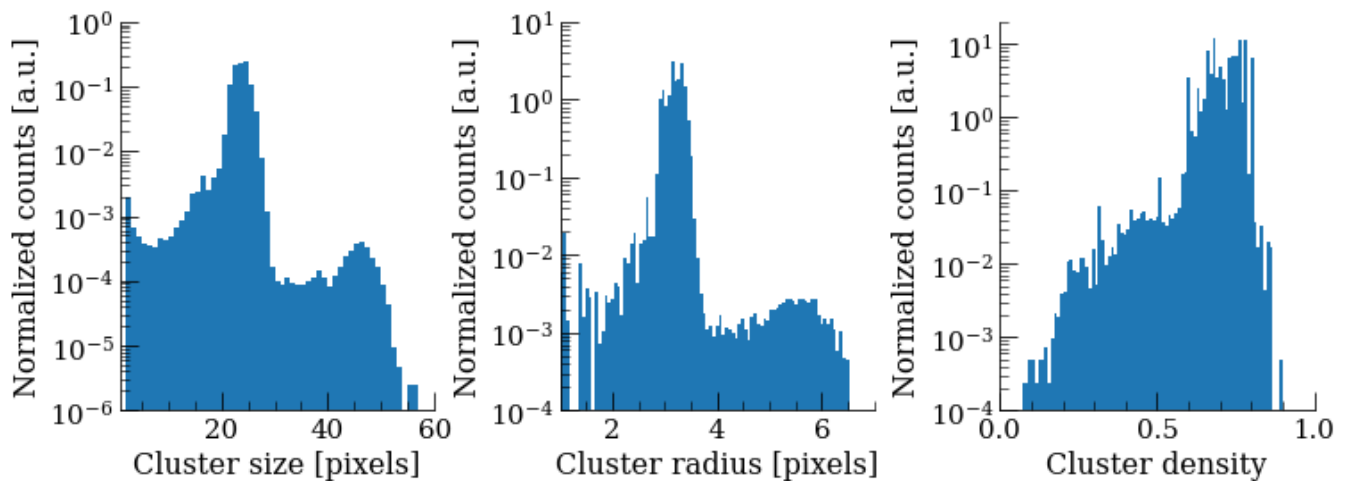
Figure 9.16: Cluster parameters for the 3 MeV protons at perpendicular irradiation.

exceeding (at least on average) Regions C and D of the above curve.

After having visualized the cluster shapes, fig. 9.19 presents the 1D distributions of the total ToT volume of the reconstructed clusters, obtained as the sum of the individual ToT of each pixel in the cluster (as previously shown in fig. 9.17), for all particle types and energies with which the Timepix3 radiation monitor is irradiated orthogonally. All ToT distributions appear as well-resolved peaks, with increasing distribution widths at higher energies, allowing us to fit them with Gaussian functions. The widening of the ToT peaks at high energies can indicate possible resolution effects and non-linearities in the calibration (i.e., saturation), likely in the pixels measuring the highest ToT inside the clusters. In particular, the shape of the ToT peak from 5 MeV protons is showing an extended tail on the low-ToT side, possibly indicating that a fraction of the protons are reaching the end of the sensitive volume and are thereby not depositing their entire energy in the sensor.

The discussion for the energy scan for alpha particles are split into two, those up to 6 MeV and those above, because of their different behaviour. One can observe clearly resolved peaks at 0.981, 2.966 and 5.59 MeV for the runs with alpha particles presented in fig. 9.19, while the runs at 7.458 and 8.405 MeV showcase a double-peak feature (in fact, the 5.59 MeV data point

as well, but the peaks are not clearly separated). Concerning the cluster size, all curves in fig. 9.19 show well-defined peaks, with the expected size increase for higher energies. This effect strongly suggests the presence of saturation effects in the central pixels of the cluster, where most of the deposited energy is lost.

Lastly, the distribution of cluster ToT volume of 597 keV protons is plotted again in fig. 9.20 (left), this time showing all the angles of incidence at which the Timepix3 radiation monitor was irradiated, ranging from 0° to 45°. These cluster ToT distributions are similar, but they can nevertheless be distinguished by fitting them with Gaussian functions, which reveal a slight decrease in the mean cluster ToT for larger angles. As anticipated, this angular sweep is necessary for the experimental estimation of the dead layer of the sensor, exploiting the fact that for larger angles, the protons are depositing a larger fraction of energy into it (proportionally to $1/\cos\theta$) before reaching the active volume. The choice of using the lowest available proton energy for the dead layer measurement is motivated by 8 μm proton range at this energy in silicon (as shown in fig. 9.15), which is comparable in size to the expected dead layer thickness (expected to be around 1 μm or smaller), such that the fraction of energy lost in the dead layer is non-negligible. In-
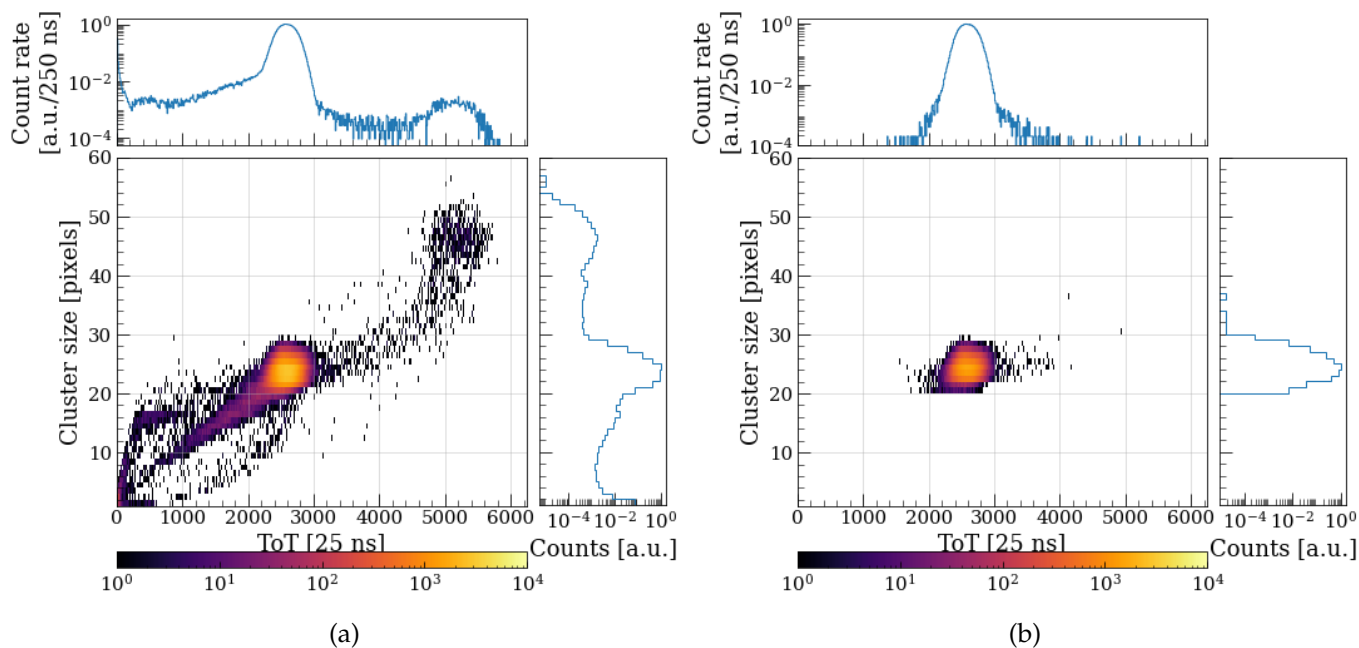
Figure 9.17: 2D plots of the cluster size against the total ToT per cluster, for protons at 3 MeV (**a**) without and (**b**) with applied filters: $\rho > 0.6$ and $3 < R < 4$.

deed, this is what ensures that the mean ToT values of the peaks in fig. 9.20 are well distinguishable.

As outlined in section 9.2.3, the dead layer estimation procedure requires the conversion of the mean ToT values of the above peaks into deposited energies using a pre-established calibration. The values are then plotted against the inverse of the cosine of the irradiation angle θ, as shown in fig. 9.20 (right). By performing a linear fit of this graph, it is then possible to obtain the values of the coefficients of eqn. 9.5 (notably the slope m), from which the value of the dead layer can be directly derived. Since this procedure requires a calibration, and in turn, the calibration requires the knowledge of the dead layer thickness, the two quantities are evaluated iteratively, as further outlined below.

9.2.4.3 Energy calibration and dead layer estimation

The cluster ToT volume data presented above serve as the basis for the Timepix3 radiation monitor calibration, obtained via the procedure outlined in sec-

tion 8.1.3, and supported by the estimation of the silicon front dead layer. Along with the ToT data, FLUKA simulations are employed to quantify the energy deposited E_{dep} in the sensor from a beam of particles E_0 via eqn. (9.3), such that one takes into account the energy lost in the aluminium metalisation layer, with a known thickness of 500 nm, and in the dead layer, with a thickness to be evaluated via the angular scan. As previously mentioned, the sensor calibration and the dead layer estimation have been obtained via an iterative process. The calibration is expressed via eqn. (8.6), where the parameters a and b are derived by performing a linear fit that uses only the four lowest energy data points (three for protons and one for alphas, up to 1 MeV) to ensure that the values are not affected by high-energy saturation effects. For all energies, a first calibration is derived by assuming that the thickness of the silicon dead layer is null. This first calibration result is used as an input to obtain a first evaluation of the dead layer, from the data of the angular scan and via eqn. (9.6). Subsequently, the calibration is recomputed using FLUKA simulations with the updated dead layer thickness, repeating the procedure until

(a) 0.62 MeV p

(b) 2 MeV p

(c) 5 MeV p

(d) 0.98 MeV α

(e) 3.0 MeV α

(f) 5.6 MeV α
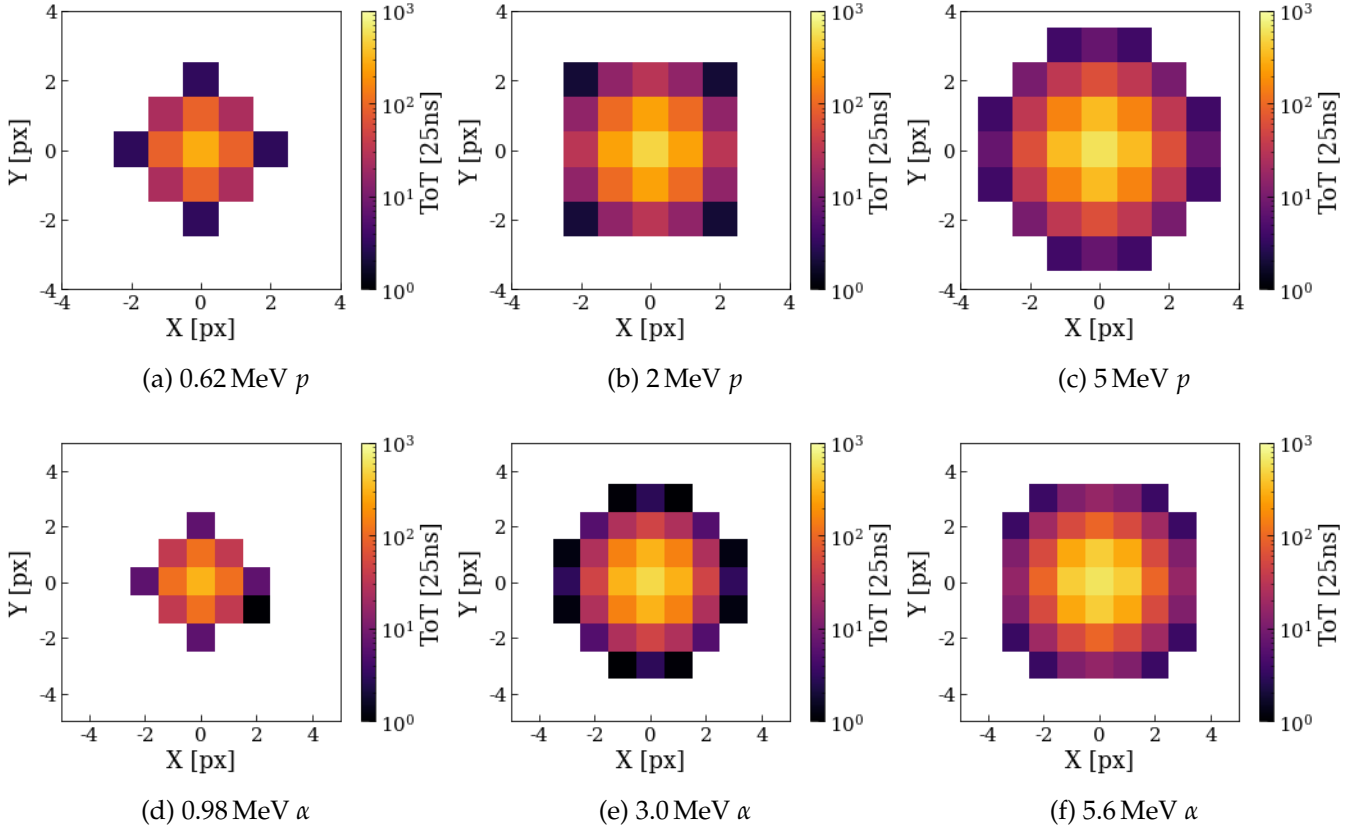
Figure 9.18: Average shapes of the clusters (averaged over millions of reconstructed clusters) for proton (**top row**) and alpha (**bottom row**) runs at different energies, with orthogonal incidence on the Timepix3 radiation monitor. Values below 1 ToT unit averaged over the entire data set are set to 0.

stable values of T_{DL}, a, and b are reached, after just six iterations, as shown in fig. 9.21.

At the end of the iterative process, the linear fit of E_{dep} as a function of $1/\cos\theta$ shown in fig. 9.20 is the following:

$$\frac{E_{dep}}{[\text{keV}]} = (598 \pm 68) - (51.5 \pm 5.8)\frac{1}{\cos\theta} \quad (9.7)$$

where the uncertainty on the fit parameters is included. Using eqn. (9.6), and considering a stopping power of $dE/dx|_{Si}(E_0 - E_{dep,Al}) = 56.45\,\text{MeV}/\mu\text{m}$ for 0.6 MeV protons in silicon (from [206]), the dead layer thickness is obtained as follows:

$$\frac{T_{DL}}{[\text{nm}]} = 333 \pm 38(\sigma_{fit}) \pm 17(\sigma_{dE/dx}) \pm 4(\sigma_\theta) \pm 1(\sigma_{ToT}) \quad (9.8)$$

which includes uncertainties associated to the fit parameters (σ_{fit}), the assumption of a constant stopping power ($\sigma_{dE/dx}$), for which a 5% error is considered (as described in section 9.2.3), the measurement of the angle (σ_θ, assuming a 1% accuracy on θ), and the error on the mean of the Guassian peaks in the measured ToT data (σ_{ToT}). The measured silicon dead layer of 333 nm is in line with the expectations, as other silicon detectors have dead layers of the order of 500 nm [215, 216].

For the above value of the silicon dead layer thickness, the FLUKA code is used to evaluate the de-
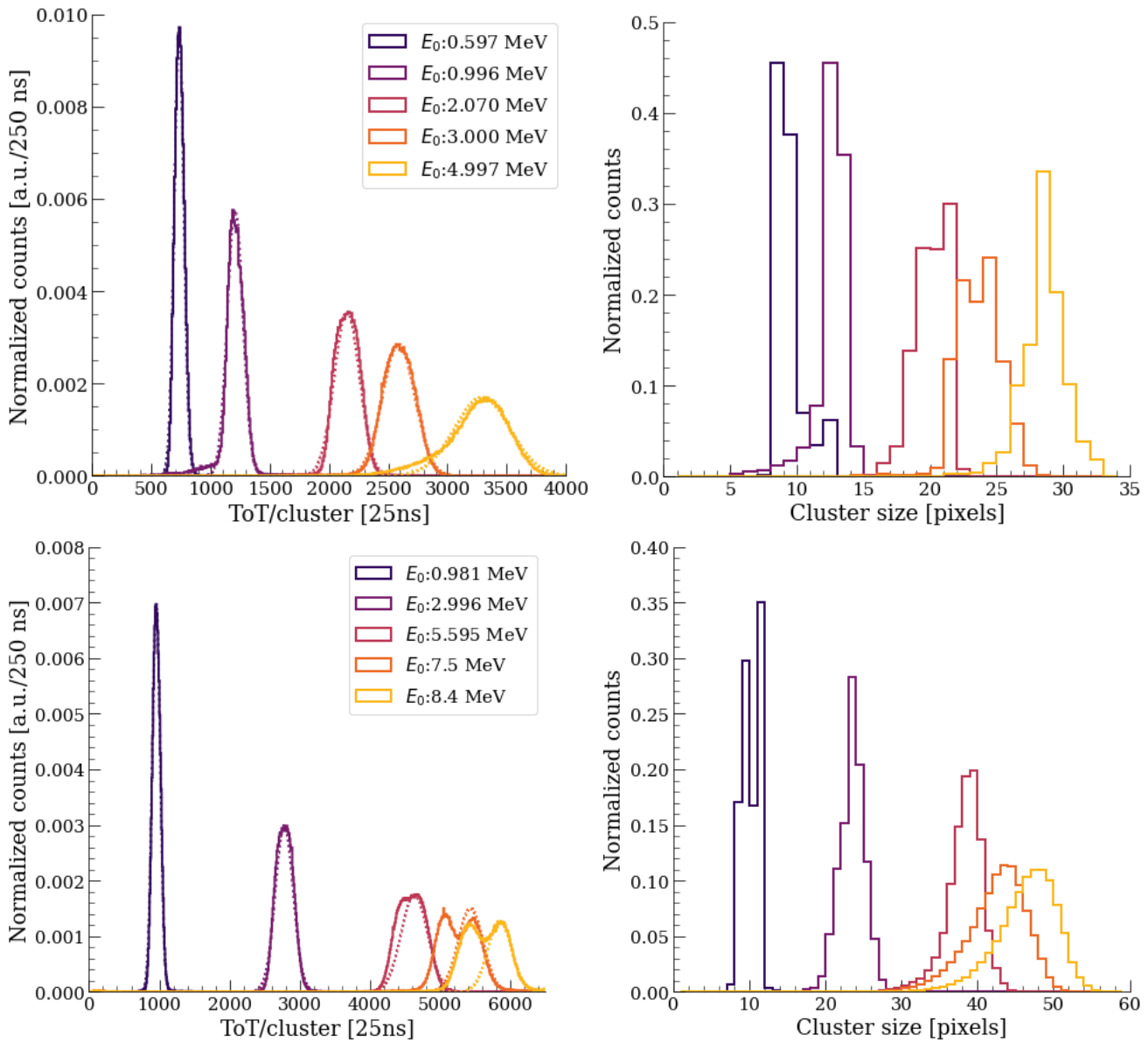
Figure 9.19: Timepix3 radiation monitor measurements for (**Top**) proton runs and (**Bottom**) alpha runs with orthogonal incidence and for different energies, displaying the distributions of total cluster ToT (**left**) and number of pixels (**right**) per cluster. The measured peaks (continuous lines) are fitted with Gaussian functions (dashed lines). For the 5.6 MeV and higher energy alphas, the right slope of the data has been fitted.

posited energies in each layer of the Timepix3 radiation monitor during the irradiations with orthogonal angle, as presented in Table 9.6 along with the measured average number of pixels per cluster N for each energy and particle type. The simulations indicate that alpha particles are losing a larger fraction of their energy in the front layers of the sensors (up to 23.3%) compared to protons with the same initial energy due to their higher stopping power. The cluster-level calibration is obtained by plotting the
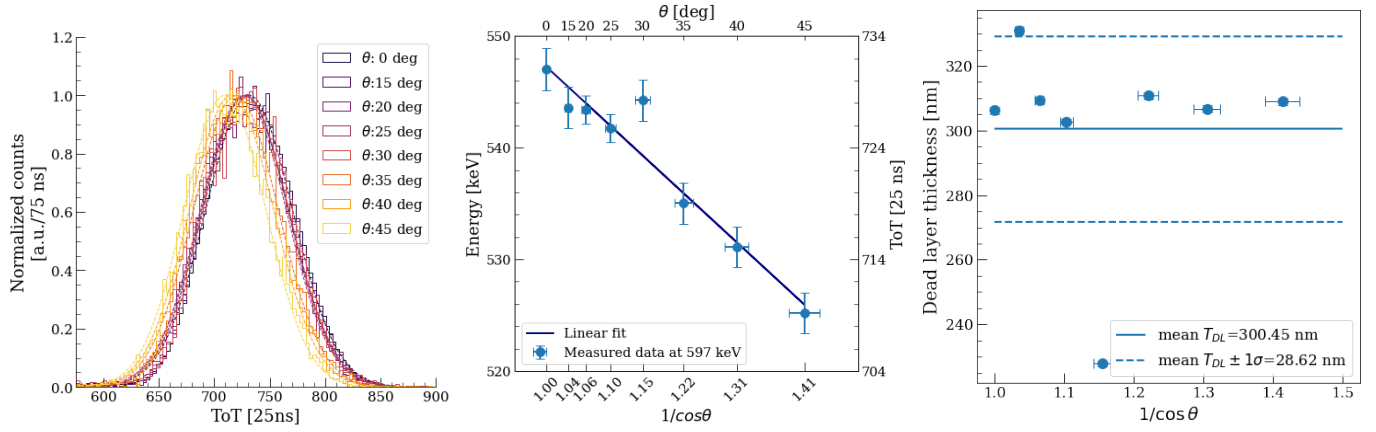
Figure 9.20: (**Left**) Timepix3 measurements for proton runs at 597 keV swiping through incident angles from 0° to 45°. The two methods for estimating the dead layer are shown: (**Centre**: Method 1) deposited energy variation that can be fitted with a straight line against the inverse of the irradiation angle cosine, and (**Right**: Method 2) the direct estimation procedure.

Table 9.6: Energy depositions E_{dep} simulated using FLUKA in each layer of the Timepix3 radiation monitor (500 nm aluminium metalisation layer, 333 nm front dead layer, and 250 μm active volume) for all beam energies E_{beam}, together with the total fraction of energy deposited in the front layers $\Delta E = (E_{beam} - E_{dep,eff})/E_{beam}$, as well as the measured average number of pixels per cluster.

Particle	E_{beam} [MeV]	$E_{dep,Al}$ [keV]	$E_{dep,DL}$ [keV]	$E_{dep,eff}$ [MeV]	ΔE [%]	No. Pixels
proton	0.597	32	19	0.543	9.2	8.2
	0.623	31	18	0.573	6.6	8.4
	0.996	23	14	0.954	6.3	11.1
	2.070	13	8	2.047	1.0	18.2
	3.000	9	5	2.978	0.6	21.9
	4.997	6	3	4.978	1.0	24.9
alpha	0.981	169	106	0.706	23.3	9.6
	2.966	111	62	2.795	10.2	22.5
	5.595	71	43	5.481	2.2	40.1
	7.46	61	36	7.31	2.0	43.2
	8.41	56	33	8.27	1.7	48.4

mean values of the cluster ToT (obtained by fitting the curves in fig. 9.19) as a function of the corresponding deposited energies in the active volume of the sensor (i.e., $E_{dep,eff}$ in the table), as illustrated in fig. 9.22. As saturation effects at high energy are clearly visible in the figure, the linear calibration fit based on eqn. (8.6) is performed using only the four lowest energy data points (i.e., those with beam energy up to 1 MeV) obtaining the following result:
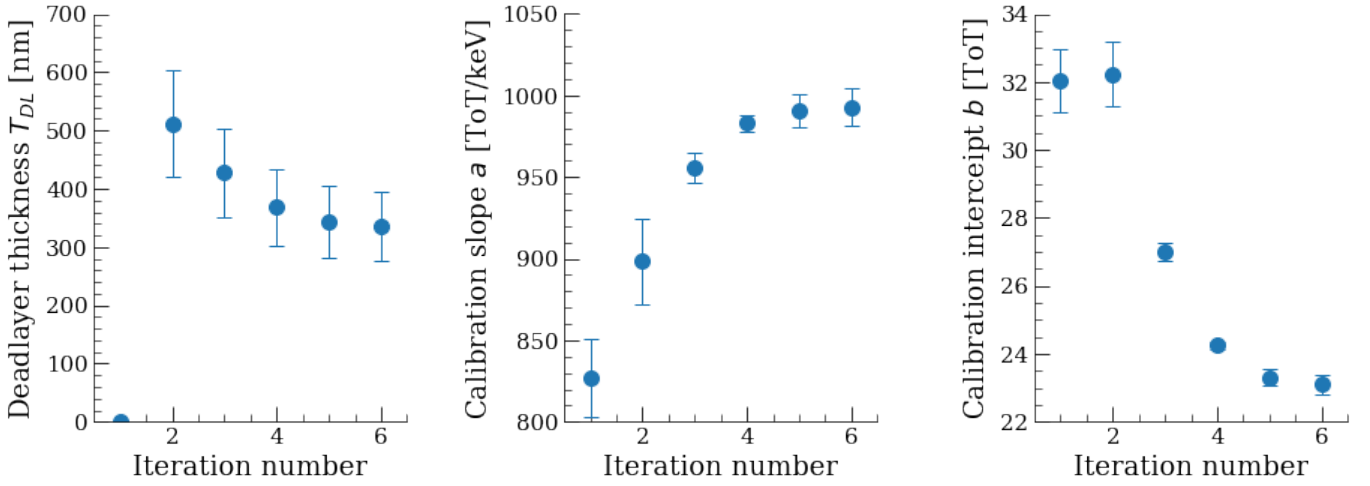
Figure 9.21: Values of the **(Left)** silicon dead layer thickness T_{DL}, and of the calibration parameters **(Centre)** a and **(Right)** b from eqn. (8.6), at each step of the iterative data analysis process employed for their evaluation.

$$ToT_{reg}(E_{dep}) =$$

$$E_{dep} \cdot \left[993 \pm 51(\sigma_{ToT}) \pm 30(\sigma_E) \pm 12(\sigma_{fit})\right] \left[\frac{25\,\text{ns}}{\text{MeV}}\right]$$

$$+N \cdot \left[23.1 \pm 1.2(\sigma_{ToT}) \pm 0.7(\sigma_E) \pm 0.3(\sigma_{fit})\right] \left[\frac{25\,\text{ns}}{\text{pixel}}\right]$$

$$(9.9)$$

where N is the cluster size (in pixels). The uncertainties are as follows: σ_{ToT} is the averaged $1 - \sigma$ of the measured ToT values per cluster for all the beam energies, σ_E is the beam energy uncertainty, evaluated at an average of 3% over all beam energies as communicated by the facility, and σ_{fit} is the error on the least squares fit of the calibration curve.

The interpolated cluster ToT volume as expected from eqn. (9.9) is included in fig. 9.22 for all energies, confirming the manifestation of saturation effects at high energies. The saturation is visible for all beam particles above 2 MeV, and more protons than for alphas, which is explored in the next section.

9.2.4.4 Saturation effects

To further explore the origin of the saturation, the distribution of the ToT per pixel is plotted in fig. 9.23
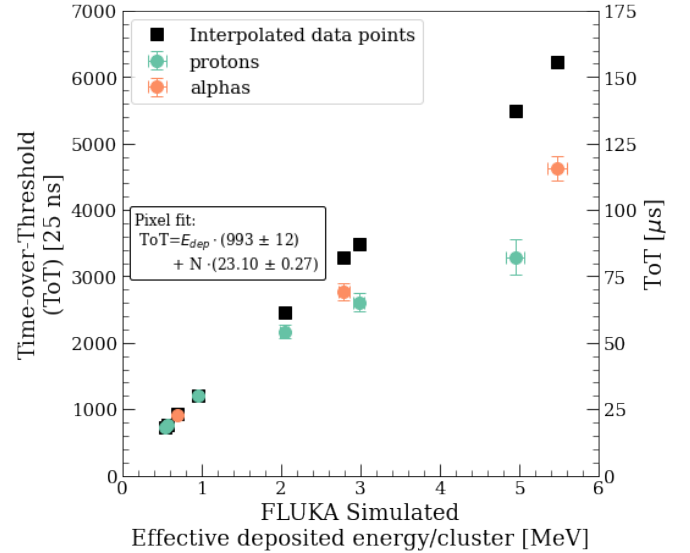
Figure 9.22: Energy calibration per cluster, with the cluster ToT volume plotted against the FLUKA simulated energy deposition in the active sensor, for protons (blue points) and alphas (red points). The interpolated data points (black squares) are computed according to eqn. (9.9), which takes into account the average number of pixels per cluster, taken from Table 9.6.

for all beam energies and particle types. Moreover, the data for alphas at 7.458 and 8.405 MeV are al-

most overlapping, possibly indicating the start of the very high-energy saturation (volcano effect) for some pixels. Nevertheless, their total reconstructed energy deposition per cluster is different (as shown in fig. 9.19), as the absolute number of pixels is larger.

For 2 MeV protons, which represent the lowest-energy beam for which a mild saturation is visible in fig. 9.22, the pixels with the highest ToT are measuring between 550 and 600 ToT [25 ns] units. The evidence of saturation effects with this beam indicates that such pixels are presumably already beyond the linear regime of the calibration (i.e., beyond Region B of fig. 8.4), and likely in the first energy range where saturation is exhibited (Region C). According to the measured calibration (eqn. (9.9)), a ToT range between 550 and 600 ToT [25 ns] units corresponds to a deposited energy of the order of 600 keV per pixel, which is rather consistent with the expectations, as the characteristic pixel-level saturation threshold found in the literature is of 850 keV [170].

Moreover, fig. 9.23 shows that a few pixels occasionally record high ToT values, beyond the edge of the main distributions, occasionally reaching the maximum digitally measurable ToT (1024 DAC units, given by the 10-bit registry), while these cases are very rare, they could indicate that such pixels have entered the parabolic calibration region (Region D in fig. 8.4). No evidence of pixels entering Region E and F of the same figure is observed, coherently with the absence of volcano effects in the cluster shapes in fig. 9.18.

Having found that saturation effects at pixel level begin between 500 and 600 ToT [25 ns] units, one can further analyze the broadened ToT volume peak observed in fig. 9.19 for 5.6 MeV alphas, which might actually represent two peaks as is the case for the 7.5 and 8.4 MeV. Following a method used in ref. [180], the graphs in fig. 9.24 present the breakdown of the distribution of the cluster ToT volume for the high energy alphas, divided into four categories based on the number of *hot* pixels that are exceeding a ToT threshold set to 565 [25 ns] units. Since one can assume with good approximation that all alphas are

depositing an equivalent amount of energy in the sensor, it is reasonable to associate these categories to a variable degree of charge sharing between the central pixels, linked to the position of the alpha particle hit within the seed pixel (where the particle has hit the sensor). In practice, when the hit occurs in the centre of a pixel, a larger fraction of the released charge remains within its boundaries, leading to a single hot pixel in the cluster, whereas if the hit occurs close to a pixel boundary, the charge sharing is enhanced, resulting in up to four hot pixels. As fig. 9.19 clearly shows that the distribution with only one hot pixel presents a lower mean cluster ToT compared to the others, it is fair to attribute the shift to a higher level of saturation in the central pixel, due to the higher fraction of alpha energy which is deposited into it. While this interpretation involves hypotheses that cannot be easily verified in the data, it provides interesting insights into the origin of the broadening of the cluster ToT peak of 5.6 MeV alphas, linking it directly to saturation effects.

Lastly, it is thorough to investigate why the level of saturation observed for protons in fig. 9.22 is larger than the one for alphas. As a first step, one can compare the cases of 3 MeV protons and 2.966 MeV alphas in Table 9.6, noting that despite a larger fraction of energy lost in the front layers (which results in less energy being measured by the sensor), the alphas result in slightly larger clusters (22.5 average pixels per cluster versus 21.9). An explanation of this feature stemming from the charge collection within the silicon detector is that the alpha hits lead to more charge sharing amongst pixels as opposed to protons with similar kinetic energy. This is presumably due to their different linear energy transfer (LET), leading to a different distribution of the energy deposition in the active volume of the sensor (visible in fig. 9.15), ultimately due to the different ranges in silicon. In turn, a difference in the amount of charge sharing determines the level of saturation at the pixel level, leading to the observed differences between proton and alpha runs.

To further verify this, the graph in fig. 9.25 presents the distribution of the time-of-arrival (ToA) of the pixel hits, measured with the fToA timing resolution
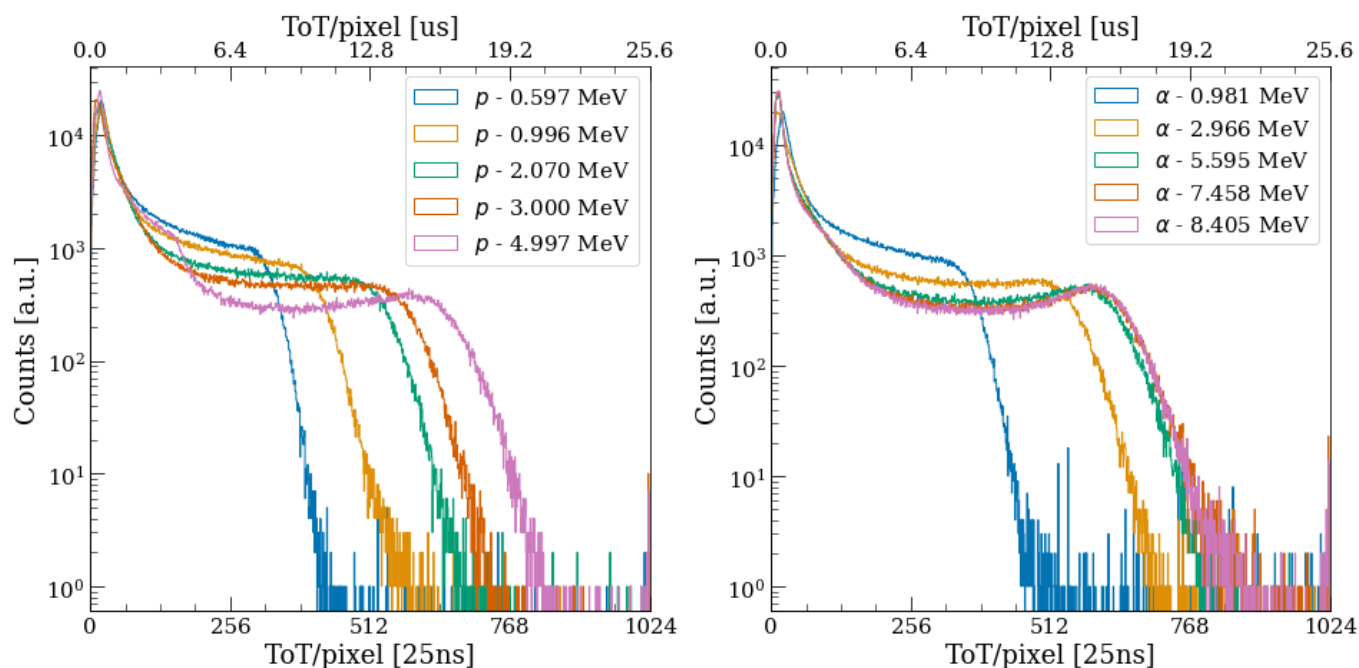
Figure 9.23: Measured distribution of pixel time over threshold (ToT) at different beam energies, for (**Left**) protons and (**Right**) alphas. The maximum ToT is given by the 10-bit registry as $2^{10} = 1024$ ToT units.

of 1.5625 ns, for clusters formed by 3 MeV protons and alphas (recalling that the actual energy deposited in the active volume is lower than the beam energy, especially for alphas, as shown in Table 9.6). Since most of the charge is deposited closer to the front layer (and further from the collection electrode) for alphas (due to the shorter range at the same energy) than for protons, the charge collection time is also larger. In turn, this prolonged time allows for more charge sharing to occur, which happens at a constant diffusion speed. Within the clusters, it is straightforward to associate larger amounts of charge sharing between pixels with a longer average amount of time taken by the charge to propagate to all pixels. Indeed, the average ToA of pixel hits in alpha clusters is larger compared to the case of proton clusters, fully confirming the above interpretation.

9.2.4.5 Compensation methods

Taking note of the several effects that occur during the measurements, these could be corrected for in the post-processing. Amongst the existing methods

and possibilities proposed in the literature, two of them have been further assessed for the Timepix3 radiation monitor data.

Hole filling

The high energy beams (particularly relevant for the 7.5 and 8.4 MeV alphas) display a tail in between the 0 and the peak value, as can be better seen in the 2D plots of the ToT against the number of pixels, exemplary in fig. 9.17. In this work, these are considered to come from partially clustered data, revealing shortcomings of the setup at high data transmission rate between the Timepix3 chip and the front-end (even if just instantaneous).

In the data presented above, all the cluster with holes (as those shown in fig. 9.26) have been removed from the analysis, either implicitly through the cluster density selection, or explicitly by identifying the holes as prescribed below. Compensating for this effect is expected to improve the response of the Timepix3 detector, and as such a procedure coined hole-filling is described here. For each pixel
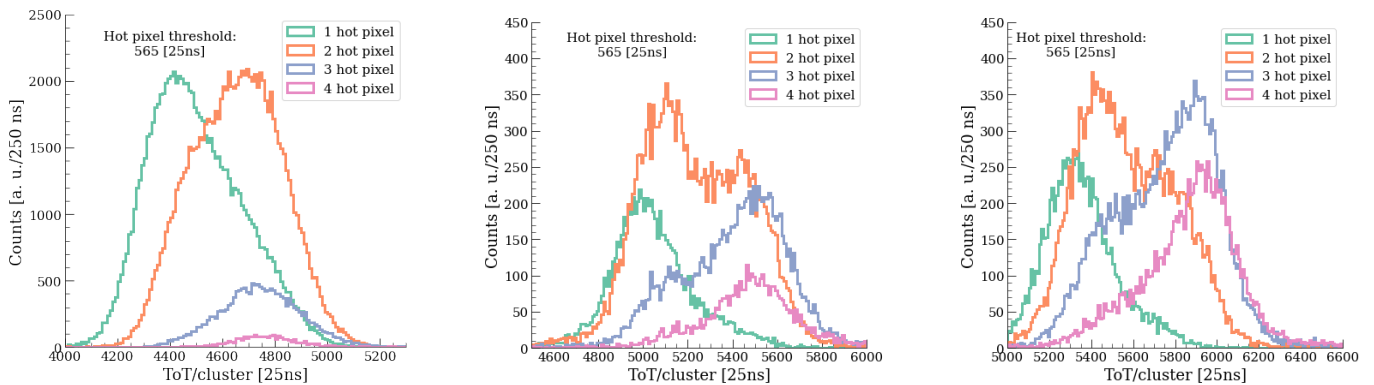
Figure 9.24: Distribution of cluster ToT volume for (**Left**) 5.6 MeV, (**Centre**) 7.5 MeV and (**Right**) 8.4 MeV alphas with variable number of pixels exceeding a threshold set to 565 [25 ns] ToT units.
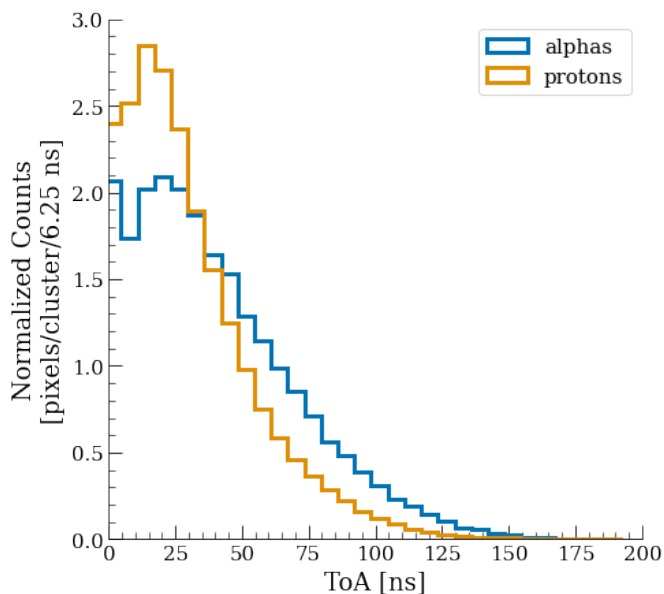
Figure 9.25: Distribution of pixel time of arrival (ToA) in 3 MeV proton and alpha clusters, where the bin at ToA = 0 corresponds to the first pixel that is hit, and the bin width is set to four times the fast time of arrival (fToA) timing resolution of 1.5625 ns.

inside a cluster, one looks at its neighbouring pixels $(dx, dy \in [-1, 0, 1])$. If the neighbouring pixel is not part of the cluster (has no energy deposition), then consider the current pixel as a hole candidate. If a pixel has been identified as a hole candidate by N_h or more pixels inside the cluster, then it is considered a hole, and it is 'filled' with a ToT value as the av-

erage of the neighbouring pixels. Several values of required neighbours have been tested, and a value of $N = 5$ has been found to yield the best results in correctly identifying the holes within the cluster, and these events have been discarded from the analysis. To asses the impact of this filter, the cluster ToT volume, defined as the sum of the pixels ToTs, is plotted in fig. 9.27 for the two highest energy alpha beams with and without the holes, revealing a much cleaner signal, correcting as well for the double peak feature.

Pedestal fitting

The saturation effects at large energy deposition per pixel leads to missing information in the total ToT volume per cluster. Different methods [180] are proposed in the literature to compensate for the effect, by assuming a certain 2D profile for the energy deposition (such as Gaussian or pyramidal), and then extrapolating the measured data.

9.2.5 Test campaign summary

The energy calibration of the Timepix3 radiation monitor was carried out at the centro nacional de aceleradores (CNA) using quasi-mono energetic beams of protons (alphas) from 0.6 (1) to 5 (8.4) MeV stopping in the active volume of the sensor. The energy deposition in the passive front layers (a known 500 nm metalization layer and a silicon dead layer of an unknown thickness but experimentally de-
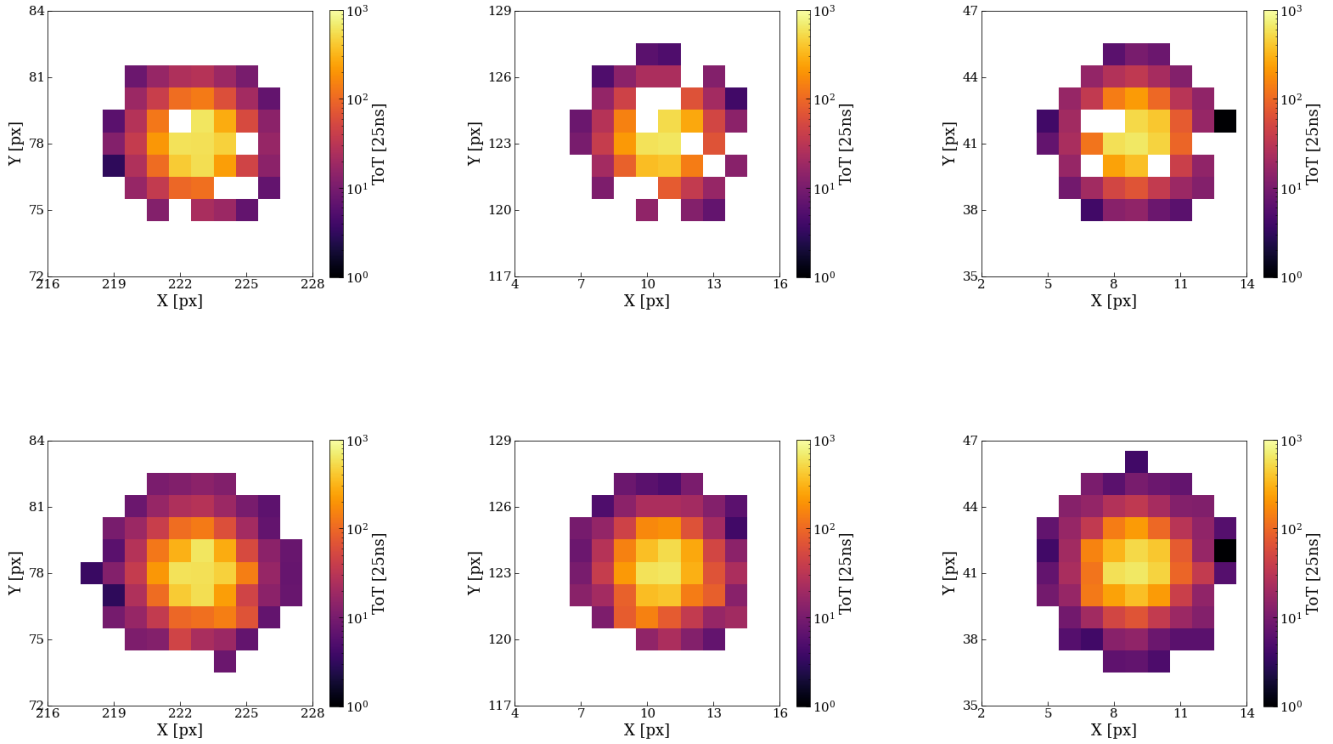
Figure 9.26: **(Top)** Example of 8.4 MeV alpha clusters with holes, that have been discarded from the analysis. **(Bottom)** The same clusters, with holes filled, showcasing the procedure.

termined) is computed using dedicated Monte Carlo simulations, performed with FLUKA. The clusters formed by the CNA beams are reconstructed and filtered using dedicated shape parameters, ensuring that single particle hits are fully reconstructed and isolated. The cluster-level calibration analysis indicates that the detector operates in a linear regime with $ToT_{reg}(E_{dep}) = E_{dep} \cdot 993 \pm 93$ [25 ns/MeV] + $N \cdot 23.10 \cdot 2.14$ [25 ns/pixel], while evidence of saturation effects is visible for energy depositions above 2 MeV, especially for the case of proton beams. At the pixel level, the saturation is estimated to occur from around 600 keV. The larger levels of saturation observed with protons compared to alphas are found to be associated with a different degree of charge sharing in the respective clusters, thus confirming that operating the sensor with a reduced bias voltage to enhance charge sharing is a good strategy to mitig-

ate the saturation. No evidence of high-energy non-linear saturation or volcano effect is observed in the data. As part of the calibration measurements, the detector was irradiated at several angles up to 45° with 597 keV protons to estimate the dead layer thickness of the chip, quantified to be 333±60 nm.
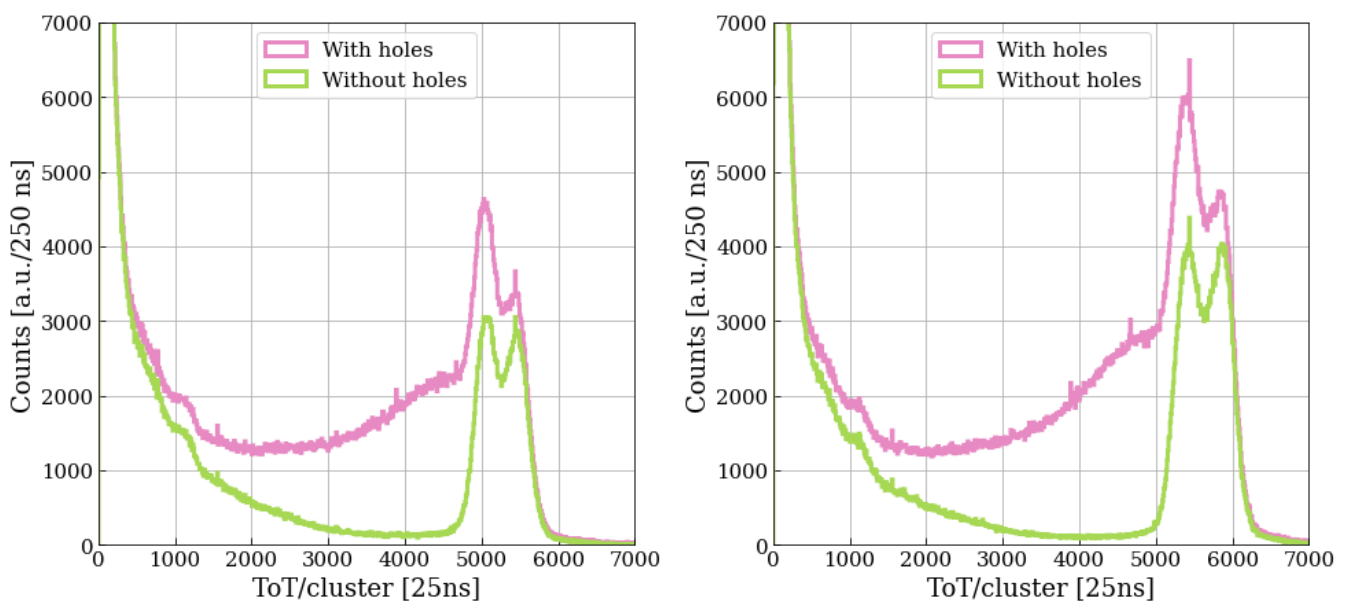
Figure 9.27: Cluster volume, defined as the sum of the pixel ToTs, for high energy alpha beams, with and without holes, **(Left)** at 7.5 MeV and **(Right)** at 8.3 MeV.

10

Test campaigns: neutron detection

Introduction

In addition to the Timepix calibration procedure, which was used to convert the measured time over threshold (ToT) per pixel into a deposited energy, the detection efficiency of the detector for different particle species was also scrutinized. If for charged particles, as those used above, one assumed a 100% detection efficiency, neutral particles relevant for radiation effects in electronics, in particular neutrons, have a significantly lower interaction probability inside the Silicon material of the Timepix3 radiation monitor. As such, two energy regimes for neutrons have been explored:

1. at institute Laue-Langevin (ILL), using a beam of cold neutrons peaks at 6.67 meV, with high fluxes in the order of $3 \cdot 10^9$ [n/cm^2/s].

2. at the CERN calibration laboratory (CALLAB), using an AmBe source, generating neutrons up to 10 MeV, with lower fluxes in the order of $5 \cdot 10^5$ [n/4π/s]

10.1 ILL: cold neutrons at 6.67 meV

10.1.1 Introduction

In this study, the aim for the Timepix3 radiation monitor was two-fold:

1. to study the detector response to neutrons,

2. to verify the beam profile monitor capabilities.

10.1.2 Facility description

The institute Laue-Langevin (ILL) [217] is an international research centre at the leading edge of neutron science and technology. The institute provides scientists with a very high flux of neutrons feeding some 40 state-of-the-art instruments, which are constantly being developed and upgraded. As a service institute, ILL makes its facilities and expertise available to visiting scientists. Every year, about 1400 researchers from over 40 countries visit the ILL and 640 experiments selected by a scientific review committee are performed. Research focuses primarily on fundamental science in a variety of fields: condensed matter physics, chemistry, biology, nuclear physics and materials science, etc.

All the neutrons on earth are bound in nuclei. Some of these nuclei are unstable, and they free up neutrons when they decay. This is the case of uranium, used in the ILL reactor. In commercial power plants the decay process is exploited to produce energy. At the ILL the reactor is used to extract neutrons from uranium nuclei for scientific exploitation. This explains the small size and overall design of the ILL reactor. During this test campaign, the Timepix3 detector was irradiated with cold neutrons beam with a spectrum peaked at 6.67 meV and extending up to 25 meV, with an expected flux received from the facility of $3 \cdot 10^9$ [n/cm^2/s].

10.1.3 Installation and data taking

The detector module of the Timepix3 radiation monitor was installed at the exit of the neutron beam from the ILL reactor, attached to the neutron guide

output, as shown in fig. 10.1, with a diagram of the setup also given in fig. 10.2, showcasing also a boron shielding collimator sheet used to reduced the beam flux. The rubber layer thickness was either 2 or 5 mm, and the opening aperture was decreased from an initial diameter of $\oslash$5 to $\oslash$1.6 mm. The data acquisition runs with the most important parameters are listed in Table 10.2. In addition, the main Timepix3 operational parameters summarised in tab. 10.2.
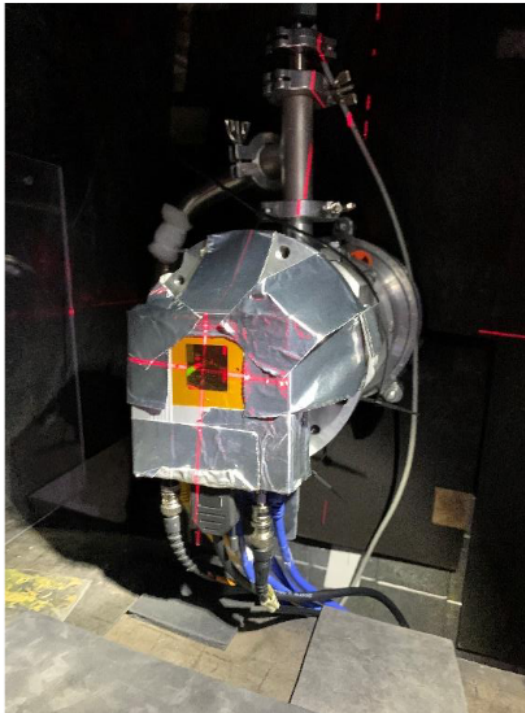
Figure 10.1: Timepix3 radiation monitor attached to the neutron guide output.

Table 10.1: Test beam conditions at institute Laue-Langevin (ILL).

Boron shielding collimator diameter [mm]	Rubber layer thickness [mm]
5	5
5	2
1.6	0

Table 10.2: Timepix3 radiation monitor operational parameters at the ILL test campaign.

Parameter	value
Bias voltage [V]	35
Panda GUI firmware version	2.4.0

10.1.4 Data analysis

The in-house clustering algorithm based on the field programmable gate array (FPGA) timestamp (described in section 8.1.2) has been used to process the data. The main issue observed with the Timepix3 detector was the quick saturation of the graphical user interface (GUI), as can be seen in fig. 10.3, due to the beam's high flux, leading to the risk of pile-up events.
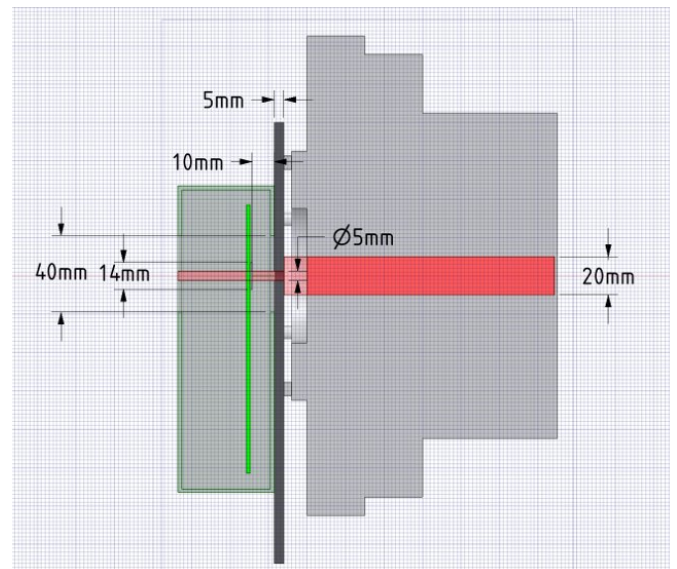
Figure 10.2: An exemplary diagram illustrating the Timepix3 radiation monitor setup (side view), with the beam coming from the right hitting the sensor (green). The detector module (the object on the left) was mounted in front of the neutron guide (the object on the right), with a 5 mm rubber sheet (black) with Boron admixture placed in front of the detector and a $\oslash$5 mm circular opening (light red) was made in the rubber to achieve a smaller neutron flux, as opposed to the 20 mm wide neutron beam (red).
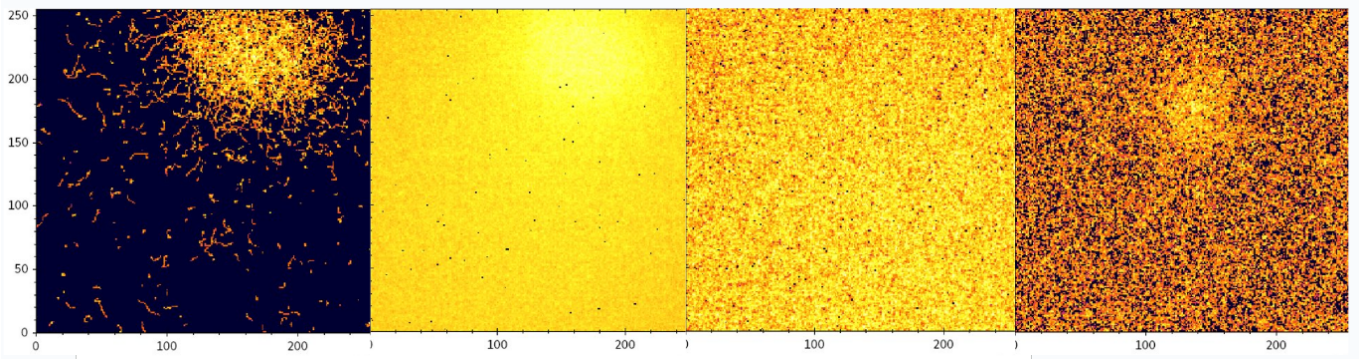
Figure 10.3: Timepix3 setup graphical user interface (GUI) for several runs, from left to right:
(i) Boron shielding with ⌀5 mm collimator and no beam.
(ii) No shielding, showing an apparent saturation of the Panda GUI.
(iii) Boron shielding with ⌀5 mm collimator and a 2 mm Boron layer, yielding a lower flux and no saturation.
(iv) Boron shielding with ⌀1.6 mm collimator, yielding a significantly lower flux and no saturation.

10.1.4.1 Beam profile analysis

During the tests with the boronized rubber shielding, the visible contribution of particles of different kind was deemed due to the neutron capture reactions of Boron either in the ground or the first excited state:

$$
{}^{10}_{5}B + n_{th}
$$

$$
\rightarrow {}^{7}_{3} Li(1.01 \text{ MeV}) + {}^{4}_{2} He(1.78 \text{ MeV}) \quad (6\%) \tag{10.1}
$$

$$
\rightarrow {}^{7}_{3} Li(0.84 \text{ MeV}) + {}^{4}_{2} He(1.47 \text{ MeV}) + \gamma(0.48 \text{ MeV}) \quad (94\%) \tag{10.2}
$$
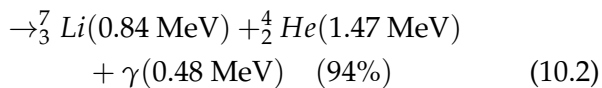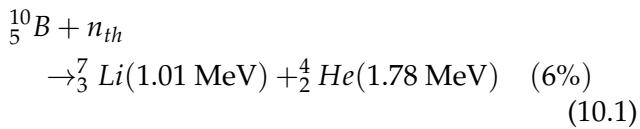
The decay to the excited state of ^{7}Li is followed by the emission of a 0.48 MeV gamma ray that leaves the nucleus in its ground state. Such a gamma ray can interfere with the detection of the reaction products, representing itself an additional background and thus worsening the energy resolution. The collimator runs do not impact in so much the energy distribution as much as the measured flux, namely a reduction in the flux with the smaller collimator aperture, as expected. To conclude this section, the beam profiles imposed by the collimators were clearly visible with the detector.

10.1.4.2 Neutron detection device with ^{6}LiF converter layer

In ref. [218, 219], it was shown that the use of a fully depleted silicon detector, in combination with a ^{6}LiF neutron converter film, can be successfully exploited to detect thermal neutrons with a reasonable efficiency, as suggested as well by other authors [220, 221]. The reliability of this technique, along with a characterization in terms of response, efficiency and gamma sensitivity, was also assessed by means of GEANT4 simulations [222]. The neutron conversion mechanism is based on the well known reaction:

$$
{}^{6}_{3}Li + n \rightarrow {}^{3}_{1} H(2.73 \text{ MeV}) + \alpha(2.05 \text{ MeV}) \tag{10.3}
$$
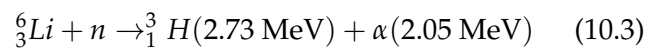
which is the only possible decay channel following the neutron capture in ^{6}Li, and is free of gamma rays. Its cross section at thermal neutron energy is $\sigma = 940$ b, and it scales with $1/v$ up to ≈ 200 keV with a back-to-back isotropic emission of the reaction products. The energy spectrum measured by the silicon detector in such a configuration has a characteristic shape, and allows to discriminate the capture reaction products from the low-energy background basically due to gamma rays. This technique is in-

deed well established [223], and several applications are already in use, like for instance at the neutron time of flight (nToF) spallation neutron beam facility [33, 34]. Moreover, the stopping power and the energy of produced tritium is displayed in fig. 10.4, both in air and in silicon, indicating that at 2.73 MeV, the tritium is expected to stop within 40 μm inside the Timepix3 sensor.

The ^{6}LiF converter layer used in this work has a thickness of 1.321 mm and a density of $\rho = 500$ g/cm^2, attached to a printed circuit board (PCB) frame of 1.193 mm. The neutrons penetrate these layers inducing secondaries as described by Eqn. 10.3. Because of the distance between the layer and the detector itself, most of the alphas are expected not to reach the Timepix3 detector. The interaction probability of the neutrons in the LiF converter layer at depth z can be computed using:

$$P(z) = \exp{-\frac{z}{\lambda}} \qquad (10.4)$$

where λ is the interaction length of neutrons inside the material, which can be computed from:

$$\lambda = \frac{1}{\sigma \cdot n} \qquad (10.5)$$

where σ=940 b is the interaction cross section as described above, and $n = \dfrac{N_A}{M} \cdot \rho$ is the atomic density, with $N_A = 6.022 \cdot 10^{23}$ is Avogadro's constant, $M = 25.939$ g/mol is the molar mass, and $\rho = 500$ g/cm^2 is the density of LiF.

The Timepix3 radiation monitor results are shown in fig. 10.5, displaying that only the LiF converter leads to a change in the measured energy deposition, as expected from eqn. 10.3. Moreover, one can observe higher order peaks, corresponding to pile-up events due to the beam's high flux.

10.1.5 Test campaign summary

The interaction rate of cold neutrons with the Timepix3 radiation monitor was investigated in this test campaign. The 300 μm thick Silicon sensor of the Timepix3 chip was irradiated with a neutron beam with a spectrum peaked at 6.67 meV and extending up to 25 meV, with an expected flux received from the facility of $3 \cdot 10^9$ [n/cm^2/s]. The feasibility in operating the Timepix3 radiation monitor setup in such a high neutron flux yielding also high count rate, and implicitly data transmission rate, has also been assessed. Due to this high flux, several setup configurations have been used in order to decrease the measured count rate, but also to observe the beam shape, via the usage of boron collimators with diameters of $\oslash = 1.6$ and 5 mm, or rubber thickness of 2 and 5 mm. Concluding, the detector was able to act as a beam monitor.

The energy deposition due to the neutron interactions in the Timepix3 detector has also been investigated, with the help of converter layers made from different materials, such as Al, Cd and LiF. Only for the last material, there is a known reaction channel which generates secondary products (tritium and alpha particles) that are then measured by the detector. Due to the high flux, a non-negligible fraction of the reconstructed cluster hits included pile-up events.
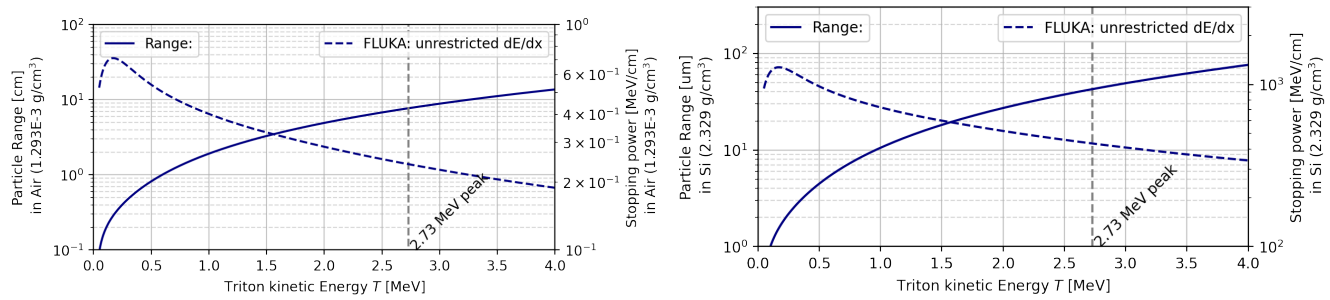
Figure 10.4: Tritium particle range and stopping power in air (**Left**) and silicon (**Right**) in the energy range of the ^{6}Li decay of Eqn. 10.3. The stopping power data is obtained from FLUKA, and the range is then computed from it.
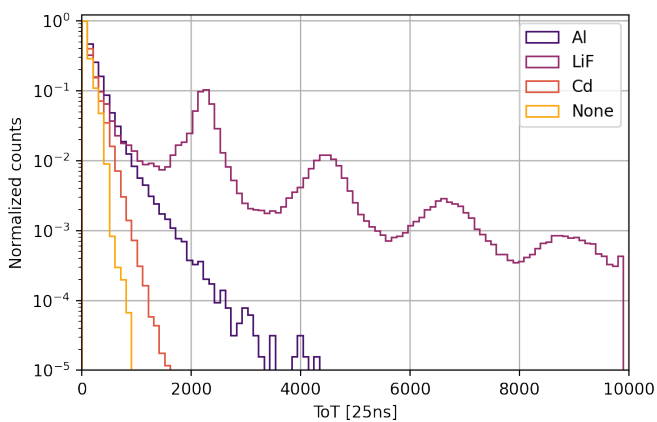
Figure 10.5: Timepix3 radiation monitor clusters ToT at ILL, for different converter setups, showing that only for LiF a significant change is observed.

10.2 AmBe: neutrons up to 10 MeV

10.2.1 Introduction

In this test campaign, in addition to the Timepix3 radiation monitor, a (single pixel) diode[66] is also used. The two silicon detectors currently under study for R2E applications at the CERN accelerator complex. The measurements of the two detectors in a neutron field are compared with each other and against dedicated Monte Carlo simulations, performed with FLUKA.CERN [18–20] and GEANT4 for single event effects (G4SEE) [224, 225]. Both codes are capable of a point-wise neutron treatment, as further described in section 10.2.5.

The response of both silicon detectors is examined in the neutron field of the known americium-beryllium (AmBe) source at the radiation protection (RP) calibration laboratory (CALLAB) at CERN, which in fact was used to benchmark the static random-access memory (SRAM) within the radiation monitor (RadMon) by comparing the simulated high energy hadron equivalent (HEHeq) fluence with the measured single event upsets (SEU) rate [226]. In case of high energy hadron equivalent (HEHeq) fluence monitoring in mixed field radiation environment, ref. [66] already points towards an enhanced sensitivity (by 3-4 orders of magnitude) of the silicon detectors with respect to SRAM-based solutions. However, this work focuses on the detector capabilities to measure the energy deposition spectra of the neutron field responsible for the above SEU rates (as estimated in ref. [227]).

10.2.2 Detectors

The two detector technologies investigated in this work share the same low-level setup, while being significantly different in the signal post-processing. Both are silicon sensors with a thickness of 300 µm, and a bias voltage is applied on the p-in-n junction, thereby creating a sensitive volume with the values summarised in tab. 10.3. For the diode, a voltage of 120 V that leads to the full depletion of the sensor is used, while for the Timepix3 radiation monitor a partial bias voltage of 50 V has been used, leading to a depletion volume thickness of 250 µm.

119

Table 10.3: Main properties of the two silicon detector technologies used in the AmBe test campaign.

Detector	Applied bias [V]	Surface [cm^2]	Effective Sensitive Thickness [μm]
Diode	120	4.00	299
Timepix3	50	2.56	250

Table 10.4: Timepix3 threshold settings at the americium-beryllium (AmBe) test campaign.

Parameter	Default	High threshold
$V_{thres,coarse}$ [DAC]	8	1
$V_{thres,fine}$ [DAC]	110	120
E_{thres} [keV]	$\mathcal{O}(10)$	$\mathcal{O}(170)$

10.2.2.1 Diode detector

The first detector is a single silicon diode [66], where the signal from the diode is amplified with a CIVIDEC C2-HV broadband current sensitive amplifier. The output of each acquisition is the current signal $I(t) = V(t)/R$ with the resistance $R = 50\ \Omega$, sampled every nanosecond with a digitizer. In the post-processing, the signal is converted to the number of generated electron-hole pairs via the current $I(t)$ time integral:

$$E_{dep} = \frac{E_{eh}}{eg} \int I(t)dt \qquad (10.6)$$

where $E_{eh} = 3.6\ \mathrm{eV/e^-}$ is the average energy to create an electron-hole pair, e is the electron charge and $g = 43.5\ \mathrm{dB}$ is the amplification.

10.2.2.2 Timepix3 detector

The time over threshold (ToT) output of the Timepix3 detector can be converted into energy based on several calibration methods, and a calibration has been obtained for the Timepix3 radiation monitor, described in chapter 9.2.3. Moreover, the detector has been used at two different threshold levels, summarised in tab. 10.4.

While the diode has no spatial resolution since it is a single large pixel, the Timepix3 detector is composed of an array of 65 536 micrometry pixels. The interaction of a single particle can induce multi-pixel signals, offering a spatial resolution but also leading to a more complicated data analysis requiring an event reconstruction with pixel clustering in space

and time depending on the particle type and interaction mechanism. Therefore, the raw pixel data has to be clustered to reconstruct the full event. For the neutrons in this analysis, an algorithm developed within R2E has been employed (as described in section 8.1.2).

10.2.3 AmBe Neutron source and installation

The AmBe source at CERN provides a continuous neutron flux of $5.03 \cdot 10^5$ [n/(s·4π)] peaking at 3 MeV and reaching a maximum energy of 11 MeV [226], emitted isotropic with an activity of 888 GBq. The source is typically employed for calibration of dosimeters. In our experimental campaign, the detectors were placed around the source, at a distance of 20 or 59 cm, with or without a cylindrical polyethilene (PE) moderator with $R = 9$ cm that is designed to thermalize fast neutrons. Table 10.5 includes the count rate for the detectors for each setup configuration; note that the increased count rate for the Timepix3 is due to its sensitivity to lower energy deposition events.

10.2.4 Detector results

The shape of the energy deposition spectrum is similar for both detectors, as further confirmed by the Monte Carlo simulations presented in Section 10.2.5. One can discriminate between elastic and inelastic neutron interactions and their energy deposition patterns. The maximum elastic transfer energy for a neutron at 11 MeV hitting a silicon atom can be computed from kinematic considerations and is estimated at 1.47 MeV. Considering the significantly lower inelastic cross section, one expects a large amount
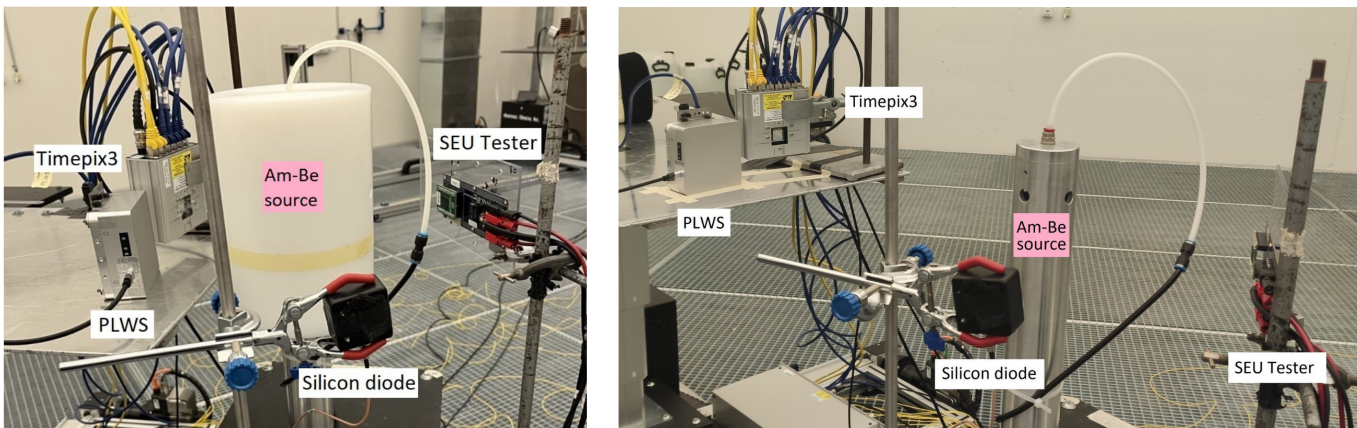
Figure 10.6: All radiation to electronics (R2E) detectors around the AmBe source, at **(Left)** 20 cm with the PE moderator, and **(Right)** without the PE moderator, and with the Timepix3 and PLWS detectors at 59 cm.

of elastic neutron interaction events at low energies, but which will be cut off depending on the detector's detection threshold. Above 1.47 MeV, the inelastic neutron interaction events become dominant and the energy deposition spectra stop at 11 MeV, the maximum energy of the AmBe neutron source.

10.2.4.1 Diode results

The diode has been used at only one distance (20 cm) from the AmBe source, either with a polyethilene (PE) moderator or without. The obtained results are shown in fig. 10.7a, where one notices that the neutron inelastic interactions are reduced as the faster neutrons have their momentum reduced by the PE moderator, leading also to slightly lower integrated count rates, as seen in tab. 10.5. Note that the fall off at lower energies is not physical, but linked to the threshold, and in fact, both detectors are hardly sensitive to thermal neutrons in the eV range.

10.2.4.2 Timepix3 results

The Timepix3 detector has been placed at both 20 and 59 cm, either with the PE moderator or without, but also operated at a high threshold level, with the values given in tab. 10.4. fig. 10.7b displays the reconstructed cluster count rate as a function of the total cluster ToT (summed over all pixels) for these configurations, which are discussed in more detail below.

Firstly, the Timepix3 detector is reliably measuring different integrated count rates at 20 and 59 cm, consistently with an isotropic source for which count rate is expected to decrease with distance R as $1/R^2$. Secondly, there is a clear difference between the energy deposition of the neutrons in the Timepix3 with and without the PE moderator there is a visible change in the spectrum, consistent with the diode results in fig. 10.7a. Thirdly, the higher threshold runs reveals a shift of 500 ToT units in the spectra to lower ToT values, as it results in less time over the threshold. This significantly suppresses the elastic (lower energy than the threshold) interactions count rate, as expected.

Thanks to the pixel array, one can exploit the geometry (shape, orientation, linearity, etc.) of the cluster. In this study, we shall restrict only to the total number of pixels N in the cluster, which is plotted against the total ToT volume of the clusters in fig. 10.8. One can see the clusters aligned along two distinct lines, corresponding to the elastic (lower energy) and inelastic (higher energy) interactions. The run with higher threshold clearly removes the elastic interactions line, as the energy deposition in the individual pixels falls below the threshold.
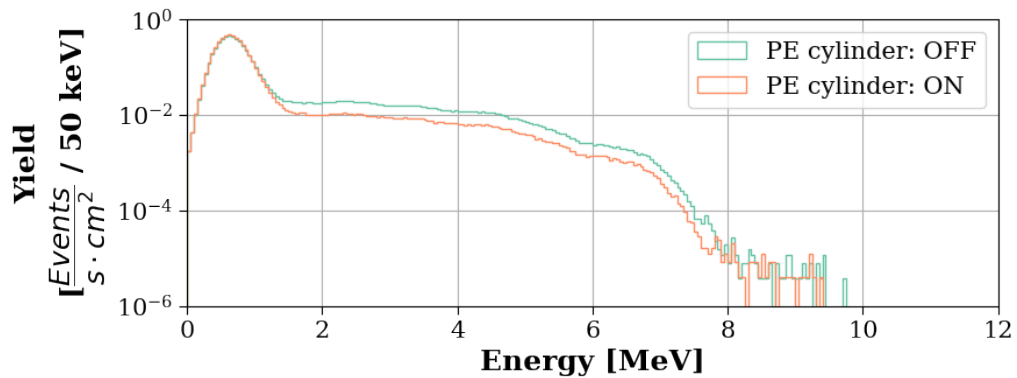
(a) The silicon diode detector placed at 20 cm from the AmBe source, without and with the PE moderator on the source.
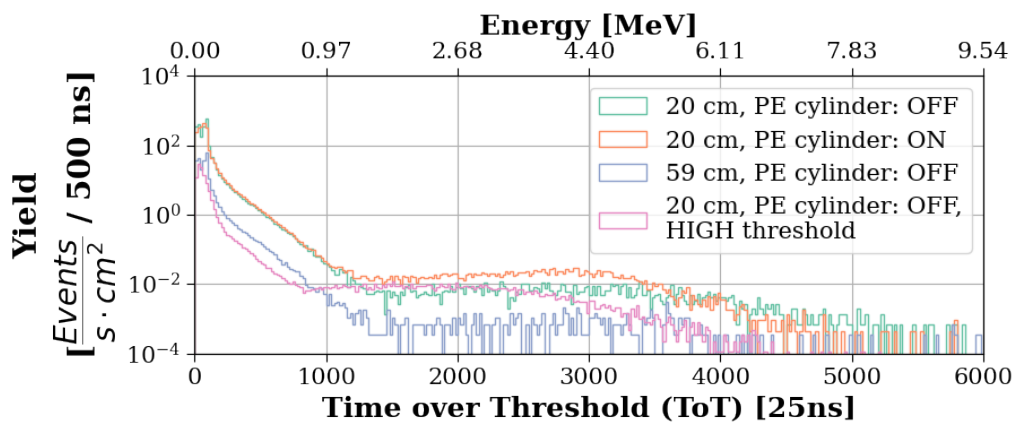
(b) The Timepix3 detector placed at 20 cm and 59 cm from and AmBe source, without and with the PE moderator on the source and with a standard and higher detection threshold.

Figure 10.7: The event-by-event energy deposition spectra measured by **(a)** the silicon diode detector and (b) the Timepix3 detector.

Table 10.5: Different setup configurations for the detectors. The count rate is given in particles/(s·cm^2).

Distance [cm]	PE Moderator	Diode Count rate	Timepix3 Threshold	Count rate
20	no	5.91	default	2114
59	no	-	default	227
20	yes	5.50	default	1924
59	yes	-	default	202
20	no	-	high	101
59	no	-	high	13

10.2.5 Monte Carlo simulations

The simulation work of this study is performed with two Monte Carlo codes and their recent de-
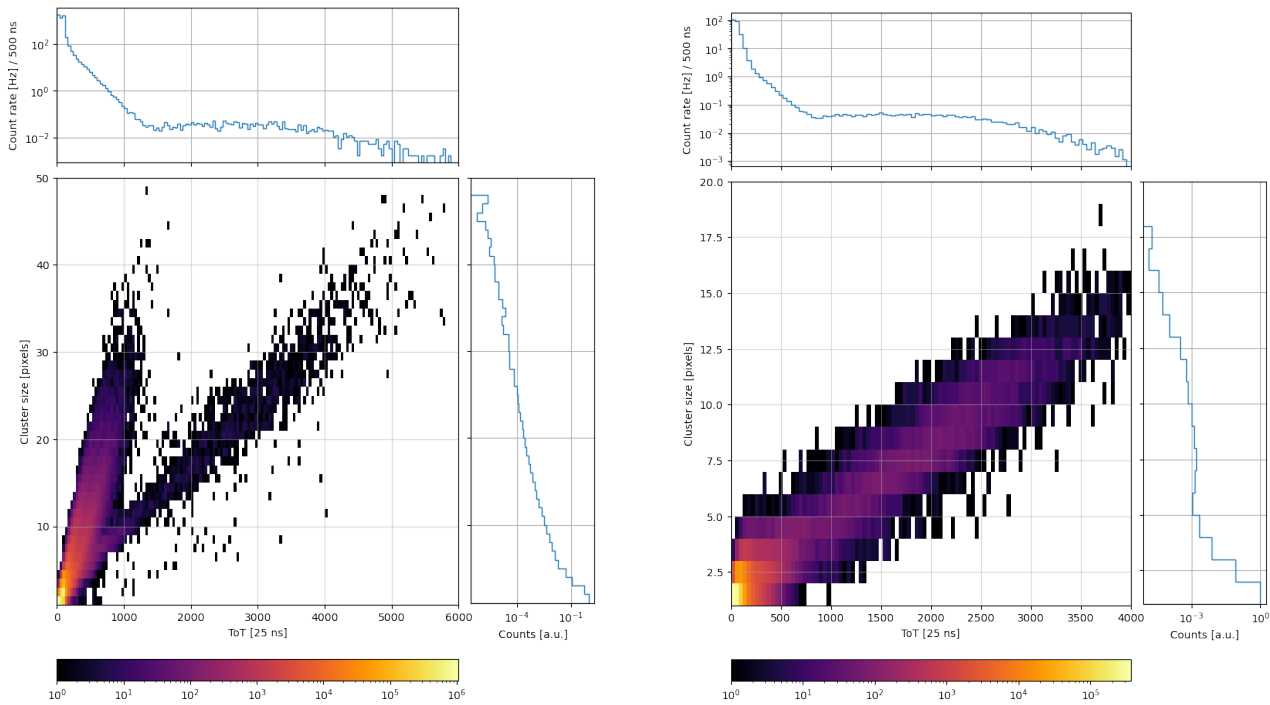
Figure 10.8: 2D plots of ToT distribution (x-axis) and cluster size (y-axis) at 20 cm for default and higher threshold.

velopments. On one side, the recently released FLUKA.CERN version 4.3.0 [228, 229], where the neutron transport benefits from a point-wise treatment. The major drawback of previous FLUKA versions was the transport of low energy neutrons ($E_n \leq 20$ MeV) using a multi-group approach, due to several difficulties that were too difficult to previously overcome, such as performance issues in speed and huge memory footprint of the data. On the other side, the recently released simulation toolkit G4SEE [224, 225, 230], developed within R2E and designed to simulate single event effects (SEE)s on an event-by-event basis, inheriting the neutron pointwise treatment from the Monte Carlo code geometry and tracking (GEANT4).

Most of the differences that exist between the FLUKA and G4SEE simulations come from the fact that the physical models are not identical. FLUKA offers a defined set of physical models with a limited number of parameters that define thresholds and variables to activate exotic processes to improve accuracy and

execution time, while G4SEE has a number of physics lists from GEANT4 [69, 183, 184] available. For the FLUKA input, the following parameters (adjustable physics settings) were used:

1. Lowest energy threshold values (PRECISIO card defaults).

2. Evaporation and coalescence processes are activated.

In the G4SEE input file, the following models were selected:

1. EM Opt4 for the electromagnetic physics.

2. G4HadronElasticPhysicsHP for the hadronic elastic interactions.

3. G4HadronPhysicsFTFP_BERT_HP for the hadronic inelastic interactions.

HP stands for high precision model, which are suitable to simulate the interactions of neutrons

with energies below 20 MeV, down to thermal energies.

As for the thresholds, FLUKA employs transport thresholds for all the particles and production thresholds for electrons and photons, while G4SEE (as an application of GEANT4) uses as input production thresholds. The parameters have been selected to match as much as possible, and presented in tab. 10.6.

Concerning the size and shapes of the used geometries, the matching between FLUKA and G4SEE simulations is optimal, since exactly the same G4SEE volumes have been used, together with the same elements and compounds, sharing the same density and atomic composition.

In both FLUKA and G4SEE, the scored quantity is the deposited energy in a layer of pure silicon within a sensitive volume of thicknesses described in tab. 10.3. A realistic model of the detectors is used, including the additional layers found upstream, such as the detector aluminum case, PVC layers on top and thin aluminum slabs.

The Monte Carlo simulations using FLUKA and G4SEE (revealing the expected behaviour of the neutrons in the detector) are compared to each other and with the measurements and are presented in fig. 10.9. The two simulations show an excellent agreement with each other, within the Monte Carlo statistical uncertainty.

10.2.6 Detector comparison

The bottom panel of fig. 10.9 displays together the results of the two detectors and the simulations for comparison, as well as their ratio pads. We shall divide the discussion into three energy regimes: high energy inelastic interactions with deposited energy above 7 MeV, intermediate interactions from 7 MeV down to the detection threshold (different for the two detectors) and lower energy interactions below threshold.

Starting from the high energy deposition events, the Timepix3 detector measurements agree with the sim-

ulations up to 8 MeV, but then falls short due to low statistics. This shortcoming can be corrected in future runs by a longer acquisition time. In order not to avoid running into data storage issues due to the significantly more prevalent low energy events, one can adjust the detector's operational parameters in order to optimize the collection of higher energy (above 6 MeV) signals. One method is to increase the threshold level, as done for the institute Laue-Langevin (ILL) test campaign presented in section 10.1. Another method designed to reduce the detector dead time is to increase the pre-amplifier discharge current I_{krum}, leading to a faster reading of the signal, as described in section 8.1.1, fig. 8.2. Another known issue at the higher energy events is the saturation of the Timepix3 pre-amplifier, in which case more events would be measured at a lower ToT compared to the correct energy deposition. Similarly, the diode measures a lower count rate compared to the simulations above 7.5 MeV.

The intermediate energy deposition results for both detectors agree with each other, and with the simulations. The agreement is preserved beyond the transition between the inelastic and elastic interactions (at 1.47 MeV) until the detector thresholds. In the case of the diode, this is at around 0.6 MeV below which the detectable count rate is negligible. The noise of the Timepix3 is much lower than the noise of the diode, therefore the detection threshold can also be significantly lower, which allowed to detect events of very low energy that the diode could not distinguish from the noise. In fact, the lower threshold is adjustable for both detectors (and for the Timepix3 has even been increased in the some runs), but should nevertheless lie above noise level. At very low energy (below 0.15 MeV), the Timepix3 measurements are actually higher than the simulations, hinting that some particles other than neutrons were detected (such as photons or electrons).

10.2.7 Test campaign summary

The energy deposition in a Timepix3 detector and a silicon diode sensor has been investigated with an AmBe neutron source, in order to asses the suitability

Table 10.6: Production and transport thresholds used in the Monte Carlo simulations for the AmBe test campaign.

Particle	G4SEE production cut	FLUKA production threshold	FLUKA transport threshold
Protons	1 kev - 10 μm	-	1 keV
Neutrons	-	-	0.01 meV
Electrons	1 kev - 1 μm	1 keV	1 keV
Photons	10 kev - 10 μm	1 keV	1 keV

of the detectors within the radiation to electronics (R2E) project at CERN. The measured energy deposition spectra have also been compared with Monte Carlo simulations that have a point-wise treatment of neutrons, namely the recent FLUKA.CERN 4.3.0 release and the G4SEE application developed within R2E. Both detectors agree satisfactorily with the simulation, with caveats at higher energy depositions ($E_{dep} > 7$ MeV) and at energies below the detection thresholds.

Within the R2E activity, the end goal is to perform a mixed-field characterization, for which different particles species are investigated to assess their energy deposition patterns within the detector.
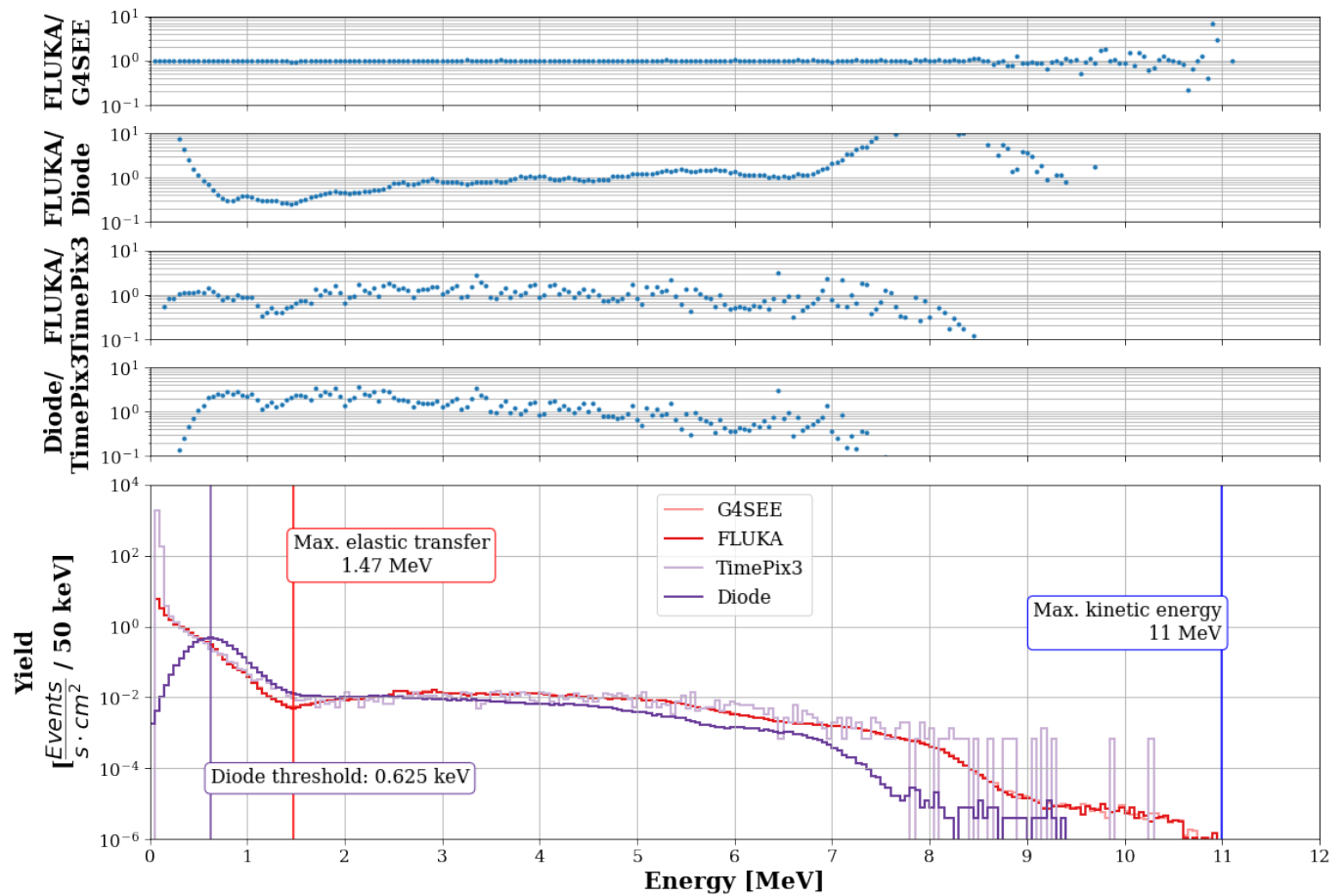
Figure 10.9: **Top four pannels:** Comparison of FLUKA and G4SEE simulations for the AmBe neutron field inside a 300 µm Si detector placed at 20 cm from the source and with no moderator, and their measurements for the diode and the Timepix3 detectors. **Bottom pannel:** Absolute measurements for the detectors, as well as the simulations. The neutron flux at 20 cm is estimated at 10^4 n/s/cm^2.

The second act - summary

The key features of a 300 μm-thick silicon Timepix3 detector have been established and characterised as a radiation monitor for the measurement of the mixed radiation field of the CERN accelerator complex, in particular for the Large Hadron Collider (LHC). Importantly, the modus operandi of the detector with charged (protons and alphas) and neutral (photons and neutrons) particles has been tested, and the practical limitations of the setup exploited and further constrained.

A detailed description of the Timepix3 radiation monitor was given, covering the hardware setup and the Timepix detection principle based on the simultaneous measurement of the time over threshold (ToT) and time of arrival (ToA). The charge released in the interaction of ionizing particles within the pixel matrix is typically spread over multiple pixels, leading to the need for a cluster reconstruction algorithm to identify the individual particle hits. To mitigate possible saturation effects, the Timepix3 radiation monitor has been operated with a partial bias voltage at 50 V that leads to a partially depleted p-in-n sensor of around 250 μm instead of the full 300 μm thickness of the silicon sensor, thereby reducing the amount of collected charge in the core pixel thanks to the enhanced charge diffusion to the adjacent ones.

The energy calibration of the Timepix3 radiation monitor was carried out in two test campaigns. The former, at the radiation protection (RP) calibration laboratory (CALLAB) facility at CERN, using a ^{241}Am source emitting alpha α particles up to 4.8 MeV, which get attenuated in air to lower energies, however they are considered to be part of the detector's saturation regime. Hence, a second campaign at centro nacional de aceleradores (CNA) using quasi-mono energetic beams of protons (alphas) from 0.6 (1) to 5 (8.4) MeV, fully stopping in the active volume of the sensor. The cluster-level calibration analysis indicates that the detector operates in a linear regime with $ToT_{reg}(E_{dep}) = E_{dep} \cdot 993 \pm$

93 [25 ns/MeV] $+ N \cdot 23.10 \pm 2.14$ [25 ns/pixel], with N being the number of pixels, while evidence of saturation effects is visible for energy depositions above 2 MeV, especially for the case of proton beams. At the pixel level, the saturation is estimated to occur from around 600 keV. The larger levels of saturation observed with protons compared to alphas are found to be associated with a different degree of charge sharing in the respective clusters, thus confirming that operating the sensor with a reduced bias voltage to enhance charge sharing is a good strategy to mitigate the saturation. Additionally, as part of the calibration measurements, the detector was irradiated at several angles up to 45° with 597 keV protons to estimate the dead layer thickness of the chip, quantified to be $T_{DL} = 333 \pm 60$ nm.

Furthermore, two test campaigns have also been performed using beams of neutrons. The former, at institute Laue-Langevin (ILL), consisted of using cold neutrons peaked at 6.67 meV, confirming that only a small fraction of the neutrons interact in the Si sensor of the Timepix3 radiation monitor. Collimators made out of boron carbide B_4C were used to reduce the high beam flux and to observe the spatial structure of the beam, while neutron conversion layers made out of lithium flouride LiF were used to increase the neutron count rate by measuring the secondary products from the $^6_3Li + n \rightarrow ^3_1H + \alpha$ reaction. The second neutron campign was performed at calibration laboratory (CALLAB) using an americium-beryllium (AmBe) source emitting neutrons up to 10 MeV, with or without a polyethilene (PE) moderator to slow down the fast neutrons. The results of this test campaign are compared with another detector under study in the R2E activities at CERN, namely a silicon diode detector, as well as with two Monte Carlo (MC) codes: FLUKA and G4SEE.

The third act - Timepix3 as a radiation monitor at the LHC

11
Timepix3 radiation monitor at the LHC IR4

Having established the key features of the Timepix3 radiation monitor [22] in the second act, namely its calibration curve and modus operandi, the setup has been deployed at insertion region 4 (IR4) in order to assess the radiation field during nominal Large Hadron Collider (LHC) [1] operation (considered as background), and particularly, by the Beam Gas Curtain (BGC) [99–101] operation (considered as signal), as described in detail via FLUKA [18–20] simulations in the first act. This brings together the two newly developed monitoring tools of this thesis, complementing and assisting each other for a better understanding of the composition of the radiation field.

The existing radiation monitors used for machine protection, the beam loss monitor (BLM)s [149], and for radiation to electronics (R2E) purposes (BLMs, radiation monitor (RadMon)s [150–152], distributed optical fibre system (DOFRS) [153], and radio photo luminescence (RPL) detectors [154]) are all capable of measuring the total ionizing dose (TID) via different mechanisms. The RadMon system can also measure single event effects (SEE)s induced by high energy hadron (HEH) and thermal energy neutrons (THN) in static random-access memory (SRAM) devices, calibrated to measure the respective flux, and it also provides measurements of the silicon 1-MeV neutron equivalent fluence via p-in-n diodes.

The Timepix3 radiation monitor has a lower detection threshold of $\mathcal{O}(\text{keV})$ compared to the other monitors, which makes it an excellent instrument to be deployed in the accelerator's shielded alcoves and galleries, the typical location for electronics racks, where the radiation levels to be measured are relatively low compared to the accelerator tunnel. For the case of this study at IR4, the existing RadMons in the UX45 shielded alcove measured only 5 single event

upsets (SEU) counts during the entire operational year of 2023, while the Timepix3 allows for instantaneous ($\mathcal{O}(25\,\text{ns})$) dose and particle rate measurements, even in cases where the radiation levels are at the same scale of the natural background. The Timepix technology is already in use at the LHC experiments, for example within the vertex locator (VELO) system [231] for the large hadron collider beauty (LHCb) detector [10], or, more similar to this work, also for the characterisation of the radiation field within the experimental cavern for the a toroidal LHC apparatus (ATLAS) detector [160, 232].

Divided into three chapters, this third act serves to answer the question of whether the Timepix3 radiation monitor presented in this work can also be used to measure the same quantities as the existing radiation monitors, and to which extent can go beyond their existing capabilities. In the first chapter, it is used (i) as a dose rate monitor (e.g. by simply summing the energy deposited in its pixel matrix), and (ii) as a particle fluence monitor (e.g. by counting the cluster hit rate), during the nominal LHC operation, since it is capable of promptly detecting radiation showers caused by localised beam losses. The second act isolates the BGC induced signal and compares with the FLUKA simulated results of IR4. The third chapter aims explore more applications useful for the R2E community, since the Timepix3 is an interesting instrument to study if more information (if any, at all) can be extracted from the measured data, such as to provide information about the origin of radiation or to extract the linear energy transfer (LET) information of the incoming particles.

11.1 Timepix3 installation in US450 alcove

Several locations for the Timepix3 radiation monitor have been considered for the deployment at IR4, with the main considerations being:

1. the relevance of the BGC generated shower at the deployed location,

2. the expected radiation hardness of the setup (whether the back-end and/or laptop could also be deployed next to the detector),

3. integration constraints coming from the LHC engineering team,

4. internet accessibility in order to soft restart the setup, if needed, and to upload the data to the online databases for storage.
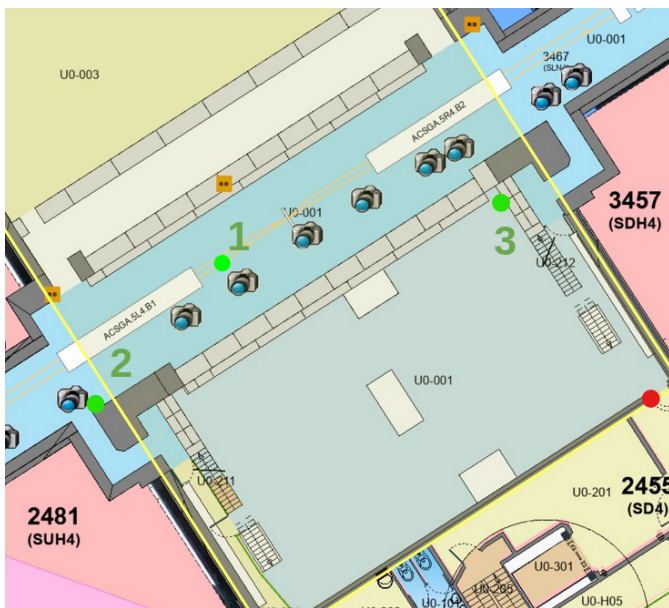
Figure 11.1: Location of the Timepix3 radiation monitor inside the shielded alcove, accessible via the US450 door close to the elevator leading to the positions of interest. The detector was finally installed in position 3.

Three possible locations arose in the survey, also indicated in fig. 11.1:

1. inside the tunnel, on the beam pipe, close to the radio frequency (RF) cavities,

2. inside the tunnel, on the wall,

3. inside the UX45 shielded alcove.

All locations benefit from the proximity to the UX45 shielded alcove and the possibility to host the back-end electronics here, and to eventually deploy only the radiation tolerant components of the setup inside the tunnel. Locations further away from the UX45 shielded alcove were excluded due to the logistic constraints and integration of the connection cables in the LHC accelerator, as the setup was supposed to be just a "temporary" installation, to allow for fast deployment. Since this was the first deployment of the Timepix3 radiation monitor for the mixed field radiation caused by beam losses, a prudent approach was deemed operationally more feasible. Finally, the installation was done in location 3, which presents several more advantages:

1. proximity to the RadMon RADMON.4RM.UX45, for which the radiation levels for nominal LHC operation are known, of about 5 counts/year,

2. possibility to physically access during no beam (emergency interventions, if needed).

The total duration for the test campaign was of 119 days, as summarised in table 11.1, during the progressive increase in beam intensity at the beginning of the year up to the first LHC technical stop (TS). The operational parameters are shown in table 11.2. Initially oriented at a $40°$ wrt. the beam, the Timepix3 radiation monitor was later moved at a $5°$ angle wrt. the beam. The measurement campaign suffered from some downtime (time with the detector as non-operational or with corrupted data), but the online status was restored via soft resets. Nevertheless, a total time integrated beam intensity of $6.73 \cdot 10^{20}$ charges circulated in the accelerator during this test campaign.
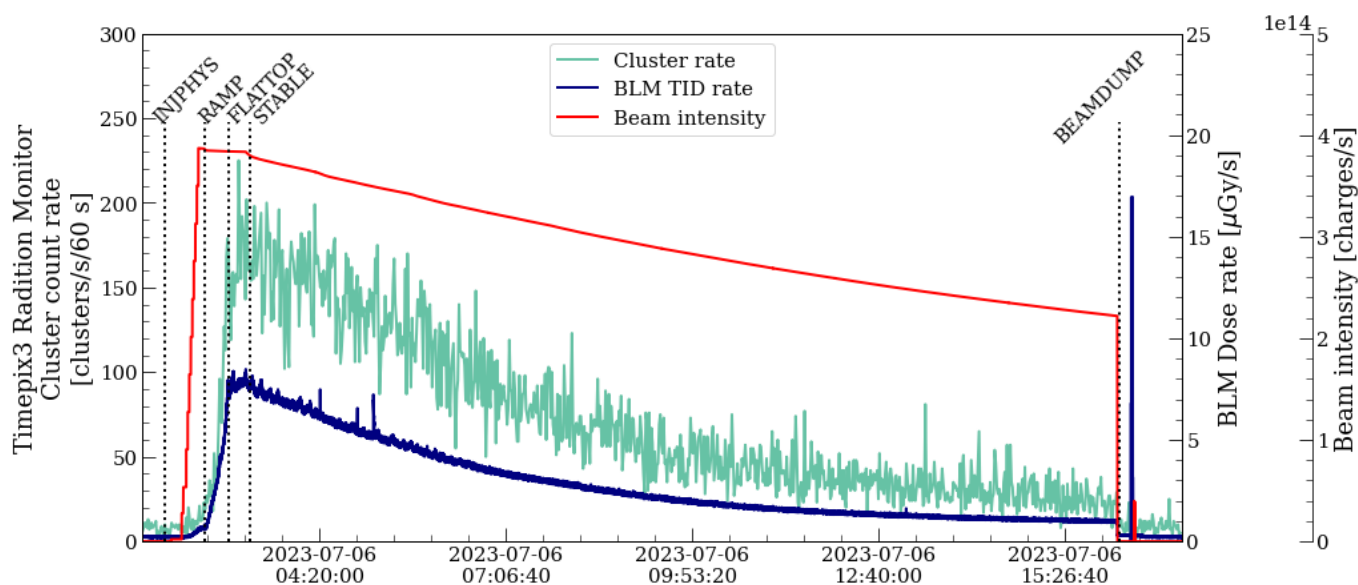
Figure 11.2: The beam cycle of a nominal LHC fill (shown here, fill #9063), with the intensity of beam 1 is represented in red. The dashed black lines represent the moments of time in which the beam mode is changed, and the name of each beam mode displayed. The Timepix3 radiation monitor count rate is shown in light green, together with the dose rate in blue for most irradiated beam loss monitor (BLM) downstream of the Beam Gas Curtain (BGC).

Table 11.2: Timepix3 radiation monitor operational parameters at the LHC insertion region 4 (IR4) test campaign.

Parameter	value
Bias voltage [V]	50
Panda GUI firmware version	3.18.0

11.2 Measurements of the nominal LHC cycle operation

11.2.1 The typical LHC cycle

In fig. 11.2, the measured data of the Timepix3 radiation monitor in the absence of any beam gas monitor injection is super-imposed to an example of the nominal beam cycle (fill #9063) of the LHC (as the one shown in fig. 2.4), together with the TID rate for the most exposed BLM downstream of the BGC instrument (as the one shown in fig. 7.3). This display already exhibits that in addition to the dosimetric (TID rate) capabilities, the Timepix3 detector can act as an individual particle counter with a very low

Table 11.1: Logbook and summary for the Timepix3 radiation monitor measurements at IR4 in 2023.

T_{start}	T_{end}	Angle [deg]	Total duration [days]	Downtime [days]	Number of clusters	Total cirulating charges [10^{20}]
March 20th	May 29th	40	70	24	1 481 614	2.55
May 29th	July 17th	5	49	28	1 846 531	4.18

detection limit (threshold level) compared to the existing monitoring systems, e.g. the RadMon. Due to high fluctuations in the cluster and ToT measured rates, the data of the Timepix radiation monitor are averaged for an interval of Δt_{avg}=60 s, for analysis purposes. In what follows, the discussion is divided per LHC beam mode.

11.2.1.1 Natural radiation background (no beam)

Placed inside a shielded alcove at IR4, an LHC shielded alcove with relatively lower radiation levels compared to the experimental collision points, the Timepix3 radiation monitor measurements are expected to correlate with the losses from the accelerator, but without a bunch-per-bunch resolution, due to the low particle flux in the shielded alcove. This choice has been done due to the accessibility of the location, as well as the concern of whether the setup would survive a harsh LHC tunnel environment. For this reason, an assessment of the background (primarily cosmic radiation) has been done. It consists of averaging the Timepix3 measurements in the absence of any beam within the machine, revealing a background count rate of:

$$CR_{background} = \frac{N}{\Delta t} = 8.4 \pm 3.9 \text{ counts/60 s} \quad (11.1)$$

This background is assumed to come primarily from the cosmic galactic rays, with a lower count rate compared to the surface (the same detector measured about 20 counts/60 seconds) since the LHC is about 100 m underground. Moreover, natural decay chains could also occur underground (e.g. radon). Finally, there is no background assumed to come from beam-induced activation of materials or other equipment at the installed location.

11.2.1.2 Beam injection

The first relevant stage in the cycle of the beam is the INJECTION beam mode, when more and more protons at 450 GeV are periodically injected inside
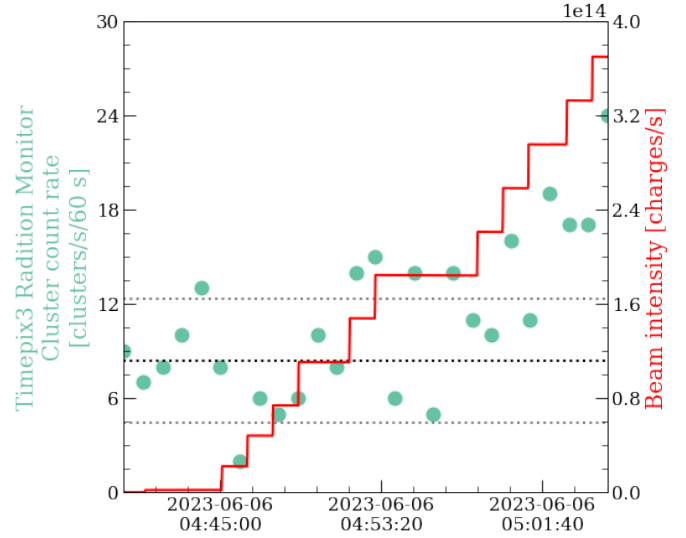
Figure 11.3: The measured Timepix3 radiation monitor cluster rate and the beam intensity during IN-JECTION beam mode, for fill #8890. The horizontal black (gray) line represents the average (standard deviation) from eqn. 11.1.

the LHC accelerator, as shown in fig. 11.3 for fill #8890. Figure 11.4 indicates how the Timepix3 radiation monitor count rate increases slightly above background in some fills, and only at high beam intensities (i.e. more than 10^{13} charges per beam).

11.2.1.3 Energy ramp up

The second beam mode of interest is the energy RAMP, when the proton beam is accelerated from an injection energy at 450 GeV to collisions at 6.8 TeV in Run 3 (2022-to date). At higher energy, the radiation showers that the beam losses generate are more powerful, leading to the production of more secondary particles, themselves at higher energies. The increase in the Timepix3 radiation monitor measurements in terms of cluster count rate and ToT rate with the beam energy is shown exemplarily for fill #8880 in fig. 11.5, while fig. 11.6 displays the measurements normalized to the beam intensity for all the fills. During energy ramp, the Timepix3 radiation monitor count rate increases significantly above the background rate. Nevertheless, some fills were ded-
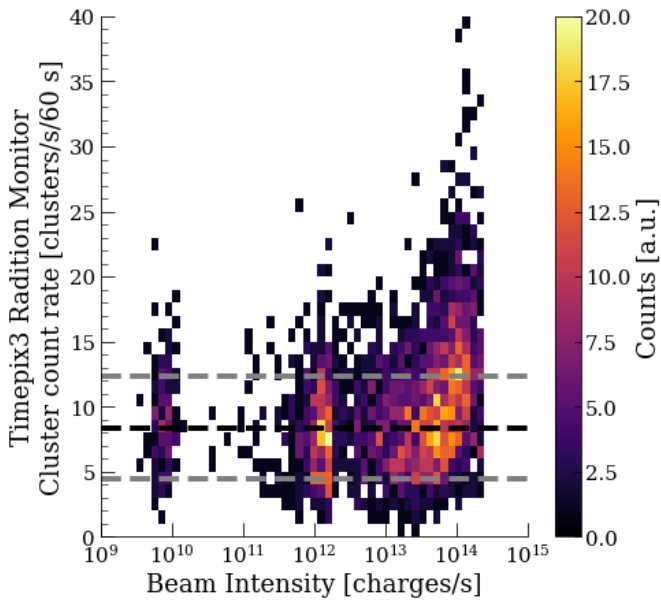
Figure 11.4: The measured Timepix3 radiation monitor cluster rate plotted against the beam intensity, but for all the fills, indicating that at high intensity beams, rates above the background (dashed lines) are measurable. The horizontal black (gray) line represents the average (standard deviation) of the natural radiation background from eqn. 11.1.

icated to energy ramp with just a couple of bunches (i.e. very low intensity), and these fills appear in fig. 11.6 as the data points that are overimposed with the horizontal line denoting the background.

11.2.1.4 Top energy

The previous beam modes revealed interesting patterns in the data, but the main priority of the analysis is the nominal top energy operation of the LHC, namely physics runs with luminosity productions during the STABLE beam mode until a BEAMDUMP is triggered or planned; such a fill is shown in fig. 11.7 for fill number #8880, while all the fills are shown in fig. 11.8, revealing a rather non-linear relation between the radiation levels and the beam intensity. This could be alluding to two possible explanations:

1. At higher beam intensities, there is more out-
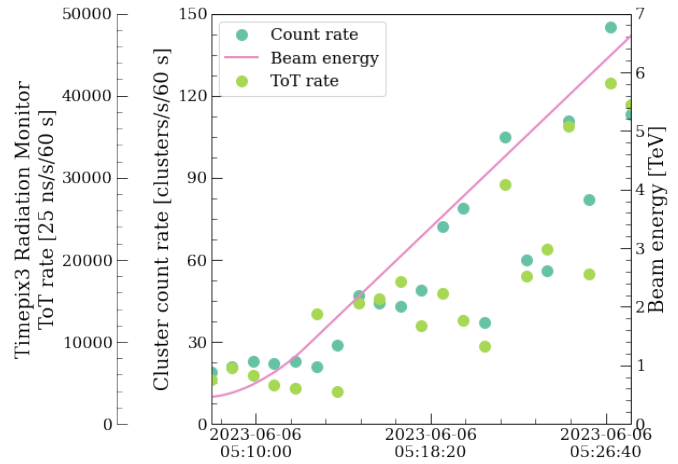
Figure 11.5: The measured Timepix3 radiation monitor cluster and ToT rate and the beam energy during RAMP, for fill #8880, with a nominal beam intensity at $3.7 \cdot 10^{14}$ charges/s.
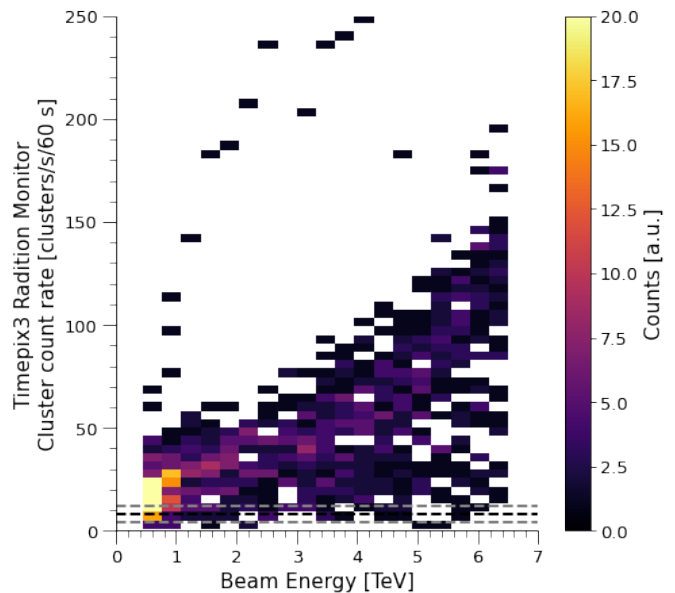
Figure 11.6: The measured Timepix3 radiation monitor cluster rate plotted against the beam energy, for all the fills, indicating a linear increase with beam energy, for high beam intensity fill (>10^{14} charges). The black (gray) line represents the average (standard deviation) background from eqn. 11.1.

gassing from the internal beam pipe surfaces, which leads to a temporary local increase in the

gas pressure, triggering more beam-gas colli-
sions and their associated radiation levels.

2. The vacuum of the LHC becomes better over
   time within a fill due to the same beam-residual
   gas interactions, which progressively remove
   more gas molecules from within the beam pipe
   and thereby reducing the collision rate.
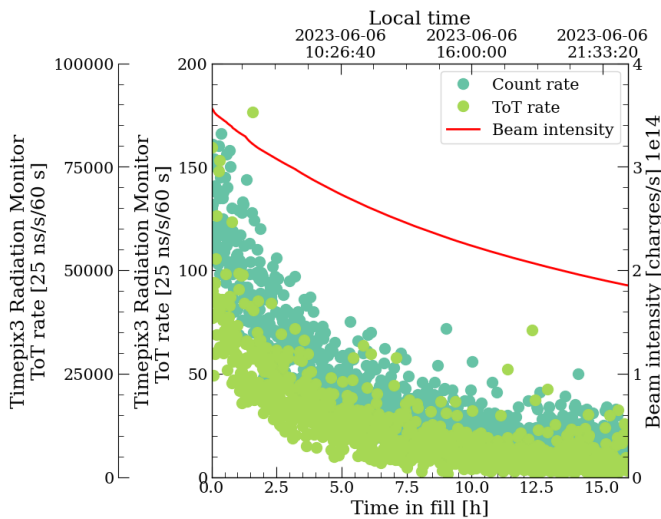
Figure 11.7: The measured Timepix3 radiation mon-
itor cluster and ToT rate and the beam intensity dur-
ing STABLE beam mode, for fill #8880.
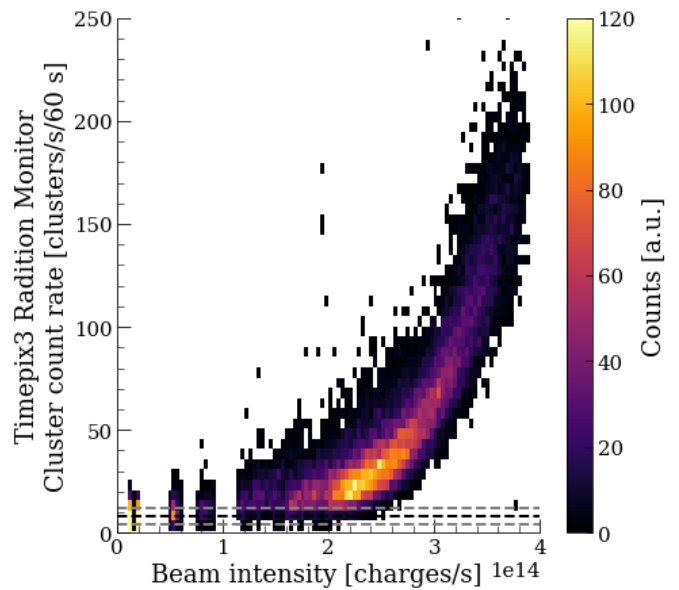
Figure 11.8: The measured Timepix3 radiation mon-
itor cluster rate for all STABLE beam fills, plotted
against the beam intensity, revealing an exponential
decrease.

11.2.2 Count rate vs. dose rate measurements

An important feature to be understood is not only
the count rate of particles and the deposited energy,
but also how these two measurements correlate to
each other. Figure 11.9 displays the ToT rate against
the count rate, revealing a linear relationship across
the energy increase from injection to flattop. This
linearity implies that the individual particles are not
depositing more energy in the Timepix3 sensor, but
the increase in the ToT rate is due to the increase
in the particle flux. This would imply that many
of the particles that arrive at the Timepix3 radiation
monitor are energetic enough to be within the min-
imum ionising particle (MIP) regime rather than stop-
ping within the active volume of the detector. As
such, if the measured particles are indeed MIPs, in-
creasing the energy would not significantly change
their stopping power, implicitly the measured depos-
ited energy. With the increase in the beam energy,
however, more particles could be generated in the
showers.

In particular for the Timepix3 radiation monitor, the
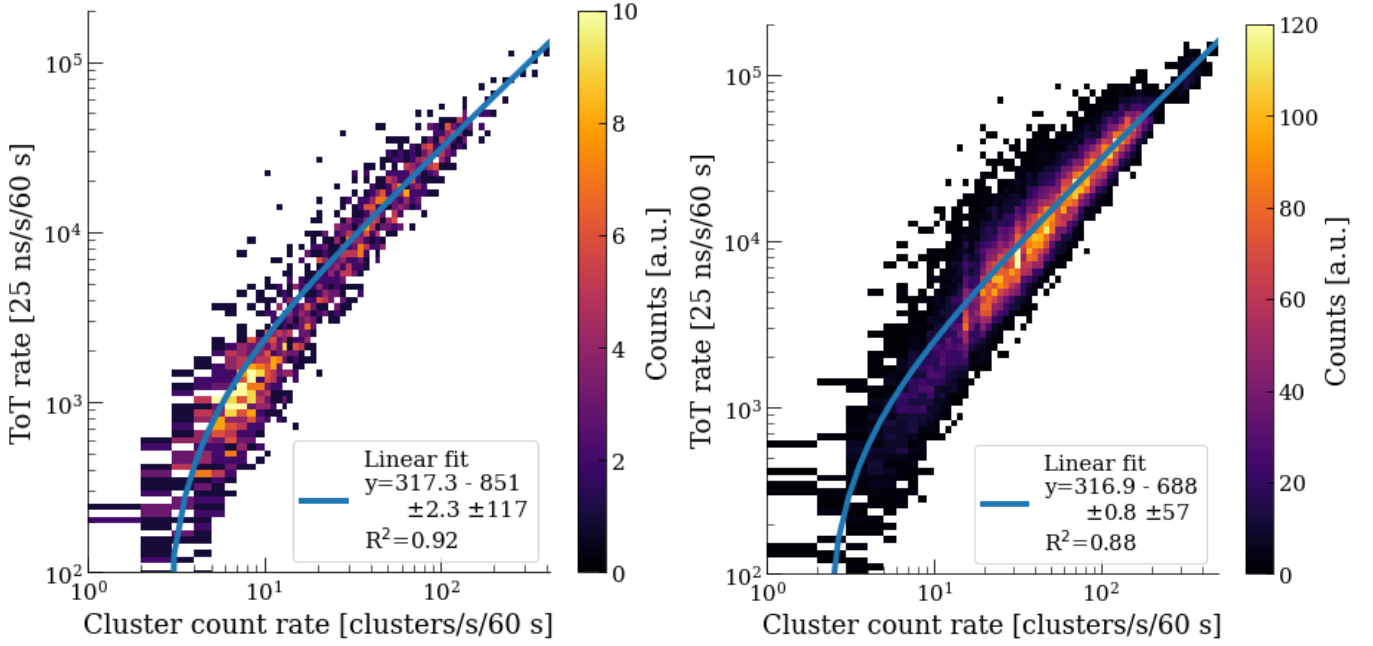
Figure 11.9: The measured Timepix3 radiation monitor cluster vs. ToT rate, for all the measured fills during **(Left)** the energy RAMP and **(Right)** STABLE beam modes, displaying a linear correlation (in log-log scale). Moreover, one can observe the difference in statistics, due to the duration of each beam mode: about 20 minutes for the energy ramp, and an average of about 10 h for stable beams.

conversion coefficients between the measured ToT rate (ToTR) and the counting rate (CR) is readily available from fig. 11.9. At nominal LHC top beam energy operation, the values are:

$$\text{ToTR}\left[\frac{25\,\text{ns}}{\text{s}}\right] = \text{CR}\cdot[316.9 \pm 0.8(\sigma_{fit})]\left[\frac{25\,\text{ns}}{\text{counts}}\right] \tag{11.2}$$

$$-[688 \pm 57(\sigma_{fit})][25\,\text{ns}] \tag{11.3}$$

However, the ToT is a quantity pertaining only to the Timepix3 radiation monitor. In addition, one would be interested to convert directly from/to the standard R2E quantities, e.g. from a dose (measured in Gy) value into a count rate value (ideally, particle flux, but in this case interaction rate with the caveats further discussed in section 12.2). The raw ToT measurement of the Timepix radiation monitor is converted into a dose rate in two steps:

1. the ToT is converted into deposited energy E_{dep}

via the calibration carried out in section 9.2.3, by inverting eqn. 9.9 at a cluster (N pixels) level:

$$E_{dep} = \frac{ToT_{reg} - N \cdot a}{b} \tag{11.4}$$

where a and b are the experimentally determined linear coefficients. This assumes that all the pixels are operating within the linear (regular) region of their calibration.

2. the energy is converted into dose (energy per unit mass), dividing by the mass of the silicon sensor, $m_{tpx} = V_{tpx} \cdot \rho_{Si}$, with the detector volume $V_{tpx} = 0.049\,\text{cm}^3$ and silicon density $\rho_{Si} = 2.65\,\text{g/cm}^3$. The total (active) volume of $V_{tpx} = A_{tpx} \cdot W_{50\,V} = 0.049\,\text{cm}^3$, where the chip area is $A_{tpx} = (255 \cdot 55\,\mu\text{m})^2 = 1.967\,\text{cm}^2$ and the depletion thickness $W = 250\,\mu\text{m}$

$$\text{Dose [Gy]} = E[\text{GeV}] \cdot \frac{c}{\rho_{Si} \cdot V_{tpx}} \tag{11.5}$$

where the constant $c = 1.6 \cdot 10^{-7} \text{mJ/GeV}$ yields the dose value in Gy. By combining the two eqn. 11.3 and 11.5, one can obtain an estimate of the dose rate (DR) from a counting rate (CR), and vice-versa, as:

$$ \text{DR} \left[\frac{\text{Gy}}{\text{s}} \right] = 4.42 \cdot 10^{-10} \text{ CR} \left[\frac{\text{particles}}{\text{s}} \right] $$

$$ \tag{11.6} $$

$$ \text{CR} \left[\frac{\text{particles}}{\text{s}} \right] = 2.26 \cdot 10^9 \text{ DR} \left[\frac{\text{Gy}}{\text{s}} \right] \tag{11.7} $$

$$ \tag{11.8} $$

The relation between the deposited energy (in this case, ToT) and the particle flux/fluence represent an on-going endeavour within the R2E activity. Going beyond the Timepix3 detector, the conversion coefficients between different measured or simulated radiation quantities would allow to infer the values for the other quantities with just one measurement; however, they could vary significantly depending on the radiation source and location. An example of conversion coefficients used for radiation levels specifications is readily available in ref. [80, 233, 234], and have been used for the High Luminosity LHC (HL-LHC) radiation levels specifications of sections 6.3 and 7.3.

12

Radiation field characterisation from the BGC operation using the Timepix3 radiation monitor

The previous section served to understand the measured values for the Timepix3 radiation monitor [22] in the absence of the Beam Gas Curtain (BGC) demonstrator [99–101]. Now, similarly to the first act, the discussion focuses on the isolation of the BGC signal from the Timepix3 radiation monitor data and its comparison with the FLUKA [18–20] simulation of the Large Hadron Collider (LHC) insertion region 4 (IR4), described in chapter 7.

The discussion is divided into two, first on the total ionizing dose (TID), where the comparison of the measured data with the simulated results is more straightforward. The particle count rate benchmark requires further analysis to be able to disentangle the contribution from each particle species, in particular important for the neutrons with a low detection efficiency.

12.1 Dose rate

For the benchmark between the simulated and measured data, the values are provided as rates, normalized per unit charge (based on the beam intensity) and pressure profile (based on the pressure readings), as highlighted in eqn. 5.1 in chapter 5.1.

12.1.1 Measured data

As already mentioned in chapter 7 about the BGC instrument, a gas target in the instrument has been injected in 2023 only during two fills within STABLE

BEAMS mode[1] before the 2023 proton run was prematurely ended on Monday, 17th of July, due to quenching of the superconducting inner triplet magnets located to the left of interaction point 8 (LHCb) of the LHC. The two fills with BGC gas injection at top energy in 2023 were fill numbers #8817 and #9035.

The raw ToT measurement of the Timepix radiation monitor is converted into a dose rate in as described in the previous section via eqn. 11.5. The dose rate measured by the Timepix3 radiation monitor is shown in fig. 12.1 for the two fills. For the data analysis, the same procedure as for the standard LHC beam loss monitor (BLM) described in section 7.2.1 has been followed: the background dose rate is fitted using exponentially decaying or constant functions based on the structure of the time periods before and after the gas injection, and the signal is extracted only during gas injection.

Due to the high fluctuations of the instantaneous count rates, an averaging approach similar to the BLM dose rate analysis of chapter 6 has been preferred, whereby the values in the entire time period under consideration are integrated, revealing the results of table 12.1. Regarding the dose measurement, no difference is observed for the values normalized to unit gas pressure and unit beam intensity between the two fills when the detector was placed at different incidence angles wrt. the accelerator, as expected since the dose is an intrinsic quantity. As such, the

---

[1]

average value of the two fills is used, yielding the dose rate (DR):

$$DR_{meas} = [7.36 \pm 1.69(\Delta_{syst}) + 0.22(\Delta_{stat})]$$
$$\cdot 10^{-8} \frac{\text{nGy}}{\text{s charge mbar}} \quad (12.1)$$

where the considered systematic uncertainty Δ_{syst} is the total of those presented in section 5.4, while the statistical ones $\Delta_{stat,meas} = 1/\sqrt{N}$ stems from the number of data points N measured (and averaged over 60 s) within the signal time period during BGC gas injection. To increase the robustness of this analysis, the detector has been redeployed during the technical stop 1 (TS1) in 2024 (June 6th), this time at $0°$ wrt. the beam. It is planned to take data until the end of the year, to cover also the ion operation of the LHC.

12.1.2 Simulated data

This study relies on the good benchmark achieved in chapter 7 between the beam loss monitor (BLM) [21] measured data and the FLUKA simulation. Using the same geometry, one can also include scoring regions at the Timepix3 location. Because of the small size of the detector with an area of $A_{tpx} = (255 \cdot 55 \ \mu\text{m})^2 = 1.967 \ \text{cm}^2$ and a volume of $V_{tpx} = A_{tpx} \cdot W_{50\,\text{V}} = 0.049 \ \text{cm}^3$, compared to the LHC accelerator spanning hundreds of meters, it is not computationally realistic to include an exact replica of the detector within the full geometry. For this reason, an equivalent larger air voxel as a cube with side length $L = 40$ cm is considered, assuming a uniform radiation field at detector's location inside the shielded alcove. A similar method has been previously applied successfully for radiation monitors (RadMons) [150–152] and for silicon diodes [66] at the CERN high energy accelerator mixed-field (CHARM) facility [30], as well as for RadMons and distributed optical fibre system (DOFRS) [153] at the LHC [43]. The scoring quantities of interest in this region are those that can be compared to the experimental data, in this case the dose (energy) deposition as it is done for the BLMs.

The radiation levels obtained from the FLUKA simulation are given normalized per nuclear inelastic interaction. In order to obtain the same parameters as in eqn. 5.1, one has to multiply by the longitudinal integrated gas density $\Theta_{BGC} = 5.27 \cdot 10^{-6} \ 1/\text{cm}^2$ (with the entire profile shown in fig. 7.2), normalized to the BGC pressured reading $p_{BGC,meas}$, thereby yielding the radiation levels as a rate per unit time, and per unit charge and pressure.

The FLUKA simulated dose rate (DR) at the Timepix3 location is then:

$$DR_{sim} = [4.44 \pm 0.80(\Delta_{stat}) \pm 0.62(\Delta_{syst})]$$
$$\cdot 10^{-8} \frac{\text{nGy}}{\text{s charge mbar}} \quad (12.2)$$

where the considered systematic uncertainty Δ_{syst} is the total of those presented in section 5.4, while the statistical one $\Delta_{stat,sim} = 18\%$ stems from the number of simulated particles that arrive at the Timepix3 location, in the shielded alcove of UX45, yielding a lower dose rate by a factor of 10^3 compared to the accelerator tunnel. To further improve this statistical error, one would require to launch further simulations, with only a $1/\sqrt{N}$ gain in the relative error.

12.1.3 Benchmark

The comparison of these measured data with FLUKA simulated values is straightforward: using the same simulation geometry of chapter 7, one can retrieve also the dose at the Timepix3 location, revealing an agreement level shown in table 12.2, with the ratio of the simulated to measured data results as:

$$R_{Dose} = \frac{Dose_{sim}}{Dose_{meas}} = 0.60 \pm 37\% \quad (12.3)$$

within the typical factor of 2 usually expected for these type of studies [37, 43], and similar to the agreement levels for the BLMs obtained in chapter 7.

Table 12.1: Timepix3 radiation monitor measured values, for the **dose rate**, average beam intensity N_p and pressure gauge reading p_{gas}, during the two fills with BGC gas injection, providing the numerical values during the signal and background time periods.

fill number	angle [deg]	N_p 10^{14} [charges]	Signal - bkg Dose rate [nGy/s]	Signal - bkg p_{gas} 10^{-8} [mbar]	Bkg. before Dose rate [nGy/s]	Bkg. before p_{gas} 10^{-8} [mbar]	Signal Dose rate [nGy/s]	Signal p_{gas} 10^{-8} [mbar]	Bkg. after Dose rate [nGy/s]	Bkg. after p_{gas} 10^{-8} [mbar]
8817	40	2.18	0.64	4.01	0.11	0.32	0.75	4.39	0.10	0.45
9035	10	3.19	0.99	4.25	0.28	1.50	1.28	5.24	0.14	0.48

Moreover, it almost agrees with unity, considering the 37% uncertainty. Regarding the dose agreement, there are a couple of considerations to be made:

1. The simulated dose is obtained in air, and assumed to match the one in silicon. This assumption could introduce systematic errors in the presence of particles involving different interaction mechanisms between the two materials. The most notable example is the ^{14}N(n,p)^{14}C reaction of thermal neutrons leading to an overestimation of the deposited dose in air [235]: the resulting 590 keV proton will deposits its energy through ionization processes [236]. Such a study of the dose deposition difference between air and silicon, within the scope of R2E, has been carried out in ref. [43], hinting towards a systematic 20% simulated underestimation.

2. The energy deposition of the particles in the Timepix3 sensor has been assumed to be within the linear regime of the calibration. However, it is known that for high energy deposition events, as mostly expected from neutron (albeit also protons, but to a lesser extent) nuclear inelastic interaction there is significant saturation, thereby practically lowering the measured value. Several correction factors for such events are currently under study, with one example given in section 9.2.4.5.

Table 12.2: Timepix3 radiation monitor measured dose rate values for the two fills with BGC gas injection, as well as the FLUKA simulated value.

fill number	Dose rate [10^{-8} nGy / (s·charge·mbar)]	Δ_{stat} [%]	Δ_{syst} [%]
simulation	4.44	18	14
8817	7.35	19	23
9035	7.37	3	23
ratio	0.60	37	

12.2 Particle count rate and discrimination

If the previous chapter described the average dose rate measurements of the Timepix3 radiation monitor, this chapter is dedicated to the particle count rate from Beam Gas Curtain (BGC) operation and its event-per-event energy deposition. The FLUKA code is used to evaluate the radiation field composition (particles species and their energy distribution), as well as the expected energy deposition in the Timepix3 sensor (detector response).

The same simulation as for chapters 7 can**not** be used, due to the low statistics at the Timepix3 radiation monitor location. If just for the dose (0D quantity) result, a statistical error of 18% was obtained, the computational time to obtain a satisfactory energy distribution (1D quantity) is not realistic. Nevertheless, from the existing simulation results, one notices that the electromagnetic component (gammas γ, electrons and positrons $e^{\pm}$) is negligible. One alternative
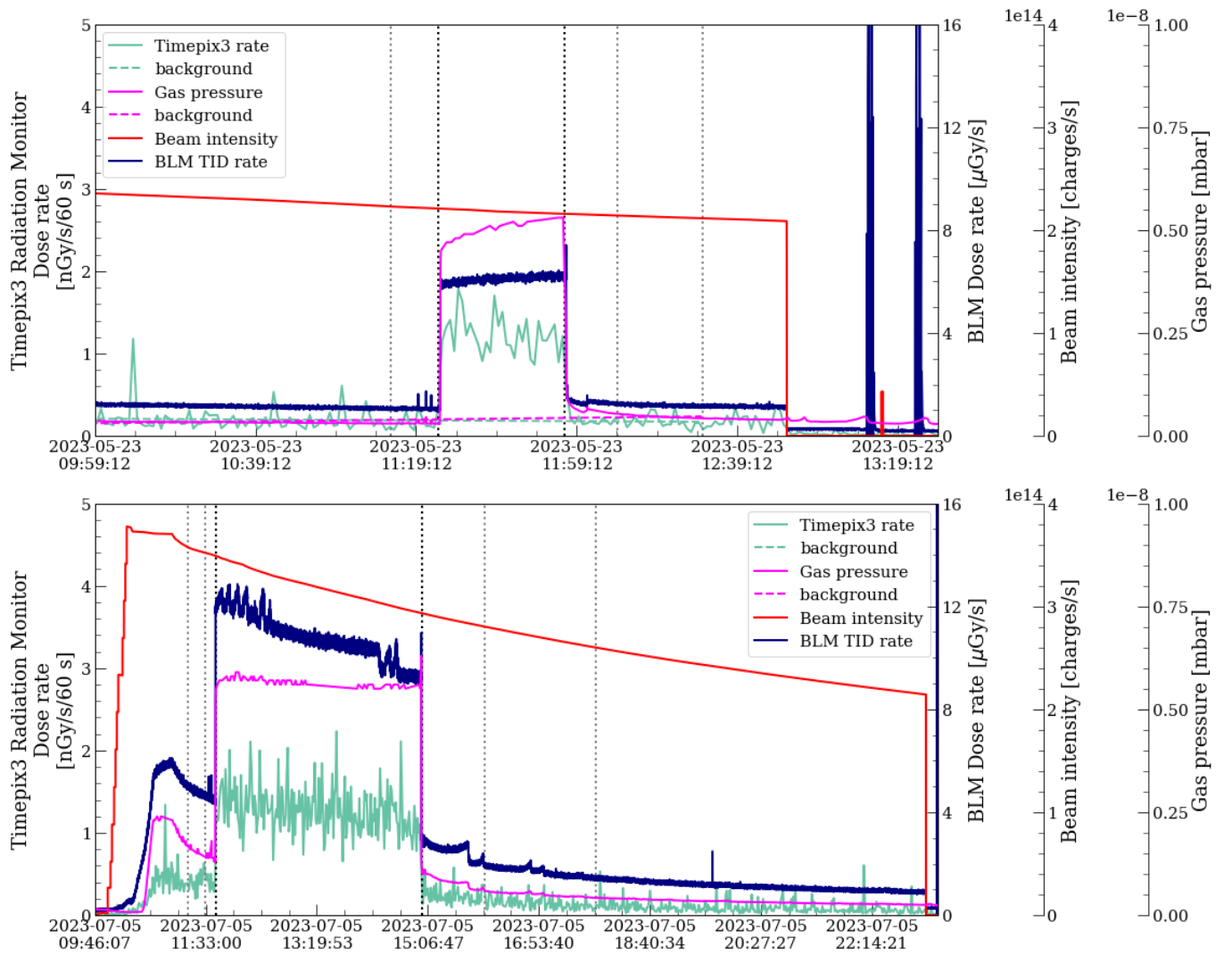
Figure 12.1: The measured dose rate for the Timepix3 radiation monitor (calibrated according to Section 9.2) and for the most exposed BLM downstream of the BGC during the LHC fills (**Top**) #8817 and (**Bottom**) #9035, with BGC gas injection, plotted alongside the beam 1 intensity N_p and the BGC pressure gauge reading p_{BGC}. Both the dose rates and the gas pressure measurements have been fitted with either exponentially decaying (following the beam intensity evolution) or constant background models.

that the FLUKA code provides is to deactivate the electromagnetic interactions[2], thereby speeding up the computational time[3] need for the simulation by a factor of $\mathcal{O}(20)$.

With previously well benchmarked simulations [37, 43] using the FLUKA Monte Carlo code on the dose rate, one can assume that the radiation field composition is also correctly evaluated. For this analysis, all

---

[2]The consequences of running the simulation with electromagnetic FLUKA (EMF) OFF is that the EMF particles are still produced, but not tracked (i.e. dumped on the spot), thereby altering the dose/energy deposition results; however, the kinematics of the hadrons and their interactions is correctly maintained.

[3]From an average central processing unit (CPU) time used to follow a primary particle of $\mathcal{O}(8 \cdot 10^2)$ down to $\mathcal{O}(3 \cdot 10^1)$

the simulated particles that arrive at the Timepix3 location are tracked, storing all their properties, in particular their particle species and kinematic variables (angle, energy, etc.). The radiation field includes different kinds of particles with broad energy spectra, all originating from the loss of TeV-scale beam particles or secondary collision products [43]. The case of insertion region 4 (IR4) is discussed in detail, and an overview of the implications in the harsher interaction point 1 (IP1) (ATLAS) accelerator tunnel is also presented.

12.2.1 Measured data

The first method to extract the measured data is similar to the one done before for the dose rate in section 12.1.1, namely, the background count rate is fitted using exponentially decaying or constant functions based on time periods before and after the gas injection. Similarly, due to the high spread of instantaneous count rates, an averaging approach has been preferred, namely: the values in the entire time period under consideration are integrated, revealing the results of table 12.3. Similarly as for the dose rate, no difference is observed for the measured count rate values normalized to unit gas pressure and unit beam intensity between the two fills when the detector was placed at different incidence angles wrt. the accelerator.

The comparison of the measured data of tab. 12.3 with the FLUKA simulated result is *not* straightforward, because FLUKA was used to find all the incident particles at the Timepix3 location, but not all of them will interact in the silicon sensor, yielding an equivalent cluster. As such, several considerations have to be made as outlined below; in particular, a classification of the particles tracks based on table 8.2 is performed. The scope of this detailed analysis is to disentangle as much information from the measured signal, ultimately attempting to make use of the particle identification (PID) capabilities of the Timepix technologies, some that currently studied in the literature [170, 197, 232].

1. Neutrons interact inelastically via the strong

force, with a mean free path λ in Silicon that is significantly longer than the sensor thickness of 300 μm, resulting in a very low interaction probability[4]. These inelastic interactions will leave *circular blobs* in the pixel matrix as shown in fig. 12.2 (charged particles that impinge the detector at nominal incidence also have the same shape).

2. Charged hadrons (protons, muons, pions) can result in:

   a) inelastic interactions, similarly to neutrons.

   b) ionization energy loss along their path (track). The energy loss per unit distance, also called stopping power or linear energy transfer (LET), or simply dE/dx, is described by the Bethe-Bloch formula [237], and will have a minimum ionising particle (MIP)-like interaction for high energy charged particles, leaving *straight tracks*, if not at nominal incidence.

   c) ionization energy loss from lower energy particles (few MeV), that have a larger linear energy transfer (LET), thereby depositing more energy and eventually stopping within the sensor, leaving *light or medium tracks*. Their dependence of dE/dx on depth is described then by the so-called Bragg curve [195].

   d) ionization losses followed by an inelastic interaction, which looks like a combination of a *track and a blob*, or a *heavy track*.

3. Since the simulation ignores the EMF component, tracks that are considered to stem from these particles are filtered out.

---

[4]A strategy to enhance the neutron count rate (that was not applied in this test campaign, but exploited in section 10.1) is to use neutron converters, i.e. thin material layers that have a higher neutron cross-section (e.g. lithium fluoride ^{6}LiF or boron carbide B_4C), emitting secondary particles (e.g. for ^{6}LiF, triton (at 2.73 MeV) and alpha (at 2.05 MeV) particles, that are detectable in the Timepix3 sensor. However, this strategy is only effective with thermal energy neutrons.

Table 12.3: Timepix3 radiation monitor measured values, for the **cluster count rate** and the signal-to-noise ratio (SNR), during the two fills with BGC gas injection, providing the numerical values during the signal and background time periods. The average beam intensity N_p and pressure gauge reading p_{gas} are the same as in tab. 12.1.

fill number	angle [deg]	Signal - bkg Count rate [counts/s]	SNR	Bkg. before Count rate [counts/s]	Signal Count rate [counts/s]	Bkg. after Count rate [counts/s]
8817	40	2.76	4.89	0.55	3.32	0.58
9035	10	4.07	2.94	2.04	5.46	0.73
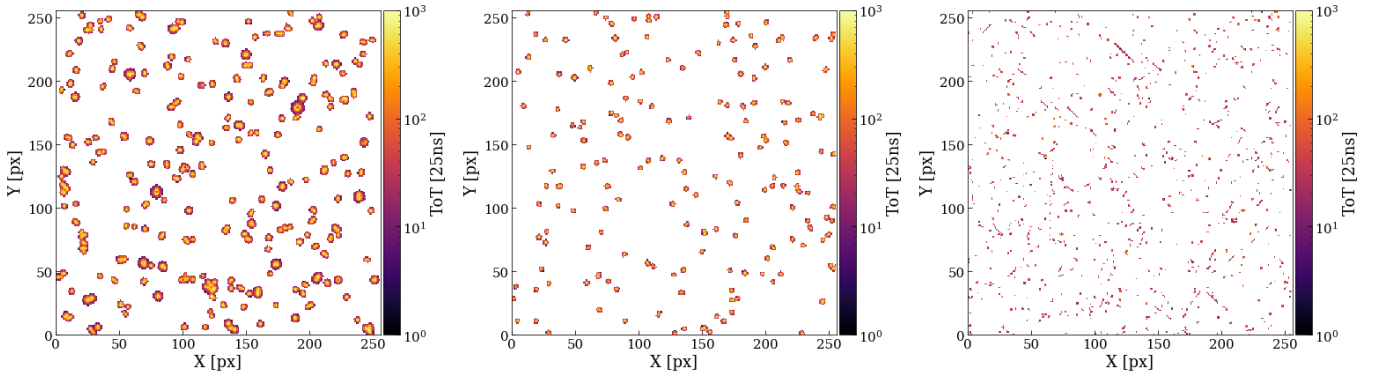
Figure 12.2: Measured IR4 Timepix3 data during BGC gas injections, represented on the pixel matrix, for several cluster types, according to the classification of table 8.2, for *blobs* that are: **(left)** heavy, **(centre)** medium, and **(right)** small.
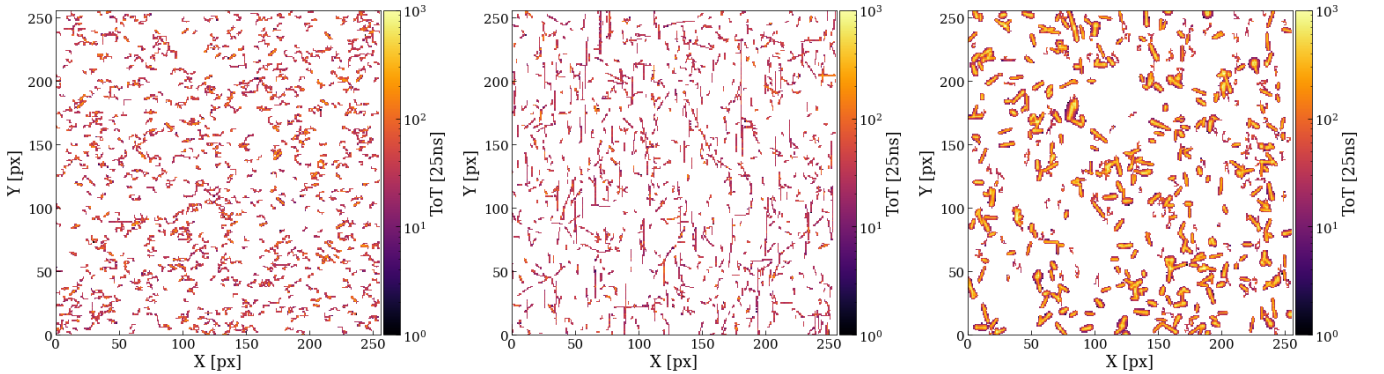
Figure 12.3: Measured IR4 Timepix3 data during BGC gas injections, represented on the pixel matrix, for several cluster types, according to the classification of table 8.2, for *tracks* that are: **(left)** curly, **(centre)** straight, and **(right)** heavy.

a) For electrons and positrons, the Bethe-Bloch formula must include additionally a term for the radiative losses (Bremsstrahlung), which starts to dominate above few tens of MeV. Moreover, since they have the a small mass (as atomic electrons), the electrons/positrons are deflected when they travel in sensors. Hence,
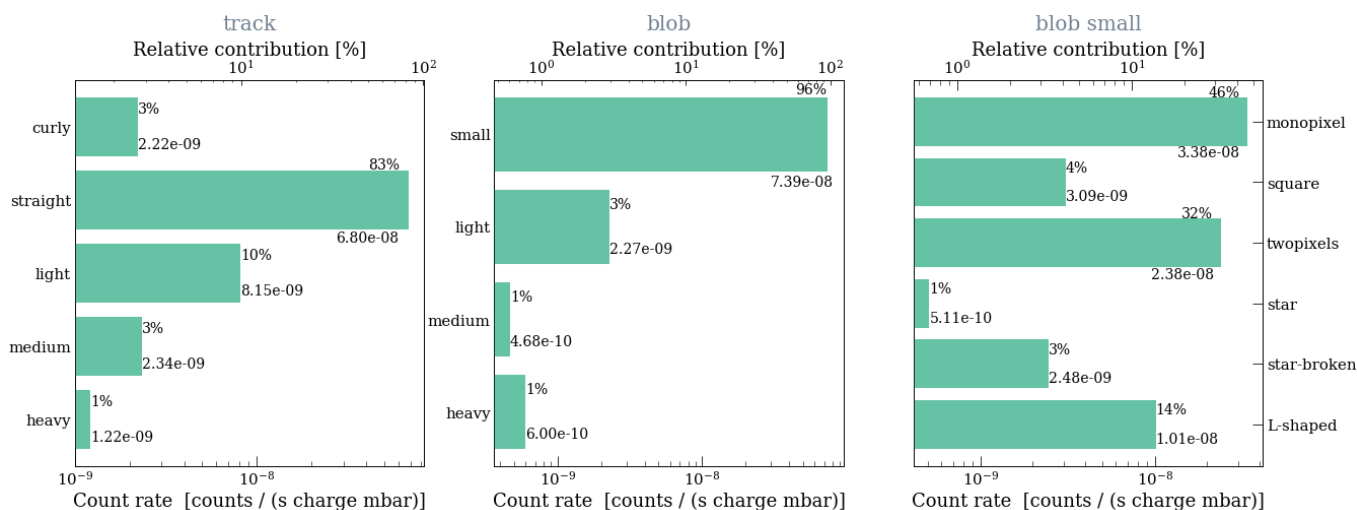
Figure 12.4: The Timepix3 radiation monitor data divided into cluster types and subtypes according to the classification from tab. 8.2, for (**left**) tracks and (**centre**) blobs. (**right**) The small blobs are further divided into their respective cluster families.

in pixelated detectors, these particles do not usually leave straight clusters, contrary to heavy charged particles, but are assumed to leave *curly tracks* inside the pixel matrix, as shown in fig. 12.3 (left). Moreover, it is important to note that in the keV energy range and below, electrons have short penetration ranges in matter and can therefore be easily stopped in detector dead layers, or in the protective case. On the opposite side of the spectrum, at higher energies (above few tens of MeV) that electrons go through the sensor in a straight line, similarly to the minimum ionising particle (MIP) regime.

b) Photons are neutral particles, and as such they do not ionize matter along their path. They interact through specific processes, emitting one or more charged particles that can then be detected. The photon spectrum is poorly populated in the radiation field at the UX45 shielded alcove of IR4, but the few photons that would arrive would interact through the photoelectric effect and Compton scattering, resulting in the ejection of an atomic electron in-

side the sensor volume, thus leaving *curly tracks* similar to lower energy electrons, with the exception that photons have a lower detection efficiency.

As such, for the comparison with simulated data, the results of tab. 12.3 can be further broken down by attempting to distinguish amongst the measured tracks several patterns that would allow to assign certain feature to a particle species. The analysis code is applied on the measured data to categorize the clusters based on the filtering criteria given in tab. 8.2, yielding the results shown in fig. 12.4, and further described in detail below.

1. One cannot distinguish at cluster level if the particle originated from the BGC operation (signal) or from the nominal LHC operation (background), with the exception of tracks for whom a further angular filter can be applied (as further investigated in section 13.2). For this reason, a global factor taking S_{eff} into account the signal-to-noise ratio (SNR) given in tab. 12.3 is considered here as

$$S_{eff} = \frac{SNR - 1}{SNR} \qquad (12.4)$$

145

is used to scale the measured results to an effective value that should correspond just to the BGC induced signal.

2. A total of 48.34% blobs and 51.26% of tracks are identified, with a remainder of about 0.41% uncategorized tracks.

3. Amongst the *tracks*, the majority (83%) are straight tracks, corresponding to MIP, with some clusters also exhibiting higher linear energy transfer (LET), thereby depositing more energy in the sensor, leading to a thicker track, categorized as *light*, *medium* or *heavy*. This class of tracks are considered to correspond to the charged particles, for which the total counting rate (CR) yields:

$$
\begin{aligned}
CR_{meas,charged,eff} &= CR_{meas,charged} \cdot S_{eff} \\
&= \left[52.9 \pm 12.2(\Delta_{syst}) \pm 1.6(\Delta_{stat}) \right] \\
&\quad \cdot 10^{-9} \frac{\text{counts}}{\text{s charge mbar}}
\end{aligned}
\tag{12.5}
$$

4. The last category of *tracks* are the *curly* ones, amounting to about 1.5% of the total number of clusters, which are assumed to be electron or positron events. As later on hinted also by the simulation results from fig. 12.5, very few electromagnetic particles are expected at the Timepix3 location in the UX45 shielded alcove.

5. Amongst the *small blobs*, almost half of the events are *mono-pixel events*, which could correspond to elastic neutron events, gamma interactions or even charged particles in the MIP regime hitting the detector at orthogonal (between -12 and 12°) incidence. Similar considerations can be applied for *two-pixel* or *L-shaped clusters*. Because of this ambiguity, these classes of clusters are not assigned to any particle species.

6. The remaining *small blobs* amount to at most 8%, and they correspond to *square* or *star* clusters, that could stem also from neutron-like events with slightly higher energy depositions,

enough for the charge to diffuse to some of the adjacent pixels.

7. Finally, amongst the *blobs*, less than 5% correspond to *light*, *medium* or *heavy* clusters, indicating that most interactions leading to blobs correspond to small energy depositions. These heavier clusters are assumed to come from inelastic neutron interactions.

$$
\begin{aligned}
CR_{meas,neutron,eff} &= CR_{meas,neutron} \cdot S_{eff} \\
&= \left[6.26 \pm 1.44(\Delta_{syst}) \pm 0.19(\Delta_{stat}) \right] \\
&\quad \cdot 10^{-9} \frac{\text{counts}}{\text{s charge mbar}}
\end{aligned}
\tag{12.6}
$$

12.2.2 Simulated data: second step simulation procedure

Figure 12.5 illustrates the simulated radiation field composition at the Timepix3 radiation monitor location inside the UX45 gallery, in the form of an energy spectrum in lethargy units[5]. The spectrum is obtained in a cubic voxel with length 40 cm (artificially large to increase the statistics). The radiation field contains charged hadrons (mostly protons, pions and muons) with energies up to at most 1 GeV and neutrons with energy extending down to the meV range (thermal scale). In order to quantitatively estimate from the simulation the effective count rate inside the Timepix3 radiation monitor, a second step simulation in FLUKA is performed, where a beam with the particle field composition and with the energy distribution from fig. 12.5 is shot at the detector model. Then, one retrieves not just the count rate (hit/no hit), but also the expected energy deposition, shown in fig. 12.6 in the LHC mixed field at IR4. Finally, table 12.4 quantifies the fraction of particle hits

---

[5]Lethargy plots must be used in general for any particle type with an energy spectrum extended over many orders of magnitude. It allows giving the correct importance to different energy ranges in the plot, i.e. the area of each bin is proportional to the corresponding integral flux, and comparing the bins one has immediately the feeling in which energy bin one has more/less particles.
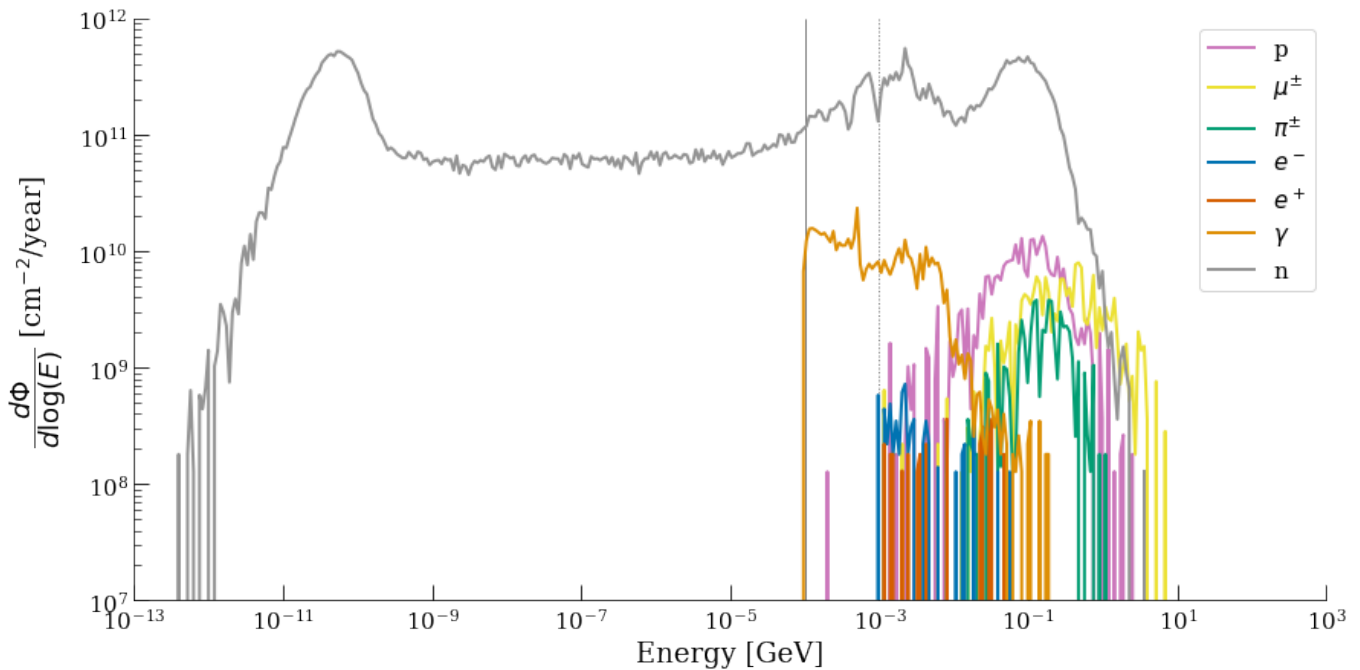
Figure 12.5: Energy spectra (in iso-lethargic units) simulated with FLUKA at the Timepix3 radiation monitor location inside the UX45 gallery. The electromagnetic FLUKA (EMF) component is obtained from the initial simulation (used for the dose rate), while the hadrons are obtained from a dedicated simulation ignoring the EMF interactions. The vertical continuous (dotted) gray lines indicate the lower energy threshold set for hadrons and gammas (electrons and positrons) in the simulation, i.e. 10^{-4} GeV (10^{-3} GeV).

from different particles in the LHC mixed field at insertion region 4 (IR4), leading to energy depositions in three energy regimes of the Timepix3 detector: (i) below the detection threshold of 8 keV, which will not be recorded in the measured data, (ii) in the linear calibration region, and (iii) above the 2 MeV cluster-level saturation threshold. In addition, table 12.4 also quantifies the fraction of the particle count rates and the total ionizing dose (equivalent to the fraction of deposited energy) falling into the same three energy regimes. The discussion is separated, as for the measured data, amongst three particle categories: the electromagnetic component, hadrons and neutrons.

1. **The electromagnetic component**: Photons, electrons and positrons are virtually absent, as the location is shielded by a concrete wall of 1.2 m, and, as such, the environment also does not display heavy ions (e.g. alpha particles).

2. **Neutrons**: Although very abundant in number, the neutrons have a wide spread of energy ranging from GeV down to the meV (thermal) scale. As neutral hadrons, neutrons typically undergo inelastic nuclear interactions, with varying cross-sections (however, very small) depending the material and possible capture cross-sections at specific energies. As such, the measured count rate is expected to scale with the particle fluence (and not total count rate as for the charged hadrons) passing through the Timepix3 detector. Moreover, a fraction (7.74%) of them are expected to yield energy depositions below the ASICs detection threshold of $\mathcal{O}(10\,\text{keV})$, however amounting to less than 0.03% of the total deposited TID. The majority (78.5%) of neutrons will lead to energy depositions within the linear calibration regime, but again amounting only to 15.7% of the total deposited TID. Finally, although only 13.8% of the
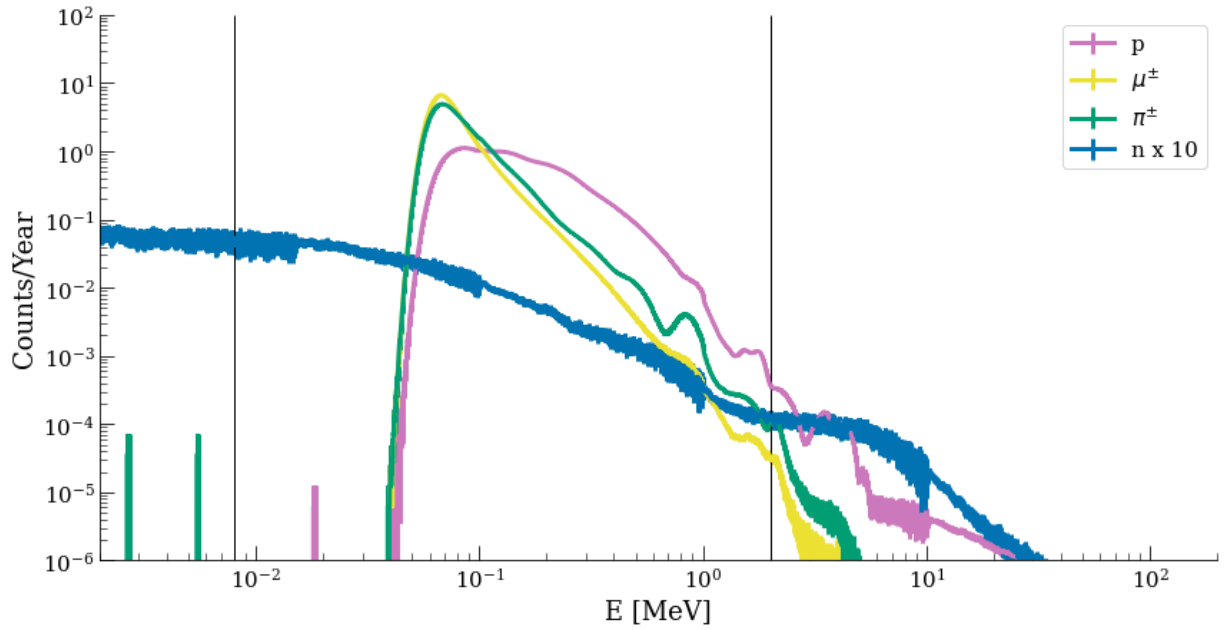
Figure 12.6: Distribution of the energy deposited in the active volume of the Timepix3 radiation monitor by the particles composing the LHC mixed radiation field (from fig. 12.5), simulated with FLUKA with perpendicular incidence on the sensor. The vertical lines correspond to the detection threshold at 8 keV, below which pixel hits are missed, and the 2 MeV/cluster level, above which one sees evidence of saturation effects. The neutron histogram is affected by the low detection efficiency, and it is scaled up by a factor of 10 for visualization purposes.

Table 12.4: The expected fraction of particle counts and fraction of the total ionizing dose (TID) deposited in the Timepix3 radiation monitor, as simulated in FLUKA from the radiation field shown in fig. 12.5, below the detection threshold (8 keV), in the linear calibration regime, and above the saturation threshold of 2 MeV.

Particle	Below threshold		Linear Regime		Saturation effects		Total Detection Efficiency [%]	Count rate [10^{-9} counts/ (s charge mbar)]	
	counts [%]	TID [%]	counts [%]	TID [%]	counts [%]	TID [%]		Relative [%]	
Protons	0	0	99.7	94.4	0.26	5.56	100	36.6	17.2
Muons	0	0	99.9	99.8	<0.01	0.18	100	37.4	17.6
Pions	<0.01	<0.01	99	99.4	<0.01	0.61	100	12.5	5.9
Neutrons	7.74	0.03	78.5	15.7	13.8	84.3	0.256	13.5	6.4

neutrons are expected to yield energy depositions above the saturation threshold of 2 MeV, these events would actually contribute to 84.3% of the total deposited TID. Finally, the simulated neutron count rate is:

$$CR_{sim,neutron} = \Phi_n \cdot \epsilon n, eff \cdot (1 - f_{n,\text{below threshold}})$$
$$= \left[6.41 \pm 1.20(\Delta_{stat}) \pm 0.90(\Delta_{syst}) \right]$$
$$\cdot 10^{-9} \frac{\text{counts}}{\text{s charge mbar}} \qquad (12.7)$$

where Φ_n is the neutrons fluence (in counts/(s cm^2), with $\epsilon n, eff = 0.256$ the total effective cross section for neutrons as per the second step FLUKA simulation shown in tab. 12.4. The considered systematic uncertainties Δ_{syst} are those presented in section 5.4, while the statistical one stems from the number of simulated neutrons that arrive at the Timepix3 location and interact with the sensor.

3. **Charged hadrons**: Protons, pions and muons have energies up to at most 10 GeV, and they are expected to have a 100% detection efficiency; as such, the measured count rate is expected to scale with the absolute number of particles reaching the Timepix3 detector. The majority of the charged hadrons that would reach the detector in the LHC tunnel have high energies and long ranges, such that they pass through the entire active volume depositing similar amounts of energy (corresponding to the main peaks in fig. 12.6), implying that the detector can be used to measure charged particle fluxes, but not capable of restoring the full energy spectrum of fig. 12.6. Charged particles with shorter range can deposit more energy, up to a maximum given by the particle energy for which the range is equal to the active volume thickness (which is evaluated at $W = 250\,\mu\text{m}$, for a bias voltage of $V_{bias} = 50\,\text{V}$), which is about 5 MeV for protons and about 2 MeV for muons and pions. At these energies, the distributions in the figure are exhibiting visible *knees*[6]. The vast majority of the hits fall in the linear calibration regime, and most of the TID also fall into the same category, with a small fraction of hits ($<0.3\%$) depositing more than 2 MeV each). Finally, the simulated charged particles count rate is:

$$CR_{sim,charged} = \Phi_{c.h.} \cdot \epsilon_{c.h}^{eff} \cdot (1 - f_{n,\text{below threshold}})$$
$$= [40.79 \pm 5.71(\Delta syst) \pm 0.57(\Delta stat)]$$
$$\cdot 10^{-9} \frac{\text{counts}}{\text{s charge mbar}} \qquad (12.8)$$

where $\Phi_{\text{charged hadrons}}$ is the charged hadrons flux (in counts/s), with $\epsilon_{c.h.,eff}$ being the effective detection efficiency for charged hadrons (assumed at 100%), and $f_{\text{below threshold}}$ the fraction of particle hits leading to energy depositions below the Timepix3 detection threshold, as per the second step FLUKA simulation shown in tab. 12.4. The considered systematic uncertainties Δ_{syst} are those presented in section 5.4, while the statistical one stems from the number of simulated charged hadrons that arrive at the Timepix3 location and interact with the sensor.

All hadrons can also interact inelastically, in which case higher energy deposits are expected, often well beyond the saturation threshold, as clearly visible in fig. 12.6. Indeed, the simulations show that the largest energy depositions in the Timepix3 radiation monitor at the LHC are caused by inelastic nuclear reactions. Such high energy deposition clusters could potentially be used to indirectly measure the high energy hadron equivalent (HEHeq) fluence (similarly to the radiation monitor (RadMon) detection mechanism [150]). This can be done either by operating with a high threshold, thereby filtering out the lower energy deposition events (i.e., the elastic interactions), but then the advantages wrt. the RadMon are diminished, or if the cluster properties would exhibit clear signatures that would allow the discrimination of such events (e.g. *heavy blobs*).

12.2.3 Benchmark

Now, the comparison of the count rates for the measured with FLUKA simulated data can be performed, based on the selection criteria shown in tab. 12.5. The ratios of simulated to measured data value is shown in tab. 12.6, with the total values as:

---

[6]drastic changes, typically connected to threshold and/or binning effects.

Table 12.5: Data selection criteria for both the simulated and the measured data for the Timepix3 radiation monitor benchmark of the particle count rate.

Data	Particle species	Selection criteria/Normalization
Simulated	electrons, positrons, gammas	discarded EMF component
	charged hadrons	normalized to flux (counts)
	neutrons	normalized to fluence (counts/cm^2)
Measured	global	SNR scaling factor: eqn. 12.4
	charged hadrons	selected: tracks
	neutrons	selected: blobs (non-small) and small blobs (square and stars)
	electrons/positrons	removed: curly tracks
	photons	removed: small blobs (except square and stars)

Table 12.6: Timepix3 radiation monitor measured **count rate** values for the two fills with BGC gas injection, as well as the FLUKA simulated values. The results here are filtered based on the criteria described in the text and in tab. 12.5.

particle species	Data	Count rate [10^{-9} counts / (s·charge·mbar)]	Errors Δ_{stat} [%]	Errors Δ_{syst} [%]
neutrons	sim.	6.41	2.9	14
	meas.	6.26	1.14	23
	ratio	1.02		27
charged hadrons	sim.	40.79	1.41	14
	meas.	52.93	0.56	23
	ratio	0.77		27
total	sim.	47.2	3.3	14
	meas.	59.19	1.3	23
	ratio	0.80		27

$$R_{CR} = \frac{CR_{sim}}{CR_{meas}} = 0.80 \pm 27\% \qquad (12.9)$$

within the typical factor of 2 usually expected for these type of studies [37, 43], and similar to the agreement levels for the BLMs obtained in chapter 7. Moreover, it agrees with unity, considering the 27% uncertainty level. Similarly to the dose agreement, it hints towards a simulation underestimation compared to the measured data. Moreover, there are a couple of considerations to be made:

1. On the measurement side, the very small (mono- and two-pixel) clusters are ignored, but they could originate from particle interactions that are nevertheless simulated. This could explain why this agreement is slightly better than the previous TID results.

2. The majority of the expected count rates come from charged particles (more than 85% according to the simulation, and at least 50% from the measurement side), which can be better predicted and isolated, as opposed to the neutrons which can can a wide range of energy depositions, with a very small interaction rate.

12.3 Other interaction regions

12.3.1 Interaction point 1

Similarly, the case of the radiation field at the accelerator around interaction point 1 (IP1) is presented, from a simulation standpoint, while ref. [160] presents Timepix3 measurements from the a toroidal LHC apparatus (ATLAS) cavern [8].

Figure 12.7 illustrates an example of the radiation field composition in the LHC tunnel in the proximity of the final focusing magnets at 50 m from interaction point 1 (IP1), hosting the ATLAS experiment, in the form of an energy spectrum in lethargy units simulated with the FLUKA code. In this position, the radiation field originates from the secondary products of inelastic proton-proton collisions in the IP, and the
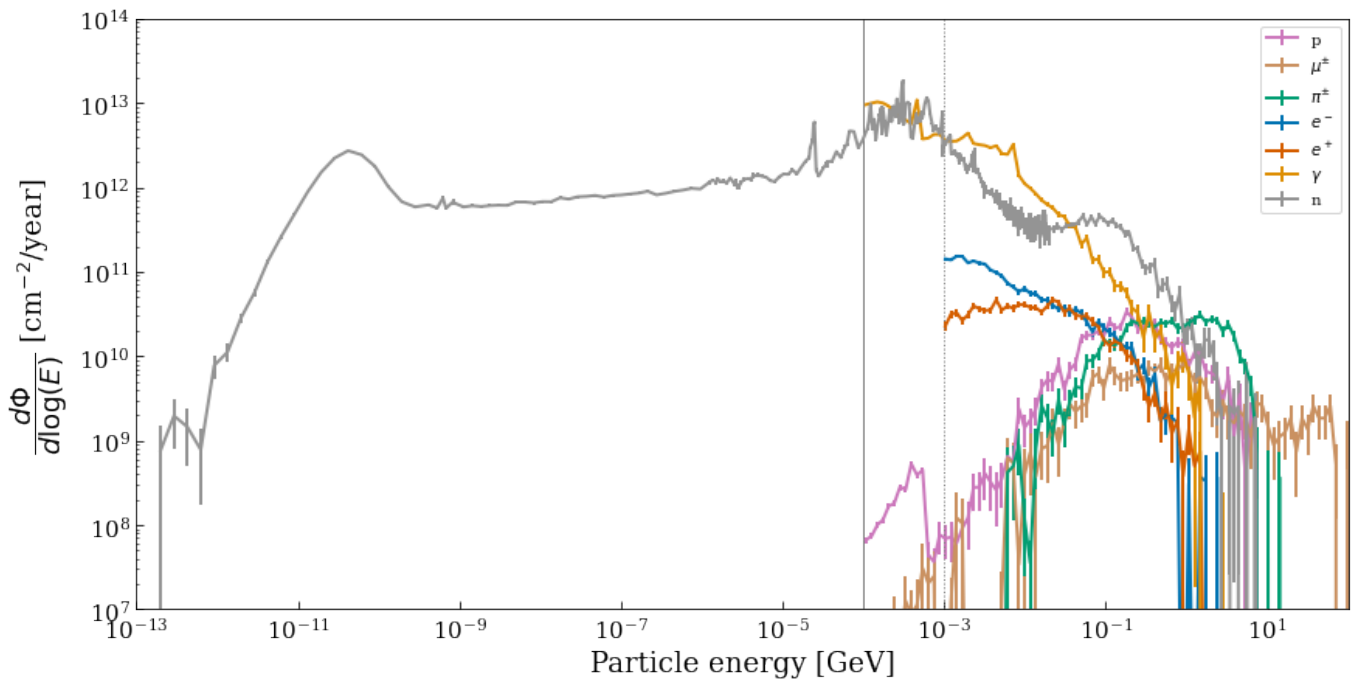
Figure 12.7: Energy spectra (in lethargy units) simulated with FLUKA at floor level below the beam in the LHC accelerator tunnel near the interaction point 1 (IP1) hosting the ATLAS experiment in 2018, immediately downstream of the inner triplet magnets. The vertical continuous (dotted) gray lines indicate the lower energy threshold set for hadrons and gammas (electrons and positrons) in the simulation, i.e., 10^{-4} GeV (10^{-3} GeV) [43].

spectrum is obtained in a $20 \times 20 \times 20\,\mathrm{cm}^3$ volume at floor level around 1 m below the accelerator beam line. The radiation field contains charged hadrons (mostly pions and protons) with energies up to several GeV, neutrons with energy extending from the meV range (thermal) to the GeV scale, electromagnetic particles (photons, electrons, positrons) from below the MeV scale to the GeV scale, and muons up to tens of GeV. Instead, the environment is characterised by the absence of heavy ions and by a scarce presence of alpha particles, while the relative contribution of the different particle types and the respective energy distributions can vary depending on the position. The spectrum given in fig. 12.7 is used as an example of the radiation field for which the Timepix3 radiation monitor could be optimised for.

Similarly as before, table 12.7 quantifies the fraction of particle hits from different particles in the LHC mixed field, leading to energy depositions below the

detection threshold of 8 keV in the linear calibration region, and above the 2 MeV cluster-level saturation threshold. In addition, the table also quantifies the fraction of the total ionizing dose (equivalent to the fraction of deposited energy) falling into the same three categories.

1. For charged particles, the vast majority of the hits fall in the linear calibration regime, and most of the TID also fall into the same category (with the partial exception of protons, for which 24% of the TID is deposited by the small fraction of hits depositing more than 2 MeV each).

2. Concerning photons, 22% of the hits fall below the detection threshold, but they only correspond to 2% of the TID and no hits are expected to be above the saturation limit.

3. Lastly, a very large fraction of neutron hits lead to negligible amounts of TID, but while only
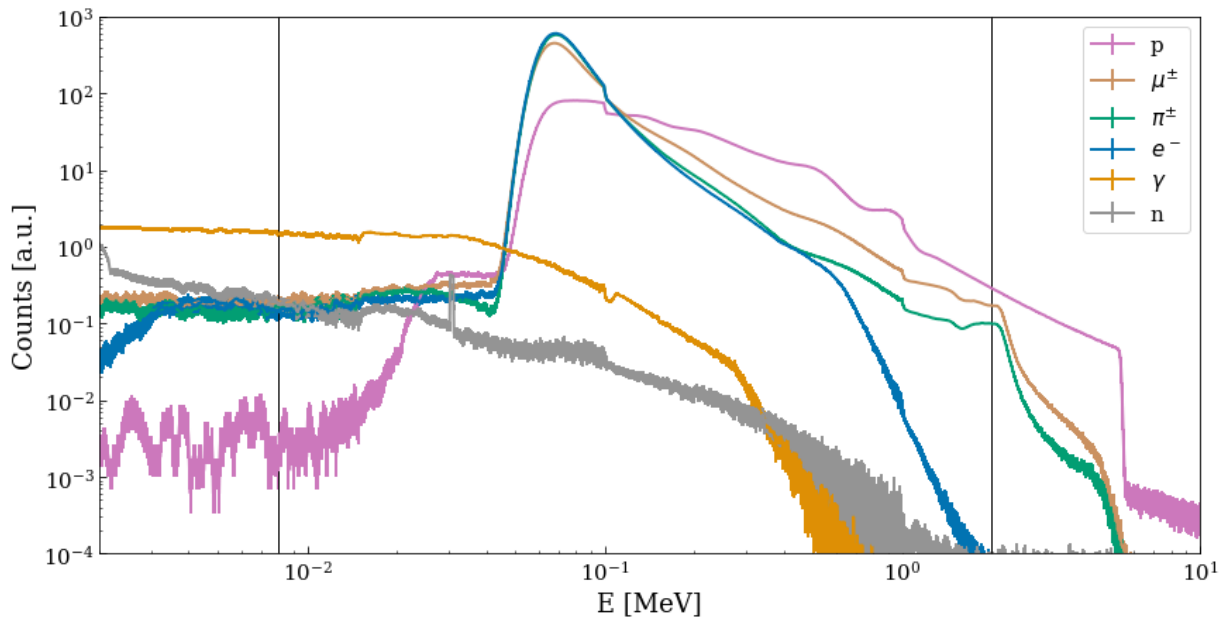
Figure 12.8: Distribution of the energy deposited in the active volume of the Timepix3 radiation monitor by the particles composing the LHC mixed radiation field (from fig. 12.7), simulated with FLUKA with perpendicular incidence on the sensor. The vertical lines correspond to the detection threshold at 8 keV, below which pixel hits are missed, and the 2 MeV/cluster level, above which one sees evidence of saturation effects.

a small fraction of the hits is above the saturation threshold, these correspond to inelastic collisions that are responsible for the dominant fraction of the total TID.

12.4 Summary

The results of this chapter confirm that the Timepix3 detector technology can be used as a reliable radiation monitor for the LHC mixed field. The results in table 12.2 prove the detector's capabilities as an instantaneous dose rate detector, agreeing with the FLUKA simulated values with a ratio of simulated to measured data at $R_{Dose} = 0.60 \pm 35\%$, within the expected factor of 2 for this type of studies. The advantage of the low detection threshold is that it can be placed in a shielded alcove such as UX45, far away from the highest radiation levels, but still capable of measuring the Beam Gas Curtain (BGC) signal

from the nominal LHC operation, with good sensitivity.

Complementarily, the results in table 12.6 also confirm that the Timepix3 radiation monitor can be regarded as a count rate monitor. Differently compared to the RadMons, which measure single event upsets (SEU) and indirectly inferring the high energy hadron equivalent (HEHeq) from previous calibrations, the Timepix3 technology is capable to measure at a particle by particle resolution, at least for charged hadrons. The measured values are compared with FLUKA simulated results, revealing a simulated to measured data ratio of $R_{CR} = 0.80 \pm 27\%$. However, the slightly better agreement comes with several assumptions done on the selections done on both the measured and simulated data.

Moreover, the expected energy deposition is also provided via the FLUKA simulation. Most of the charged particles are expected to deposit most of their TID within the linear regime of the Timepix3

Table 12.7: The expected fraction of particle counts and fraction of the total ionizing dose (TID) deposited in the Timepix3 radiation monitor, as simulated in FLUKA, below the detection threshold (8 keV), in the linear calibration regime, and above the saturation threshold of 2 MeV, for the radiation field simulated in IP1.

Particle	Below Threshold		Linear Regime		Saturation Effects	
	Counts [%]	TID [%]	Counts [%]	TID [%]	Counts [%]	TID [%]
Protons	12×10^{-6}	1.14×10^{-8}	97	76	3	24
Muons	0.7×10^{-3}	7.51×10^{-4}	99	93	0.8	7
Pions	15×10^{-3}	8.16×10^{-4}	99	95	0.3	5
Electrons	12×10^{-3}	9.73×10^{-4}	99	99	1.25×10^{-4}	2.93×10^{-3}
Photons	22	2	78	98	0	0
Neutrons	92	1	7.4	28	0.4	71

calibration. However, for the neutrons, a fraction of the energy depositions will be either below threshold, 7.74% of the total counts, but only amounting to 0.03% of the total TID, or above the saturation limit, 15.7% of the total counts, leading to a loss of 84.3% from the TID information.

Finally, the usages of the Timepix3 as a standard radiation monitor are proven in the low radiation field of IR4, with the harsher case of interaction point 1 (IP1) evaluated here from a simulation perspective only.

13

More capabilities of the Timepix3 radiation monitor at the LHC IR4

Having now proven the usability of the Timepix3 detector [22] as a standard monitor for radiation to electronics (R2E) [16] purposes at the Large Hadron Collider (LHC) [1] at CERN, it is natural to further examine what else can this novel detector provide. In addition to acting as a dose and particle rate monitor, two more possibilities are explored here thanks to the pixel matrix information, namely using the monitor as a: (i) radiation source locator, by deducing the origin of the incoming radiation, and (ii) linear energy transfer (LET) detector.

Similarly to the previous act, the discussion focuses on the isolation of the BGC signal from the Timepix3 radiation monitor data and its comparison with the FLUKA [18–20] simulation of the Large Hadron Collider (LHC) insertion region 4 (IR4), described in chapter 7.

13.1 Timepix3 as a radiation source locator

Benefiting from the pixel matrix, charged particles that leave *straight* tracks within the detector across multiple pixels can be used as a tool to infer the spatial origin of radiation. Several cluster variables can be computed (as outlined in section 9.2.4.1), in particular the cluster polar angle Θ (or angle of incidence wrt. the normal to the surface). Figure 13.1 exemplifies how a track with length of 1 pixel (*mono-pixel*) corresponds to a polar angle between -12 and 12°, a track with length of 2 pixels (*two-pixel*) to an angle between 0 and 24°, a track with length of 3 pixels

(if straight) to an angle between 12 and 36°, and so on. Considering the position of the detector inside the UX45 gallery, with its plane at an angle wrt. the accelerator beam (either 40° or 5°, as summarised in table 11.1), one can convert the angle of incidence Θ of incoming particles into a specific region along the accelerator tunnel, as illustrated in fig. 13.2.
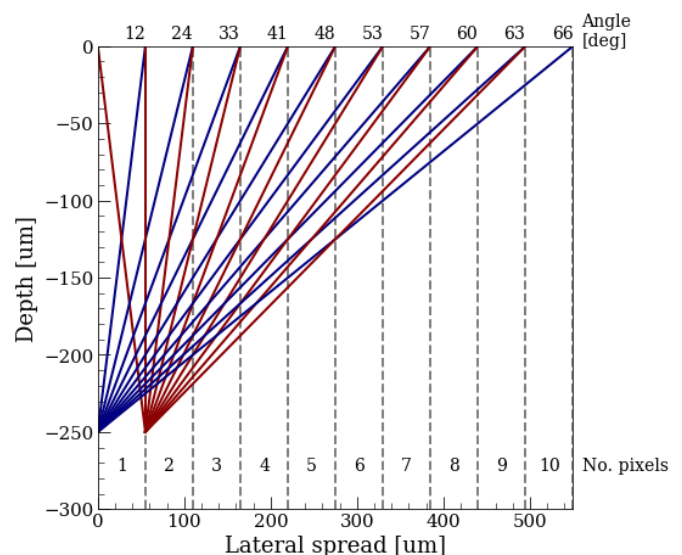
Figure 13.1: Geometry of the Timepix3 matrix, translated into angle of incidence (polar angle Θ) based on the length of the cluster (in number of pixels), assuming a depletion volume thickness of $W = 250\,\mu m$ out of the sensor thickness of $300\,\mu m$. The blue lines indicate the maximum angle, while the red lines indicate the minimum angle.
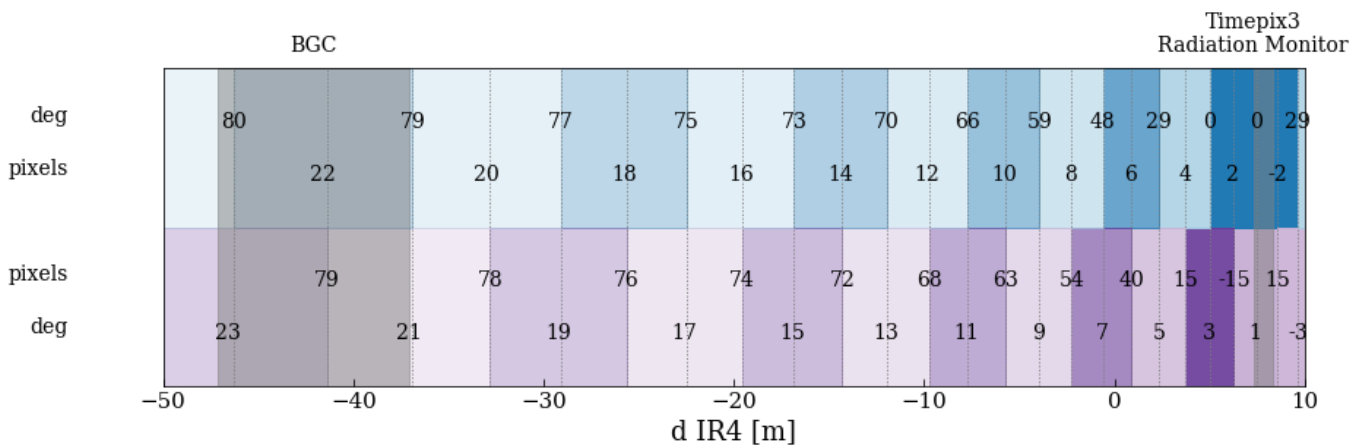
Figure 13.2: The distance wrt. insertion region 4 (IR4) corresponding to the different polar angles for particles on the Timepix3 detector plane. The position of the Beam Gas Curtain (BGC) and of the Timepix3 radiation monitor are also indicated with gray shading.

13.1.1 Measured data

On the measured data side, several filters (summarised in tab. 13.1) are applied to select only the relevant clusters that can be used to retrieve information about their possible location:

1. Cluster type: In particular, as per the classification from table 8.2, *blobs* are not useful, and only *tracks* can be used for this reconstruction procedure. A consequence of this is that only tracks with at least 3 pixels ($A \geq 3$) are considered.

2. Azimuthal angle ϕ: one distinction that can be done to differentiate between the radiation coming from the accelerator line and other sources of background radiation (e.g. cosmic radiation, assumed as isotropic) is to apply a cut on the azimuthal angle ϕ (representing the angle on the 2D pixel matrix). Based on the geometry of the detector placement in the shielded alcove adjacent to the accelerator tunnel, one expects that tracks coming from the beamline to be aligned with the y-axis of the detector (along $\phi = \pm 90°$). Figure 13.3 confirms these expectations, showcasing that most of the radiation comes indeed from the $\pm 90°$ direction. Due to the discrete pixel array with a pixel pitch

of $p = 55\,\mu\text{m}$, some artefacts (more peaks) are visible, at multiples of $\pm 11.25°$. A selection of $\Delta\phi = \pm 10°$ around the maxima at $\pm 90°$ is performed. This is done also for the simulated data, though it is less relevant since the only simulated radiation source is the Beam Gas Curtain (BGC), situated at the beam axis.

3. Moreover, taking advantage of the time of arrival (ToA) information, one could further infer whether the track came from the positive (+90°, corresponding to the left side of the accelerator, where the BGC is located) or the negative (-90°, corresponding to the right side of the accelerator wrt. the Timepix3 location) direction, i.e. the smallest ToA corresponds to the pixel on which the particle entered the detector (incidence) and the largest ToA corresponds to the pixel on which the particle exited the detector (emergence). Since it is assumed that the radiation would originate from the BGC side, only the tracks corresponding to the positive +90±10° direction are kept. This removes the need to include the global factor taking into account the signal-to-noise ratio (SNR) given in eqn. 12.4.
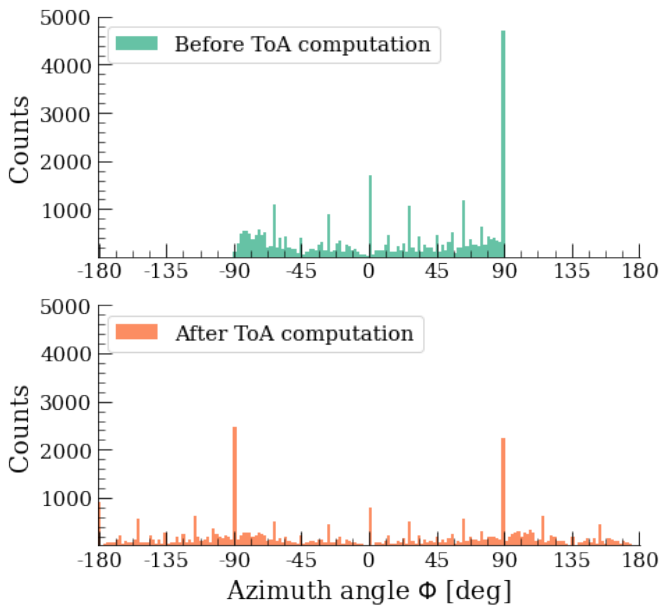
Figure 13.3: The azimuthal angle ϕ for the measured clusters during fill number #9035, as obtained (**Top pannel**) before the time of arrival (ToA) slope is computed (as such, the range is from (-90, 90]°), and (**bottom pannel**) after the ToA information is taken into consideration (as such, the range is extended to [-180, 180]°). A cluster track with an azimuthal angle $\phi=90°$ would correspond to the left side of the accelerator wrt. the Timepix3 location.

Table 13.1: Data selection criteria for the measured data for the Timepix3 radiation monitor application as a radiation source locator.

Selection criteria	Value
cluster size (area) A	≥ 3
cluster type	tracks (except curly)
azimuth angle ϕ	$+90\pm10\,\mathrm{deg}$

13.1.2 Simulated data

To verify the quality of the data, the measured signal induced by the Beam Gas Curtain (BGC) only, as isolated in the previous section and summarised in tab. 13.1, is compared to FLUKA predictions obtained from the simulation described in section 12.2.2, where the electromagnetic FLUKA (EMF) component is ignored to sped up the computation. The simulation

readily provides the kinematic variables (position and angle of incidence) for all the tracked particles at the Timepix3 location. For this benchmark, only charged hadrons (protons p, muons $\mu^\pm$, pions $\pi^\pm$ and kaons $k^\pm$) are considered (implying that neutrons are discarded, as well as the electromagnetic FLUKA (EMF) component), as these would yield (in most cases) tracks in the Timepix3 sensor as seen in section 12.2.1.

13.1.3 Benchmark

Both the measured and FLUKA simulated results for the polar angle θ (angle of incidence) are shown in fig. 13.4. In this analysis, the average ratio of simulated to measured data, weighted on the measured values, is:

$$R_\Theta = \frac{\Theta_{sim}}{\Theta_{meas}} = 0.85 \pm 20\% \qquad (13.1)$$

where the error is the standard deviation of the ratio values, as shown in the lower pad of fig. 13.4. The result is better than the previously reported values of chapter 7, which could be due to the better signal identification cuts. The simulated data seems to indicate that the muons $\mu^\pm$ can originate more frequently at larger incidence angles, i.e. corresponding to locations at larger distances in the accelerator tunnel wrt. the detector location, compared to protons, that are more likely to arrive at lower angles (i.e. from closer distance in the accelerator). This is consistent with the fact that muons can travel longer distances through matter without substantially altering their trajectories.

13.2 Timepix3 as a linear energy transfer detector

Taking advantage of the pixel array again, another quantity that is now accessible to compute is the linear energy transfer (LET), which could be used to distinguish charged particles (or at least their interaction mechanisms) from the mixed radiation field.
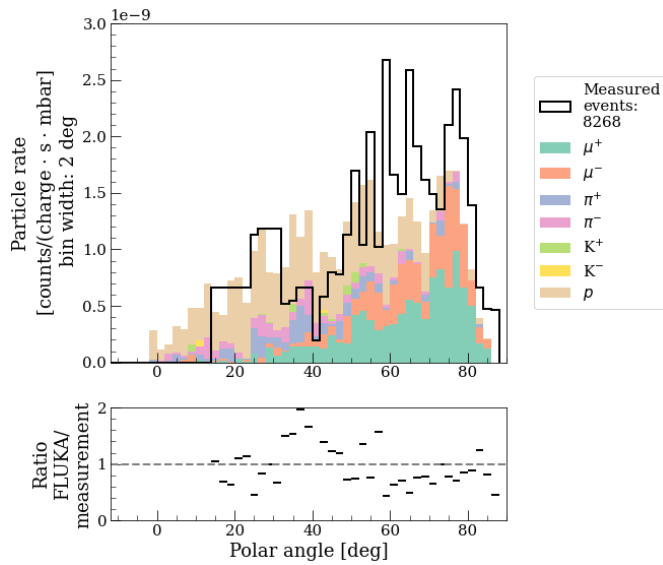
Figure 13.4: **Top panel:** Benchmark between the polar angle Θ (angle of incidence on the Timepix3 plane) as simulated by FLUKA predictions for charged hadrons, and the filtered measurements. The absence of measured values below $12°$ stems from the selection of tracks, filtering out clusters with less than 3 pixels. **Bottom panel:** Ratio of the total FLUKA simulated over the total Timepix3 measured count rates.

The same selection criteria and simulation as for the previous section 13.1 are used.

13.2.1 Measured data

The LET can be obtained from the measured data as described in section 9.2.4.1, by simply summing the total cluster ToT volume $V_{ToT} = \sum_i^A ToT_i$, for all A pixels, converted to energy according to the experimental calibration of eqn. 8.6, and dividing by the length of the cluster L, assumed to be the distance traveled by the particle in the sensor, as:

$$LET = \frac{V_{ToT}}{L} \tag{13.2}$$

Implicitly, this computation method assumes a uniform LET along the measured clusters. The tracks are further divided based on the morphological properties summarised in tab. 8.2 into 4 subtypes: *straight*,

light, *medium*, and *heavy*. Examples of such cluster are given in fig. 12.3.

13.2.2 Simulated data

To verify the quality of the data, the measured signal induced by the Beam Gas Curtain (BGC) only, as isolated via the criteria summarised in tab. 13.1, is compared to FLUKA predictions obtained from the simulation described in section 12.2.2, where the electromagnetic FLUKA (EMF) component is ignored to sped up the computation. The simulation readily provides both the energy of the particle and its LET, for each of the particle species. For this benchmark, only the charged hadrons (protons p, muons $\mu^{\pm}$ and pions $\pi^{\pm}$) are considered.

13.2.3 Benchmark

The results are shown in fig. 13.5, where the measured peak for an LET of $2\,\mathrm{MeV\,cm^2/g}$ for the *straight tracks* is confirmed to originate mostly from muons in the minimum ionising particle (MIP) regime. Increasingly larger LETs are measured for the other *tracks*, as expected, and these mostly originate from proton interactions. As such, one can classify the interactions in two categories:

1. The first category of particles, already introduced, are the MIP, which would correspond to charged hadrons at high energies.

2. The second type of particles (or interaction mechanism) are those leaving a larger energy deposits, but still having a track like shape rather than circular blobs. Both can be collectively referred to as high energy transfer events (HETE). There are typically two distinctive components in a HETE cluster, as visible in fig. 12.3: (i) a track core with high energy values, and (ii) a surrounding halo due to charge sharing and possible δ-rays. A possible improvement [232] in the length computation of these type of the cluster would be the halo removal and a more accurate determination of the impact point, even at a sub-pixel resolution [238].
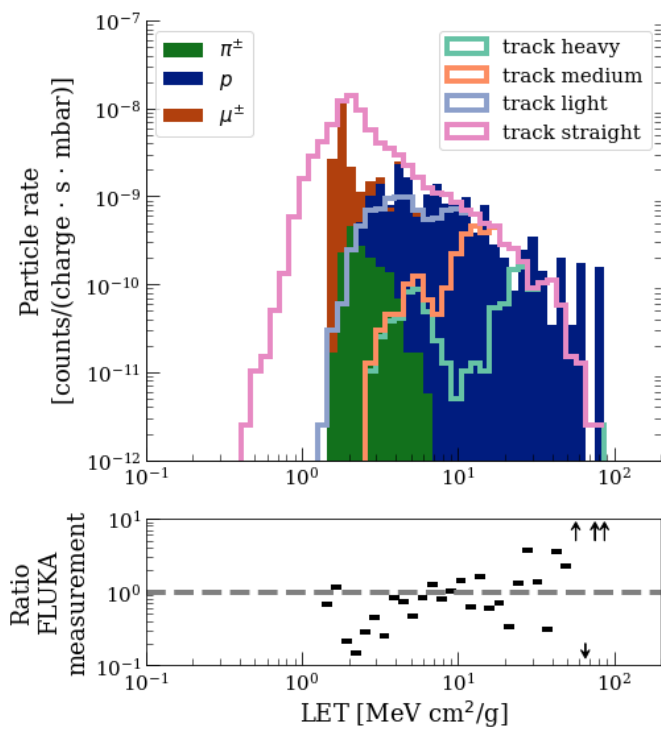
Figure 13.5: **Top panel:** The linear energy transfer (LET) (dE/dX) of clusters categorized as tracks, as measured by the Timepix3 radiation monitor in the shielded alcove of IR4, during LHC fill number #9035. The measured tracks are further divided into four sub-types, plotted here as stacked bars. The FLUKA simulation is used for cross-check, showing the LET for the charged hadrons (protons p, muons $\mu^{\pm}$ and pions $\pi^{\pm}$). **Bottom panel:** Ratio of the total FLUKA simulated over the total Timepix3 measured count rates. The arrows indicate data points outside the plotting range.

In this analysis, the average ratio of simulated to measured data, weighted on the measured values, is:

$$R_{\text{LET}} = \frac{(dE/dx)_{sim}}{(dE/dx)_{meas}} = 0.59 \pm 87\% \qquad (13.3)$$

where the error is the standard deviation of the ratio values, as shown in the lower pad of fig. 13.4. The agreement is within the typical factor of 2, but the large error bar requires further study. The main disagreement sources are:

1. The absence of simulated particles with LETs smaller than $1\,\text{MeV}\,\text{cm}^2/\text{g}$, corresponding to the smallest LET that the charged hadrons can have. The measured values in this range could correspond to other particles rather than the charged hadrons that were also identified as tracks.

2. The gap between the simulated and measured data in the 2 to $5\,\text{MeV}\,\text{cm}^2/\text{g}$ range.

At higher LET values, these particles corresponds typically to heavier ions or particles stopping within the detector. The sensitivity to discriminate amongst these would be enhanced if the incidence angle of these particles wrt. the normal on the detector plane were to increase. Previous experience highlights this capability, with the caveat of the per-pixel saturation level, especially for lower impact angles [239].

13.3 Summary

Two new possible applications that are explored in this work consists in using the Timepix3 radiation monitor as a radiation source locator and as a linear energy transfer (LET) detector. Both usages make use of the pixel array, thereby identifying *tracks* from the reconstructed clusters. The measured data are compared and cross-checked with the FLUKA simulated results.

Charged particles interacting elastically leave *straighter* tracks within the detector across multiple pixels, and their incident angle Θ can be computed on a track by track basis, and used as a tool to infer the spatial origin of radiation, especially if coming from the accelerator beamline. For this, further selection criteria are imposed on the measured data, in particular on the cluster azimuth angle Φ, i.e. the angle of the track in the 2D pixel array, in order to keep only the particles that would come from the accelerator beam line and not from other radiation sources. The average ratio for the polar angle θ of the

simulated to measured data reveals an agreement of $R_\theta = \theta_{sim}/\theta_{meas} = 0.85 \pm 20\%$.

For the LET application, the detector measures a total ToT volume (which can be converted to energy deposition via the previously performed calibration) per cluster, and the pixel array allows to compute cluster length L. The division of the two values yields then the LET. From the measured data, the particle tracks categorized into four classes: *straight*, *light*, *medium* and *heavy*, leaving increasingly larger LETs in the detector. The comparison with the charged hadrons from the FLUKA simulation confirms the expectations, that muons $\mu^\pm$ are behaving as MIPs, leaving straight tracks, and protons p are capable of higher LETs, thereby being the dominant contributor for HETE. The average ratio for the LET of the simulated to measured data reveals an agreement of $R_{\mathrm{LET}} = (dE/dx)_{sim}/(dE/dx)_{meas} = 0.59 \pm 87\%$. The LET analysis can be further expanded and used in radiation environments containing also heavier particles, such as ions.

The third act - summary

This third act continues the investigation started in the first act about the characterisation of the mixed radiation field at insertion region 4 (IR4) of the Large Hadron Collider (LHC) [1], in particular that generated from the operation of the Beam Gas Curtain (BGC) [99–101]. The features of the Timepix3 radiation monitor [22] that have been well understood in the second act are used both to: (i) assess its complementarity to the existing radiation monitors, and (ii) probe new capabilities for radiation level monitoring.

The Timepix3 radiation monitor successfully measured the radiation levels during the nominal LHC fills, in the absence of the BGC operation. Starting from beam injection at 450 GeV with low beam intensity, no signal was measured above the background counting rate (CR) of $CR_{bkg} = 8.4 \pm 3.9$ counts/60 s unless a beam intensity above 10^{13} charges/s was circulating in the accelerator. During beam energy ramp up from 450 GeV to the nominal 6.8 TeV, a clear increase in the Timepix3 counting rate can be observed. Subsequently, during stable beams at the collisions energy of 6.8 TeV, a rather non-linear relation between the counting rate and the beam intensity can be seen, likely due to the enhanced outgassing effects from the vacuum chamber surfaces in the presence of high intensity beams.

During the 2023 operation when the Timepix3 radiation monitor was deployed, only two gas injections have been performed in the BGC during proton beams, namely in fills #8817 and #9035. These two fills are the only ones that allow a direct comparison with the BGC FLUKA simulations of chapter 7. To obtain a total ionizing dose (TID) measurement, the total energy deposited in the Timepix3 pixel array is summed and compared with the simulated predictions, revealing an agreement of $\mathcal{R}_{TID} = TID_{sim}/TID_{meas} = 0.60 \pm 37\%$.

To compare the particle count rates, further analysis is required, both on the simulated and measured data. If the charged hadrons have almost a 100% detection efficiency, neutrons only rarely interact because of their large mean free path in Silicon, substantially longer than the sensor thickness. In order to quantify the interaction rate for neutrons, but also to estimate the energy depositions for all particles, a second step FLUKA simulation has been performed. On the measurement side, owing to the Timepix3 ASIC pixel matrix, different particles and their interaction mechanisms leave different morphological tracks within the detector, allowing to perform a particle categorization, mainly into blobs (more circular) and tracks (elongated or curved). The benchmark for the particle counting rate reveals a total agreement of $\mathcal{R}_{CR} = CR_{sim}/CR_{meas} = 0.80 \pm 27\%$. Moreover, the energy deposition per particle species reveals that almost all charged hadrons will deposit their energy within the linear regime of the detector, while for neutrons have a more complicated behaviour, with expected energy depositions both below the detection threshold and above the saturation limit.

Two new possible applications that are explored in this work consist in using the Timepix3 radiation monitor (i) as a radiation source locator and (ii) as a linear energy transfer (LET) detector. Both usages make use of the pixel array, thereby identifying *tracks* from the reconstructed clusters. The measured data is compared and cross-checked with the FLUKA simulated results. Charged particles interacting elastically leave tracks within the detector across multiple pixels, allowing for several other parameters to be computed. The average ratio for the 1D distribution of polar angle θ of reconstructed tracks for the simulated to measured data reveals an agreement of $\mathcal{R}_{\theta} = \theta_{sim}/\theta_{meas} = 0.85 \pm 20\%$. For the LET application, the average ratio of simulated to measured LET data reveals an agreement of $\mathcal{R}_{LET} = (dE/dx)_{sim}/(dE/dx)_{meas} = 0.59 \pm 87\%$. The larger error stems from the absence of simulated particles with LET $< 2\,\mathrm{MeV\,cm^2/g}$, while on the measurement side there are tracks with such properties.

Coda - Measurement of the transveral muon rate from LHCb at the proposed CODEXb experiment location

14

The CODEXb experiment

14.1 Introduction

Most searches at the Large Hadron Collider (LHC) [1] experiments have mostly focused on production of particles that decay close to the collision point, and can therefore be detected within the detector volume. However, a number of important beyond the standard model (BSM) scenarios, such as any theory with multiple mass scales, broken symmetries, or restricted phase-space, predict long lived particles (LLP) [240]. The standard model (SM) itself contains a number of unstable particles with low mass, but long-lived, such as pions, kaons, muons and neutrons. A wide variety of new experiments have been proposed within the complex to probe the BSM LLP sector, which include: massive timing hodoscope for ultra stable neutral particles (MATHUSLA) [241], forward search experiment (FASER) [242], milli-charged (MilliQan) [243], search for hidden particles (SHIP) [244], a laboratory for long-lived exotics (AL3X) [245] and compact detector for exotics at LHCb (CODEXb) [246–248].

Data-driven calibration using real collision data is required to test the feasibility of the proposals. For this purpose, a test campaign to measure the background flux in the foreseen location of the CODEXb experiment, which is envisioned as an SM background-free detector searching for LLPs. The measurements have been performed in the D1 shielded area, behind an existing 3.2 m thick concrete wall that separates the LHCb cavern from the detector with lepton, photon and hadron identification (DELPHI)[1] cavern, during

October and November of 2022, the first year of Run 3 operation with proton-proton collisions.

Within the radiation to electronics (R2E) [16, 17] activity at CERN, the muon flux during luminosity production at the large hadron collider beauty (LHCb) experiment was quantified with the recently developed Timepix3 radiation monitor [22]. Moreover, the standard R2E radiation monitor at CERN, namely, the radiation monitor (RadMon) [151, 249] in its battery powered version (BatMon) [152] was used to confirm the expectations that the neutron flux in this area is negligible. Indeed, the BatMon did not measure any signal above its detection thresholds, while the Timepix3 radiation monitor measured an increased count rate during luminosity production, owing to its ability to detect minimum ionising particle (MIP)s, as well as to infer the origin of the radiation, as described in section 13.1. The measured signal, both as a flux rate and as energy deposition, was compared with simulations performed with the flukturiende kaskade (FLUKA) Monte Carlo code [18–20].

A previous campaign for muon measurements [250] was done with re-used scintillators, light-guides and photomultiplier tubes, revealing a systematic disagreement (under-measurement) with simulations, which is not the case for this study.

14.2 R2E safe area: BatMon measurement campaign

One battery radiation monitor (BatMon) unit, also known as wireless internet of things (IoT) system, has been installed in UX85 alcove of the LHCb experiment. The scope of this measurement was to verify that the position that will host the CODEXb exper-

---

[1]DELPHI was one of four large detectors on the large electron-positron (LEP). It took 7 years to design and build, and it started up in 1989. In December 2000, DELPHI stopped taking data and was dismantled to leave room for the construction of the Large Hadron Collider (LHC) in the LEP tunnel.

iment is R2E safe, as expected from an area that is already safe from a radiation protection (RP) point of view (accessible even during accelerator operation and luminosity production).

To characterize the radiation environment permeating the investigated location, the BatMon measured: the total ionizing dose (TID), by using floating gate dosimeters, and high energy hadron equivalent (HEHeq) (Φ_{HEH}) the thermal energy neutrons equivalent (THNeq) (Φ_{ThN}) fluences, by exploiting the technique shown in ref. [251], namely by counted the single event upsets (SEU)s induced by radiation in two different well-calibrated parallel SRAM, whose sensitivity to both Φ_{ThN} and Φ_{HeH} is known.

The LHCb area was not covered by the long range (LoRa)connection [252] and therefore the BatMon is installed in passive mode (LoRa OFF). In this mode, measurements are stored on the external non-volatile flash memory available on board and it can only be read when accessing the location. Since the BatMon is based on a duty cycle mode and all operations are performed following a precise schedule, it is possible to reconstruct the time by knowing the data rate (in this test campaign, at an interval of 30 minutes).

The layout of UX85 is shown in fig. 14.1. The BatMon was installed for 81.96 days (from September 15th to December 6th, 2022) in UX85, during which a total luminosity of $\mathcal{L}_{int} = 2.8\,1/\text{nb}$ has been produced at LHCb and no counts have been measured in any of the BatMon detectors. Nevertheless, one can infer an upper limit based on the detectors sensitivities to a radiation field that consists of at most:

$$\Phi_{HEH} < 1.18 \cdot 10^6\,\text{pp/cm}^2/\text{fb}^{-1} \quad (14.1)$$
$$\Phi_{THN} < 1.83 \cdot 10^6\,\text{pp/cm}^2/\text{fb}^{-1}$$
$$TID < 1.79\,\text{mGy/fb}^{-1}$$

The measurement showed that this area is R2E safe because no radiation was detected by the BatMon sensors.

14.3 Simulation

Prior to these measurements, a full FLUKA geometry of the LHCb insertion region 8 (IR8) has been developed [63]. The FLUKA predictions have been benchmarked with the BLM system in the tunnel and RadMon in the shielded alcoves, similar to other IRs [37, 43], although not in the DELPHI cavern. Still, the FLUKA model represents the best available tool to predict the collision-driven muon flux in the location of interest for the CODEXb experiment.

14.3.1 Geometry

A full FLUKA geometry has been implemented as a collective effort within the SY-STI-BMI section, as described in detail in ref. [63]. The radiation shower is dominated by inelastic proton–proton collisions at the interaction point (IP)8, the LHCb experiment.

In the DELPHI cavern, where the Timepix3 radiation monitor and the BatMon were installed, only muons and possibly neutrons are assumed to arrive, as the other particles would stop within the concrete shieldings. To understand the muon flux that arrives at the detectors, there are several features of the LHCb cavern that are critical, covered in ref. [247, 250]. In this study, the focus is on the expected muon flux rate and energy spectrum at the location of the deployed detectors.

In the context of the energy deposition studies for LHCb [63], the spatial distribution of the muon rate shown fig. 14.1 has been simulated with FLUKA, which uses the DPMJET-III generator [253].

14.3.2 Simulated muon rate and energy spectrum

Although the FLUKA simulation can readily provide the muon energy distribution at the location of the detectors, the previous measurement campaign [254] has setup a simulation with Gauss [255, 256] (the standard LHCb simulation package) using the Pythia8 [257] generator to more carefully take into con-
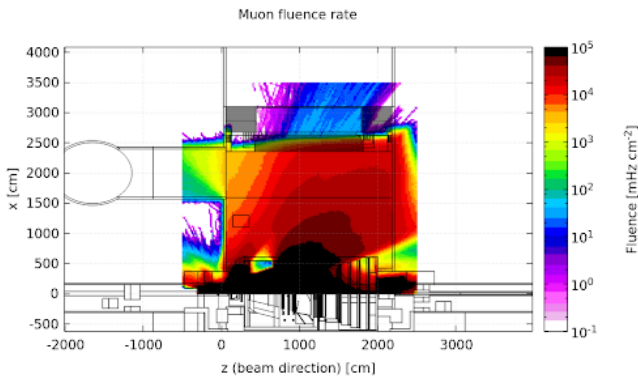
Figure 14.1: Top view of instantanous muon fluence rate during Run 3, as simulated using FLUKA, for the nominal instantaneous luminosity of $\mathcal{L}_{inst} = 2.32\,\text{pb}^{-1}/\text{h}$ (fig. from ref. [63]).
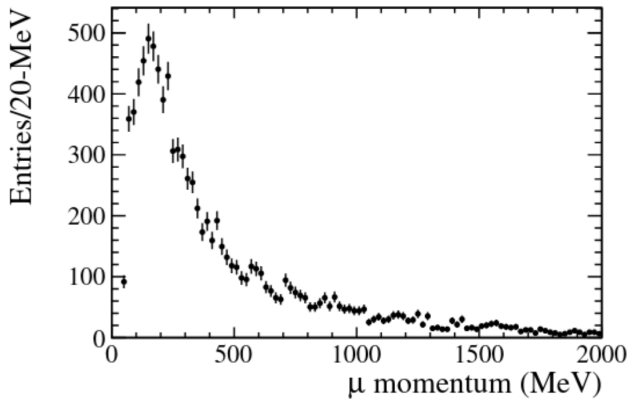
Figure 14.2: The final momentum distribution of muons reaching the detector location, after all energy losses showing that the slowed-down muons have quite low momenta (fig. from ref. [250]).

sideration the generation the proton-proton collisions with minimum bias setting and specific LHCb tunings. It indicates that the infrastructure of the LHCb cavern generally stops muons with momentum below $\approx 1500\,\text{MeV}$. The slowed-down muon momenta at the detector position shown in fig. 14.2, after energy losses, peaks around a momentum of $\approx 200\,\text{MeV}$ and displays a long tail at high momenta. Moreover, additional shielding, either passive or active, or both, might be required to suit the needs for CODEXb.

The previously mentioned simulations [250] reveal a muon peak with momentum $p = 200\,\text{MeV/c}$ (or kinetic energy $T=120\,\text{MeV}$), which are close to the minimum ionising particle (MIP) regime with roughly constant $dE/dx \approx 4.148\,\text{MeV/cm}$, as shown in fig. 14.3. Considering the track length inside the sensitive volume, the energy deposition of muons coming from the IP in the Timepix3 sensor is expected to be approximatively:

$$E_{dep} = \int\limits_0^L \frac{dE}{dx}dx \approx L \cdot \frac{dE}{dx}\bigg|_{120\,\text{MeV}} = 107\,\text{keV} \quad (14.2)$$
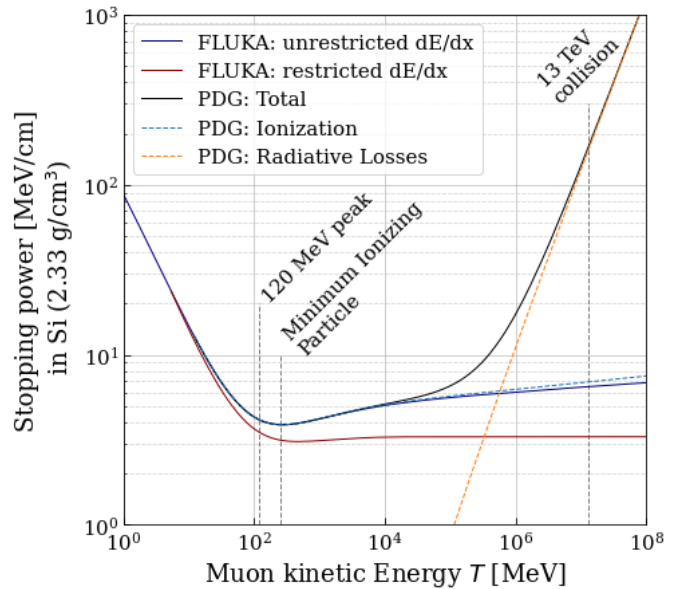
Figure 14.3: Muon stopping power, as simulated with FLUKA and according to tabulated data from ref. [114].

14.4 Timepix3 radiation monitor data

The Timepix3 radiation monitor setup has been installed in the DELPHI cavern, with the operational parameters summarised in tab. 14.1.

Table 14.1: Timepix3 radiation monitor operational parameters at the CODEXb test campaign.

Parameter	value
Bias voltage [V]	50
Panda GUI firmware version	3.18.0

14.4.1 Installation and data collection

The detector has been oriented with an incidence (polar) angle of $\theta = 15°$ wrt. to the expected incoming muons, similary to the pixel detectors inside the inner tracker detectors of the a toroidal LHC apparatus (ATLAS) and compact muon solenoid (CMS) experiments. This choice has been made because a particle that arrives at an angle of $\Theta_{monopixel,max}=12°$ or larger must interact with at least two pixels of the detector, thereby enhancing the signal selection capabilities by improving the spatial discrimination criteria.
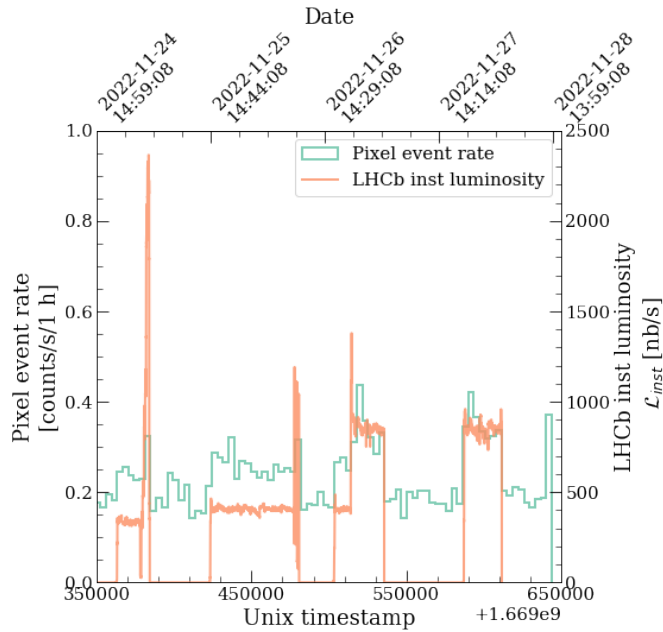
Figure 14.4: The instantaneous delivered luminosity at LHCb and the Timepix3 counting rate.

The instantaneous delivered luminosity at LHCb and the Timepix3 pixel count rate are shown in fig. 14.4. Unlike the previously reported measurement campaign using scintillating fibres of a large area in ref. [250], the count rate does not increase signific-

antly during collisions, due to the small active area of the detector (about 2.4 cm^2). As such, the natural background will have to be taken into account during the analysis.

The total acquisition time of about 104.01 hours has been divided into signal time periods, during proton-proton pp collisions (luminosity production) summing up to $\tau_{signal} = 43.45$ hours, and background (no pp collisions) for $\tau_{bkg} = 58.66$ hours. The reconstructed cluster event rate during collisions increases with the total integrated luminosity as shown in fig. 14.5, however the signal-to-noise ratio (SNR) is less than 2. For this reason, an assessment of the background has been done. It consists of averaging the total Timepix3 counts N_{bkg} over the M background time periods, revealing an average background count rate of:

$$R_{bkg} = \sum_{i}^{M} \frac{N_{i,bkg}}{\tau_{i,bkg}} = 7.54 \pm 0.26 \text{ counts/60 s} \quad (14.3)$$

This background is assumed to come primarily from the cosmic galactic rays, with a lower count rate compared to the surface (the same detector measured about 20 counts/60 seconds) since the LHC is about 100 m underground. Moreover, natural decay chains could also occur underground (e.g. radon). Finally, there is no background assumed to come from beam-induced activation of materials or other equipment at the installed location.

To extract the signal from the total Timepix3 particle counts and to correlate it with the total luminosity delivered, the background count rate from eqn. 14.3 multiplied by the duration of luminosity production is subtracted for each time period, thus obtaining only the signal induced by proton-proton collisions at IR8 (LHCb), as:

$$N_{signal} = N_{signal} - R_{bkg} \cdot \tau_{signal} \quad (14.4)$$

shown in fig. 14.5. A good linear correlation is thus obtained between the Timepix3 reconstructed count rate and the total luminosity, at 38 ± 1 counts/pb^{-1}.
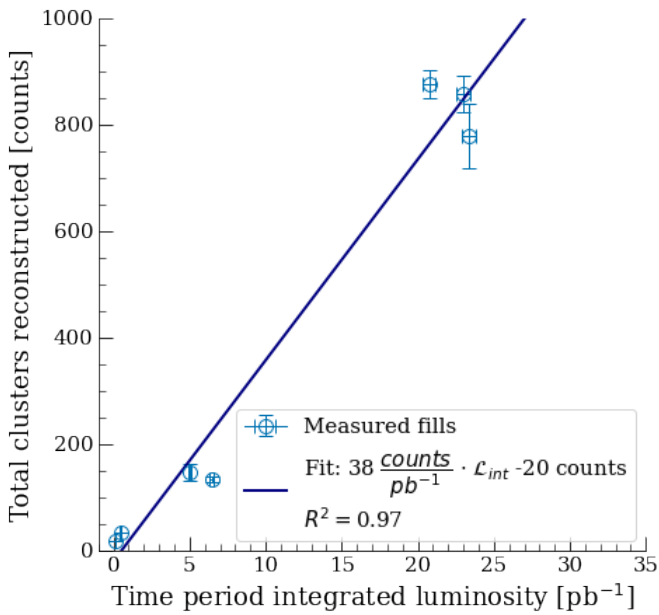
Figure 14.5: The total reconstructed cluster hits plotted against the total integrated luminosity of the time periods during LHCb luminosity production, revealing a linear relation.

Figure 14.6: The total ToT distribution of clusters with one pixel during signal (luminosity production) and background (no circulating beam), revealing no significant difference, neither in the total rate nor in the shape of the distribution.

14.4.2 Signal and background selection

The signal discrimination from background is done using the directionality of the incoming muons, by analysing their tracks inside the detector pixel array, forming multi-pixel clusters. The x (y) axis of the detector was placed parallel (perpendicular) to the normal from the IP, in order to discriminate the muons coming from the collision point and those that constitute background. As such, amongst the clusters parameters than can be computed, a special attention is given to the azimuthal angle Φ, denoting the angle on the pixel array of the particle track.

The discussion is divided in the following per number of pixels (pixel area) A in the cluster. At first, the difference between the signal and background time periods is tackled, by looking at the raw (non-normalized) counts measured by the Timepix3 radiation monitor. Then, the values along the x-direction, aligned with the expected direction coming from the IP, are normalized to a count rate per unit time (second), as well as per unit luminosity (pb).

The instantaneous luminosity during the measurement campaign exhibits several values, as visible in fig. 14.4, but the comparison with the FLUKA simulated results and the previous measurement campaign using scintillating fibers requires further renormalization.

14.4.2.1 Clusters with 1 pixel

Clusters that constitute of just one pixel cannot be attributed to any direction. However, from the detector geometry wrt. the interaction point, if a muon originates from a collision it should have an angle of at least $\Theta_{incidence} = 15°$ as mentioned above, implying that its track inside the Timepix3 is strictly greater than 1 pixel. This is confirmed by the ToT distribution for 1-pixel cluster in fig. 14.6, where no difference can be observed between the signal and the background data sets.

14.4.2.2 Clusters with 2 pixels
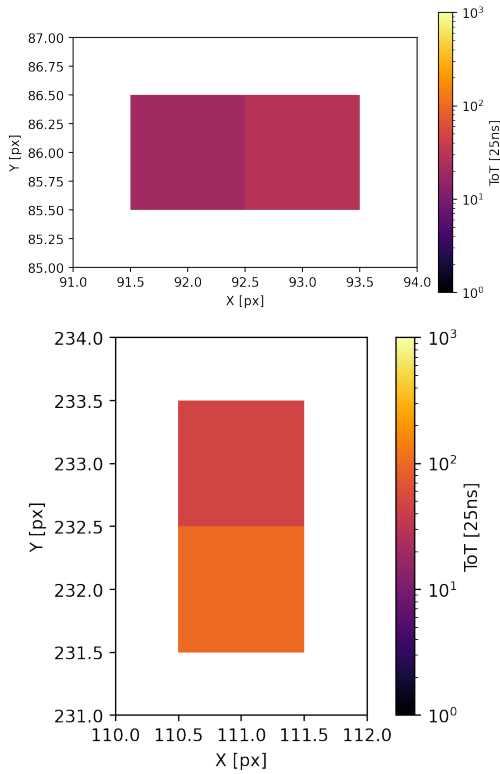
Figure 14.7: Example of 2-pixel clusters aligned along (**Top**) x- and (**Bottom**) y-direction.

Figure 14.8: ToT distribution of the 2-pixel clusters aligned along the x- and y-direction, for (**Top**) background data sets, revealing no difference in directionality, assuming an isotropic cosmic radiation environment, and (**Bottom**) for signal data sets, revealing a clear peak at the expected signal location and along the expected direction.

For clusters with 2 and more pixels, a directionality can be assigned. For the purpose of this analysis, the directionality is restricted to either horizontal (x, parallel to the normal from the IP, the line corresponding to the signal) or vertical (y, perpendicular to the normal from the IP). For the case of 2 pixel clusters, there are only 2 types of clusters, as shown in fig. 14.7. The background data set shown in fig. 14.8 does not reveal any difference between the two aforementioned directions, confirming the angular isotropy of the cosmic background radiation arriving at the detector location. Differently, the signal data sets shown in fig. 14.8 reveal a cluster rate excess in the x-direction.

The background for 2-pixel clusters is fitted using a Landau distribution and then subtracted from the signal histogram, as shown in fig. 14.9. Then, the signal thus obtained is fitted as well using

a Landau distribution revealing a peak at 120 ± 13 ToT units [25 ns], which calibrated to energy according to section 9.2.4.3 translates around the 98 ± 11 keV, as expected from eqn. 14.2.
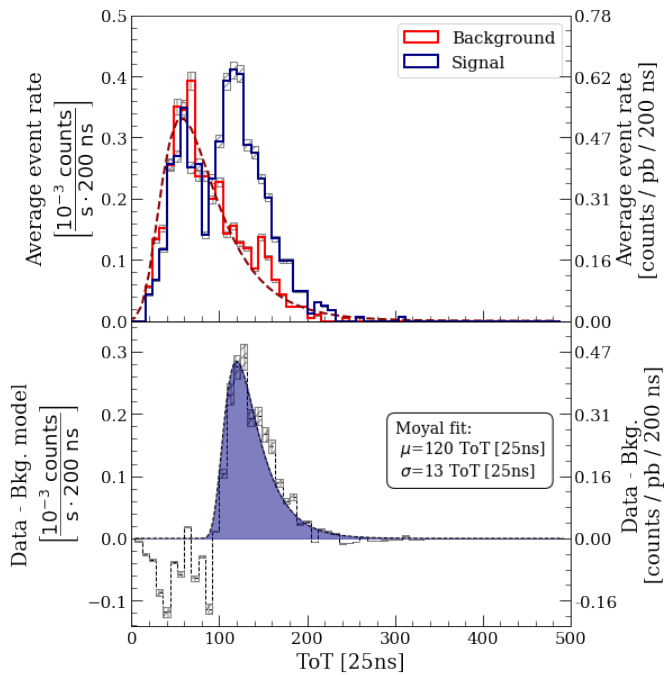
Figure 14.9: (**Top panel**) ToT distribution of the 2-pixel clusters aligned along the x-, for signal and background data sets. The background is fitted using a Moyal distribution and subtracted from the signal. (**Bottom panel**) Signal after the background subtraction, fitted using a Moyal distribution, revealing a clear peak at the expected signal location and along the expected direction.

obtained is fitted as well using a Landau distribution revealing a peak at 134 ± 14 ToT units [25 ns], translating to 113 ± 12 keV, increasing compared to the 2-pixel clusters, confirming that the muons travel over a longer distance through the detector, thereby depositing more energy.
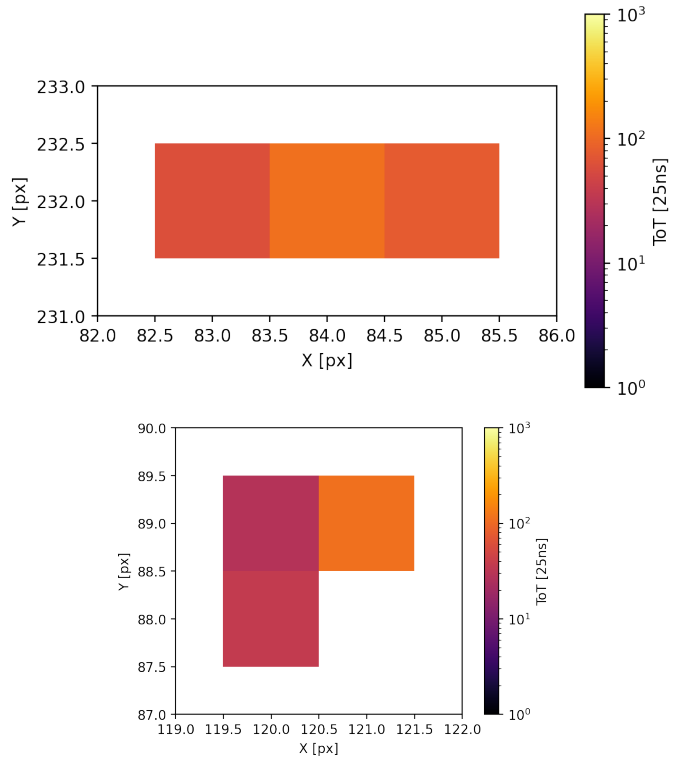
Figure 14.10: Example of 3-pixel clusters aligned along (**Top**) x-direction, as well as (**Bottom**) unassigned.

14.4.2.3 Clusters with 3 pixels

For clusters with 3 pixels, there are 2 possible geometries, as displayed in fig. 14.10: (i) either a straight line, along either the x- or y-axis, or (ii) an L-shaped cluster, which is discarded from the analysis, as no directionality can be assign to it. Looking just at the 3-pixel clusters, the background data set shown in fig. 14.11 does not reveal any difference between the two aforementioned directions, again confirming the angular isotropy of the background; however, the signal data set reveals again a cluster rate excess in the x-direction. In this case, the background for 3-pixel clusters is not populated enough to be fitted with a model as for the 2-pixel clusters, but it is taken into account by a (normalized) bin-wise subtraction from the signal. Then, the signal thus

Figure 14.12: Same as fig. 14.9, but for 3-pixel clusters, without fitting the background data.

The same considerations about 3-pixels clusters apply to the 4-pixels clusters, with the fitted signal results revealing a peak at 148 ± 19 ToT units [25 ns], translating to 125 ± 16 keV, again increasing compared to the 2- and 3-pixel clusters cases.

14.4.2.5 Clusters with 5 pixels

The last considered case consists of clusters with 5 pixels, which can be categorized into two types, depending on their elongation along each axis, they would correspond to that respective direction. The data shown in fig. 14.16 displays however a reduced count rate excess in the x-direction, compared to the previous cases. The data from 6-pixel reveal no excess/difference in cluster directionality. The fitted signal results revealing a peak at 177 ± 16 ToT units [25 ns], translating to 154 ± 16 keV, significantly larger than for the other cases.

Figure 14.11: Same as fig. 14.8, but for 3-pixel clusters, displaying a significantly lower background.

14.4.2.4 Clusters with 4 pixels

For clusters with 4 pixels, there are 3 possible geometries, as displayed in fig. 14.13:

1. a straight line, in which case the directionality is obvious,

2. a line of 3-pixels with a fourth pixel on either side, which is assumed to also belong to a direction,

3. a square blob cluster, which is discarded from the analysis

Figure 14.13: Example of 4-pixel clusters aligned along (**left**) x- and (**centre**) y-direction, as well as (**right**) unassigned.

Table 14.2: Summary of the Timepix3 radiation monitor results, showing for each number of pixels *A* inside the cluster, the mean *ToT* and its standard deviation for the Moyal fitted distribution, as well as this values converted into energy deposition E_{dep}. The measured count rates are provided, in both per second and per unit luminosity. The relative contribution to the total count rate is also provided.

A [no. pixels]	**ToT** [25 ns]	**Δ ToT** [25 ns]	**Δ ToT**$_{rel}$ [%]	E_{dep} [keV]	ΔE_{dep} [keV]	Φ [10^{-3}/s]	Φ [$1/(pb^{-1})$]	**Rel. contr.** [%]
2	120	13	11	98	11	1.95	3.02	34
3	135	14	10	113	12	1.27	3.06	22
4	148	19	13	126	16	1.86	2.89	33
5	177	18	10	155	16	0.71	1.11	12
Total	140	19	14	118	16	5.69	8.83	100

14.4.3 Final hit rate as a function of transversal distance in the D1 shielded alcove

The results are summarised in table 14.2. Combining the 2-, 3-, 4- and 5-pixel cluster signals yields a the total average event rate of $\Phi_0 = 5.64 \cdot 10^{-3}$ counts/s, or, equivalently 8.60 counts/(pb^{-1}), with its energy distribution shown in fig. 14.18. However, in order to compare to previous measurements reported in ref. [250] and FLUKA simulations reported in ref. [63], the total measured result of fig. 14.18 has to be corrected for three factors:

1. the Timepix3 detector area of $A_{tpx} = 2.12$ cm^2,

2. the acceptance angle via $\cos \theta = 15.17°$ factor

3. the average instantaneous luminosity of $\mathcal{L}_{inst,meas} = 2.32$ pb^{-1}/h $= 0.645$ nb^{-1}/s dur-

ing the Timepix3 campaign, compared to the nominal $\mathcal{L}_{inst,nominal} = 0.45$ nb^{-1}/s used for both the previous measurements [250] and the simulations [63].

Thus, the Timepix3 radiation monitor measured a muon flux of:

$$\Phi_{tpx3,calib} = \Phi_0 \cdot \frac{1}{A_{tpx}} \cdot \frac{1}{\cos \theta} \cdot \frac{\mathcal{L}_{inst,nominal}}{\mathcal{L}_{inst,meas}} = \quad (14.5)$$
$$1.94 \cdot 10^{-3} \frac{\text{counts}}{(\text{cm}^2 \, \text{s})}$$

Figure 14.19 shows the hit rate from the simulation across a vertical plane parallel to the beam line, normalized to the Run 2 (2015-2018) LHCb luminosity production and per unit area. Geometrically, from

173

Figure 14.15: Same as fig. 14.9, but for 4-pixel clusters, without fitting the background data.

lation uncertainty of $\sigma_{sim,syst} = 20\%$ and a statistical measured error of $\sigma_{meas,stat} = 6\%$.

However, these Timepix3 results do not agree with the previous measurements reported in ref. [250]. Thanks to this work and the agreement that the Timepix3 radiation monitor has with the results coming from two different simulation tools (FLUKA and GAUSS), the results from the previous test campaign were re-examined, resulting in the discovery of a faulty trigger system on the detectors, explaining the significant underestimation.

14.4.4 Total measured data

The total ToT of the clustered data is shown in fig. 14.20. There is a clear peak at low energy depositions (about ~ 100 ToT units), which is the expected range of the signal according to eqn. 14.2, which was analysed in the previous section. Furthermore, there seems to be a slight excess of higher energy events during collisions compared to the background, but

Figure 14.14: Same as fig. 14.8, but for 4-pixel clusters.

the installation location, the Timepix3 radiation monitor result corresponds to a data point at $z = 700$ cm, agreeing very well with the FLUKA simulations of LHCb/IP8 reported in ref. [63] at:

$$\Phi_{FLUKA} = 3.80 \cdot 10^{-3} \frac{\text{counts}}{(\text{cm}^2 \, \text{s})} \qquad (14.6)$$

with a ratio of FLUKA to data at:

$$R_\Phi = \frac{\Phi_{FLUKA}}{\Phi_{tpx3,calib}} = 1.96 \pm 26\% \qquad (14.7)$$

where the considered errors are the systematic simu-

Figure 14.16: Same as fig. 14.8, but for 5-pixel clusters.

no conclusion can be drawn from the available statistics.

14.5 Summary and prospects

In summary, a successful background measurement campaign was held in November 2022 to measure the muon radiation flux in the CODEXb volume area during LHCb data taking. A BatMon unit has been deployed for almost 82 days, measuring no radiation above threshold, indicating that the proposed area is safe from a point of view of radiation effects on electronics.
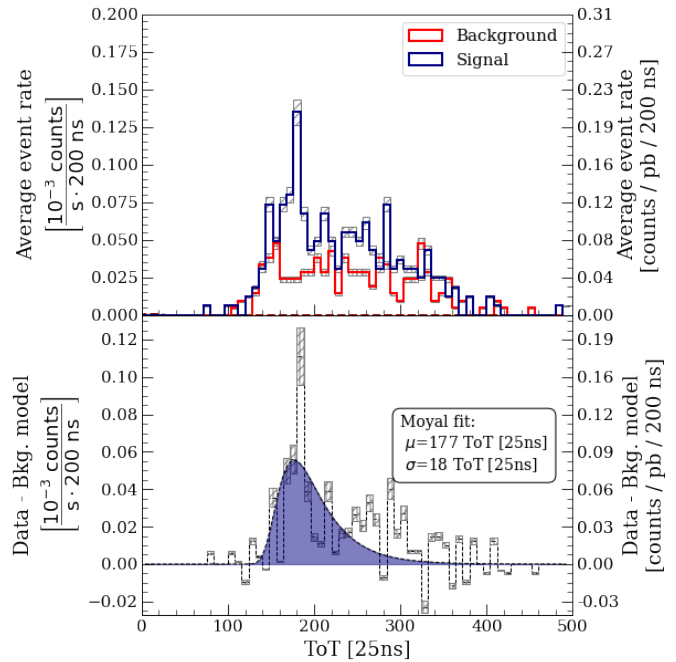
Figure 14.17: Same as fig. 14.9, but for 5-pixel clusters, without fitting the background data.
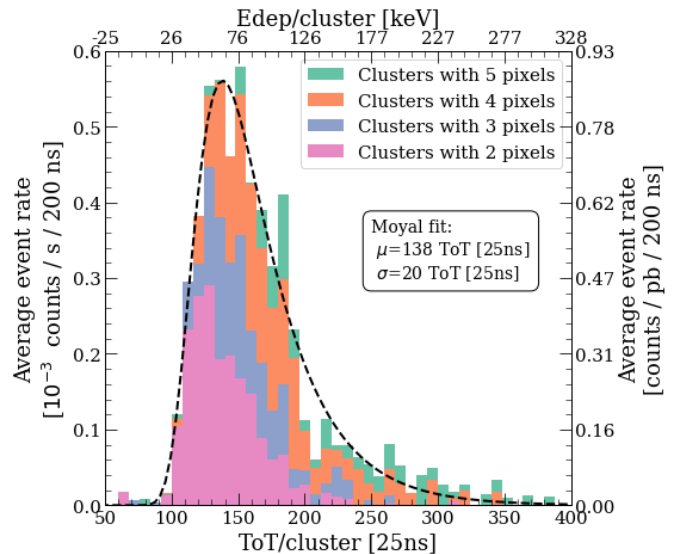
Figure 14.18: The full reconstructed signal using 2-, 3- and 4-pixel clusters reveals an integrated count rate at $5.80 \cdot 10^{-3}$ counts/s. A Moyal function fit describing to MIP particles passing through the detectors is estimated at $5.69 \cdot 10^{-3}$ counts/s.
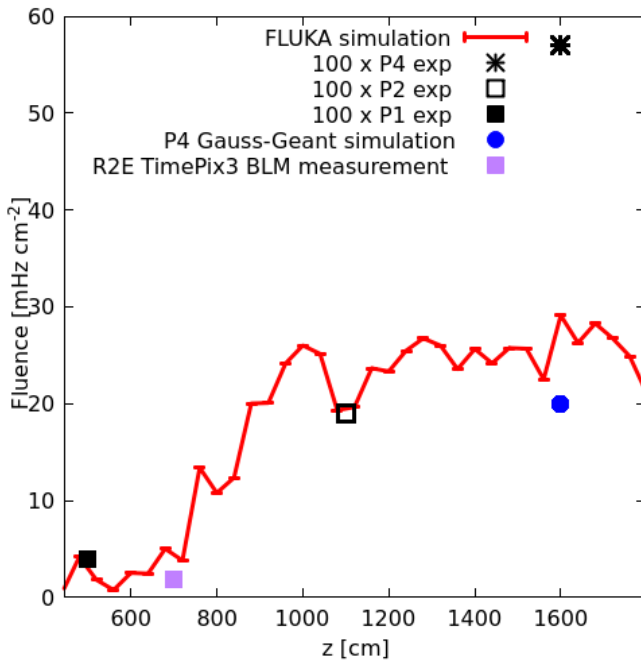
Figure 14.19: Comparison of muon fluence from FLUKA simulations and measurements. This study adds the Timepix3 measurement (purple square), compared to the previous measured results using scintillating fibers reported in ref. [63] (here, scaled up by a factor of 100). The assumed luminosity rate production was the nominal $0.45 \mathrm{nb}^{-1}/\mathrm{s}$.
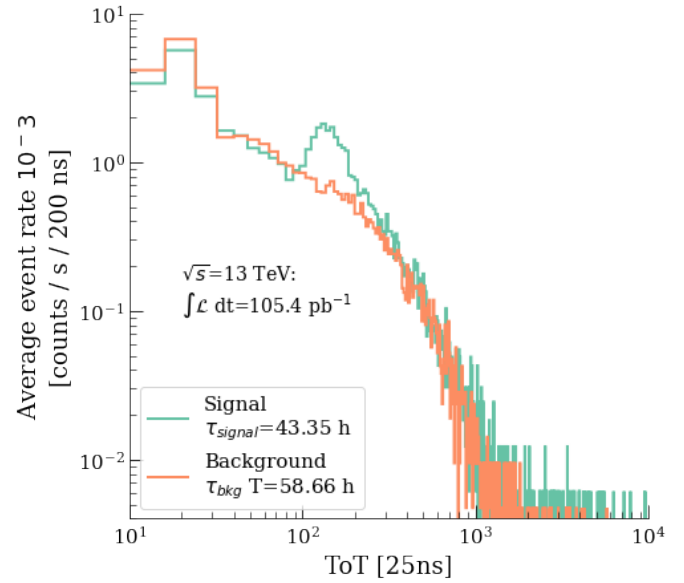
Figure 14.20: The total event-by-event energy in the Timepix3 sensor.

The lower energy threshold of the Timepix3 sensor is a clear advantage compare to the BatMon, which allowed to measure a slight increase in the instantaneous count rate during luminosity production at interaction point 8 (IP8), with a signal-to-noise ratio (SNR) of about 2. In order to isolate the signal clusters from the background, a selection on the cluster morphological properties has been applied. Namely, it is expected that muons originating from the proton-proton pp collision point would only by aligned along the y-direction (azimuth angle $\Phi = \pm 90$). Cluster tracks that cannot be assigned to any direction are discarded from the analysis.

Thanks to the angular orientation of the Timepix3 installation at an incidence (polar) angle of $\Theta = 15°$, greater than the max. accepted angle for a monopixel event of $\Theta = 12°$. In the measured data, no excess count rate is observed for the monopixel events. The analysis then looks at clusters with an area A up to 5 pixels, identifying the signal and background ToT contribution. The summed results reveal an excess count rate that is fitted with a Moyal distribution, revealing a peak at 140 ± 19 ToT units [25 ns], which can be translated via the calibration to an energy deposition of 118 ± 16 keV, matching the expected

signal for the muons mostly peaked at kinetic energy of 120 MeV.

Finally, the count results are compared to dedicated FLUKA simulations reported in ref. [63]. The average count rate $8.6 \cdot 10^{-3}$ counts/cm^2/pb^{-1}, matching the normalized simulated predictions with a ratio of simulated to measured data of $R = 1.96 \pm 26$, significantly better compared to the previous measurements using scintillating fibres reported in ref. [250].

To conclude, the observed performance of the Timepix3 detector with a low detection threshold opens the door for its usage for a muon flux monitor in a variety of locations, particularly interesting for physics beyond colliders (PBC) experiments. A similar study [258] is expected for the scattering neutrino detector (SND) experiement [259], situated on the line of sight an 430 m away from interaction point 1 (IP1) (ATLAS).

Epilogue

15
Conclusions

This thesis presents a detailed characterisation of the Large Hadron Collider (LHC) [1] radiation field in a previously insufficiently explored area in light of the High Luminosity LHC (HL-LHC) upgrade [2]. The study of the radiation field is aided by (i) the development of a novel Timepix3 radiation monitor [22] for the new application of radiation measurements at the European organisation for nuclear research (CERN) accelerator complex, and (ii) theoretical simulations done using the FLUKA Monte Carlo code [18–20], benchmarked with experimental measurements during Run 2 (2015-2018) and Run 3 (2022-to date), performed with the beam loss monitor (BLM) system [21]. The achieved goals are the development of two new tools for the HL-LHC radiation levels monitoring in the context of the radiation to electronics (R2E) activities [16] at CERN. The thesis is structured into three main parts: (1) the completely new FLUKA simulation model of LHC insertion region 4 (IR4) (straight region of the accelerator, with a designated role; here, beam acceleration), including the radiation levels analysis of the Beam Gas Vertex (BGV) [96–98] and Beam Gas Curtain (BGC) [99–101] instruments, (2) the characterisation of a radiation monitor as a new application of the existing Timepix3 technology, and (3) combining the two tools for the analysis of the radiation levels induced by the BGC in the 2023 LHC operation.

In the first act, the benchmarking results for the Beam Gas Vertex (BGV) and the Beam Gas Curtain (BGC) demonstrators are of paramount importance to cross check the two independent tools used for assessing the radiation levels in the large hadron collider (LHC) accelerator environment: (i) measured data from radiation monitors, and (ii) FLUKA simulations. The new work consists in modelling the IR4 accelerator and identifying the correct radi-

ation source term in the very difficult scenario of IR4, which consists of a complex radiation field, a geometry that spans hundreds of meters and for several radiation sources far away from the regions of interest. The LHC radiation field includes different kinds of particles with broad energy spectra, all originating from the interaction of TeV-scale beam particles or secondary collision products. The general level of agreement of the BLM simulated to measured data that results from this study is a factor of $\mathcal{R}_{BGV} = TID_{sim}/TID_{meas} = 1.09 \pm 0.29\%$ for the BGV instrument, and $\mathcal{R}_{BGC} = TID_{sim}/TID_{meas} = 2.19 \pm 80\%$ for the BGC instrument. No issues regarding the critical operation of the present LHC or future HL-LHC machines are foreseen.

In the second act, the study of a well known detector technology, the Timepix3 chip [161], bonded to a 300 μm thick silicon pixel sensor was characterized as a novel radiation monitor for the measurement of the mixed field of the LHC accelerator. This act is further divided into three main chapters. Firstly, a detailed description of the Timepix3 radiation monitor was given, covering the hardware setup and the Timepix detection principle based on the simultaneous measurement of the time over threshold (ToT) and time of arrival (ToA), allowing for dose and particle rate measurements. Moreover, the Timepix calibration procedure, which translates the measured ToT per pixel into deposited energy, presents complex saturation effects at high energy. To mitigate these effects, the Timepix3 radiation monitor is operated in hole collection mode, and as a novelty, at a partial bias voltage of 50 V, enhancing the charge sharing between pixels.

Secondly, the energy calibration of the Timepix3 radiation monitor was carried out in two test campaigns

using hadron beams. The former experiment, at the radiation protection (RP) calibration laboratory (CALLAB) facility at CERN [203], Geneva, Switzerland, using a ^{241}Am source emitting alpha particles α with up to 4.8 MeV, which get attenuated in air to lower energies. The operational settings of the setup have been tested and familiarity with the setup was achieved. Several data points for energy calibration have been collected using the detector, however they are considered to be part of the saturation regime and not in the regular (normal) operation for the detector. For this reason, a second campaign at centro nacional de aceleradores (CNA) [209, 210, 212], Sevilla, Spain, using quasi-mono energetic beams of protons (alphas) from 0.6 (1) to 5 (8.4) MeV, fully stopping in the active volume of the sensor.

The calibration analysis aims to extract the energy deposited E_{dep} from the measured Timepix3 quantity, the time over threshold (ToT). The sensor operates at a predefined threshold level, and counts the clock units when the collected signal is above this threshold, hence time over threshold. The cluster level calibration analysis indicates that the detector operates in a linear regime up to 2 MeV, with $ToT_{reg}(E_{dep}) = E_{dep} \cdot (993 \pm 93)$ [25 ns/MeV] $+ N \cdot (23.10 \pm 2.14)$ [25 ns/pixel], with N being the number of active pixels in a cluster, while evidence of saturation effects is visible for energy depositions above this regime, especially for the case of proton beams.

At the pixel level, the saturation is estimated to occur from around 600 keV. The larger levels of saturation observed with protons compared to alphas are found to be associated with a different degree of charge sharing in the respective clusters, thus confirming that operating the sensor with a reduced bias voltage to enhance charge sharing is a good strategy to mitigate the saturation. No evidence of high-energy non-linear saturation or volcano effect is observed in the data. As part of the calibration measurements, the detector was irradiated at several angles up to 45° with 597 keV protons to estimate the dead layer thickness of the chip, quantified to be $T_{DL} = (333 \pm 60)$ nm.

Thirdly, two test campaigns have also been performed using neutron beams in different energy regimes. The former, at institute Laue-Langevin (ILL) [217], Grenoble, France, consisted of using cold neutrons (moderated from a nuclear fission reactor) peaked at 6.67 meV, confirming that only a small fraction of the neutrons interact in the Si sensor of the Timepix3 radiation monitor. Collimators made out of boron carbide B_4C were used to reduce the high beam flux and to observe the spatial structure of the beam, while neutron conversion layers made out of lithium flouride LiF were used to increase the neutron count rate by measuring the secondary products from the $n + ^6Li$ reaction. The second neutron campaign was performed at the calibration laboratory (CALLAB) facility at CERN, Geneva, Switzerland, using an americium-beryllium (AmBe) source emitting neutrons up to 10 MeV, with or without a polyethilene (PE) moderator to slow down the fast neutrons. The results of this test campaign are compared with another detector under study in the R2E activities at CERN, namely a silicon diode detector, as well as with two Monte Carlo (MC) codes: FLUKA and G4SEE [224, 225, 230], allowing to compare the codes.

In the third act, the Timepix3 radiation monitor has been deployed for the first time in the LHC at IR4 in order to assess the radiation field during nominal LHC operation (considered as background), and particularly, by the BGC operation (considered as signal), as described in detail via the simulations in the first act. This brings together the two newly developed tools of this thesis, for radiation monitoring at the present LHC machine and for the future HL-LHC operation, complementing and assisting each other for a better understanding of the composition of the radiation field, in this thesis focused on IR4. Moreover, the usages of the Timepix3 detector have been compared to the existing monitoring technologies; in particular, it lowers the energy detection threshold and allows for a particle-by-particle measurement.

By studying with FLUKA the energy deposited in the sensors by particles in the LHC mixed radiation field, the detector is found to be suitable as a dose rate monitor since the particles are expected to deposit energy

within the linear calibration regime, with only a small fraction of the hits leading to saturation effects. As a partial exception, saturation is expected to play a non-negligible role when measuring neutron-induced TID due to the large energy deposited by inelastic nuclear reactions. To summarise, the ratio of the FLUKA simulated to measured data for the dose rate presents itself at $\mathcal{R}_{Dose} = Dose_{sim}/Dose_{meas} = 0.60 \pm 35\%$, within the expected factor of 2 for this type of studies. The advantage of the low detection threshold is that it can be placed in a shielded alcove such as UX45, far away from the highest radiation levels, but still capable to isolate the Beam Gas Curtain (BGC) signal from the nominal LHC operation, with a high enough sensitivity. Moreover, the detector can be used as a particle flux monitor for charged particles with almost 100% detection efficiency, while for the neutrons further considerations have to be made, for which a second step FLUKA simulation has been employed. The measured values are compared with simulated results, revealing a simulated to measured data ratio for the counting rate (CR) of $\mathcal{R}_{CR} = CR_{sim}/CR_{meas} = 0.80 \pm 27\%$.

Furthermore, two new possible applications compared to the existing radiation monitors are explored in this work, and they consist in using the well studied Timepix3 detector as: (i) a radiation source locator, and (ii) a linear energy transfer (LET) (or dE/dx) detector. Both usages exploit the pixel array, identifying *tracks* from the reconstructed clusters. The data analysis focused on algorithms capable of extracting properties of energetic charged particles, namely their angular incidence (direction) and energy loss (LET), at the location where the detector was installed. The developed analysis methods were applied to measured data, and cross-checked with the FLUKA simulated results. Charged particles leave ionization tracks within the detector across multiple pixels, allowing for several morphological parameters to be computed, such as incidence angles: azimuthal angle Φ (on the 2D pixel array) and polar angle Θ (wrt. the orthogonal on the sensor surface). While the azimuthal angle Φ is used to identify the signal from the accelerator plane, the polar angle serves as a data point for benchmark

with the simulation: the average ratio for the polar angle θ of the simulated to measured data reveals an agreement of $\mathcal{R}_\theta = \theta_{sim}/\theta_{meas} = 0.85 \pm 20\%$, while for the LET measurement, the average ratio of the simulated to measured data reveals an agreement of $\mathcal{R}_{LET} = dE/dx_{sim}/dE/dx_{meas} = 0.59 \pm 87\%$. The high error stems from the absence of simulated particles with LETs smaller than $1 \, MeV \, cm^2/g$, and a gap between the simulated and measured data in the 2 to $5 \, MeV \, cm^2/g$ range.

In addition, a muon flux measurement campaign was performed at the proposed location of the CODEXb experiment in the LHCb cavern, during a luminosity production run in the interaction point. The lower energy threshold of the Timepix3 sensor is a clear advantage compared to the standard monitors, which allowed to measure an average hit rate during stable beams when no other monitor measured anything above their thresholds. The muon rate during luminosity production, just behind the concrete shielding wall, was around $8.6 \, counts/cm^2/pb^{-1}$, matching the FLUKA simulated predictions with a ratio of FLUKA to Timepix measurement for the counting rate (CR) at $\mathcal{R} = CR_{sim}/CR_{meas} = 1.77 \pm 26\%$.

To provide an outlook, the FLUKA geometry and the data analysis code can now be used to study the beam gas monitors also for the ion operation, which are expected to yield lower radiation levels. Moreover, the same simulation geometry can be used for other instruments which induce radiation levels (e.g. the wire scanner). In case the radiation levels are considered too dangerous for the operation of the accelerator or of other instruments, mitigation strategies (e.g. additional shielding) and their feasibility can be studied in detail.

As a continuation of the on-going measurements at IR4 (envisaged to continue the monitoring work of this thesis until the end of Run 3, scheduled end of 2026), there are several planned test campaign and analyses involving the Timepix3 radiation monitor of which only four are highlighted here.

1. The first one consists of measuring the muon rate at the scattering neutrino detector (SND), placed 480 m away on the line of sight of the a

toroidal LHC apparatus (ATLAS) experiment, and comparing with the FLUKA simulations.

2. The second campaign deals with the usage of the Timepix3 detector as a beam characterisation monitor for heavy ions as part of the HEARTS [65] project (high-energy accelerators for radiation testing and shielding), funded by the European union (EU) commission.

3. The third measurement is on the quench protection system (QPS) in the dispersion supressor (DS) region around the a large ion collider experiment (ALICE) (IP2), because of unknown failures that have been observed in the past during the LHC lead ion (Pb) operation. The linear energy transfer (LET) discrimination power of the Timepix3 radiation monitor could be used to identify heavy ions in the radiation field.

4. Finally, while in this thesis the detector was used in a low radiation area at IR4, its usage in locations with harsher radiation levels can also be explored, for example at IR7, the collimation region of the LHC.

Part I

Appendix

Radiation effects on electronics

Focusing on quantifying radiation-induced damage to electronics, the damage mechanisms that take places in the presence of various radiation fields can be classified in the two main categories discussed in the next paragraphs.

1 Cumulative effects

Cumulative effects take place through a continuous exposure to radiation that is happening during the active lifetime of the electronics, causing permanent damages and thus, making them out of specification. In cases like this, the effect is permanent and a power reset does not solve the problem.

1.1 Total ionizing dose

When charged particles and photons penetrate a medium, they interacts with electrons in the atomic shells, possibly leading to ionisation, which in semiconductors can be considered as electron - hole pairs creation. The total ionizing dose (TID) is a quantity used to describe this cumulative ionisation effect. The main issue with TID is the gradual performance deterioration of the circuits that can potentially lead to system failures. Presented in different units depending on the application, the most common one is the radiation absorbed dose (rad) and the one used in this thesis is the international system unit (ISU), gray (Gy), where $1 \, \text{Gy} = 100 \, \text{rad} = 1 \, \text{J/kg}$.

The TID impacts the conductive properties of the material, such as leakages or threshold voltage shifts. In microelectronics, TID defects imply the accumulation of trapped charges in the field oxides of the circuit. As ionization occurs, electron-hole pairs are formed in the material (e.g. silicon dioxide SiO_2). Not all of the pairs recombine, but some of them move due to the applied electric field. Owing to their much higher mobility, electrons can exit the oxide leading to trapped holes in defect centers in the oxide volume. Furthermore, this process can activate other defects at the oxide interfaces. TID causes device degradation mainly via creation of defects and charge buildup. Some examples include:

1. **Threshold voltage shifts**: Charge buildup is caused by holes trapped in the bulk of the oxide. These charges could alter the gate oxide of metal-oxide-semiconductor (MOS) transistors electric fields, leading to a change in its I-V characteristics. Most important is the shift of the power-ON (threshold) voltage which is negative for n-channel (NMOS) and positive for p-channel MOS (PMOS). As a result, a device might become unresponsive to some commands as it might be "blocked" on a specific state.

2. **Increased leakage current**: In NMOS transistors, the interface and free leakage paths could be reversed due to the charges that might create an image charge in the semiconductor. These parasitic leakage currents increased power consumption and exhibit degraded timings.

3. **Amplifier gain degradation**: TID-induced damage in bipolar transistors usually manifests as a reduction in bipolar gain with increasing total dose exposure. The device requires more supplied power in order to compensate for gain degradation.

4. **Dark signal in camera sensors**: As a direct effect of charging the gate oxides, electrostatic potential is generated in pixels which shifts and gets "un-pinned". This results in thermally generated charges that are not suppressed anymore. This manifests as an increased noise background and is observed in both and complementary MOS (CMOS) and charge-coupled devices (CCD), leading to a compromised dynamical range of the imager.

When it comes to qualifying a device for TID, it is usually done via an accelerated-life test approach, as it is not feasible to expose it over the years they

will be employed at CERN. In order to reach reasonable running times of the qualifying experiments, the accelerated testing is done at substantially higher dose rates than in the accelerator environment. However, this assumption that the component reaches its end-of-life depending only on the total dose has been proven wrong in practice for a specific family of device.

In particular, bipolar devices suffer more detrimental the effects at lower dose rate. This phenomenon is called enhanced low dose rate sensitivity (ELDRS) and is a serious risk to consider when designing power distribution systems and their shielding. For example, CERN considers a factor of 5 margin when specifying radiation levels due to ELDRS. Usually, the low dose radiation rate is considered to be less than or equal to 100 μGy/s. Compared to it, high dose rate testing at 100 Gy/s takes only to 28 hours.

To provide some context, the difference between different levels of TID qualification levels, commercially off-the-shelf (COTS) devices are typically rated below 100 Gy (SiO_2), radiation-tolerant devices below 1 kGy (SiO_2) whereas radiation-hardened devices above 100 kGy (SiO_2).

1.2 Displacement damage

Generally, structural damage (e.g. atomic rearrangement) on the crystal lattice of devices by non-ionizing energy loss in the material caused by high energy particles (e.g. neutrons) is called displacement damage (DD). This can lead to crystal imperfections, e.g. lattice atoms displaced to defect locations and vacant lattice sites. When this occurs, the electrical properties at the defect's region get modified by the creation of new energy states within the energy band gap region of the semiconductor. This effect is increasingly detrimental with the increase in the number of defects. The defects can play a role in various undesired ways: charge traps, recombination centres, generation centres of thermal charge and more other.

Compared to TID, displacement damage dose (DDD) comprise all non-ionizing dose effects on a device,

and can be referred to as total non-ionizing dose (TNID). In general, the TNID effects are independent of the flux or the device biasing and consists of an increased defect concentration throughout the device bulk. In the following, a summary of DD effects on electronic devices is presented:

- **Gain degradation**: Due to the recombination centres created by DD, the minority charge carriers will have a shorter lifetime. This leads to an increased input bias current that is necessary, thereby leading to a reduction in gain.

- **Gate-oxide breakdown**: In extreme cases, the accumulation of DD defects may result in a short in the insulating layer in the gate oxide bulk. Locally, this could melt the region and destroy the structure.

- **Charge traps and hot pixels on camera sensors**: Image sensors (CCD, CMOS etc.) are particularly affected by DD via various mechanisms. In some cases, defect clusters in the pixel array could act as regions with increased dark signal, leading to distinctly bright spots in images. In other cases, defects could act as traps for photo-generated charge, thereby reducing the charge transfer efficiency leading to signal streaks in the image.

2 Single-event effects

Stochastic events caused by energy deposition by one highly energetic particle in a sensitive volume (e.g. a memory cell) are called single event effects (SEEs). In order to ensure the reliability of semiconductor devices (and electronics, in general) in the harsh accelerator environment, the equipment should be tested for both TID and SEE. However, testing for the SEE performance of a device is more complicated than for the TID hardness; this is mainly due to the increasing complexity of modern digital devices, the different manifestations of these effects and the fact that testing for SEEs takes place during radiation exposure while TID testing does not.

SEEs are classified in hard (destructive) or soft (non-

destructive), based on whether the device can resume nominal operation after a power cycle. Soft errors consists of: single event upset (SEU), single event transient (SET) and single event functional interrupt (SEFI), while hard errors consist of: single event latch-up (SEL), single event burnout (SEB), single event snapback (SESB), single-event dielectric rupture (SEDR), single event gate rupture (SEGR) and single event burnout (SEB) [260]. The severity or harshness of SEEs is given by the effect type from the aforementioned ones and depends on how critical the system is for operation.

For example, in digital devices, information is sent/stored as bits. A type of SEE is the single event upset (SEU), which can flip the bit to its opposite value thereby altering the information.

The SEE can be produced:

- directly, caused by particles with high linear energy transfer (LET), e.g. heavy ions. The SEE is generated by direct ionisation along the particle path within the device. In this case, the more convenient energy loss metric is not particle energy but the LET, which is the rate of energy loss per unit length on a material. However, this scenario is not relevant for the LHC as only a negligible amount of high-LET ions actually reach electronic equipment.

- indirectly, the dominant source of SEEs at the LHC, caused by neutral or low-LET particles, predominantly hadrons.

Indirect ionisation can be further subdivided based on its root cause into those induced by high energy hadrons (HEH) and thermal-energy neutrons (THN), which shall be described in detail in the following sections. The total number of SEEs is then defined as the product of fluence (Φ, in units of cm^{-2}) and cross section (σ, in cm^2), as:

$$N_{SEE} = \Phi_{THN}\sigma_{THN} + \Phi_{HEH_{eq}}\sigma_{HEH_{eq}} \qquad (1)$$

As mentioned, the radiation hardness assurance (RHA) consists also in an SEE qualification approach, based on the characterization of two cross sections:

(i) 20-MeV protons (or equivalents fluxes at high-energy) and (ii) thermal neutrons with a kinetic energy of at least 0.025-eV, and it is schematically shown in figure 1.

Compared to TID, the implication is different as a single particle is capable of creating an observable effect in the device regardless of the irradiation history. For this reason, one is interested in evaluating the fluence of HEHs impacting the electronics.

2.1 Particle fluence

The mean free path λ denotes the average distance travelled by a particle in a material before an interaction, while its inverse Σ is the probability of interaction per unit distance, also called macroscopic cross section. Both λ and Σ are not only material dependent, but they also vary depending on the particle type and energy. For a stream of particles, that we shall assume to be identical, the number of interactions R occurring in a given time interval is equal to the total distance travelled l times the probability per unit distance Σ. For N particles:

$$R = Nl\Sigma \qquad (2)$$

The reaction rate is then the derivative of this quantity:

$$\dot{R} = N\frac{dl}{dt}\Sigma = Nv\Sigma \qquad (3)$$

where v is the average particle velocity. Assuming that the density of particles at spatial position r is $n(r,v) = dN/dV$, the reaction inside a volume element dV is:

$$\frac{d\dot{R}}{dV} = n(r,v)v\Sigma \qquad (4)$$

The quantity $\dot{\Phi}(r,v) = n(r,v)v$ is known as fluence rate or flux density, with dimensions of [m^{-3} m/s] = [m^{-2}/s]. The time integral of the flux density yields the fluence:

$$\Phi(r,v) = n(r,v)dl \qquad (5)$$

In practice, the fluence is measured in particles per cm^2 and it describes the density of particle tracks. Computationally, it represents a track length estimation as:

$$\dot{\Phi}(v)dt = n(v)vdt = \frac{dN(v)}{dV}\frac{dl(v)}{dt}dt = \lim_{\Delta V \to 0}\frac{\Sigma_i l_i(v)}{\Delta V} \qquad (6)$$

2.2 High energy hadrons

Hadrons are composite subatomic particles, made out of quarks (and antiquarks), such as protons, neutrons and pions. The high energy hadrons (HEH) term is employed in the R2E context to designate hadrons carrying enough energy to induce SEEs, usually in the order of MeVs through indirect ionisation. In general, charged hadrons under 20 MeV are considered not capable to generate SEEs, either due to their very low energy deposition or because they can not simply go through the component package. The 20 MeV limit does not have a universal physical mechanism, but depends on the device, and recent research [261] even points to a 1.5-3 MeV acute sensitivity for modern electronics.

Nevertheless, neutrons can still induce SEEs even at lower energies, and for this reason there is an energy dependent Weibull distribution for intermediate energy neutrons (0.2-20 MeV) and a function decreasing as $E^{-1/2}$ for thermal neutrons, as expected for processes dominated by neutron capture[1], as described in the next section.

The SEE response as a function of energy is assumed to be a Weibull function at 20 MeV as regards charged hadrons. The values of the Weibull parameters for

---

[1] An interpretation of this behaviour is: at thermal energies, the faster the neutron is the smaller its capture probability is until a point where other multiple mechanisms are activated and the cross section starts again to raise. Beyond the 20 MeV of energy threshold, hadrons have roughly a constant (independent from the energy) probability to be captured.

the response function is device-specific (see Table 1 for typical values for R2E devices).
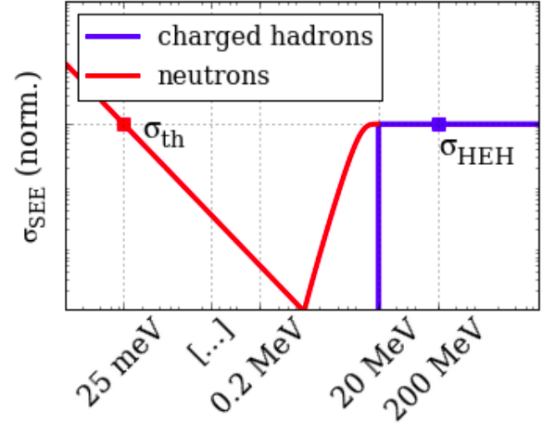
Figure 1: Charged hadrons and thermal neutrons cross sections as a function of the energy (fig. from ref. [226]).

Table 1: SEE cross section and Weibull parameters of 32Mbit ISSI and 4Mbit Toshiba static random-access memory (SRAM).

	$\sigma_{\text{HEH}}^{\text{sat}}$ [cm^2/bit]	E_{th} [MeV]	W [MeV]	s
Toshiba	$6.6 \cdot 10^{-14}$	0.2	9.25	3.02
ISSI	$1.4 \cdot 10^{-14}$	0.01	14.05	0.82

Given their high energy, the local shielding mitigation technique is not effective. Moreover, they are more abundant in the LHC tunnel as compared to the shielded alcoves, where most electronics racks are located. For the case of protons, the energy deposition normally occurs via nuclear interactions, resulting in recoil ions which ionise the neighbourhood of the impact location. The response for a given device is then convoluted with the mixed-field spectra, yielding the expected operational SEE rate, given as the HEH equivalent (HEHeq) fluence. More details concerning this approach can be found in ref. [262]. Nevertheless, we summarise here the main equations.

The sum of the differential flux of hadrons above 20 MeV is defined as the high-energy hadron (HEH) flux and measured in $\left[\dfrac{\text{particles}}{\text{cm}^2 \cdot \text{s}}\right]$.

$$\Phi_{HEH} = \int\limits_{20 MeV}^{\infty} \sum_{i=1}^{\text{hadron species}} \frac{d\phi_i(E)}{dE} dE \qquad (7)$$

$$= \int\limits_{20 MeV}^{\infty} \frac{d\phi_{HEH}(E)}{dE} dE$$

The fluence in units of $\left[\dfrac{\text{particles}}{\text{cm}^2}\right]$ is obtained by integrating the flux over time:

$$\Phi_{HEH} = \int\limits_{t_0}^{t_1} \int\limits_{20 MeV}^{\infty} \frac{d\phi_{HEH}(E)}{dE} dE dt \qquad (8)$$

$$= \int\limits_{t_0}^{t_1} \phi_{HEH} dt$$

The high energy hadron equivalent flux considers the intermediate energy neutron contributions, defined as follows:

$$\phi_{HEHeq} = \int\limits_{0.2\,MeV}^{20\,MeV} \sigma(E) \frac{d\phi_n(E)}{dE} dE + \int\limits_{20\,MeV}^{\infty} \frac{d\phi_{HEH}(E)}{dE} dE \qquad (9)$$

with the HEH equivalent fluence (HEHeq):

$$\Phi_{HEHeq} = \int\limits_{t_0}^{t_1} \phi_{HEHeq} dt \qquad (10)$$

with the general Weibull fit expression:

$$\sigma(E) = \sigma_{sat} \cdot \left(1 - \exp\left[-\left(\frac{E - E_{th}}{W}\right)^s\right]\right) \qquad (11)$$

$$= \sigma_{sat} \cdot w(E)$$

with typical values for the saturated cross sections σ_{sat}, threshold energy E_{th}, scale parameter W and shape parameter s in Table 1.

2.3 Thermal energy neutrons

Thermal energy neutrons (THN) with $E \approx 0.25$ eV are responsible for soft SEEs only, e.g. through the $^{10}B(n, \alpha)$ neutron capture reaction, as illustrated in fig. 2 and ref. [263]. This process is typically more abundant in the shielded alcoves compared to the LHC tunnel and the R-factor (described in the next section) is meant to differentiate amongst such regions.
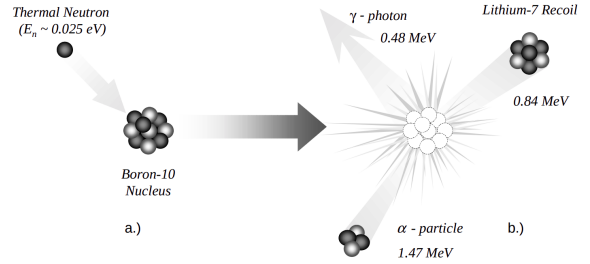
Figure 2: The **(a)** ^{10}B nuclear fission with a thermal neutron, leading to the **(b)** reaction products: photon, ^{7}Li and the α particle that will induce the SEU (fig. from ref. [263]).

The thermal neutron fluence is computed from the neutron flux ϕ_{THN} with a weight equal the inverse of the square root of the energy $w(E) = E^{-1/2}$, leading to the first decreasing curve of fig. 1. This definition includes not only the 0.025 eV neutrons, but a wider spectrum:

$$\phi_{THN} = \int\limits_{0}^{\infty} \sigma_{THN} \cdot w(E) \cdot \frac{d\phi_n(E)}{dE} dE \qquad (12)$$

$$\Phi_{THN} = \int\limits_{t_0}^{t_1} \phi_{THN} dt \qquad (13)$$

2.4 R-factor

Another quantity usually investigated in the scope of R2E is the so-called risk factor (R-factor), a dimensionless quantity that expresses how many thermal

neutrons relative to HEHeq are present as:

$$R = \frac{\Phi_{THN}}{\Phi_{HEHeq}} \quad (14)$$

Using this definition, one can invert equation 1 to estimate the HEHeq fluence from the number of SEU counts:

$$\Phi(HEH) = \frac{N_{SEU}}{R \cdot \sigma_{THN} + \sigma_{HEH}} \quad (15)$$

All LHC locations (both tunnel and shielded alcoves) are defined using the R-factor in order to assess whether the electronic component can survive in the radiation environment. The R-factor is evaluated either from experimental data (where radiation monitors were deployed) or from simulations, and is given in Table 2 [148, 264].

Table 2: List of R-factors for the areas of interest for this thesis

Area	R-factor
Tunnel	1.5
RRs shielded	5
UJs shielded	10
ULs	10

2.5 Limitations

This HEHeq approach to estimate the SEEs presents the following limitations:

- The assumption that the HEH cross-section σ_{HEH} is constant at high energies is an approximation not always hold, as already indicated for pions in ref. [265].

- The HEH cross section may depend on the hadron type. For example, pions have a cross section peak around 150 MeV, unlike protons, implying that the SEE rate can depend on the composition of the radiation field. The present consideration assumes that each hadron species contributes equally to the SEEs (see equation 8).

- It is important to assess the related risk of the neglected SEEs induced by direct ionisation from low-energy charged particles (such as electrons, muons, protons).

- The cross sections σ_{THN} and σ_{HEH} used for computing number of SEEs in equation 1 are measured in radiation test campaigns in specific conditions (energy, particle type), which can differ from the accelerator environment.

192

1 FLUKA physics models and capabilities

An overview of the flukturiende kaskade (FLUKA) physics models can be found in its online manual and references. A very short summary will be given here to highlight the main interactions of interest for this thesis.

The main source of radiation in the LHC tunnel around the interaction points (in this thesis, IP1 and IP5) are collision debris from the interaction point. Therefore, we distingush first between hadron-hadron interactions at the IP and hadron-nucleon interaction along the tunnel, both categories being simulated by different event generators depending on the energy (and projectile). For inelastic hadron-hadron interactions:

- For momentum < 20 TeV/c and > 5 GeV/c: dual parton model (DPM) [266]

- Momentum from lower particle threshold to 5 GeV/c: Resonance production and decay model [267]

The inelastic hadron-nucleon interactions:

- Momentum < 20 TeV/c and > 5 GeV/c: Glauber-Gribov multiple scattering followed by generalized intranuclear cascade (GINC)

- Below 5 GeV/c for nucleons, anti-nucleons and pions; below 1.5 GeV kinetic for kaons: Preequilibrium-cascade model PEANUT [268, 269]. In between PEANUT and DPM for kaons [270].

All three models above include evaporation and gamma deexcitation of the residual nucleus [271].

This thesis focuses on energy deposition in several radiation detectors, and hence a brief overview of the energy loss mechanisms is provided below. Amongst many mechanisms, we highlight the:

- Bethe-Bloch theory [237], Barkas Z^3 [272] and Bloch Z^4 effects [273].

- Mott correction to the Rutherford scattering cross section [274].

- Ranging out particles below energy cutoff, handling of porous substances and improved ionisation potential.

- Shell and other low-energy corrections derived from ref. [275].

- Ionisation potentials and density effect parameters [276].

- Accurate treatment of curved trajectories and boundaries in magnetic and electric fields.

- Bremsstrahlung at high energy by heavy charged particles, also with electron pair production.

A special note used to be applicable for low-energy neutrons ($E < 20$ MeV) before December 2023 [229], when FLUKA used its own neutron cross section library (P_5 Legendre angular expansion, 260 neutron energy groups [276]), containing more than 250 different materials. In particular, the transport of proton recoils and protons from ^{14}N(n,p)^{14}C reaction, relevant as they occur in the N_2 present in air and in the beam loss monitor (BLM) active volume. After this update, FLUKA now uses point-wise neutron interactions.

2 FLUKA usages

An integral part of the FLUKA code development is the benchmarking of the validity of its physics models and new features against experimental data over a wide energy range, which includes the comparison of predictions of individual models to measurement results (such as particle angular distributions and multiplicities). In the scope of this thesis, the FLUKA physics is assumed to be accurate, and any discrep-

ancy observed in the benchmarking of the complex application to the LHC is more likely due to geometrical effects or a non-ideal understanding of the beam loss mechanisms. In the more general context of radiation to electronics (R2E) at CERN, FLUKA has been extensively used not only for the experimental areas, but also to address electronics failures at intensive beam loss regions around the LHC accelerator, but also in the ARC regions.

The simulation data are continuously reevaluated to predict the radiation levels for several LHC operational conditions (in particular the nominal configuration), as well as for feasibility studies for future colliders (mostly for the High Luminosity LHC upgrade). The aim of the R2E activity is to provide specifications on the maximum fluence/dose values for each critical underground area, taking into account the related uncertainties (such as assumptions in operational constraints, equipment sensitivities, etc.). A safety rule of thumb is that the values obtained by the simulation benchmarking should rather overestimate measured data, rather than underestimate.

The outcome of such studies represents the starting point in the environment parametrization and radiation hardness qualification requirements that need to be fulfilled by considered electronic devices meant to have a reliable operation.

At CERN, in addition to R2E, FLUKA is extensively used for machine protection issues such as energy deposition or power calculations and studies of material damage to accelerator beamline elements [277, 278].

3 Geometry construction tools

The advanced graphical user interface for particle simulation programs (FLAIR) tool [132, 133] is an advanced graphical user interface for particle simulation programs that eases the geometry construction for the user. Initially for FLUKA, the interface is now separated from the functionality permitting an easy integration of other simulation packages, such as FLUKA, geometry and tracking (GEANT)4 [69,

182–184], penetration and energy loss of positrons and electrons (PENELOPE) [73], and Monte Carlo n-particle transport (MCNP) [70].

Considering the complexity of the LHC accelerator, several tools have been developed that help the user to build the simulation files. In order to implement the geometry, FLUKA Element Database (fedb) and the linebuilder (LB) have been used [**IPAC2012:Mereghetti:WEPPD071**]. The fedb is a database containing the FLUKA geometry models of different accelerator components (such as magnets, collimators, absorbers, BLMs, etc.), which are used with a modular approach to build the whole line. These elements, together with the tunnel, are implemented based on the CERN Drawing Directory [279]. The LB is a Python-based tool for assembling accelerator beam lines for FLUKA simulations (such as LHC, SPS, SPS). In particular, it allows to arrange accelerator components from fedb on the basis of Twiss file information [280]. The radiation monitors are not beamline elements, but can be added as additional components to LB by specifying their position (and orientation). This information has been extracted from the CERN layout database (LDB) [281], and visually double checked with the GIS portal [282].

Radiation monitors employed at the LHC

The radiation monitoring sensors at the LHC consist of: over 400 radiation monitors (RadMon) and 4000 beam loss monitors (BLM). For Run 3 (but already for the interaction point IP1 in 2018 of Run 2), passive measurements done with the optical fiber detectors will also be used, with the advantage of a continuous spatial resolution for the detected radiation. The last radiation monitor used at CERN are the radio photo luminescence (RPL)s, very small detectors that can absorb high levels of dose.

1 Radiation monitors (RadMon)

In total, roughly 400 radiation monitors (RadMons) [151, 152, 249] are placed in strategic locations around the LHC tunnel and its adjacent shielded areas to monitor the radiation field relevant to radiation induced failures in LHC electronics [249]. The RadMon detectors provide measured data on the total tonizing dose (TID) by means of radiation-sensitive metal-oxide-silicon field-effect transistor (RADFET)s, displacement damage (DD) by the means of p-i-n diodes and high energy hadron equivalent (HEHeq) fluence (for particle energies above 20 MeV) by counting single event upsets (SEU) of SRAM memories.

The RadMon was developed at CERN in the engineering (EN) department. The first generation of RadMon deployed in the LHC (referred to as V5) has 9 radiation sensors on the board: 2 RADFETs with different oxide thicknesses (100 nm, 400 nm and 1000 nm) for the TID measurements, 3 photodiodes in series for the measurements of 1 MeV equivalent neutron fluence and a Toshiba SRAM memory to measure the cumulative fluence of hadrons with energy higher than 20 MeV (HEHeq) and thermal energy neutrons (THN) through different voltage settings. [249]

Obsolescence of several components used for the RadMon V5, feedback from the on-field usage of the monitor in Run 1 of LHC operation (2010-2012), and, in particular, new monitoring requirements lead to

Table 1: RadMon V5 cross sections for high energy hadrons and thermal energy neutrons

Bias [V]	σ_{THN} [cm^2/bit]	σ_{HEH} [cm^2/bit]
5	$3.1 \cdot 10^{-15}$	$3.0 \cdot 10^{-14}$
3	$1.7 \cdot 10^{-13}$	$7.0 \cdot 10^{-14}$

the launch of a new design of the RadMon (referred to as V6) [151], which aims at resolving issues and limitations experienced with the previous version. The main developments are: higher radiation tolerance (more than 200 Gy, as opposed to the 80 Gy for V5), modular achitecture for easy replacement of parts and updates, remote configurability and improved measurement accuracy. On the sensor side, the RadFETs and the pins are the same as for V5, but the Toshiba SRAMs are now paired with 4 chips of Cypress 40 nm SRAM, which are insensitive to thermal neutrons. The use of two memories with different sensitivities to thermal neutrons allow the direct evaluation of the R-factor.

The RadMons can be operated at two different voltage settings in order to achieve different sensitivities to both thermal neutrons and high-energy hadrons. The Toshiba memories become significantly more sensitive to thermal neutrons when it operates a 3 V bias voltage compared to 5 V, as indicated by the cross section from Table 1. All the RadMons deployed in the tunnel are biased at 5 V and an R factor of 1.5 is considered. Reports on RadMon measurements can be found for p-p (proton) runs in ref. [148], while for the Pb-Pb and p-Pb runs in ref. [264].

Regarding the position of the RadMons, the locations are not exactly the same in all the cells and points. All the RadMon installed in the tunnel are reported on CERN's "GIS machine map" (Machine/Equipment/RadMons) [282, 283]. In the ARC regions, the RadMons are placed under the interconnection between the last bending magnet (quadrupole) of a given cell (where usually the electronic equipment

are placed) and are deployed until cell 21. The Rad-Mon in the shielded areas unfortunately are not included in the machine map, but their exact locations are collected in the drawings in the CERN database, and readily reported in the Appendix of ref. [148].

2 Radiophotoluminescence (RPL) dosimeters

Radiophotoluminescence (RPL) dosimeters are silver-doped phosphate glass rods primarily used as passive monitors of radiation levels in medical applications. At CERN, their operational range is extended thanks to a two-light measurement method that quantifies both radiation-induced luminescence and the light absorption [154]. Under radiation, electron-hole pairs are formed within the glass through ionization process. These additional carriers, when trapped by intrinsic and extrinsic point defects introduced by the silver ions, create adiophotoluminescence and color centers in the glass. The luminescence light is linearly proportional to the absorbed dose up to around 1 kGy, where it saturates due to the accumulation of color centers and the consequent self-light absorption [154]. At higher doses, the luminescence light intensity decreases with increasing dose. Thanks to their small size, stability and wide range, RPLs have been widely used at CERN for materials irradiation campaigns [284], beam characterization [285], and the monitoring of radiation levels throughout the accelerator complex [286].

3 Distributed optical fibre for radiation sensing (DOFRS)

Within R2E, a distributed optical fibre system (DOFRS) on radiation sensitive optical fibers. allowing to perform online and distributed dosimetry measurements has been developed. Presently, it is deployed in the proton synchrotron booster (PSB) [287] and proton synchrotron (PS) [288], and during long shutdown (LS)2 it has been deployed in super proton synchrotron (SPS) and Large Hadron Collider (LHC) dispersion suppressor (IP1, IP5 and IP7), while it had already been installed in IP1 dispersion supressor (DS) in 2018 for passive measurements.

The radiation sensor of choice is a p-doped OF privately produced by iXBlue Photonics [289], namely a step-index single-mode OF with an external cladding diameter of 125 µm with a pure silica cladding and a P-doped silica core, investigated the accelerator environment usage in ref. [288, 290]. The interest in this technological solution is not only thanks to the possible cost/performance advantages, but also to the technical benefits with respect to the point dosimetry systems currently employed at CERN. The optical fibre allows to perform online and distributed dosimetry measurements, and it is well adapted to be employed in long accelerators, running parallel to the beamline. It provides a linear map of the cumulated radiation dose with a spatial resolution of 1 m [291].

Sampling for the beam gas profile

The procedure to generate secondary products of (only) inelastic beam-gas interactions can be conceptually divided into three steps:

1. Setting up the gas density profile along the beam trajectory.

2. Sampling of beam-gas interaction points.

3. Simulation of particle showers.

1 Setting up a gas density profile along the beam trajectory

The procedure allows to specify different gas constituents (i.e. a mixture of gases, as the residual gas is typically made of several gas species) and their density profiles along the beam trajectory. This represents the main user input and is typically obtained from the beam gas instrument collaboration of interest (via measurements and/or simulations as is the case for the Beam Gas Vertex (BGV) and Beam Gas Curtain (BGC) in figures 6.2 and 7.2).

2 Sampling of beam-gas interaction points

The gas density profile defined in the previous step is interpolated, to the desired step size and the cumulative distribution function (CDF) of interaction probability along the particle trajectory is calculated.

The position of beam-gas interactions is sampled as a function of the s-coordinate of the curvilinear coordinate system describing particle motion in the accelerator. All beam particles are assumed to be on an unique orbit (e.g. the ideal orbit) such that the obtained s value can be uniquely mapped to cartesian coordinates used by FLUKA. Considering a s-coordinate interval $[s_a, s_b]$, the (unnormalized) beam-gas interaction probability becomes:

$$\Theta(s; s_a, s_b) = \int_{s_a}^{s} \sum_{j=1}^{N} \sigma_j \rho_j(s) ds \qquad (1)$$

Then, the cumulative distribution function (CDF) for sampling the probability at location s can then be written as:

$$C(s) = \frac{1 - \exp\left(-\Theta(s; s_a, s_b)\right)}{1 - \exp\left(-\Theta(s_b; s_a, s_b)\right)} \qquad (2)$$

For computational reasons, the gas distribution is assumed to be a discrete function of s:

$$\Theta_k = \sum_{i=1}^{k} \sum_{j=1}^{N} \sigma_j \rho_j(s) \Delta s_i \rightarrow C_k = \frac{1 - \exp\left(-\Theta_k\right)}{1 - \exp\left(-\Theta_M\right)} \qquad (3)$$

where $\Delta s_i = s_{i+1} - s_i$, and M is the number of discrete points in s.

Due to the low density of typical residual gases in vacuum chambers, the exponential term generally yields a number very close to 1. This holds also for when gas is intentionally injected for the beam-gas instruments. The subtraction $1 - \exp(-x)$ is therefore prone to loss of significant digits (even in double precision). Numerically, it is more robust to approximate the above expression by using first terms of the Taylor expansion of the exponential function:

$$1 - \exp\left(-x\right) \approx 1 - \sum_{l=1}^{\infty} (-1)^l \frac{x^l}{l!} \approx x - \frac{x^2}{2!} + \dots \qquad (4)$$

Using such an approximation, the natural question to ask next is what is the error that we introduce. For example, for the beam gas demonstrator investigated in this thesis, one injects Neon gas up to 10^{-7} mbar (roughly 10^4 larger than the residual gas). Considering the cross sections discussed in section 5.1.2, this

yields terms of the order of $\Theta_k \approx 10^{-8}$. If one were to compute the second order term, then it would be in the order of 10^{-16}, which is 10^8 smaller than the previous term. Hence, we retain only the first term, and the CDF then simplifies to:

$$C_k = \frac{\Theta_k}{\Theta_M} = \frac{\sum_{i=1}^{k} \sum_{j=1}^{N} \sigma_j A_j(s_i) \Delta s_i}{\sum_{i=1}^{M-1} \sum_{j=1}^{N} \sigma_j A_j(s_i) \Delta s_i} \qquad (5)$$

In this form, the CDF is implemented in the source routine to sample the position as a function of discrete s-coordinates.

3 Simulation of particle showers

As a third step, an inelastic interaction is enforced and secondary products are loaded on the stack. This step is further divided into four actions:

1. The position of interaction is sampled according to the aforementioned CDF.

2. At this position, a collision partner is sampled, according to the local gas composition and the cross section of the constituents.

   Once the location of the interactions has been determined, the source routine randomly selects an elemental species among the gas constituents. Assuming the obtained coordinate is $s = s_n$, the collision partner is sampled by means of the following CDF:

$$C_l = \frac{\sum_{j=1}^{k} \sigma_j \rho_j(s_n)}{\sum_{j=1}^{N} \sigma_j \rho_j(s_n)} \qquad (6)$$

   where l=1, ..., N.

3. The FLUKA event generator is called. The collision is generated and the secondary particle showers from this single geam-gas event are sampled.

4. FLUKA simulated the shower development of these secondary particles

This routine ensures a high efficiency, as all primary particles are scattered. Finally, the interaction probability is calculated which is used as a normalization factor.

$$P = \sum_{i=1}^{M-1} \sum_{j=1}^{N} \sigma_j A_j(s_i) \Delta s_i \qquad (7)$$

The output of the FLUKA simulations will be given in the value of interest (e.g. TID) per primary for a given pressure, and have to be renormalized to the values of interest.

Fit procedure

When analysing the data and plotting histograms of the several values of interest (e.g. the total ToT volume for the clusters), the signal was fitted with well known theoretical models. Particularly relevant for the calibration data, where the peak signal was thus isolated. The fitting procedure is summarised below:

1. Find maxima, by identifying the bin location ToT_{max} with most counts y_0.

2. Fit Gaussian distributions, using as first guess the parameters $\mu_G = ToT_{max}$, y_0 and $\sigma = ToT_{max}/10$

$$G(x; \mu_G, \sigma_G, y_{0,G}) = y_{0,G} \cdot \exp -\frac{(x - \mu_G)^2}{2\sigma_G^2} \quad (1)$$

3. Fit more physical models, where relevant, using as first guess the Gaussian parameters μ_G, σ_G and $y_{0,G}$. Here, the Landau distribution is considered for its utility in high-energy physics and radiation detection. It describes the energy loss of a charged relativistic particle due to ionization of the medium [292–294]. It is approximated numerically via an implementation using the Python scipy moyal package [295]. The probability density function for moyal is given as:

$$M(x; \mu, \sigma) = \frac{1}{\sqrt{2\pi}} \cdot \frac{1}{\sigma} \quad (2)$$
$$\exp\left(-\frac{1}{2}\left(\frac{x - \mu}{\sigma} + \exp\left(-\frac{x - \mu}{\sigma}\right)\right)\right)$$

From these fitting functions, the peak ToT (or energy) and the associated errors as: $E_0^{+\Delta E_+}_{-\Delta E_-}$, or for symmetric distributions simply $E_0 \pm \Delta E$, are retrieved.

Bibliography

[1] O. S. Brüning et al., *LHC Design Report, Vol. I: The LHC Main Ring*, CERN Yellow Report, Geneva, 2004, URL: `https://cds.cern.ch/record/782076`.

[2] *High-Luminosity Large Hadron Collider (HL-LHC): Technical design report*, CERN Yellow Reports: Monographs, Geneva: CERN, 2020.

[3] *High Luminosity LHC Project*, http://hilumilhc.web.cern.ch, (visited on 12th August 2023).

[4] A. Dainese et al., *Report on the Physics at the HL-LHC, and Perspectives for the HE-LHC*, tech. rep., Geneva, Switzerland, 2019, URL: `https://cds.cern.ch/record/2703572`.

[5] B. Schmidt, »The High-Luminosity upgrade of the LHC: Physics and Technology Challenges for the Accelerator and the Experiments«, in: *J. Phys.: Conf. Ser.* 706.2 (2016), p. 022002, URL: `https://cds.cern.ch/record/2263093`.

[6] ATLAS Collaboration., »Observation of a new particle in the search for the Standard Model Higgs boson with the ATLAS detector at the LHC«, in: *Physics Letters B* 716.1 (September 2012), pp. 1–29, URL: `http://dx.doi.org/10.1016/j.physletb.2012.08.020`.

[7] CMS Collaboration, »Observation of a new boson at a mass of 125 GeV with the CMS experiment at the LHC«, in: *Physics Letters B* 716.1 (September 2012), pp. 30–61, URL: `http://dx.doi.org/10.1016/j.physletb.2012.08.021`.

[8] ATLAS Collaboration, »The ATLAS Experiment at the CERN Large Hadron Collider«, in: *JINST* 3 (2008), S08003.

[9] CMS Collaboration, »The CMS Experiment at the CERN Large Hadron Collider«, in: *JINST* 3 (2008), S08004.

[10] LHCb Collaboration, »The LHCb Detector at the CERN Large Hadron Collider«, in: *JINST* 3 (2008), S08005.

[11] ALICE Collaboration, »The ALICE Experiment at the CERN Large Hadron Collider«, in: *JINST* 3 (2008), S08002.

[12] *CERN Council updates: European strategy for particle physics*, Available online: `https://home.cern/news/news/cern/cern-council-updates-european-strategy-particle-physics`, (visited on 11th December 2023).

[13] *Longer term LHC schedule*, URL: `https://lhc-commissioning.web.cern.ch/schedule/LHC-long-term.htm` (visited on 30th April 2022).

[14] *LHC Performance Workshop 2022*, 2022, URL: `https://indico.cern.ch/event/1097716/`.

[15] I. Dawson, *Radiation effects in the LHC experiments: Impact on detector performance and operation*, CERN Yellow Reports: Monographs, Geneva: CERN, 2021, URL: `http://cds.cern.ch/record/2764325`.

[16] *Radiation to Electronics (R2E) at CERN*, Available online: https://r2e.web.cern.ch/ (Accessed on 31 5 2022).

[17] R. García Alía et al., »LHC and HL-LHC: Present and future radiation environment in the high-luminosity collision points and RHA implications«, in: *IEEE Trans. Nucl. Sci.* 65 (2018), pages 448–456. URL: `https://cds.cern.ch/record/2310128`.

[18] *FLUKA website*, Available online: https://fluka.cern (Accessed on 30 August 2023).

[19] FLUKA.CERN collaboration, »New Capabilities of the FLUKA Multi-Purpose Code«, in: *Frontiers in Physics* 9 (2022), URL: `https://www.frontiersin.org/article/10.3389/fphy.2021.788253`.

[20] G. Battistoni et al., »Overview of the FLUKA code«, in: *Annals of Nuclear Energy* 82 (2015), pp. 10–18, URL: `http://www.sciencedirect.com/science/article/pii/S0306454914005878`.

[21] E. B. Holzer et al., »Beam Loss Monitoring System for the LHC«, in: *IEEE Nuclear Science Symposium* 2 (October 2005), pp. 1052–1056.

[22] D. Prelipcean et al., »Towards a Timepix3 Radiation Monitor for the Accelerator Mixed Radiation Field: Characterisation with Protons and Alphas from 0.6 MeV to 5.6 MeV«, in: *Applied Sciences* 14.2 (2024), URL: `https://www.mdpi.com/2076-3417/14/2/624`.

[23] E. Mobs, *The CERN accelerator complex*, 2019, URL: `https://cds.cern.ch/record/2684277` (visited on 29th September 2020).

[24] J. Beacham et al., »Physics beyond colliders at CERN: beyond the Standard Model working group report«, in: *Journal of Physics G: Nuclear and Particle Physics* 47.1 (December 2019), p. 010501, URL: `http://dx.doi.org/10.1088/1361-6471/ab4cd2`.

[25] *ISOLDE website*, https://home.cern/science/experiments/isolde, (visited on 20th April 2021).

[26] R. M. Dos Santos Augusto et al., »CERN-MEDICIS (Medical Isotopes Collected from ISOLDE): A New Facility«, in: *Applied Sciences* 4.2 (2014), pp. 265–281, URL: `https://www.mdpi.com/2076-3417/4/2/265`.

[27] S. Maury, *The Antiproton Decelerator (AD)*, tech. rep., Geneva: CERN, 1999, URL: `https://cds.cern.ch/record/405621`.

[28] V. Chohan et al., *Extra Low ENergy Antiproton (ELENA) ring and its Transfer Lines: Design Report*, CERN Yellow Reports: Monographs, Geneva: CERN, 2014, URL: `https://cds.cern.ch/record/1694484`.

[29] *The official website of the Cern High-energy AcceleRator test facility (CHARM)*, (accessed September 8th, 2020), URL: `https://charm.web.cern.ch/`.

[30] D. Prelipcean et al., »Benchmark Between Measured and Simulated Radiation Level Data at the Mixed-Field CHARM Facility at CERN«, in: *IEEE Transactions on Nuclear Science* 69.7 (2022), pp. 1557–1564.

[31] D. Gamba et al., »The CLEAR user facility at CERN«, in: *Nuclear Instruments and Methods in Physics Research Section A: Accelerators, Spectrometers, Detectors and Associated Equipment* 909 (2018), 3rd European Advanced Accelerator Concepts workshop (EAAC2017), pp. 480–483, URL: `https://www.sciencedirect.com/science/article/pii/S0168900217313311`.

[32] *nTOF website*, https://ntof-exp.web.cern.ch/, (visited on 1st July 2021).

[33] F. Gunsing et al., »Status and outlook of the neutron time-of-flight facility n_TOF at CERN«, in: *Nucl. Instrum. Meth. B* 261 (2007), ed. by Floyd Del McDaniel et al., pp. 925–929.

[34] n_TOF Collaboration, *Proposal for n_TOF Experimental Area 2*, tech. rep., Geneva: CERN, 2012, URL: `https://cds.cern.ch/record/1411635`.

[35] J. M. Jowett and Michaela Schaumann, »Overview of Heavy Ions in LHC Run 2«, in: *9th LHC Operations Evian Workshop*, 2019, pp. 15–25.

[36] J. Jowett, »Ions in the LHC«, in: (2009), URL: `https://cds.cern.ch/record/1172833`.

[37] A. Lechner et al., »Validation of energy deposition simulations for proton and heavy ion losses in the CERN Large Hadron Collider«, in: *Phys. Rev. Accel. Beams* 22 (7 July 2019).

[38] R. Bruce et al., »Beam losses from ultraperipheral nuclear collisions between $^{208}Pb^{82+}$ ions in the Large Hadron Collider and their alleviation«, in: *Phys. Rev. ST Accel. Beams* 12 (7 July 2009), p. 071002, URL: `https://link.aps.org/doi/10.1103/PhysRevSTAB.12.071002`.

[39] C. Bahamonde Castro et al., »Power Deposition in LHC Magnets Due to Bound-Free Pair Production in the Experimental Insertions«, in: (2016), TUPMW006, URL: `https://cds.cern.ch/record/2207361`.

[40] *Radiation to Electronics (R2E) Monitoring Dashboard*, URL: `https://r2e-monitoring.web.cern.ch` (visited on 18th July 2024).

[41] *CERN Annual report 2017*, 2018, URL: `http://cds.cern.ch/record/2624296` (visited on 3rd October 2020).

[42] *CERN Annual report 2018*, Geneva, 2019, URL: `https://cds.cern.ch/record/2671714` (visited on 3rd October 2020).

[43] D. Prelipcean, *Comparison between measured radiation levels and FLUKA simulations at CHARM and in the LHC tunnel of P1-5 within the R2E project in Run 2*. Accessed on 10 September 2022, July 2021, URL: `https://cds.cern.ch/record/2777059`.

[44] M. Lamont et al., »Functional specification: LHC MODES.«, in: *Tech. rep.* Tech. rep. 865811 (October 2009), URL: `https://edms.cern.ch/ui/file/865811/1.1/LHC-OP-ES-0005-10-10.pdf`.

[45] S. Morales Vigo, *Beam Loss Monitors in the Large Hadron Collider*, 8 July 2020, 2020, URL: `http://cds.cern.ch/record/2747978`.

[46] M. Lamont, »How to reach the required availability in the HL-LHC era«, in: (2014), URL: `https://cds.cern.ch/record/1977366`.

[47] M. Lamont, *Accelerators and technology sector*, https://indico.cern.ch/event/1422391/, (visited on 24th June 2024).

[48] N. V. Mokhov et al., »Energy deposition studies for the high-luminosity Large Hadron Collider inner triplet magnets«, in: *Phys. Rev. ST Accel. Beams* 18 (5 May 2015), p. 051001, URL: `https://link.aps.org/doi/10.1103/PhysRevSTAB.18.051001`.

[49] I. Novitski and A. V. Zlobin, »Thermal Analysis of SC Quadrupoles in Accelerator Interaction Regions«, in: *IEEE Transactions on Applied Superconductivity* 17.2 (2007), pp. 1059–1062.

[50] C. Zamantzas, *The Real-Time Data Analysis and Decision System for Particle Flux Detection in the LHC Accelerator at CERN*. 28 2 2006, 2006, URL: `http://cds.cern.ch/record/976628`.

[51] W. Friesenbichler, *Development of the Readout Electronics for the Beam Loss Monitors of the LHC*, 1 06 2002, 2002, URL: `https://cds.cern.ch/record/570940`.

[52] *Future Circular Collider (FCC)*, URL: `https://fcc.web.cern.ch/` (visited on 30th April 2024).

[53] C. Accettura et al., »Towards a Muon Collider«, in: *The European Physical Journal C* (2023).

[54] A. Robson et al., *The Compact Linear e^+e^- Collider (CLIC): Accelerator and Detector*, 2018, arXiv: `1812.07987 [physics.acc-ph]`.

[55] K. Biłko et al., »CERN Super Proton Synchrotron Radiation Environment and Related Radiation Hardness Assurance Implications«, in: *IEEE Trans. Nucl. Sci.* 70.8 (2023), pp. 1606–1615.

[56] S. Uznanski et al., *Qualification of electronic components for a radiation environment: When standards do not exist — high-energy physics*, tech. rep., Short course material prepared by R2E project member at CERN and presented at RADECS 2017, see https://dx.doi.org/10.1109/RADECS.2017.8696173 ., Geneva: CERN, 2017, URL: http://cds.cern.ch/record/2765495.

[57] A. Apollonio et al., »Lessons Learnt from the 2016 LHC Run and Prospects for HL-LHC Availability«, in: (2017), TUPVA006. 4 p, URL: http://cds.cern.ch/record/2289684.

[58] Y. Aguiar et al., »Radiation to Electronics Impact on CERN LHC Operation: Run 2 Overview and HL-LHC Outlook«, in: *Proc. 12th International Particle Accelerator Conference* (August 2021).

[59] M. Brugger, »R2E and Availability«, in: *Proc. of Workshop on LHC Performance*, CERN Yellow Report, 2014.

[60] T. Sykora, *Total, elastic and inelastic pp cross section at the LHC*, August 2016, URL: https://indico.cern.ch/event/432527/contributions/1072410 (visited on 8th June 2021).

[61] M. Giovannozzi, *Simple models describing the time-evolution of luminosity in hadron colliders*, June 2014, URL: https://cds.cern.ch/record/1742039.

[62] O. Stein et al., »A Systematic Analysis of the Prompt Dose Distribution at the Large Hadron Collider«, in: *Proc. 9th International Particle Accelerator Conference*, JACoW Publishing, 2018, pp. 2036–2038.

[63] A. Ciccotelli et al., »Energy deposition studies for the Upgrade II of LHCb at the CERN Large Hadron Collider«, in: *Phys. Rev. Accel. Beams* 27 (6 June 2024), p. 061003, URL: https://link.aps.org/doi/10.1103/PhysRevAccelBeams.27.061003.

[64] A. Canesse et al., »Overview of the radiation levels in the CERN accelerator complex after LS2.«, in: *14th International Particle Accelerator Conference*, IPAC'23 - 14th International Particle Accelerator Conference IPAC2023.14 (May 2023), pp. 4004–4007, URL: https://indico.jacow.org/event/41/contributions/2757.

[65] A. Waets et al., »Very-High-Energy Heavy Ion Beam Dosimetry using Solid State Detectors for Electronics Testing«, in: (2024), pp. 1–1.

[66] K. Bilko et al., »Silicon solid-state detectors for monitoring high-energy accelerator mixed field radiation environments«, in: *2021 21th European Conference on Radiation and Its Effects on Components and Systems (RADECS)* (2021), pp. 1–5.

[67] S. A. Dupree and S. K. Fraley, *A Monte Carlo Primer: a Practical Approach to Radiation Transport*, Berlin, 2002, URL: https://cds.cern.ch/record/1100826.

[68] B. Humann, »FCC-ee Radiation Challenges and Mitigation Measures«, Presented 20 Oct 2023, TU Vienna, 2023, URL: http://cds.cern.ch/record/2879400.

[69] *GEANT4 website*, Available online: https://geant4.web.cern.ch/node/1, (visited on 29th April 2021).

[70] J. A. Kulesza et al., *MCNP® Code Version 6.3.0 Theory & User Manual*, tech. rep. LA-UR-22-30006, Rev. 1, Los Alamos, NM, USA: Los Alamos National Laboratory, September 2022, URL: https://www.osti.gov/biblio/1889957.

[71] N. V. Mokhov and C. C. James, »The MARS Code System User's Guide Version 15(2016)«, in: (February 2017), URL: https://www.osti.gov/biblio/1462233.

[72] T. Sato et al., »Features of Particle and Heavy Ion Transport code System (PHITS) version 3.02«, in: *Journal of Nuclear Science and Technology* 55.6 (2018), pp. 684–690, eprint: `https://doi.org/10.1080/00223131.2017.1419890`, URL: `https://doi.org/10.1080/00223131.2017.1419890`.

[73] Nuclear Energy Agency, *PENELOPE 2018: A code system for Monte Carlo simulation of electron and photon transport*, 2019, p. 420, URL: `https://www.oecd-ilibrary.org/content/publication/32da5043-en`.

[74] A. Ciccotelli et al., »Energy deposition studies for the Upgrade II of LHCb at the CERN Large Hadron Collider«, in: *Phys. Rev. Accel. Beams* 27 (6 June 2024), p. 061003, URL: `https://link.aps.org/doi/10.1103/PhysRevAccelBeams.27.061003`.

[75] C. Accettura et al., *Interim report for the International Muon Collider Collaboration (IMCC)*, tech. rep., This document summarises the International Muon Collider Collaboration (IMCC) progress and status of the Muon Collider RD programme, 2024, arXiv: `2407.12450`, URL: `https://cds.cern.ch/record/2904891`.

[76] C. Accettura et al., »Conceptual Design of a Target and Capture Channel for a Muon Collider«, in: *IEEE Transactions on Applied Superconductivity* 34.5 (2024), pp. 1–5.

[77] F. J. Saura Esteban et al., »Muon Collider Graphite Target Studies and Demonstrator Layout Possibilities at CERN«, in: *JACoW IPAC* 2022 (2022), pp. 2895–2898, URL: `https://cds.cern.ch/record/2845829`.

[78] N.V. Mokhov and F. Cerutti, »Beam-Material Interaction.«, in: (2016), Comments: 28 pages, contribution to the 2014 Joint International Accelerator School: Beam Loss and Accelerator Protection, Newport Beach, CA, USA , 5-14 Nov 2014, pp. 83–110, arXiv: `1608.02476`, URL: `https://cds.cern.ch/record/2206746`.

[79] B. Auchmann et al., »Testing beam-induced quench levels of LHC superconducting magnets«, in: *Phys. Rev. ST Accel. Beams* 18 (6 June 2015), p. 061002, URL: `https://link.aps.org/doi/10.1103/PhysRevSTAB.18.061002`.

[80] G. Lerner et. al, *Radiation Level Specifications for HL-LHC*, URL: `https://edms.cern.ch/ui/file/2302154/1.0/HLLHC_Specification_Document_v1.0.pdf` (visited on 29th April 2022).

[81] R. García Alía et al., »Single event effects in high-energy accelerators«, in: *Semiconductor Science and Technology* 32.3 (February 2017), p. 034003, URL: `https://dx.doi.org/10.1088/1361-6641/aa5695`.

[82] M. Kalliokoski et al., »Beam Loss Monitoring for Run 2 of the LHC«, in: (2015), MOPTY055. 4 p, URL: `http://cds.cern.ch/record/2141806`.

[83] E. Gschwendtner et al., »The Beam loss detection system of the LHC ring«, in: *8th European Particle Accelerator Conference*, June 2002, pp. 1894–1896.

[84] *The LHC Logging Service*, Available online: https://core.ac.uk/download/pdf/44153909.pdf, (visited on 20th April 2021).

[85] *TIMBER*, https://twiki.cern.ch/twiki/bin/view/ABPComputing/LhcDataStorage, (visited on 20th April 2021).

[86] *Next Generation Accelerator Logging Service (NXCALS) website*, Available online: http://nxcals-docs.web.cern.ch/, (visited on 29th March 2022).

[87] A. Canesse, *56th MCWG meeting, Update on the 2023 radiation level measurements in the LHC ring*, URL: `https://indico.cern.ch/event/1319993/` (visited on 23rd December 2023).

[88] R. Garcia-Alia, *54th MCWG meeting, Radiation level measurements in the LHC ring in 2022*, URL: `https://indico.cern.ch/event/1253624/` (visited on 23rd December 2023).

[89] D. Prelipcean, *49th MCWG meeting, FLUKA simulations of beam losses in BGV detectors in Point 4*, URL: `https://indico.cern.ch/event/1097265/` (visited on 23rd December 2023).

[90] G. Arduini et al., »LHC Beam Size Measurement Review: Findings, comments and recommendations«, 2019, URL: `https://indico.cern.ch/event/837340`.

[91] J. Emery et al., »A fast and accurate wire scanner instrument for the CERN accelerators to cope with severe environmental constraints and an increased demand for availability«, in: *2014 IEEE Conference on Control Applications (CCA)*, 2014, pp. 1139–1145.

[92] G. Burtin et al., »First beam measurements with the LHC synchrotron light monitors«, in: (January 2010).

[93] S. Levasseur et al., »Development of a rest gas ionisation profile monitor for the CERN Proton Synchrotron based on a Timepix3 pixel detector«, in: *Journal of Instrumentation* 12.02 (February 2017), p. C02050, URL: `https://dx.doi.org/10.1088/1748-0221/12/02/C02050`.

[94] S. Levasseur, *Development of a Hybrid Pixel Detector Based Transverse Profile Monitor for the CERN Proton Synchrotron*, Presented 05 12 2019, 2019, URL: `http://cds.cern.ch/record/2720090`.

[95] H. Sandberg, *Development of a Novel Transverse Beam Profile and Emittance Monitor for the CERN Proton Synchrotron*, Presented 2020, 2020, URL: `https://cds.cern.ch/record/2747870`.

[96] *Beam Gas Vertex monitor website*, URL: `https://twiki.cern.ch/twiki/bin/view/BGV/WebHome` (visited on 27th July 2024).

[97] A. Alexopoulos et al., »Noninvasive LHC transverse beam size measurement using inelastic beam-gas interactions«, in: *Physical Review Accelerators and Beams* 22.4 (2019), p. 042801.

[98] A. Alexopoulos et al., »Noninvasive LHC transverse beam size measurement using inelastic beam-gas interactions«, in: *Physical Review Accelerators and Beams* 22.4 (2019), p. 042801, URL: `https://doi.org/10.1103/PhysRevAccelBeams.22.042801%20https://link.aps.org/doi/10.1103/PhysRevAccelBeams.22.042801`.

[99] R. Veness et al., »Development of a Beam-Gas Curtain Profile Monitor for the High Luminosity Upgrade of the LHC«, in: Proc. 7th International Particle Accelerator Conference, 5 p, September 2019.

[100] H. D. Zhang et al., »Characterization of a supersonic molecular beam for charged particle beam profile monitor«, in: *Vacuum* 208 (2023), p. 111701, URL: `https://www.sciencedirect.com/science/article/pii/S0042207X22008235`.

[101] A. Salehilashkajani et al., »A gas curtain beam profile monitor using beam induced fluorescence for high intensity charged particle beams«, in: *Applied Physics Letters* 120.17 (April 2022), p. 174101, eprint: `https://pubs.aip.org/aip/apl/article-pdf/doi/10.1063/5.0085491/16480328/174101\_1\_online.pdf`, URL: `https://doi.org/10.1063/5.0085491`.

[102] D. Boussard, T. Linnecar and W. Höfle, »The LHC Transverse Damper (ADT) Performance Specification«, in: (March 2000).

[103] M. Fitterer et al., *Analysis of BSRT Profiles in the LHC at Injection*, tech. rep., 2017, URL: `https://cds.cern.ch/record/2621636`.

[104] G. Trad, »Development and Optimisation of the SPS and LHC beam diagnostics based on Synchrotron Radiation monitors«, Presented 22 Jan 2015, U. Grenoble Alpes, 2014, URL: `https://cds.cern.ch/record/2266055`.

[105] N. Elias et al., »Fabrication and Test of a Nb_3Sn Model Magnet With Ceramic Insulation for the Next Generation Undulator of the LHC«, in: *IEEE Transactions on Applied Superconductivity* 20.3 (2010), pp. 258–261.

[106] E. L. Wanvik, »Real-Time Schottky Measurements in the LHC«, Presented 18 Dec 2017, Norwegian U. Sci. Tech., 2017, URL: `https://cds.cern.ch/record/2302378`.

[107] M. Betz et al., »Bunched-beam Schottky monitoring in the LHC«, in: *Nuclear Instruments and Methods in Physics Research Section A: Accelerators, Spectrometers, Detectors and Associated Equipment* 874 (2017), pp. 113–126, URL: `https://www.sciencedirect.com/science/article/pii/S0168900217309452`.

[108] M. Ehret, »Untersuchung eines breitbandigen Koaxial-Hohlleiterübergangs für einen Schottky-Strahldiagnosedetektor«, Presented 20 Dec 2013, Offenburg U. Appl. Sci., 2013, URL: `http://cds.cern.ch/record/1642139`.

[109] C. Ahdida et al., »New Capabilities of the FLUKA Multi-Purpose Code«, in: *Frontiers in Physics* 9 (2022), URL: `https://www.frontiersin.org/article/10.3389/fphy.2021.788253`.

[110] A. Rossi, »Estimates of Residual Gas Density in the LHC«, in: (2009), URL: `https://cds.cern.ch/record/1184445`.

[111] V. Baglin and G. Bregliozzi, *HL-LHC WP12 Vacuum & Beam Screen Technical Update since July 2021*, URL: `https://edms.cern.ch/ui/file/2716515/1/WP12_Technical__Update_March_2022_pptx_cpdf.pdf` (visited on 30th April 2022).

[112] R. Jones et al., »Introduction to beam instrumentation and diagnostics«, in: (2014), URL: `https://cds.cern.ch/record/1982418`.

[113] C. Barschel et al., »Results of the LHC DCCT Calibration Studies«, in: (2012), URL: `https://cds.cern.ch/record/1425904`.

[114] P. A. Zyla et al., »Review of Particle Physics«, in: *PTEP* 2020.8 (2020), p. 083C01.

[115] J. Carvalho, »Compilation of cross sections for proton–nucleus interactions at the HERA energy«, in: *Nuclear Physics A* 725 (2003), pp. 269–275, URL: `https://www.sciencedirect.com/science/article/pii/S0375947403015975`.

[116] M. Ferro-Luzzi, *Beam-Gas Interactions*, 2020, URL: `https://arxiv.org/abs/2006.06490`.

[117] M. Tanabashi et al., »Review of Particle Physics«, in: *Phys. Rev. D* 98 (3 August 2018), p. 030001, URL: `http://pdg.lbl.gov/2018/hadronic-xsections/hadron.html`.

[118] H. J. Mohring, *HADRON—NUCLEUS INELASTIC CROSS-SECTIONS FOR USE INHADRON—CASCAD CALCULATIONS AT HIGH ENERGIES*, 1983.

[119] O. Stein, *MD456: Monitoring of abort gap population with diamond particle detectors at the BGI in IP 4*, tech. rep., Geneva: CERN, 2016, URL: `https://cds.cern.ch/record/2131864`.

[120] M. Ady, »Monte Carlo simulations of ultra high vacuum and synchrotron radiation for particle accelerators«, Presented 03 May 2016, Ecole Polytechnique, Lausanne, 2016, URL: `https://cds.cern.ch/record/2157666`.

[121] *HL-LHC Beam Gas Vertex (BGV) Monitor*, URL: `https://edms.cern.ch/ui/file/2823013` (visited on 18th January 2024).

[122] *Private communications with M. Ady and R. Kersevan.*

[123] O. Sedlacek, *10th BGC Collaboration Meeting at CERN, Experimental Results in the LHC*, URL: `https://indico.cern.ch/event/1350731/` (visited on 28th March 2024).

[124] E. Todesco and J. Wenninger, »Large Hadron Collider momentum calibration and accuracy«, in: *Phys. Rev. Accel. Beams* 20 (8 August 2017), p. 081003, URL: `https://link.aps.org/doi/10.1103/PhysRevAccelBeams.20.081003`.

[125] D. Prelipcean, *150th HL-LHC TCC, BGV Beam gas collisions at IR4 and related radiation levels and heat load*, 2022, URL: `https://indico.cern.ch/event/1129683/` (visited on 28th July 2024).

[126] D. Prelipcean, *193rd HL-LHC TCC, Update of radiation level specifications in IR4 (from beam gas collisions)*, 2024, URL: `https://indico.cern.ch/event/1397881/` (visited on 28th July 2024).

[127] D. Prelipcean et al., »Radiation levels produced by the operation of the Beam Gas Vertex monitor in the LHC tunnel at IR4«, in: *14th International Particle Accelerator Conference* IPAC2023 (2023).

[128] B. Wurkner, *Measurement of the LHC Beam Profile Using the Beam Gas Vertex Detector*, Ph.D. thesis, Vienna, Tech. University, Germany, 2019, URL: `https://cds.cern.ch/record/2702690`.

[129] *HL-LHC Review of the Beam Gas Vertex Detector (BGV) and the Beam Gas Ionisation Detector (BGI) as possible instruments for continuous, non-invasive beam profile measurement*, URL: `https://edms.cern.ch/ui/file/2794870/1/BGV-BGI_Review_2022_-_Final_Report.pdf` (visited on 22nd September 2023).

[130] R. Kersevan and M. Ady, »Recent Developments of Monte-Carlo Codes Molflow+ and Synrad+«, in: 10th Int. Particle Accelerator Conference (IPAC'19), Melbourne, Australia, June 2019, pp. 1327–1330.

[131] H. Guerin, »Development of a non-invasive beam profile monitor based on hadronic beam-gas interactions for the High Luminosity Large Hadron Collider«, Presented 22 Mar 2024, Royal Holloway university of London, 2024, URL: `https://cds.cern.ch/record/2908050`.

[132] *FLAIR website*, Available online: https://flair.web.cern.ch/flair/ (Accessed on 07 July 2024).

[133] V. Vlachoudis, »FLAIR: A powerful but user friendly graphical interface for FLUKA«, in: April 2009, URL: `https://cds.cern.ch/record/2749540`.

[134] K. Biłko et al., »Automated Analysis of the Prompt Radiation Levels in the CERN Accelerator Complex«, in: Proc. 13th International Particle Accelerator Conference (IPAC'22), MOPOMS043 (July 2022), pp. 736–739.

[135] D. Prelipcean et al., »Comparison Between Run 2 TID Measurements and FLUKA Simulations in the CERN LHC Tunnel of the ATLAS Insertion Region«, in: *13th International Particle Accelerator Conference* IPAC2022 (2022), pp. 732–735.

[136] D. Prelipcean et al., »Comparison between Run 2 SEU measurements and FLUKA simulations in the CERN LHC tunnel and shielded alcoves around IP1/5«, in: *14th International Particle Accelerator Conference* IPAC2023 (2023).

[137] *9th DITANET Topical Workshop on Non-Invasibe Beam Size Measurement for High Brightness Proton and Heavy Ion*, URL: https://indico.cern.ch/event/229959/timetable/#20130415 (visited on 22nd September 2023).

[138] *LHC Beam Size Measurement Review*, URL: https://indico.cern.ch/event/837340/ (visited on 22nd September 2023).

[139] D. Prelipcean, *9th BGC Collaboration Meeting at CERN, Predictions of ionising radiation*, 2023, URL: https://indico.cern.ch/event/1281084/ (visited on 28th July 2024).

[140] D. Prelipcean, *10th BGC Collaboration Meeting at CERN, BGC radiation hard background simulation and camera protection*, 2023, URL: https://indico.cern.ch/event/1350731/ (visited on 28th July 2024).

[141] D. Prelipcean et al., »Radiation levels from a Beam Gas Curtain instrument at the LHC at CERN«, in: *15th International Particle Accelerator Conference IPAC2024* (2024).

[142] V. Shiltsev et al., »Experimental Demonstration of Colliding-Beam-Lifetime Improvement by Electron Lenses«, in: *Phys. Rev. Lett.* 99 (24 December 2007), p. 244801, URL: https://link.aps.org/doi/10.1103/PhysRevLett.99.244801.

[143] G. Stancari et al., »Collimation with Hollow Electron Beams«, in: *Phys. Rev. Lett.* 107 (8 August 2011), p. 084802, URL: https://link.aps.org/doi/10.1103/PhysRevLett.107.084802.

[144] X. Gu et al., »Halo removal experiments with hollow electron lens in the BNL Relativistic Heavy Ion Collider«, in: *Phys. Rev. Accel. Beams* 23 (3 March 2020), p. 031001, URL: https://link.aps.org/doi/10.1103/PhysRevAccelBeams.23.031001.

[145] M. Fitterer et al., »Resonant and random excitations on the proton beam in the Large Hadron Collider for active halo control with pulsed hollow electron lenses«, in: *Phys. Rev. Accel. Beams* 24 (2 February 2021), p. 021001, URL: https://link.aps.org/doi/10.1103/PhysRevAccelBeams.24.021001.

[146] S. Redaelli et al., »Hollow electron lenses for beam collimation at the High-Luminosity Large Hadron Collider (HL-LHC)«, in: *Journal of Instrumentation* 16.03 (March 2021), P03042, URL: https://dx.doi.org/10.1088/1748-0221/16/03/P03042.

[147] C. Castro Sequeiro et al., »Beam gas curtain monitor: Vacuum studies for LHC integration and operation«, in: *Phys. Rev. Accel. Beams* 27 (4 April 2024), p. 043201, URL: https://link.aps.org/doi/10.1103/PhysRevAccelBeams.27.043201.

[148] C. Martinella et al., *Radiation levels in the LHC during the 2015 Pb-Pb and 2016 p-Pb run and mitigation strategy for the electronic systems during HL-LHC operation*, October 2018, URL: https://cds.cern.ch/record/2647363.

[149] E. B. Holzer et al., »Beam loss monitoring system for the LHC«, in: *IEEE Nuclear Science Symposium* 2 (October 2005), pp. 1052–1056.

[150] G. Spiezia et al., »The LHC radiation monitoring system - RadMon«, in: *Proceedings of Science* 143 (2011), pp. 1–12, URL: https://pdfs.semanticscholar.org/78a0/5e489d7ad51deed31b6e178a29d476d33349.pdf.

[151] G. Spiezia et al., »A New RadMon Version for the LHC and its Injection Lines«, in: *IEEE Trans. Nucl. Sci.* 61.6 (2014), pp. 3424–3431, URL: https://cds.cern.ch/record/2011660.

[152] S. Danzeca et al., »Wireless IoT in Particle Accelerators: A Proof of Concept with the IoT Radiation Monitor at CERN«, in: *JACoW IPAC* 2022 (2022), pp. 772–775, URL: https://cds.cern.ch/record/2845851.

[153] D. Di Francesca et al., »Qualification and Calibration of Single-Mode Phosphosilicate Optical Fiber for Dosimetry at CERN«, in: *Journal of Lightwave Technology* 37.18 (2019), pp. 4643–4649.

[154] D. Pramberger et al., »Characterization of Radio-Photo-Luminescence (RPL) Dosimeters as Radiation Monitors in the CERN Accelerator Complex«, in: *IEEE Trans. Nucl. Sci.* 69.7 (2022), pp. 1618–1624, URL: https://cds.cern.ch/record/2823939.

[155] M. Martivsíková et al., »Study of the capabilities of the Timepix detector for Ion Beam radiotherapy applications«, in: *2012 IEEE Nuclear Science Symposium and Medical Imaging Conference Record (NSS/MIC)* (October 2012), pp. 4324–4328.

[156] A. Tremsin et al., »High Resolution Photon Counting With MCP-Timepix Quad Parallel Readout Operating at > 1 KHz Frame Rates«, in: *IEEE Transactions on Nuclear Science* 60 (April 2013), pp. 578–585.

[157] N. Stoffle et al., »Timepix-based radiation environment monitor measurements aboard the International Space Station«, in: *Nuclear Instruments and Methods in Physics Research Section A: Accelerators, Spectrometers, Detectors and Associated Equipment* 782 (2015), pp. 143–148, URL: https://www.sciencedirect.com/science/article/pii/S0168900215001977.

[158] A. Le Gall, *New 3D colour X-rays made possible with CERN technology*, URL: https://home.cern/news/news/knowledge-sharing/new-3d-colour-x-rays-made-possible-cern-technology.

[159] J. Jakubek, *Imaging Based on Tracking of Individual Particles with the Timepix Pixel Detector*, URL: https://indico.cern.ch/event/48618/contributions/1163509 (visited on 29th March 2023).

[160] B. Bergmann et al., »Characterization of the Radiation Field in the ATLAS Experiment With Timepix Detectors«, in: *IEEE Transactions on Nuclear Science* 66.7 (2019), pp. 1861–1869.

[161] T. Poikela et al., »Timepix3: a 65K channel hybrid pixel readout chip with simultaneous ToA/ToT and sparse readout«, in: *Journal of Instrumentation* 9.05 (May 2014), pp. C05013–C05013, URL: https://doi.org/10.1088/1748-0221/9/05/c05013.

[162] X. Llopart et al., »Timepix, a 65k programmable pixel readout chip for arrival time, energy and/or photon counting measurements«, in: *Nuclear Instruments and Methods in Physics Research Section A: Accelerators, Spectrometers, Detectors and Associated Equipment* 581.1 (2007), VCI 2007, pp. 485–494, URL: https://www.sciencedirect.com/science/article/pii/S0168900207017020.

[163] *Medipix Collaboration*, Available online: https://medipix.web.cern.ch/home (Accessed on 09 2 2023).

[164] N. Alipour Tehrani, »Test-beam measurements and simulation studies of thin pixel sensors for the CLIC vertex detector«, PhD thesis, 2017, URL: https://www.research-collection.ethz.ch/handle/20.500.11850/164813.

[165] W. Shockley, »Currents to Conductors Induced by a Moving Point Charge«, in: *Journal of Applied Physics* 9.10 (April 2004), pp. 635–636, eprint: https://pubs.aip.org/aip/jap/article-pdf/9/10/635/8059000/635_1_online.pdf, URL: https://doi.org/10.1063/1.1710367.

[166] S. Ramo, »Currents Induced by Electron Motion«, in: *Proceedings of the IRE* 27.9 (1939), pp. 584–585.

[167] W. Riegler, »An application of extensions of the Ramo–Shockley theorem to signals in silicon sensors«, in: *Nuclear Instruments and Methods in Physics Research Section A: Accelerators, Spectrometers, Detectors and Associated Equipment* 940 (2019), pp. 453–461, URL: `https://www.sciencedirect.com/science/article/pii/S0168900219309015`.

[168] F. Krummenacher, »Pixel detectors with local intelligence: an IC designer point of view«, in: *Nuclear Instruments and Methods in Physics Research Section A: Accelerators, Spectrometers, Detectors and Associated Equipment* 305.3 (1991), pp. 527–532, URL: `https://www.sciencedirect.com/science/article/pii/016890029190152G`.

[169] W. Adam et al., »Comparative evaluation of analogue front-end designs for the CMS Inner Tracker at the High Luminosity LHC«, in: *Journal of Instrumentation* 16 (December 2021), P12014.

[170] M. Sommer et al., »High-energy per-pixel calibration of timepix pixel detector with laboratory alpha source«, in: *Nuclear Instruments and Methods in Physics Research Section A: Accelerators, Spectrometers, Detectors and Associated Equipment* 1022 (2022), p. 165957, URL: `https://www.sciencedirect.com/science/article/pii/S0168900221009049`.

[171] J. Bouchami et al., »Study of the charge sharing in silicon pixel detector by means of heavy ionizing particles interacting with a Medipix2 device«, in: 633 (Suppl.1 May 2011).

[172] M. Platkevic et al., »Characterization of charge collection in various semiconductor sensors with energetic protons and Timepix device«, in: *2011 IEEE Nuclear Science Symposium Conference Record*, 2011, pp. 4715–4719.

[173] L. Meduna et al., *Real-time Timepix3 data clustering, visualization and classification with a new Clusterer framework*, https://indico.cern.ch/event/742793/contributions/3298745/, (visited on 27th June 2022).

[174] J. Wen et al., »Optimization of Timepix3-based conventional Compton camera using electron track algorithm«, in: *Nuclear Instruments and Methods in Physics Research Section A: Accelerators, Spectrometers, Detectors and Associated Equipment* 1021 (January 2022), p. 165954, URL: `https://doi.org/10.1016%202Fj.nima.2021.165954`.

[175] L. Marek, C. Granja and J. Jakubek, *DPE - Data processing engine for radiation field monitoring with Timepix type detectors*, https://indico.cern.ch/event/1193219/contributions/5056229/, (visited on 7th February 2023).

[176] *ADVACAM: Timepix3 licence*, URL: `https://medipix.web.cern.ch/news/news/timepix/advacam-timepix3-licence`.

[177] *DBSCAN sklearn*, https://scikit-learn.org/stable/modules/generated/sklearn.cluster.DBSCAN.html, (visited on 30th May 2022).

[178] C. Granja et al., »Energy loss and online directional track visualization of fast electrons with the pixel detector Timepix«, in: *Radiation Measurements* 59 (2013), pp. 245–261, URL: `https://www.sciencedirect.com/science/article/pii/S1350448713002874`.

[179] J. Jakubek et al., »Pixel detectors for imaging with heavy charged particles«, in: *Nuclear Instruments and Methods in Physics Research Section A: Accelerators, Spectrometers, Detectors and Associated Equipment* 591.1 (2008), Radiation Imaging Detectors 2007, pp. 155–158, URL: `https://www.sciencedirect.com/science/article/pii/S0168900208004245`.

[180] S. P. George et al., »Very high energy calibration of silicon Timepix detectors«, in: *JINST* 13.11 (2018), P11014, URL: `https://cds.cern.ch/record/2654554`.

[181] N. Alipour Tehrani et al., »Calibration of ultra-thin hybrid pixel detector assemblies with Timepix readout ASICs«, in: (2015), URL: http://cds.cern.ch/record/2054922.

[182] S. Agostinelli et al., »Geant4—a simulation toolkit«, in: *Nuclear Instruments and Methods in Physics Research Section A: Accelerators, Spectrometers, Detectors and Associated Equipment* 506.3 (2003), pp. 250–303, URL: https://www.sciencedirect.com/science/article/pii/S0168900203013688.

[183] J. Allison et al., »Geant4 developments and applications«, in: 53.1 (2006), pp. 270–278.

[184] J. Allison et al., »Recent developments in Geant4«, in: *Nuclear Instruments and Methods in Physics Research Section A: Accelerators, Spectrometers, Detectors and Associated Equipment* 835 (2016), pp. 186–225, URL: https://www.sciencedirect.com/science/article/pii/S0168900216306957.

[185] M. Platkevic et al., »Evaluation of local radiation damage in silicon sensor via charge collection mapping with the Timepix read-out chip«, in: *Journal of Instrumentation* 8 (April 2013), p. C04001.

[186] S. Hoang et al., »Data Analysis of Tracks of Heavy Ion Particles in Timepix Detector«, in: *Journal of Physics: Conference Series* 523.1 (June 2014), p. 012026, URL: https://dx.doi.org/10.1088/1742-6596/523/1/012026.

[187] T. E. J. Campbell-Ricketts, M. Kroupa and L. S. Pinsky, »Spectroscopy of high-energy ions with Timepix3«, in: *Journal of Instrumentation* 11.11 (November 2016), P11007, URL: https://dx.doi.org/10.1088/1748-0221/11/11/P11007.

[188] M. Kroupa et al., »Techniques for precise energy calibration of particle pixel detectors«, in: *Review of Scientific Instruments* 88.3 (2017), p. 033301, eprint: https://doi.org/10.1063/1.4978281, URL: https://doi.org/10.1063/1.4978281.

[189] D. Turecek et al., »Energy calibration of pixel detector working in Time-Over-Threshold mode using test pulses«, in: *2011 IEEE Nuclear Science Symposium Conference Record*, 2011, pp. 1722–1725.

[190] M. Kroupa, J. Jakubek and P. Soukup, »Optimization of the spectroscopic response of the Timepix detector«, in: *Journal of Instrumentation* 7.02 (February 2012), p. C02058, URL: https://dx.doi.org/10.1088/1748-0221/7/02/C02058.

[191] M. Holik et al., »Alpha calibration of the Timepix pixel detector exploiting energy information gained from a common electrode signal«, in: *Journal of Instrumentation* 14.6 (June 2019), p. C06022, URL: https://dx.doi.org/10.1088/1748-0221/14/06/C06022.

[192] S. M. Abu Al Azm et al., »Response of timepix detector with GaAs:Cr and Si sensor to heavy ions«, in: *Physics of Particles and Nuclei Letters* 13 (May 2016), pp. 363–369, URL: https://doi.org/10.1134/S154747711603002X.

[193] F. M. Pitters et al., »Time and Energy Calibration of Timepix3 Assemblies with Thin Silicon Sensors«, in: (November 2018), URL: https://cds.cern.ch/record/2649493.

[194] C. Granja et al., »Resolving power of pixel detector Timepix for wide-range electron, proton and ion detection«, in: *Nuclear Instruments and Methods in Physics Research Section A: Accelerators, Spectrometers, Detectors and Associated Equipment* 908 (2018), pp. 60–71, URL: https://www.sciencedirect.com/science/article/pii/S0168900218309586.

[195] C. Leroy and P. G. Rancoita, *Principles of Radiation Interaction in Matter and Detection*, 4th, WORLD SCIENTIFIC, 2016, eprint: https://www.worldscientific.com/doi/pdf/10.1142/9167, URL: https://www.worldscientific.com/doi/abs/10.1142/9167.

[196] T. Holy et al., »Pattern recognition of tracks induced by individual quanta of ionizing radiation in Medipix2 silicon detector«, in: *Nuclear Instruments and Methods in Physics Research Section A: Accelerators, Spectrometers, Detectors and Associated Equipment* 591.1 (2008), Radiation Imaging Detectors 2007, pp. 287–290, URL: `https : / / www . sciencedirect . com/science/article/pii/S0168900208004592`.

[197] M. L. Perez-Lara et al., »First Study of a HEXITEC Detector for Secondary Particle Characterisation during Proton Beam Therapy«, in: *Applied Sciences* 13.13 (2023), URL: `https://www.mdpi. com/2076-3417/13/13/7735`.

[198] K. Sykorova et al., *Machine learning models for single-particle classification with Timepix 3 detectors*, https://indico.cern.ch/event/1284854/contributions/5951409//.

[199] J. Leidner, F. Murtas and M. Silari, »Energy calibration of the GEMPix in the energy range of 6 keV to 2 MeV«, in: *Journal of Instrumentation* 16.10 (October 2021), P10004, URL: `https://dx.doi.org/10. 1088/1748-0221/16/10/P10004`.

[200] J. Jakubek, »Precise energy calibration of pixel detector working in time-over-threshold mode«, in: *Nuclear Instruments and Methods in Physics Research Section A: Accelerators, Spectrometers, Detectors and Associated Equipment* 633 (2011), 11th International Workshop on Radiation Imaging Detectors (IWORID), S262–S266, URL: `https : / / www . sciencedirect . com/science/article/pii/S0168900210013732`.

[201] M. Campbell et al., »Study of the charge sharing in a silicon pixel detector by means of α-particles interacting with a Medipix2 device«, in: *Nuclear Instruments and Methods in Physics Research Section A: Accelerators, Spectrometers, Detectors and Associated Equipment* 591.1 (2008), Radiation Imaging Detectors 2007, pp. 38–41, URL: `https : / / www . sciencedirect . com/science/article/pii/S0168900208003963`.

[202] E. G. Villani, »Charge diffusion in undepleted regions of silicon particle detectors: analysis and simulation«, in: *Nuclear Instruments and Methods in Physics Research Section A: Accelerators, Spectrometers, Detectors and Associated Equipment* 539.1 (2005), pp. 125–131, URL: `https://www.sciencedirect. com/science/article/pii/S0168900204022703`.

[203] F. Pozzi et al., »CERN irradiation facilities«, in: vol. 180, September 2017.

[204] *ISO/IEC 17025, Testing and calibration laboratories*, https://www.iso.org/ISO-IEC-17025-testing-and-calibration-laboratories.html, (visited on 23rd July 2024).

[205] *IAEA, Live chart of Nuclides: nuclear structure and decay data*, https://www-nds.iaea.org/relnsd/vcharthtml/VCha (visited on 12th May 2022).

[206] *PSTAR : Stopping Power and Range Tables for Protons*, https://physics.nist.gov/PhysRefData/Star/Text/PSTAR.ht (visited on 12th May 2022).

[207] *Cobalt-60*, https://en.wikipedia.org/wiki/Cobalt-60, (visited on 16th February 2023).

[208] *What is X-ray Attenuation – Definition*, https://material-properties.org/what-is-x-ray-attenuation-definition/, (visited on 16th February 2023).

[209] *Centro Nacional de Aceleradores*, Available online: http://cna.us.es/index.php/en/facilities/tandem-3mv-accelerator/89-lines (Accessed on 13 5 2022).

[210] Y. Morilla et al., »Progress of CNA to become the Spanish facility for combined irradiation testing in aerospace«, in: September 2018, pp. 1–5.

[211] J. López et al., »CNA: The first accelerator-based IBA facility in Spain«, in: *Nuclear Instruments and Methods in Physics Research Section B: Beam Interactions with Materials and Atoms* 161-163 (March 2000), pp. 1137–1142.

[212] M. Respaldiza et al., »Accelerator-based research activities at "Centro Nacional de Aceleradores", Seville (Spain)«, in: *Nuclear Instruments and Methods in Physics Research Section B: Beam Interactions with Materials and Atoms* 266 (May 2008), pp. 2105–2109.

[213] C. R. Rose and R. E. Shafer, »A 200-A, 500-Hz, triangle current-wave modulator and magnet used for particle beam rastering«, in: *Conf. Proc. C* 970512 (1997), pp. 1293–1295.

[214] C. Cazzaniga et al., »Measurements of Low-Energy Protons Using a Silicon Detector for Application to SEE Testing«, in: *IEEE Transactions on Nuclear Science* 69.3 (2022), pp. 485–490.

[215] J. Manfredi et al., »On determining dead layer and detector thicknesses for a position-sensitive silicon detector«, in: *Nuclear Instruments and Methods in Physics Research Section A: Accelerators, Spectrometers, Detectors and Associated Equipment* 888 (2018), pp. 177–183, URL: https://www.sciencedirect.com/science/article/pii/S016890021731505X.

[216] B. Bergmann et al., »Experimental study of the adaptive gain feature for improved position-sensitive ion spectroscopy with Timepix2«, in: *Journal of Instrumentation* 17.01 (January 2022), p. C01025, URL: https://dx.doi.org/10.1088/1748-0221/17/01/C01025.

[217] *Institut Laue-Langevin*, https://www.ill.eu/about-the-ill/what-is-the-ill, (visited on 24th February 2023).

[218] A. Pappalardo et al., »Characterization of the silicon+6LiF thermal neutron detection technique«, in: *Nuclear Instruments and Methods in Physics Research Section A: Accelerators, Spectrometers, Detectors and Associated Equipment* 810 (February 2016), pp. 6–13, URL: https://doi.org/10.1016%5C%202Fj.nima.2015.11.114.

[219] P. Finocchiaro et al., »Neutron detection devices with 6LiF converter layers«, in: *EPJ Web Conf.* 170 (2018), p. 01004, URL: https://doi.org/10.1051/epjconf/201817001004.

[220] D. S. McGregor et al., »Design considerations for thin film coated semiconductor thermal neutron detectors–I: basics regarding alpha particle emitting neutron reactive films.«, in: *Nuclear Instruments and Methods in Physics Research Section A, Accelerators, Spectrometers, Detectors and Associated Equipment* 500(1-3) (2003), pp. 272–308, URL: http://cds.cern.ch/record/2054922.

[221] M. Barbagallo et al., »Thermal neutron detection using a silicon pad detector and 6LiF removable converters«, in: *Review of Scientific Instruments* 84.3 (2013), p. 033503, eprint: https://doi.org/10.1063/1.4794768, URL: https://doi.org/10.1063/1.4794768.

[222] S. Lo Meo et al., »Study of silicon+6LiF thermal neutron detectors: GEANT4 simulations versus real data«, in: *Nuclear Instruments and Methods in Physics Research Section A: Accelerators, Spectrometers, Detectors and Associated Equipment* 866 (2017), pp. 48–57, URL: https://www.sciencedirect.com/science/article/pii/S0168900217304801.

[223] L. Cosentino et al., »Silicon detectors for monitoring neutron beams in n-TOF beamlines«, in: *Rev. Sci. Instrum.* 86.7 (2015), p. 073509.

[224] *G4SEE website*, Available online: https://g4see.web.cern.ch/ (Accessed on 29 March 2023).

[225] D. Lucsányi et al., »G4SEE: A Geant4-Based Single Event Effect Simulation Toolkit and Its Validation Through Monoenergetic Neutron Measurements«, in: *IEEE Transactions on Nuclear Science* 69.3 (2022), pp. 273–281.

[226] M. Cecchetto, *Impact of thermal and intermediate energy neutrons on the semiconductor memories for the CERN accelerators*, Presented 10 7 2017, 2017, URL: https://cds.cern.ch/record/2282268.

[227] M. Cecchetto et al., »0.1–10 MeV Neutron Soft Error Rate in Accelerator and Atmospheric Environments«, in: *IEEE Transactions on Nuclear Science* 68.5 (2021), pp. 873–883.

[228] *FLUKA release 4.3.0*, Available online: https://fluka.cern/news/release-fluka-4-30 (Accessed on 05 April 2023).

[229] V. Vlachoudis et al., »Recent developments in the point wise neutron treatment for FLUKA v4«, in: *EPJ Web of Conf.* 284 (2023), p. 03021, URL: https://doi.org/10.1051/epjconf/202328403021.

[230] M. Sacristan Barbero, *FLUKA and G4SEE point-wise neutron treatment study in a silicon detector*, EDMS document 2781372, (visited on 27th March 2023).

[231] K. Akiba et al., »LHCb VELO Timepix3 telescope«, in: *Journal of Instrumentation* 14.05 (May 2019), P05026, URL: https://dx.doi.org/10.1088/1748-0221/14/05/P05026.

[232] T. Billoud, »Characterization of the radiation field in ATLAS using Timepix detectors«, Presented 16 Oct 2019, University of Montreal, 2020, URL: https://cds.cern.ch/record/2805760.

[233] D. Prelipcean, *44th MCWG meeting, Conversion coefficients between different quantities measuring radiation levels at the LHC*, URL: https://indico.cern.ch/event/978953/ (visited on 7th July 2024).

[234] J. Maly, »Computing conversion coefficients between different quantities used for radiation measurements at the CERN accelerator complex«, in: (2024), URL: https://cds.cern.ch/record/2909393.

[235] P. G. Young and D. G. Foster Jr., »Evaluation of the neutron and gamma-ray production cross sections for nitrogen«, in: *Tech. Rep. Los Alamos Sci. Lab.* (1972).

[236] E. Bougamont et al., »Neutron spectroscopy with the Spherical Proportional Counter based on nitrogen gas«, in: *Nucl.Instrum.Meth.A* 847 (2017), pp. 10–14, URL: https://hal.archives-ouvertes.fr/hal-01553919.

[237] H. Bethe, »Zur Theorie des Durchgangs schneller Korpuskularstrahlen durch Materie«, in: *Annalen der Physik* 397.3 (1930), pp. 325–400.

[238] P. Christodoulou et al., »Probability distribution maps of deposited energy with sub-pixel resolution for Timepix3 detectors«, in: *Journal of Instrumentation* 19.01 (January 2024), p. C01026, URL: https://dx.doi.org/10.1088/1748-0221/19/01/C01026.

[239] B. Bergmann et al., »Detector response and performance of a 500 m thick GaAs attached to Timepix3 in relativistic particle beams«, in: *Journal of Instrumentation* 15.03 (March 2020), p. C03013, URL: https://dx.doi.org/10.1088/1748-0221/15/03/C03013.

[240] D. Curtin et al., »Long-lived particles at the energy frontier: the MATHUSLA physics case«, in: *Reports on Progress in Physics* 82.11 (October 2019), p. 116201, URL: https://doi.org/10.1088%2F1361-6633%2Fab28d6.

[241] J. P. Chou, D. Curtin and H. J. Lubatti, »New detectors to explore the lifetime frontier«, in: *Physics Letters B* 767 (2017), pp. 29–36, URL: https://www.sciencedirect.com/science/article/pii/S0370269317300618.

[242] J. L. Feng et al., »ForwArd Search ExpeRiment at the LHC«, in: *Phys. Rev. D* 97 (3 February 2018), p. 035001, URL: https://link.aps.org/doi/10.1103/PhysRevD.97.035001.

[243] A. Ball et al., *A Letter of Intent to Install a milli-charged Particle Detector at LHC P5*, 2016, arXiv: `1607.04669 [physics.ins-det]`.

[244] A. Sergey et al., »A facility to search for hidden particles at the CERN SPS: the SHiP physics case«, in: *Reports on Progress in Physics* 79.12 (October 2016), p. 124201, URL: `https://dx.doi.org/10.1088/0034-4885/79/12/124201`.

[245] V. V. Gligorov et al., »Leveraging the ALICE/L3 cavern for long-lived particle searches«, in: *Phys. Rev. D* 99 (1 January 2019), p. 015023, URL: `https://link.aps.org/doi/10.1103/PhysRevD.99.015023`.

[246] V. V. Gligorov et al., »Searching for long-lived particles: A compact detector for exotics at LHCb«, in: *Phys. Rev. D* 97 (1 January 2018), p. 015023, URL: `https://link.aps.org/doi/10.1103/PhysRevD.97.015023`.

[247] G. Aielli et al., »Expression of Interest for the CODEX-b Detector«, in: *Eur. Phys. J. C* 80.12 (2020), p. 1177, arXiv: `1911.00481`, URL: `http://cds.cern.ch/record/2699473`.

[248] G. Aielli et al., *The Road Ahead for CODEX-b*, tech. rep., 2022, arXiv: `2203.07316`, URL: `https://cds.cern.ch/record/2805287`.

[249] G. Spiezia et al., »The LHC radiation monitoring system - RadMon«, in: *Proceedings of Science* 143 (2011), pp. 1–12, URL: `https://pdfs.semanticscholar.org/78a0/5e489d7ad51deed31b6e178a29d476d33349.pdf`.

[250] B. Dey et al., *Background studies for the CODEX-b experiment: measurements and simulation*, 2019, URL: `https://arxiv.org/abs/1912.03846`.

[251] D. Kramer et al., »LHC RadMon SRAM Detectors Used at Different Voltages to Determine the Thermal Neutron to High Energy Hadron Fluence Ratio«, in: *IEEE Transactions on Nuclear Science* 58.3 (2011), pp. 1117–1122.

[252] L. Gallego Manzano et al., »An IoT LoRaWAN Network for Environmental Radiation Monitoring«, in: *IEEE Trans. Instrum. Meas.* 70 (2021), pp. 1–12, URL: `https://cds.cern.ch/record/2778544`.

[253] S. Roesler, R. Engel and J. Ranft, »The Monte Carlo event generator DPMJET-III«, in: *International Conference on Advanced Monte Carlo for Radiation Physics, Particle Transport Simulation and Applications (MC 2000)*, December 2000, pp. 1033–1038, arXiv: `hep-ph/0012252`.

[254] *BIPXL-Software-Panda-GUI*, Available online: https://gitlab.cern.ch/be-bi-bgi/bipxl-software-panda-gui, (visited on 12th May 2022).

[255] I. Belyaev et al., »Handling of the generation of primary events in Gauss, the LHCb simulation framework«, in: *Journal of Physics: Conference Series* 331.3 (December 2011), p. 032047, URL: `https://dx.doi.org/10.1088/1742-6596/331/3/032047`.

[256] M. Clemencic et al., »The LHCb Simulation Application, Gauss: Design, Evolution and Experience«, in: *Journal of Physics: Conference Series* 331.3 (December 2011), p. 032023, URL: `https://dx.doi.org/10.1088/1742-6596/331/3/032023`.

[257] T. Sjöstrand et al., »An introduction to PYTHIA 8.2«, in: *Computer Physics Communications* 191 (June 2015), pp. 159–177, URL: `https://doi.org/10.1016%2Fj.cpc.2015.01.024`.

[258] E. Revani, *Timepix3 radiation monitor at SND - muon rate from IP*, URL: `https://edms.cern.ch/ui/#!master/navigator/document?D:101645879:101645879:subDocs` (visited on 6th November 2024).

[259] SND Collaboration, *SND@LHC - Scattering and Neutrino Detector at the LHC*, tech. rep. CERN-LHCC-2021-003. LHCC-P-016, Geneva: CERN, January 2021, URL: `https://cds.cern.ch/record/2750060`.

[260] E. G. Stassinopoulos and J. P. Raymond, »The space radiation environment for electronics«, in: *Proc. IEEE* 76:11 (November 1988), 10 1988, URL: `https://www.osti.gov/biblio/6042035`.

[261] A. L. Bosser, *Single-event effects from space and atmospheric radiation in memory components*, Theses, 12 2017, December 2017, URL: `https://tel.archives-ouvertes.fr/tel-01952831`.

[262] A. Infantino, *FLUKA Monte Carlo Modelling of the CHARM Facility's Test Area: Update of the Radiation Field Assessment*, September 2017, URL: `https://cds.cern.ch/record/2291683`.

[263] R. Baumann and E. Smith, »Neutron-induced boron fission as a major source of soft errors in deep submicron SRAM devices«, in: (February 2000), 2 2000, pp. 152–157.

[264] C. Martinella, *High Energy Hadrons Fluence Measurements in the LHC during 2015, 2016 and 2017 Proton Physics Operations.* December 2018, URL: `https://cds.cern.ch/record/2652458`.

[265] A. Coronetti et al., »The Pion Single-Event Effect Resonance and its Impact in an Accelerator Environment«, in: *IEEE Trans. Nucl. Sci.* 67 (2020), 2020, pp. 1606–1613, URL: `http://cds.cern.ch/record/2725324`.

[266] A. Capella et al., »Dual parton model«, in: *Phys. Rept.* 236 (1994), pp. 225–329, URL: `https://inspirehep.net/literature/33197`.

[267] A. Ferrari et al., »The physics of high energy reactions.«, in: (1998), URL: `https://inis.iaea.org/search/search.aspx?orig_q=RN:29067414`.

[268] A. Ferrari and P. R. Sala, »A new model for hadronic interactions at intermediate-energies for the FLUKA code«, in: *International Conference on Monte Carlo Simulation in High-Energy and Nuclear Physics - MC 93*, 1993, URL: `https://inspirehep.net/literature/367781`.

[269] A. Fasso et al., »FLUKA: performances and applications in the intermediate energy range«, in: *1st Specialists' Meeting on Shielding Aspects of Accelerators, Targets and Irradiation Facilities - SATIF1*, 29 April 1994, 18 p, URL: `http://cds.cern.ch/record/2724814`.

[270] K. Haenssgen et al., »Monte Carlo simulation of inelastic hadron-hadron reactions in the medium energy range ($\sqrt{s} < 3$ GeV). Description of the model used and of the Monte Carlo code HADRIN«, in: (1979).

[271] A. Ferrari et al., »The production of residual nuclei in peripheral high energy nucleus-nucleus interactions«, in: *Zeitschrift für Physik C: Particles and Fields* 71.1 (March 1996), March 1996, pp. 75–86, URL: `http://dx.doi.org/10.1007/s002880050149`.

[272] W. H. Barkas et al., »Mass-Ratio Method Applied to the Measurement of *L*-Meson Masses and the Energy Balance in Pion Decay«, in: *Phys. Rev.* 101 (2 January 1956), pp. 778–795, URL: `https://link.aps.org/doi/10.1103/PhysRev.101.778`.

[273] F. Bloch, »Zur Bremsung Rasch Bewegter Teilchen beim Durchgang durch Materie«, in: *Annalen Phys.* 408 (1933), pp. 285–320.

[274] N. F. Mott, »The Scattering of Fast Electrons by Atomic Nuclei«, in: *Sir Nevill Mott – 65 Years in Physics*, 1929, pp. 13–30.

[275] J. F. Ziegler et al., *The stopping and range of ions in solids*, English, Pergamon New York, 1985, pp. 321.

[276] R. M. Sternheimer et al., »Density Effect for the Ionization Loss of Charged Particles in Various Substances«, in: *Atom. Data Nucl. Data Tabl.* 30 (1984), pp. 261–271.

[277] M. Brugger et al., »LHC Accelerator Design Studies on the Example of Passive Absorbers«, in: *Nuclear Technology* 168.3 (2009), pp. 659–664.

[278] K. Roeed et al., »Method for Measuring Mixed Field Radiation Levels Relevant for SEEs at the LHC«, in: *IEEE Transactions on Nuclear Science* 59.4 (2012), pp. 1040–1047.

[279] *CERN Drawing Directory website*, URL: `Available%20online:%20https://edms-service.web.cern.ch/cdd/%20(Accessed%20on%2029%20April%202021)`.

[280] *TWISS files website*, Available online: https://twiki.cern.ch/twiki/bin/view/Sandbox/ TwissFileProduction (Accessed on 29 April 2021).

[281] *CERN Layout Database*, URL: `Available%20online:%20https://layout.cern.ch/` (visited on 29th April 2021).

[282] *Geographic information system (GIS) portal*, URL: `Available%20online:%20https://smb-dep.web.cern.ch/content/maps` (visited on 29th April 2021).

[283] *Geographic information system (GIS) machine map*, URL: `ttps://gis.cern.ch/gisportal/Machine.htm` (visited on 11th June 2021).

[284] M. Ferrari et al., »"Radiation to Materials" at CERN«, in: *IEEE Transactions on Nuclear Science* 70.8 (2023), pp. 1580–1586.

[285] M. Sacristán Barbero et al., »Characterization of Fragmented Ultra-high Energy Heavy Ion Beam and its Effects on Electronics Single Event Effect Testing«, in: *IEEE Transactions on Nuclear Science* (2024).

[286] K. Biłko et al., »Mixed-field Radiation Monitoring and Beam Characterisation Through Silicon Diode Detectors«, in: *IEEE Transactions on Nuclear Science* (2024).

[287] D. Di Francesca et al., »Distributed Optical Fiber Radiation Sensing in the Proton Synchrotron Booster at CERN.«, in: *IEEE Trans. Nucl. Sci.* 65 (2018), pp. 1639–1644, URL: `https://cds.cern.ch/record/2644042`.

[288] D. Di Francesca et al., »Dosimetry Mapping of Mixed-Field Radiation Environment Through Combined Distributed Optical Fiber Sensing and FLUKA Simulation«, in: *IEEE Transactions on Nuclear Science* 66.1 (2019), pp. 299–305, URL: `https://ieeexplore.ieee.org/document/8540062`.

[289] *iXblue Photonics*, URL: `https://photonics.ixblue.com` (visited on 11th June 2021).

[290] D. Di Francesca et al., »Radiation Hardened Architecture of a Single-Ended Raman-Based Distributed Temperature Sensor«, in: *IEEE Transactions on Nuclear Science* 64.1 (2017), pp. 54–60, URL: `https://hal.archives-ouvertes.fr/hal-02061611`.

[291] H. Henschel et al., »Fibre optic radiation sensor systems for particle accelerators«, in: *Nucl. Instrum. Meth. A* 526 (2004), pp. 537–550, URL: `https://inspirehep.net/literature/660318`.

[292] J. E. Moyal, »Theory of ionization fluctuations«, in: *The London, Edinburgh, and Dublin Philosophical Magazine and Journal of Science* 46.374 (1955), pp. 263–280, eprint: `https://doi.org/10.1080/14786440308521076`, URL: `https://doi.org/10.1080/14786440308521076`.

[293] G. Cordeiro et al., »The beta Moyal: a useful skew distribution«, in: *International Journal of Research and Reviews in Applied Sciences* 10 (2012), pp. 171–192, URL: `https://www.arpapress.com/Volumes/Vol10Issue2/IJRRAS_10_2_02.pdf`.

[294] C. Walck, *Handbook on Statistical Distributions for Experimentalists; International Report SUF-PFY/96-01*, Stockholm, Sweden: University of Stockholm, 2007.

[295] *scipy moyal package*, https://docs.scipy.org/doc/scipy/reference/generated/scipy.stats.moyal.html, (visited on 31st May 2022).

List of Abbreviations

AD antiproton decelarator. 7

ADT transverse damper. 31

ADTA transverse damper amplifier. 31

ADTK transverse damper kicker. 31

AL3X a laboratory for long-lived exotics. 165

ALICE a large ion collider experiment. 3, 7, 184

AmBe americium-beryllium. v, vii, xii, 119–127, 182, 232, 238

ASIC application specific integrated circuit. 75, 78, 84, 147, 161

ATLAS a toroidal LHC apparatus. 3, 4, 7, 10, 12, 75, 131, 143, 150, 151, 168, 177, 183, 225, 233

BatMon battery radiation monitor. xiii, 75, 165, 166, 175, 176

BCT beam current transformer. 37, 46, 49, 59, 60, 63, 71, 226, 228

BGC Beam Gas Curtain. v, vii, x, xi, xiii, 5, 22, 27, 28, 31, 32, 37, 39, 40, 43, 45, 57–69, 71, 131–133, 139–142, 144–146, 148, 150, 152, 155–158, 161, 181–183, 197, 225, 226, 228, 229, 232–234, 237, 238

BGI Beam Gas Ionisation. 27, 41, 53

BGV Beam Gas Vertex. v, vii, ix, x, 5, 27–29, 37–40, 47–58, 62, 63, 71, 181, 197, 225–227, 237

BI beam instrumentation. 67

BLM beam loss monitor. 4, 21, 22, 43, 46–53, 56, 57, 59–67, 71, 75, 131, 133, 139, 140, 142, 150, 166, 181, 193–195, 225–229, 232, 233

BLMs beam loss monitors. 22

BQS beam quality Schottky. 34

BSM beyond the standard model. 3, 165

BSRT beam screen radiation telescope. 27, 33, 34, 59, 226, 228

CALLAB calibration laboratory. 91, 92, 94, 96, 115, 119, 127, 182, 230, 238

CALS CERN accelerators logging service. 22

CCD charged-coupled device. 187, 188

CDF cumulative distribution function. 41, 48, 49, 52, 58, 63, 65, 197, 198, 226–228

CERN European organisation for nuclear research. ix, 3–5, 7, 9, 11, 12, 17, 18, 47, 53, 57, 75, 82, 92, 96, 97, 119, 125, 127, 155, 165, 181, 182, 188, 194–196, 225, 241

CHARM CERN high energy accelerator mixed-field. 7, 140

CLEAR CERN linear electron accelerator for research. 7

CLIC compact linear collider. 11

CMOS Complementary MOS. 187, 188

CMS compact muon solenoid. 3, 4, 7, 12, 168

CNA centro nacional de acceleradores. 92, 97–99, 101, 103, 112, 113, 127, 182, 230, 238

CODEXb compact detector for exotics at LHCb. 5, 165–168, 175, 183, 239

COTS commercial off-the-shelf. 12, 71, 188

CP charge parity. 3

CPU central processing unit. 142

CR counting rate. v, 137, 138, 146, 161, 183

DAC digital to analogue converter. 77, 78, 85, 103, 110, 120

DBCT direct beam current transformer. 37, 38

List of Figures

List of Tables

Acknowledgements

Working towards this doctorate has been an intensive journey that culminated in the writing of this thesis. If the content has extended to more than two hundred pages, then one more page to acknowledge the key players in my academic journey and the collective effort that research means will not disturb anyone, I hope. The acknowledgments are typically personal, and this one is no different.

Knowing that continuous supervision and support was always there allowed me to advance at the pace I aimed for. Innanzitutto vorrei ringraziare Giuseppe Lerner, il mio supervisore del CERN, per la sua attenta guida in tutte le fasi di questo lavoro. Mi ha fatto sentire completamente libero di condurre la mia ricerca come volevo, pur avendo obiettivi chiari da raggiungere. Secondly, it goes without saying that the wider picture of the R2E context would not have been possible if it had not been for the R2E team, in particular, Rubén García Alía, the R2E project leader. Thirdly, I am thankful for the advice and useful tips leadership received from the SY-STI-BMI section leader, Francesco Cerutti, but also in a wider sense to my colleagues for making me feel at home and turning my stay at CERN into one of the best experiences I had.

A mis amigos españoles, Álvaro, Mario y Andre, solo puedo agradecerles por sacarme de casa más a menudo de lo que lo hubiera hecho solo, pero también por ayudarme a aprender español. Amongst many friends&colleagues, onder vele vrienden en collega's kan ik Andreas niet vergeten, met wie we bijna twee keer de CERN estafetterace hebben gewonnen; Natalia, moja kolegyňa z kancelárie, ktorá mi vždy pomohla s otázkami týkajúcimi sa Timepixu. Un loc special îl are fără îndoială Robică, împreună cu care visăm la România precum ne-am dori noi să fie. Člověku by slunce nechybělo, kdyby nikdy nepršelo. Podobně byla Eva nějakou dobu mým sluncem v CERNu. Děkuji, že děláte mé dny více vzrušujícími. O único grupo onde eu sempre me senti incluído foi o meu incrível time de Futsal: Cris, Jorge, João, Rafa, Manu, Joe, Ricardo, Javi, José. Juntos, enfrentamos muitas batalhas, conseguindo até vencer dois torneios. Em comparação com essas lutas, o trabalho desta tese de doutorado definitivamente pareceu mais fácil.

La final, le sunt recunoscator membrilor familiei mele "extinse" de acasă, nu numai pentru susținere și încurajare, ci și pentru că au crezut în mine că sunt capabil să îmi urmez visele academice. Doamna profesoară de fizică Mirela Chelba mi-a fost ca o a doua mamă, descoperind și sădind în mine pasiunea pentru fizică. Tin minte și acum cum m-a intrebat pentru prima dată dacă vreau "să lucrez suplimentar câteva exerciții". Muschetorilor mei, George, Ștefan și Cosmin, le urez ca toată susținerea și încrederea pe care mi-au acordat-o să li se întoarcă cel puțin înzecit.

M-am bucurat de-a lungul anilor de dragostea necondiționată a părinților mei, Gheorghe și Mărioara, și a fratelui meu, Adrian. In pofida distanței, am știut mereu că sunteți acolo dacă aș fi avut nevoie de ajutor. Cea mai mare dorință pe care o am este sa împărtășesc cu voi entuziasmul pentru știință, și aș vrea, în mod special, să le spun lor ca îi iubesc. Este un sentiment special să îi am alături de mine.